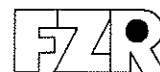# Institute of Nuclear
and Hadron Physics
&
Radiation Source ELBE

Annual Report 2001

FORSCHUNGSZENTRUM ROSSENDORF   FZR

Mitglied der Wissenschaftsgemeinschaft Gottfried Wilhelm Leibniz

Annual Report 2001

Institute of Nuclear and Hadron Physics
&
Radiation Source ELBE

Editors:

F. Dönau, W. Enghardt, E. Grosse,
B. Kämpfer, U. Lehnert, P. Michel, M. Schlett

Contents

Hadron Physics   47

Nuclear Physics   71

Biomedical Research   87

Author Index

Publications and Talks

Personnel

Preface

In the Forschungszentrum Rossendorf (FZR) at Dresden research is performed using radiation and radioactivity in the life sciences as well as in environmental chemistry, materials research, nuclear physics and safety research. The center belongs to the Wissenschaftsgemeinschaft G. W. Leibniz (WGL), one of the German institutions devoted to extra-university research.

Among the five institutes of the FZR the "**Institut für Kern- und Hadronenphysik**" (Nuclear and Hadron Physics, IKH) is special in the sense that it is equally engaged in fundamental research on subatomic systems and radiation as well as in the transfer of experimental and theoretical techniques from particle and nuclear physics to the life sciences. A second pillar of the FZR's involvement in the technology transfer to biomedical research and other non-nuclear fields is the newly founded central department "**Strahlungsquelle ELBE**", responsible for operation and further development of the Radiation Source ELBE. This new research instrument of the FZR is centered around a state-of-the-art superconducting electron linac which started its operation in May 2001. From the electron beam of up to 1 mA at energies between 10 and 40 MeV intensive secondary radiation is generated: for the medium and far infrared (IR) two free electron lasers (FEL) have been installed, whereas keV-X-rays will be produced via electron channeling in single crystals. Bremsstrahlung photons in the MeV range are a very interesting probe for investigations in nuclear spectroscopy and astrophysics. Such high energy photons also allow the generation of fast neutrons in sub-ns bunches as typical for ELBE; these are of special interest for cross section measurements using time-of-flight techniques.

The Institute for Nuclear and Hadron Physics (IKH) and the ELBE-department publish this Annual Report 2001 together. Its first chapter describes the progress made in the completion and the commissioning of ELBE and especially its central part, the superconducting accelerator with its electron injector. It also contains contributions on the production stations for the different kinds of secondary radiation and on the development and testing of experimental equipment installed for their use not only by researchers from FZR groups but also by outside users. The theoretical performance studies for the IR-FEL and the detailed work on the magnetic undulators constitute an important contribution to the successful operation of the ELBE-FEL's. Similarly numerical simulations were performed for the optimization of the X-ray and the MeV-photon production areas to allow experiments at ELBE with considerably reduced background.

Hadron Physics at the IKH - as described in the second chapter - deals with hadronic interactions as such and within the hadronic medium formed in collisions between nuclei or in violent astrophysical events like supernovae. Measurements of importance for this field were performed at the proton cooler synchrotron COSY at the Forschungszentrum Jülich and at the heavy-ion synchrotron SIS at GSI Darmstadt; the preparation and test of significant parts of the detection system of the large SIS-HADES experiment required an intensive effort at IKH. Theoretical studies refer to the question of a phase transition to a quark gluon plasma or a chirally symmetric phase which is predicted to occur at sufficient hadronic density.

The third chapter combines experimental and theoretical research in Nuclear Physics - mainly on electromagnetic processes in nuclei. The secondary ELBE beam of bremsstrahlung photons will play an important role in the simulation of processes occurring during the stellar synthesis of the elements. Photon or electron induced fission will be of interest as the source of neutron rich nuclei whose properties are of special importance for the detailed understanding of the stellar element cooking. Neutrons in the MeV range can also be used to answer nuclear astrophysics questions. They and especially the bremsstrahlung photons will as well allow interesting investigations on specific nuclear structure problems.

Furthermore this Annual Report contains a chapter on Biomedical Research performed by using nuclear technology. In the past the main contribution of the institute to this field came from Positron Emission Tomography (PET) and the outstanding achievement here is the successful operation of a PET scanner at the time of tumor irradiation. The experience obtained with this device from the ^{12}C-ion beam treatment of more than 100 patients at the experimental tumour therapy facility of GSI shows that precision, reliability and reproducibility of dose deposition is considerably improved. Recent experiments indicate the PET-method, as developed at the institute, to have a similar potential for proton beams, which are more frequently applied for therapy than heavy ions. In the upcoming years biomedical research will be performed increasingly with the beams coming from ELBE: The quasi-monochromatic X-rays of easily variable energy as produced in electron channeling will be used for preparatory studies in the field of photon activation therapy (PAT). Additionally they will be applied as a clean way to induce the elementary processes responsible for any type of damage in tissue caused by radiation. For a corresponding experimental study a cell laboratory was installed at ELBE, which will also be used for investigating the interactions of cells with the tunable infrared-radiation (IR) as available from the ELBE-FEL's. Interesting research in the life sciences will become possible by the combination of IR with the low bandwidth X-rays.

The scientific activities of the institute have benefitted from the support by various sources. First of all, we gratefully acknowledge the close and fruitful collaboration with the colleagues from the Technical University (TU) Dresden and many other scientific institutions in Germany and abroad; such contacts are of vital importance for our research. Specific projects were subsidized by the Federal Ministry for Education and Research (BMBF), the Saxon State Ministry for Science and Art (SMWK), Forschungszentrum Jülich and GSI Darmstadt. We express our gratitude to all these as well as to the Deutsche Forschungsgemeinschaft (DFG) and to the European Union (EU) for supporting several ELBE research projects.

Radiation Source ELBE

The superconducting electron linac

The new radiation source at the Forschungszentrum Rossendorf (FZR), the "Strahlungsquelle ELBE" will use the high brilliance electron beam from a linac with superconducting rf-cavities to produce various secondary beams for experiments in nuclear science, solid state physics, materials research, environmental chemistry and the life sciences. To present a comprehensive status report of this important and innovative project the present Annual Report combines contributions made to it by the newly founded Department "Strahlungsquelle ELBE" as well as by the Institute of Nuclear and Hadron Physics.

2001 was a decisive year for the radiation source ELBE . The first cryomodule was cooled down to liquid helium temperature in January, and in May the electron beam was accelerated to an energy of 5 MeV. The members of the machine advisory committee greatly acknowledged the achieved progress at the May 23rd meeting. In the months following all components belonging to the first stage of ELBE were successfully put into operation. The main beam properties were measured and it was shown that all major design parameters could be reached with the ELBE accelerator.

The six months of commissioning ELBE were important not only for verifying the beam parameters but also for gaining experience in operating the machine - in some cases, in a quite painful way. Two times, for instance, broken RF-windows led to a sudden loss of the insulation vacuum of the cryomodule, amazingly without severe consequences. As the result of this experience a number of modifications were required to various machine elements. Many of these changes are already completed but a few are still outstanding. The problems associated with the RF waveguide window arose from true CW rather than pulsed operation. They were solved with the addition of active pumping, installing arc detectors, and adding a thermal monitor to the window. These modifications were then included into the machine interlock system, which in turn led to a safe high-power operation. At the beginning of 2001 there were high voltage discharges at the 250 keV electron gun. These repeatedly damaged electronic components of the accelerator and its control system. Actions to reduce the particularly high electric fields outside of the gun eliminated these arcs. Additionally, a sophisticated grounding and blocking system was implemented and the use of more robust electronic components prevented further failures.

In August 2001, during high-power testing, an errant electron beam damaged the beamline in the diagnostics region. This lead to a vacuum leak and contamination in the SRF cavities. As a consequence, the maximum achievable accelerating gradient, particularly in the second cavity, was reduced. Therefore, beam parameters such as bunch length and emittance were measured at 12 MeV beam energy instead of the previously reached 20 MeV. Despite this limitation, by December 2001 all planned measurements have been completed and are in good agreement with previous simulations. In order to again reach the full accelerating gradient, both cavities have to be disassembled, chemically processed, and reinstalled into the cryomodule. This procedure is planned for the second half of the year 2002, when the second cryomodule is functional and will be exchanged for the first one. To prevent the reoccurence of such an incident a fast-closing vacuum valve has been installed downstream of the cavities. This will prevent a vacuum loss in the experimental areas from reaching the accelerator. Additionally, the beam-loss monitoring system, which is crucial for safe high-power operation but which did not function properly, is being redesigned.

Based on the experience gained and the technical improvements made on ELBE there will be a smooth transition from the commissioning phase of the accelerator to first user operation during the year 2002.

Research with IR-FEL's and their radiation
The high brightness electron beam from the ELBE linac allows to make use of various processes which produce high quality electromagnetic radiation in a broad range of energies. With the electron energy range available at ELBE coherent infrared radiation from 300 μm (corresponding to 1 THz) to 3 μm (equivalent to 0.4 eV) can be produced in a Free-Electron-Laser (FEL) arrangement. The FEL radiation is emitted in short pulses of a few ps and with a large repetition rate finally allowing tens of watts average intensity. Optimum IR-beams require a sufficiently small electron beam emittance as well as maximum regularity of the undulator field and the optical resonator. A split of the undulator into two sections enables special operation regimes like an optical klystron mode. At long wavelengths some limitations result from strong diffraction effects and various theoretical and numerical studies had to be performed to optimize the transport of the IR-beam to the user laboratories and experiments.

A cell-laboratory has been put into operation in the ELBE building to promote the radiation damage studies planned by the IKH employing the IR and X-ray beams.

X-rays, bremsstrahlung photons and neutrons
At ELBE quasi-monochromatic X-rays will be generated from the fast electrons by using the channeling process in single crystals (esp. diamond). To obtain the necessary high brightness e-beam space charge effects have to be minimized by reducing the bunch charge - and simultaneously increasing the repetition rate from 13 to 260 MHz.

Bremsstrahlung will be used at ELBE in the range of several MeV for the study of nuclear dipole excitations up to the Giant Resonance. New features are expected from high sensitivity experiments on nuclear resonance fluorescence and the nuclear photo effect. The required low background will be reached by a well shielded e-beam-dump, a beam transport in vacuum from the radiator to the nuclear target, a graded collimator made from pure Al - a material with low neutron production yield, an extended photon beam stop made from hydrocarbon surrounded by Pb, anti-coincidence shields around the detectors and a coincidence circuit suppressing radiation delayed with respect to the e-bunches.

The fast neutrons produced from the ps-e-bunches available at ELBE can be tagged such that a good energy resolution is obtained already after a few meters of flight path. The research envisaged here concentrates on energy dispersive studies of the interaction of fast neutrons with matter.

Collaborations
Within the FZR a close collaboration was established with the department 'Experimental Facilities/Information Technology' responsible for the installation of ELBE. Intense contacts also exist with the other Rossendorf institutes planning to use ELBE:

The Institute of Ion Beam Physics & Materials Research and the IKH have jointly installed equipment in the optics laboratories including a fs-laser system which is ready to be synchronized to the ELBE radiation bunches. This allows studies of the temporal e-bunch structure as well as investigations of fast pre-equilibrium processes by IR-pulses from the FEL, e.g. in biological systems.

The Institute of Safety Research has joined the DFG-project on the "Interaction of fast neutrons with matter, esp. with materials for and from fusion and fission reactors", which also includes groups from IKH as well as from Dresden Technical University. Within this project intensive numerical studies have been performed on the optimization of the generation of short neutron pulses from the ELBE e-beam.

Various collaborations have been formed to make use of the novel research possibilities offered by ELBE and its secondary beams. As a typical example the EU-project 'THz-Bridge' should be mentioned here; together with researchers from Frankfurt and Stuttgart universities and from four other EU-countries IKH-scientists collaborate in a study on the interaction of far-IR and THz radiation with living cells.

Test of the ELBE Cryogenic Accelerator Module

J. Stephan[1]

Beginning in 2001 the accelerator module LA 1 was finally assembled at the ELBE clean room complex. The module LA 1 design is drawn actually in figure 1. Test results for some important properties are described below.

After some warm tests and cool-downs cycles to liquid nitrogen temperature the first real cool-down with liquid helium started January 26, 2001. All systems of the module worked well during the test. But both accelerator structures (cavities) differed by more than 500 kHz in their resonating frequency which is far beyond the tuning range and they also showed a very small bandwidth. This was corrected after warm-up by manually fixing a new tuning offset and installing wave guide tuning devices.

Already the first cool-down demonstrated the advantage of carefully checked seal surfaces and of thoroughly selected gaskets. No leak disturbs the module operation after five cool-down cycles, although more then 220 seal connections are necessary between atmospheric air, helium or nitrogen gas pipes and the vessel insulating vacuum.

The second cool-down cycle pointed out that a sophisticated window diagnostics has to be installed to protect the RF-windows, particularly those made of plastic from continuous heat load and arcs. One window without diagnostics was soon destroyed during the tests. This caused a flow of warm air towards the deep cooled module parts. The liquid helium inside the cryostat tanks rapidly evaporated and went back to the refrigerating facility as big blow. Remarkably, no further defect was obtained thereby, only the one warm window was broken and all the relief valves were checked out to work well. However, the third cool-down found its end in the same way despite installing window diagnostics. After the window diagnostics shut off the low level RF-excitation, one of both RF-clystrons kept working and excited wave guide and cavity. Parasitic oscillations of the clystron amplifier created a very high RF-field density and heated the Rexolite RF-window up to softening. Air streamed through the broken window at the velocity of sound and started burning like a deflagration after passing the hot broken window. The flame briefly reached the door knob and covered wave guides and RF-coupler inside with sooty coal. Surprisingly, this again caused no permanent harm to the module.

Some trouble was encountered with the helium supply system for the cryostats. Gas pressure oscillations detune the resonance frequency of the cavities with a mutual characteristic of about 36 Hz/mbar driving them beyond the working range of the RF phase control loop. These oscillations are caused by the refrigerating facility and could not be removed throughout the tests. A new design of the helium feed is intended to reduce the pressure oscillations inside the cryostat tanks.

The tuning system TS2000 was designed for a 2000 N load and for one tuning action per day. However, under real conditions the load reached more then 5500 N (caused by ~500 MHz offset tuning by hand) and more then five tuning actions per day. The tuning system still worked fine under these conditions over the whole duration of the test.

Both cryostat tanks are fitted together in a rather stiff mechanical tandem assembly. It hangs down from elastomer endposts using two suspension rods each side. The disalignment stayed below 10μm over the whole duration of the test. The system was proven to work well against vibrations and shock.
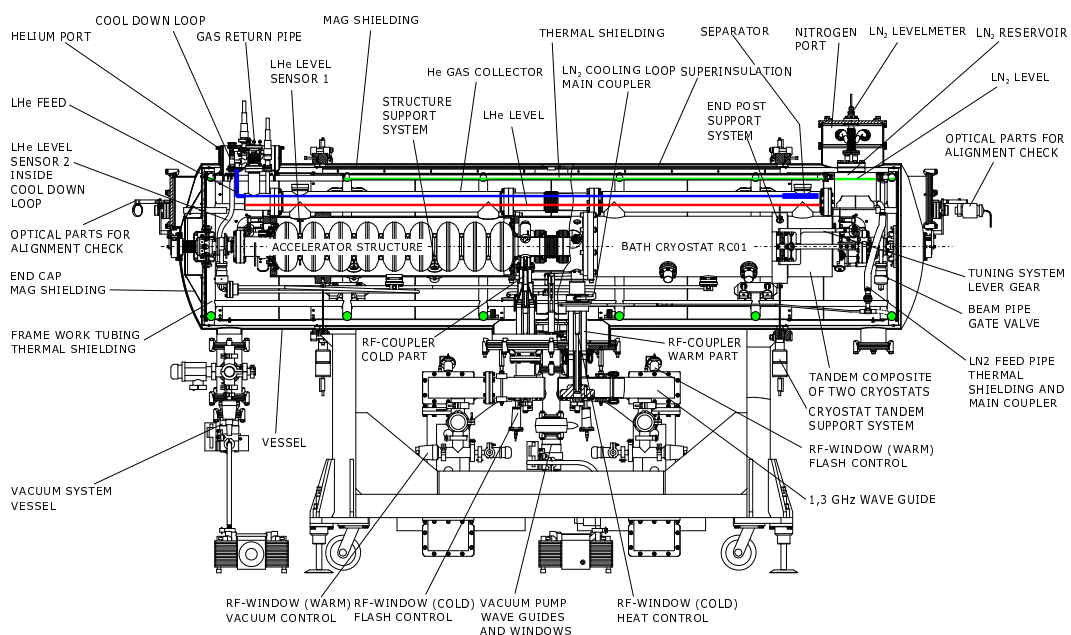
Fig. 1 *The ELBE cryogenic accelerator module LA 1.*

[1] *FZ Rossendorf, FWF*

The Helium Plant

Ch. Haberstroh[1]

For the helium plant the year 2001 was characterized mainly by putting into operation the first accelerator module. In the period before acceptance tests of the helium plant and peripheral devices were performed, as well as test runs and minor adaptations. The plant control (SIMATIC OP 37) was integrated into the overall control system; this allows today a very comfortable and effective access to all relevant actual data of the helium plant as well as trend analysis and data archive recall. Passive and (for operators) active access is available from a number of different places now. In addition a liquefier extension was specified, installed and put into operation, so that separate users of liquid helium can be supplied directly.

The operating experience from the first test period is characterized as follows: From the very beginning it was possible to uphold an continuous He-II regime. Despite intentional interrupts a several month accelerator test period could be obtained. Additional to the accelerator experiments this period was used for adjustment and adaptation between heat load (accelerator cryostat)

and cryogenic supply (helium plant). Optimal operating parameters and system behavior peculiarities were evaluated in a large number of systematic tests. A low frequency disturbance was observed mainly in the 16 ... 30 mbar pressure level. Having ruled out a number of possible effects, it could be identified finally as a pump mode of the turbo compressors due to extreme partial load conditions.

Evaluation of a number of accidental stops allows a first fault analysis. A large fraction of the events was due to faults of the electric power supply, of pressurized air or cooling water supply. In some transient regime a trip e.g. caused by turbine overspeed must be avoided. Control valves inside the cave are to be modified. The vacuum screw compressors were refurbished by the manufacturer. Losses of isolation vacuum in the accelerator cryostat resulting in heavy gas overload were endured by the helium plant without any problems. Nearly all these events could be overcome by own means, most of them within hours. At the latest after some days the plant was ready for restart again.

Helium Plant: Basic Facts

Outlines: Refrigerator and liquefier plant, specifically tailored, based on a Claude cycle with 3 expansion turbines (fourth in size all over Germany).

Components :

- 4 K basic plant: cold box; cycle compressor (split up into 266kW / 60 kW units for capacity adaptation), pure gas buffer ($20m^3$), gas management, built-in helium purifier

- 1.8 K extension: subcooling and distribution box, two stage cold compression, vacuum screw compressors

- liquefier modules: 2000 l storage dewar, decant and transfer lines, filling station for mobile dewars

- recovery system: recovery lines, gas bag (30 m^3), recovery compressor ($28 \text{ m}^3/\text{h}$), HP storage capacity (11 m^3, max. 200 bar)

Performance :

- full load
  220 W at 1.8 K + 220 W at 80 K (Pel = 417 kW)

- stand-by mode
  20 W at 1.8 K + 220 W at 80 K + 46 l/hr liquefaction (Pel = 311 kW)

- stand-alone liquefier
  75...156 l/hr (Pel = 271 kW ... 311 kW plus LN2-precooling)

- hold mode
  44 W at 70 K + 220 W at 90 K (Pel = 41 kW)

---

[1] *TU Dresden*

The RF Control System for the Superconducting Cavities - Experiences, Results, Improvements

F. Gabriel[1], H. Langenhagen[1], B. Caspar[1], A. Büchner[1], H. Büttig[1]

The commissioning of the RF control system together with the superconducting cavities began April 13th, 2001 after the cool down period. With a short break experiences were made for almost 8 months. The RF control system worked stable. This holds for a maximum mistuning of ±30% of the cavity bandwidth of roughly 100 Hz and for a He pressure stability of ±1 mbar of the cryogenic cooling system. For satisfactory accelerator operation the He pressure fluctuations should be in the range of ±0.05 mbar.

The frequency generation for ELBE is shown in Fig. 1. The first used VCO in the PLL for the 1.3 GHz reference frequency showed a phase noise which was in the order of half the working range of the phase loop of the RF controller. By replacing the LC-based VCO with a quartz controlled oscillator (VCXO) the phase noise was reduced by a factor of five.

The control loops for amplitude and phase for the 1.3 GHz cavities are shown in Fig. 2. The control loops for the bunchers are similar. A small periodic modulation of the electron beam energy, caused by the pressure instability of the He refrigerator, was suppressed by increasing the phase loop gain. The gain of the amplitude loop was reduced in order to prevent oscillations in macro pulse mode at large bunch charges. The gains are now approximately 70 for the phase loop and 25 for the amplitude loop, but they are not yet optimized. With the phase loop gain the phase jitter should be set to it's minimum value and with the amplitude gain the RF transient response should be optimized. The microphonics of the superconducting cavities at open phase loop (Fig. 1) is less then 1° (rms) corresponding to 2 Hz (rms).

To protect the accelerator against RF faults an interlock was installed which watches the control function of the amplitude loop. The measurements of the electron beam made showed the proper function of the RF control system in different accelerator operating modes.
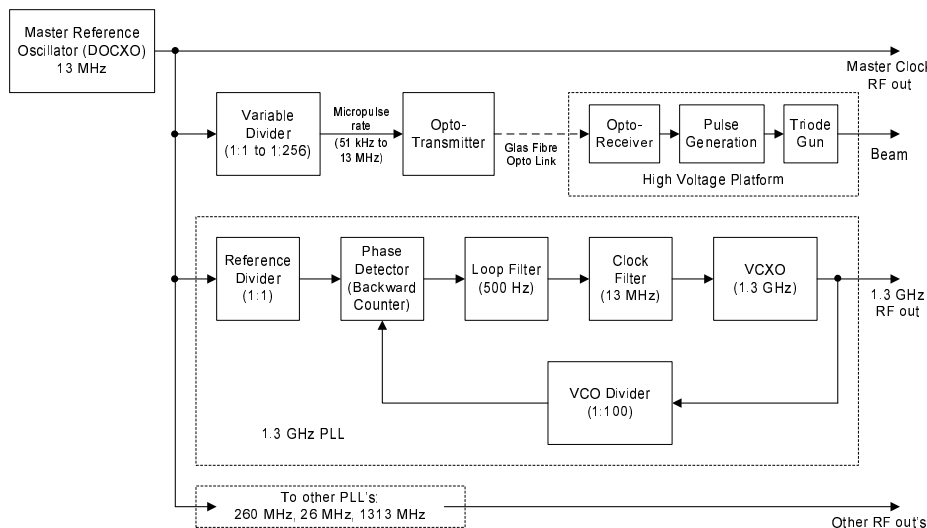
Fig. 1 *Frequency generation for ELBE.*
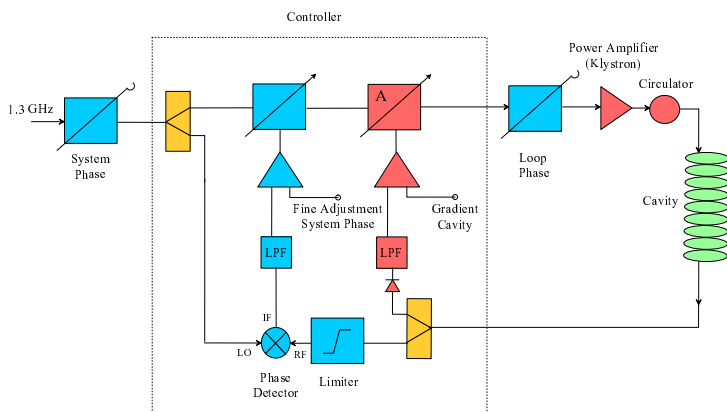
Fig. 2: *Control loop design for amplitude and phase.*
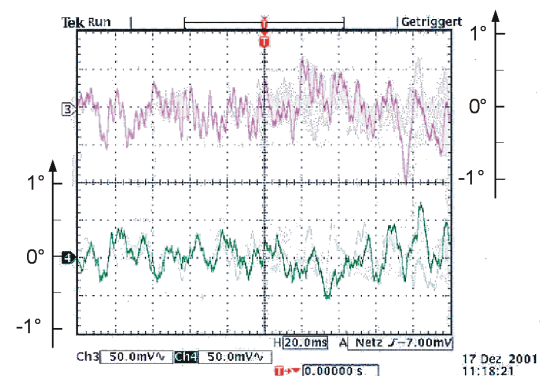
Fig. 3 *Signal of the phase detector output for open loop for cavity 1 (top) and cavity 2 (bottom).*

[1]*FZ Rossendorf, FWF*

Optimizing the Antenna Tip-Length of the ELBE Main RF Coupler

H. BÜTTIG

The first ELBE LINAC is equipped with two TESLA 9-cell cavities. The RF couplers are designed to feed 8...10 kW RF in cw-mode into each cavity. The coax-type coupler consists of a cryogenic part and was designed by Kimura and Smith at Stanford University [1]. The cold part of the coupler is directly fixed at the cavity using aluminum sealings. The other end is designed as a standard 3 1/8" coax connector cooled with liquid nitrogen (see Fig. 1). The coaxial warm part of the coupler was designed by J. Stephan at FZ-Rossendorf. Before assembling the cryostate the antenna tip-length of both RF couplers had to be optimized to fit the ELBE beam parameters. This procedure was done at room temperature with an uncleaned but tuned TESLA-cavity. The setup used is shown at Fig. 2. The coupling factor β at 2 K was chosen as a compromize between full energy transfer to the cw-beam of about 8 kW (10 MeV, 800 μA) and bandwith tolerable to deal with microphonics. The goal was to reach a loaded Q_L of about $1.25 \cdot 10^7$ and a bandwith $B = f_0/Q_L$ between 100 Hz and 150 Hz. It is assumed that the external Q_{ext} of a coupler is temperature independent and fixed by its geometry ($Q_{ext}(300\ K) \approx Q_{ext}(2\ K)$), while the unloaded Q_0 and the coupling factor β are temperature dependent. Therefore, the external Q_{ext} can be estimated from the loaded Q_L and the coupling factor β of an antenna measurement done at room temperature.

$$\beta = \frac{Q_0}{Q_{ext}}, \qquad \beta = \frac{P_t}{P_{diss}}, \qquad Q_L = \frac{Q_0}{1+\beta}$$

To measure Q_L the cavity was equipped with a perfectly matched antenna, a needle, critically coupled with β=1 and mounted on axis through the beampipe. If the antenna is not perfectly matched, one gets β by measuring the standing wave ratio using $P_{diss} = P_{fwd} - P_{ref}$. At perfect matching the transmitted power is coupled to the cavity without being reflected ($P_{ref} \sim 0$, $P_{diss} \approx P_{fwd}$) and the loaded Q_L for β=1 is half the unloaded Q_0. The unloaded Q_0 of the used cavity is $2Q_L$=17960 at 300 K. Next step is to determine β of the main coupler (used as pickup in the experimental setup) by measuring its transmitted power P_t with a spectrum analyzer. Because of the low coupling this measurement must be done very accurately. To keep an exact match during the measurements the frequency generator is phase-locked to the cavity. To meet the requirement of $Q_{ext} = 1.25 \cdot 10^7$ Q_L and β were measured at 300 K for three different antenna tips as shown in Fig. 3. From Fig. 3 one now can estimate the needed tip length of the antenna. For $Q_L = 1.25 \cdot 10^7$ β has to be $1.44 \cdot 10^{-3}$ at 300 K. Following this procedure the loaded bandwidth for the first cavity was 128 Hz. It turned out that the bandwidth of the second cavity equipped with the same antenna tip was only half of that. To avoid failures like this it is proposed to optimize each coupler if it is attached to its origin cavity. A three-stub tuner in the waveguide could be used to correct the bandwidth of that cavity and to operate both cavities with equal bandwidth. Both cavities were successfully put into operation.

Fig. 1 *RF coupler assembly.*
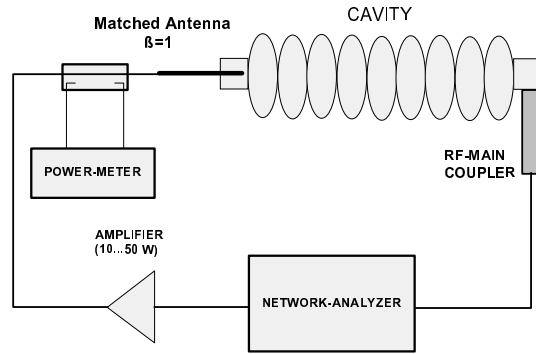
Fig. 2 *Test setup.*
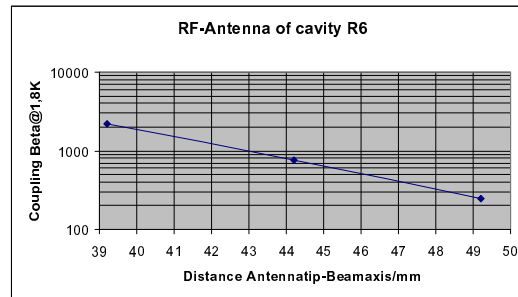
Fig. 3 *Tip-length vs. Q_L curve.*

[1] T.Kimura, T.Smith: RF Coupler for SCA Upgrade, Internal Paper, HEPL, Stanford (1997)

RF Window Diagnostics at ELBE

A. Büchner[1], J. Stephan[1]

During the RF test after the first cool-down a warm RF window was broken. The reasons were obviously a bad vacuum at the window position and the missing window diagnosis. Therefore, a test stand for the warm windows and the window diagnosis was built. The design of the parts surrounding the warm windows was changed, too. An extra pump markedly improved the vacuum conditions. The position of the standing-wave field minimum for full reflection was chosen for the window position. At low beam currents and with the use of the macro pulser the full reflection is the most common RF operating mode at ELBE. The warm window diagnosis consists of window temperature monitoring, vacuum monitoring and monitoring for light flashes.

The window temperature measurement is done by a "Thermalert GP Monitor" from Raytek with a GPM sensor 2:1. The resolution is 0.1°C. The sensor works from 8 μm till 14 μm. For vacuum measurement "TPG 251 A" devices from Balzers with "Compact FullRange Gauge PKR 250"-measuring gauges were used. The detection of light is done by a H5783 photomultiplier from Hamamatsu and a modul from DESY, which amplifies and monitors the signal. Temperature and vacuum monitoring are intrinsically safe, light monitoring is not. Therefore a test LED was built in, which produces a light signal of 0.5 lux.

To be safe, the same light monitoring was realized for the cold windows (Fig. 2). The vacuum level for the cold windows is approximately the same as for the warm windows. At the test stand two warm windows were trained with a maximum equivalent RF power of 40 kW in pulsed and in cw operation. Pulsed operation was possible up to full power. No light or vacuum events were observed. The windows showed only a warming, which limited the equivalent RF power in cw mode to 13 / 18 kW. The vacuum did not change significantly in this case. The thermal time constant is about 10 minutes, so the final window temperature is reached after 45 minutes.

After window training at the test stand the windows and the diagnosis were built into the accelerator. If any measured windows diagnosis value exceeds its limits, an interlock signal is generated which shuts down the RF power. The following limits are used:

Vacuum:	turn off limit $2.0*10^{-5}$ mbar
	turn on limit $1.0*10^{-5}$ mbar
Temperature:	turn off limit 70°C
	limit for intrinsically safe operation 10°C
	hysteresis 1°C
Light:	0.2 Lux at window position

After the second cool-down quite often flashes at all windows were recognized. Any wrong RF operation, for instance the loss of control in a control loop, caused window interlocks. It turned out that window diagnosis is a very important tool for machine protection. But it is not yet understood why flashes in the machine occur although no flashes could be observed at the window test stand during training of the warm windows.

After some changes in the RF power system a second time a warm window was broken caused by an oscillating RF power system. From the logged data it could be shown that the window diagnosis worked as expected and generated all corresponding interlock signals, but the interlock system was unable to switch off the RF power. The switches were realized in the low-level RF system which had no influence on the oscillating power system. After that event also the high voltage power supplies of the klystrons were included in the interlock system. It is hoped now that this way any further window break downs by the RF system can be avoided.
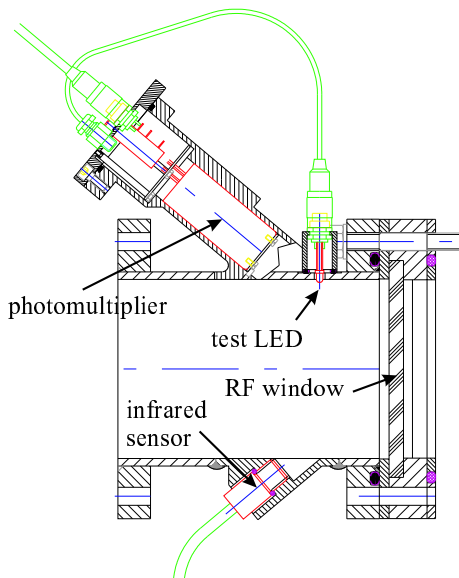
Fig. 1 *Principal view of warm window diagnosis.*
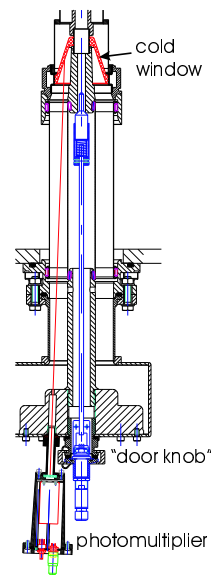
Fig. 2 *Principal view of cold window diagnosis.*

The ELBE Control System

W. Gläser[1], F. Herbrand[1], R. Jainsch[1], K.-W. Leege[1], D. Pröhl[1]

The control system provides the human-machine interface of the accelerator. It enables an easy to survey and reliable operation of the facility, providing a graphical representation of machine parameters and their time behaviour to the operator and supplying the parameters for technical and physical calculations. In addition, the system holds the data sets for different machine setups and logs measured values for later evaluations.

For these tasks the system WinCC (Windows Control Center) from SIEMENS is used as a multi-user system with a WinCC server and several WinCC clients on the basis of Personal Computers under the Microsoft Windows NT operating system.
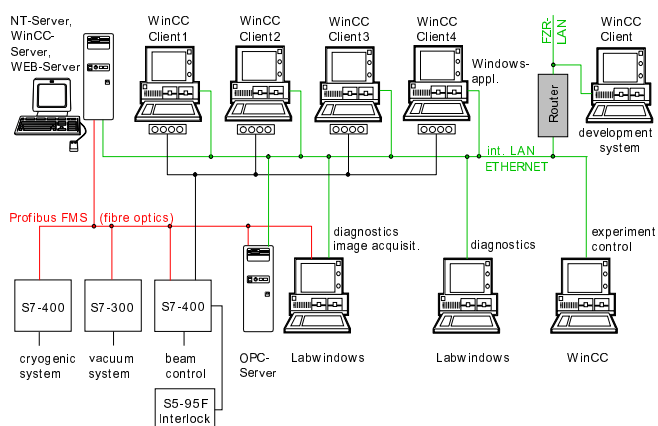
Fig. 1 *The basic structure of the control system at ELBE.*

The WinCC server communicates via PROFIBUS with the process layer and is managing the process data. The data exchange between the operator stations and the accelerator equipment is running through the WinCC server, which also performs the archiving of process data as well as global tasks in the entire project. All manipulations are done by clients in the control room and - in a restricted manner - in the experimental areas. The reliability with regard to access and operating permissions is guaranteed by the WinCC and the operating system of the PCs (Windows NT), respectively.

A lower process layer is connecting the operator level and the components of the equipment concerned and operates largely autonomously. This system comprises the control of electron beam, vacuum system, cooling system, machine interlock system and personnel safety system. For this functions programmable logic controllers (PLC) with local peripheral devices made by Siemens incorporation are used in form of a distributed system. For the personnel safety system we use a SIMATIC-S5 PLC. The used modules are designed for high safety requirements. All the other PLC's are descended from the SIMATIC-S7 system. The basic feature of these PLC's is a high availability, high efficiency, and a lot of analog, digital and serial interfaces. They serve to acquire analog input data, as currents, voltages, pressures, dose rates etc., as well as to output analog values to the pro-

cess, as set values for current, voltage etc. In parallel to that, a large number of binary values can be read (status) and written (commands). All these values are stored in so-called data sets in the buffered RAM of the PLC. They are available for display at the higher operator level and can be influenced by the control system. In addition, also logical operations, interlocks, monitoring and control are performed at this hardware-based level. The entire control system is organised in separate modules and constructed in a task-oriented manner.

The local peripheral devices as well as the WinCC are connected to the CPU of the PLC via fibre optic cables. The advantage is the low sensitivity against interference. In addition we are using this for a connection to the local peripheral device on the high voltage terminal of the electron gun. The interconnection between the computers at the operator level is implemented as Ethernet.

With serial interfaces of the PLC's we control a lot of power supplies with different currents for steerers, quadrupoles and dipoles. Part of the power supplies for currents up to 10 A are self-made. We control 8 of them with one digital serial to parallel converter. The larger power supplies (30, 60 and 160 ampere) are bought from Danfysik. In support of a "visual" beam control a special bus (DG-Bus) was developed, which enables the connection of "quasi analog" wheels for setting beam control elements (steerer, lens etc.) by the operator.

The developing and testing of the control system in the first phase has shown, that this system works reliable with several WinCC-clients and is well suited for our application. It was also established, that it is practicable to develop software in the background, while the accelerator is running (in foreground), which is very important for the build up and testing phase of the accelerator.

The connection of the WinCC graphical user interface to other Windows applications (beam diagnostics with image processing, online help system etc.) was tested successfully by using OPC-calls and OLE-objects. The signal acquisition from the fast devices for beam diagnostics is done with data acquisition boards respectively frame grabbers (for recording and analysing the view-screen displays) under LabWindows/Labview by National Instruments. The data acquisition boards are PXI and Compact PCI modules housed in PXI-Crates in the electronics room. The crates are connected with a fibre optic fast serial link (MXI-3 PCI-PXI bridge) to PCs in the control room. One crate with 6 CPCI-510L cards from DATEL (16 simultaneous channels, 12 bits) is used to acquire BPM signals. The second crate is equipped with a PXI-6071E card (64 analog channels, 12 bits, 8 digital I/O-ports) to perform RF power measurements and to control a matrix switch. A 16-port RS-232 card (PXI-8420/16) is used to readout the LB 111 Micro Gamma dose rate measuring system. All PXI components are made by National Instruments.

---

[1]*FZ Rossendorf, FWF*

The Video System for Beam Monitoring and Diagnostics at ELBE

R. Jainsch[1], D. Pröhl[1]

The video system is an integrated part of the ELBE control system. It consists of image acquisition hardware and different acquisition and evaluation programs running on PCs under Windows NT. Figure 1 shows the basic structure of the hardware. The cameras are monochrome tube cameras KH 500 (Saticon) from EG&G Heimann. Some modifications of the camera electronics were necessary to synchronise and trigger the image acquisition with the macro pulse.

A commercial video matrix system SYSTEM 1000M from Ernitec routes the video signals of the CCIR cameras to the frame grabber and the monitors. The video switch is controlled via RS-232 from the PC. A single-channel frame grabber (IMAQ PCI-1407 from National Instruments) is used for real time image acquisition.

The image acquisition program ELBE-VISION is developed in C with LabWindows/CVI and the IMAQ toolkit from National Instruments. In order to integrate ELBE-VISION into the control system, it uses the OPC technology to communicate with the WINCC to switch the camera automatically to the inserted viewscreen.

Live video images on the PC monitor give the operators a direct view to the beam, enhanced by optional graphical overlays (a cross marks the centre of the beam line). The operator can manually stop the acquisition to carry out offline processing (averaging, background subtraction and calculation of intensity profiles of the electron beam for diagnostic purposes). A ring buffer is used to store 50 images in the PCs memory.

Figure 2 shows a capture of ELBE-VISION with beam profiles. It is possible to store the images and profiles locally on the PC or send this data via DataSocket to other PCs for post processing. The video system was successfully used during the first operation period of the accelerator.

Fig. 1 Design of the ELBE video system.
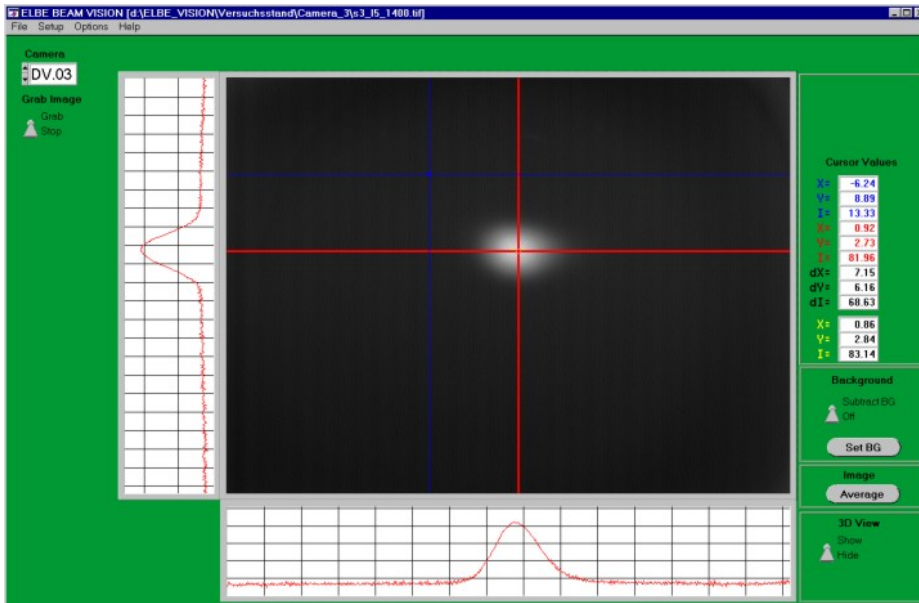
Fig. 2 Screen-shot of the ELBE-VISION display.

Electron Beam Macro Pulse Generation at ELBE

H. Langenhagen[1], D. Pröhl[1]

The macro pulsed operation mode of the ELBE accelerator is intended to control the average beam current - and therefore its power- by pulse width modulation. For that, the beam is deflected approximately 2 m behind the gun in a circular path and so kept away from the farther beam line. On this parking course the beam hits a cooled Cu aperture where its energy is converted into heat (see Fig 1.). For the duration of the beam pulse the deflection currents are switched off. The current of the vertical and horizontal deflection coils is depicted in Fig 2. The duration of the beam pulse is adjustable within 100 μs $\leq t_{dur} \leq$ 38 ms, with repetition rates of 40 ms $\leq t_{rate} \leq$ 10 s. Alternatively, it can be switched off completely for cw-operation.
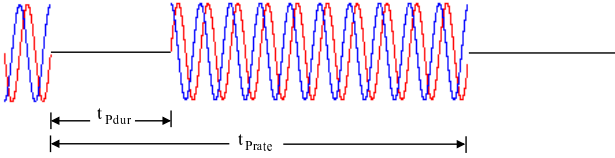
Fig. 2 *Time structure of the deflection currents.*

Except for the smallest pulse duration, for the choice of the deflection frequency also the necessary values of magnetic flux and the useable control range of the coil driver have to be considered. With the parameters flux Φ = 40 Aw, ranges of current and voltage I_O = 2 A, u_{Lmax} = 20 V (U_b = ± 24 V), one can calculate the frequency to $f \leq$ 14 kHz; it was chosen f = 10 kHz.

The coil driver operates as a current source (see Fig. 3). As a result of a stability analysis, the components C_k, R_k were determined. The input of this circuit get its signal from a stage, which shapes the sin/cos signals from two square waves with a shift of 90 degrees; the latter are derived from the micro pulse signal with a frequency of f = 13 MHz (master oscillator of the accelerator).

For diagnostics movable screens can be inserted into the beam path which produce an image of the beam cross section during the macro pulse. These screens are equipped with cameras connected to a frame grabber image acquisition system. Especially for small pulse durations it is necessary to synchronize the timing of the macro pulse, the cameras and the frame grabber (see Fig. 4).
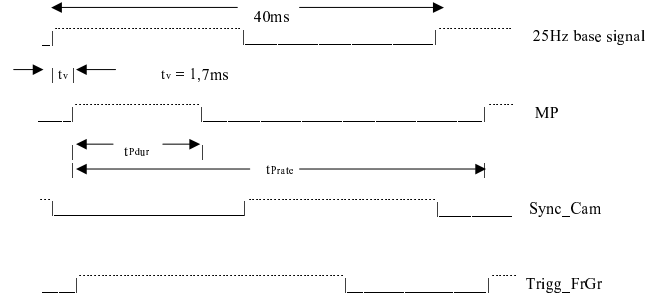
Fig. 4 *Time structure of the macro pulse and the camera synchronization signal.*

The central device for generating the signals is a counter with an adjustable divider, implemented in an FPGA. From the micro pulse frequency this counter provides a 25 Hz signal which is the base for all other time settings. Each of the signals is watched. In case of failures an alarm is activated.

All parameters of the pulser can be adjusted by the communication system SIMATIC-WINCC. The ranges of it are:

deflection current: amplitude: $0 \leq I \leq$ 2 A,
offset: $0 \leq I_{offs} \leq$ ±500 mA
pulse time: duration: 100 μs $\leq t_{dur} \leq$ 38 ms,
rate: 40 ms $\leq t_{rate} \leq$ 10 s,
both in time steps to 100 μs.

Fig. 1 *Deflection unit of the Macropulser. Two coil pairs are arranged as dipoles are fed with sin/cos- shaped currents to deflect the electron beam on a circular path.*
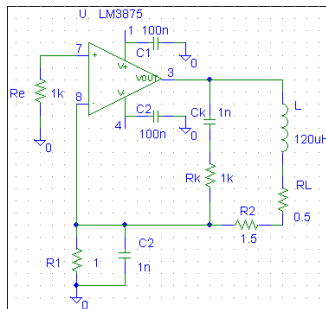
Fig. 3 *The current source and the open-loop frequency response of the circuit. C_k and R_k change the otherwise unsatisfactory characteristics and improve the phase margin at the 0-dB frequency.*
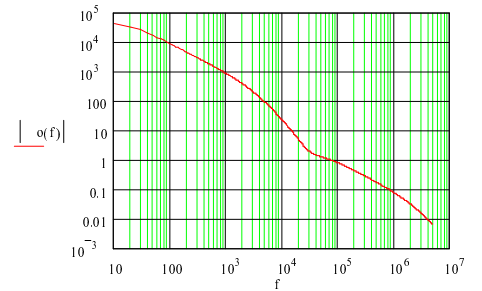
New Design of the ELBE Beam Position Monitors

P. Evtushenko, F. Gabriel[1], P. Michel, R. Schurig, B. Wustmann[1]

As reported before, [1,2] a system of stripline beam position monitors (BPM) is under construction for the ELBE accelerator. The BPM from the Jefferson Laboratory FEL machine was a prototype for the first version of the ELBE BPM. The construction was only changed to be appropriate for the ELBE beam line diameter and for the accelerator fundamental frequency of 1.3 GHz. Two BPMs were manufactured and successfully tested at ELBE. The BPM was used during the injector characterization. A resolution of about 10 μm at 1 mA beam current was achieved which is about ten times better than required.

However, we have faced some problems during the BPMs manufacturing. First of all, the SMA feedthroughs, which have to be electron beam welded to the BPM are very sensitive to mechanical stress. About half the feedthroughs were broken in the first welding attempt. Another problem is the length of the electrodes. To form the electrodes, a pipe with a diameter exactly like the beam line has to be made with four cuts. Because of mechanical stress in the beam pipe, the electrodes can change their position in respect to the pipe center. This leads to an impedance of the transmission line slightly different from the designed 50 Ω. The electrode displacement also imposes some danger for the feedthrough. Besides all of this we could not put the BPM at some desirable places because of its length and the place shortage. All these reasons required some changes in the BPM design.

The length of the BPM electrode in general is chosen such that the BPM has maximum sensitivity to the fundamental frequency of an accelerator. To satisfy this condition the length should be: $L = (2n + 1)\lambda/4$, where n is integer number and λ is the wavelength. The first ELBE BPM has the electrode length about 3/4 λ for 1.3 GHz. The main idea of the redesign was to make the strip length $\lambda/4$. At first, an electrical model of the $\lambda/4$ BPM was built and tested on a wire test bench (see Fig. 2). It was demonstrated that the resolution of the model is not worse than the 3/4 λ BPM resolution. After this successful test we have constructed a BPM with the electrode length of about $\lambda/4$ at 1.3 GHz. In the construction we used another type of the feedthrough, which is not welded to the BPM but sealed to it with a CF flange. Hard soldering is used in the construction instead of expensive electron beam welding. The feedthrough can be replaced any time, thus the BPM can be repaired without removing it form the beam line, which can keep a lot of time. Total length of the BPM is 85 mm from flange to flange. The $\lambda/4$ BPM is in factor two cheaper than first version.

For beam tests two $\lambda/4$ BPMs were manufactured without any technical and technological problems. The new BPM was tested at ELBE and has demonstrated resolution and dynamic range not worse than the first version of the BPM with an electrode length of 3/4 λ. Finally, it was decided to use the $\lambda/4$ BPM at ELBE.
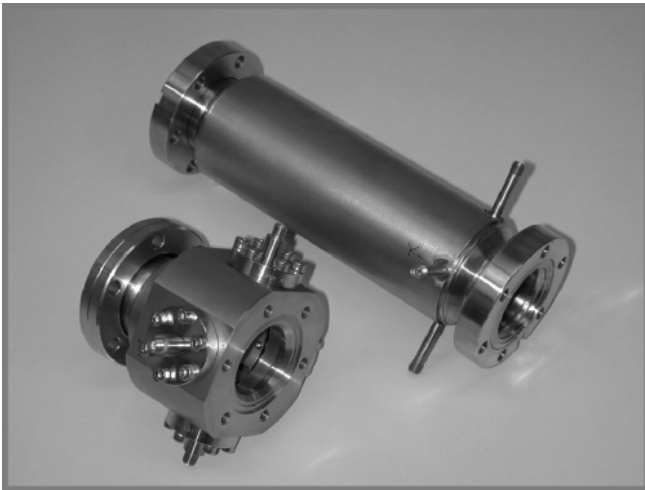
Fig. 1 *Photograph of both stripline BPM designs.*
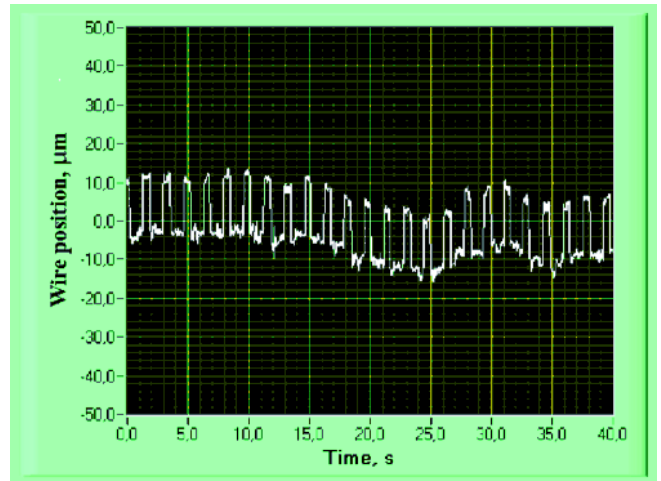
Fig. 2 *BPM test with a wire test bench.*

[1]   P. Evtushenko, A. Büchner, K. Jordan, P. Michel, FZ Rossendorf, Wiss.-Tech. Ber. FZR-319 (2001) 13
[2]   P. Evtushenko, A. Büchner, H. Büttig, P. Michel, R. Schurig, B.Wustmann, K. Jordan,
       Proceedings of the 5th European Workshop on Diagnostics and Beam Instrumentation

[1] *FZ Rossendorf, FWF*

Design, Construction and Test of Stripline BPM Electronics

R. Schurig, P. Evtushenko, F. Gabriel[1], H. Büttig

Commissioning and operating the ELBE accelerator requires exact knowledge and easy, reproduceable control of various parameters. Important parameters like beam position and beam current are measured with a system consisting of a stripline BPM (beam position monitor), conversion electronics, data acquisition and monitoring software. The design of the electronics is described in this paper.

Stripline BPMs are similar to directional couplers, they are well described in [1] and [2]. Energy from the fields generated by the electron beam is coupled out. The signal power on each of the four ports is proportional to the beam current and the beam position with respect to each "coupler" in an x/y-coordinate system.

The stripline BPM electronics has to convert the power signal from the BPM into a voltage, which is then fed into an ADC system. The BPM output power ranges from -80 dBm (lowest detectable beam current with no beam displacement) up to -25 dBm (maximum beam current, 10 mm off axis). The signal flow through the different conversion stages is shown in figure 1 (one channel).

The 1.3 GHz fundamental signal is selected by an external 5-pol interdigital filter (ID1300) having a 3 dB bandwidth of 8 MHz and 50 dB deep notches suppressing the neighbouring sidebands at ±13 MHz, caused by the 13 MHz micropulse repetition rate. Signal attenuation of the coax cables from the accelerator cave to the diagnostics room plus filter attenuation is about 5 dB, but exactly measured for each channel and considered in the software for calibration.

The first stage inside the electronics housing is an integrated MMIC amplifier with 20 dB amplification and a high IP3 level to avoid spurious signal generation. The central part is the AD8313 logarithmic detector made by Analog Devices Inc., converting the RF signal into a DC voltage. The dynamic input range of this detector is -65 dBm to -10 dBm for less than 1 dB conversion error. The two following rail to rail operational amplifiers LT1630 from Linear Technology shift and amplify the detector voltage to -5 V to +5 V which meets the input range of the ADC. Low offset voltage and temperature drift are essential here. In order to minimize crosstalk problems, each PCB-board contains the electronics for two channels housed in milled boxes, ensuring proper shielding against stray signals from the nearby klystrons, which may badly affect the measurement at low input levels. (Note, that the maximum klystron output is 10 kW, or +60 dBm and the minimum detectable electronic input is -85 dBm, so any leakage path must be prevented.) Two such boxes and a power supply make the system for one BPM.

Three units have been built and tested during commissioning of the first part of the ELBE accelerator. Sufficient sensitivity along with ruggedness against environmental effects, and long term stability were proven. Beam position resolution is 5 μm at 10 μA beam current. Crosstalk between channels was found to be lower than expected. Therefore, the next revision will house the electronics for four channels in one box and 10 such boxes in one 19" rack. It is necessary to include a sample and hold (S&H) stage to make the system work at repetition rates below 13 MHz which was not intended at the beginning of the development. A version with S&H has been built but not tested yet.
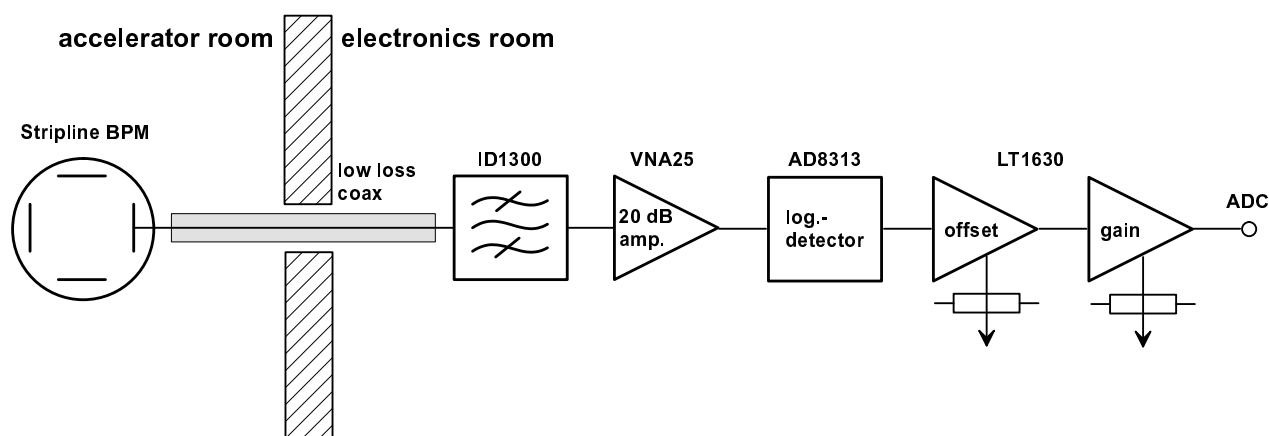
Fig. 1 *Stripline BPM electronics, showing the signal chain for one of four channels.*

[1] P. Evtushenko, A. Büchner, K. Jordan, P. Michel, FZ Rossendorf, Wiss.-Tech. Ber. FZR-319 (2001) 13
[2] P. Evtushenko, A. Büchner, H. Büttig, P. Michel, R. Schurig, B. Wustmann, K. Jordan, Proceedings of the 5th European Workshop on Diagnostics and Beam Instrumentation

---

[1]*FZ Rossendorf, FWF*

A Resonant Beam Current Monitor for ELBE

R. Schurig, H. Büttig, A. Büchner[1]

During the first stages of commissioning ELBE, the beam current could be measured directly at the gun, the macropulser aperture and at the beam dump. Later, a package consisting of a resonant beam current monitor (RBCM) and a resonant beam position monitor was added. The results of the RBCM tests are described in this paper.

The RBCM is actually a pillbox cavity made of stainless steel with a resonant frequency equal to the fundamental frequency of the accelerator (1.3 GHz at ELBE). The electron bunch excites a transversal magnetic mode (TM_{010}) when it passes the cavity. The electric field component for this mode points into the beam direction. The signal is outcoupled with two pickup antennas, as shown in Fig. 1.
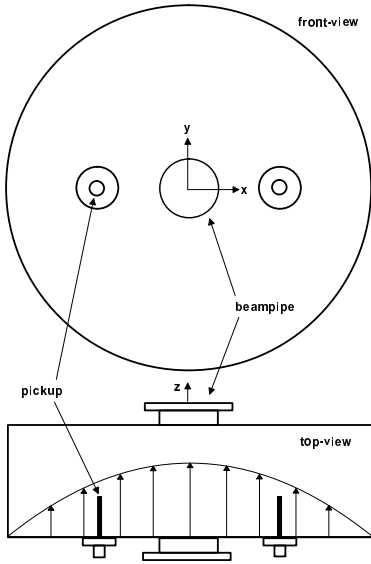
Fig. 1 TM_{010} beam current monitor.

The pickup signal is proportional to the RF power induced by the beam which in turn is proportional to the beam current scaled by the Q-factor of the cavity. The geometry and the position of the pickup antennas where calculated using Mathcad. A prototype cavity was measured on a test stand [1]. The resonance frequency was fine tuned at atmospheric pressure by slightly changing the length of the pickup antennas. It rises by 300 kHz when the cavity is evacuated. At a loaded Q of 1700 this shift is about half of the bandwidth and should be considered. No other tuning is required over the temperature range in the accelerator cave.

A second cavity was mounted at the beamline downstream the first ELBE cryostat in close proximity to a stripline BPM and a viewscreen for comparative measurements. During the measurements the macropulse rate was set to 50 ms with 5 ms pulse duration, and a bunch repetition rate of 13 MHz. The pickup signal shown in Fig. 2 was measured with a spectrum analyzer,

taking into account cable losses. Beam currents below 1 μA could not be measured because of the lack of an accurate reference. The thermal noise level can be calculated as $P_N = 10\log(kTB/1000)$ in dBm. At room temperature (300 K) and the given cavity bandwidth of 0.76 MHz the calculated noise floor is -115 dBm. Assuming cable losses of about 5 dB and 0.5 dB noise figure of the first amplifier stage, the sensitivity will be -100 dBm or 4 nA at a 10 dB signal-to-noise ratio.
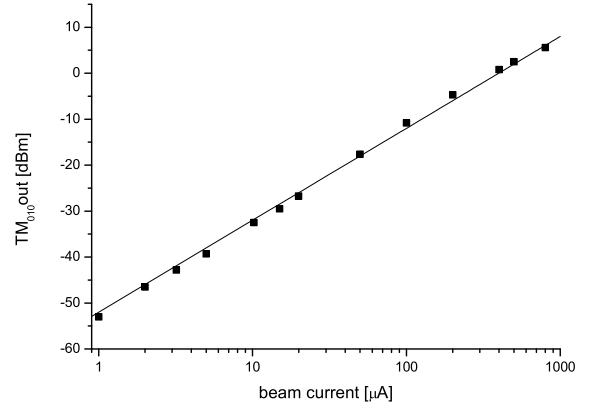
**Fig. 2** Pickup signal and 20 dB/decade regression line.

The dependence of the pickup output signal on the beam position was also measured. The beam current was set to 20 μA, a steerer about 2.5 m upstream the RBCM was used to deflect the beam in millimeter steps. A calibrated stripline BPM was used as reference. Fig. 3 shows the pickup output signal with respect to the beam displacement.
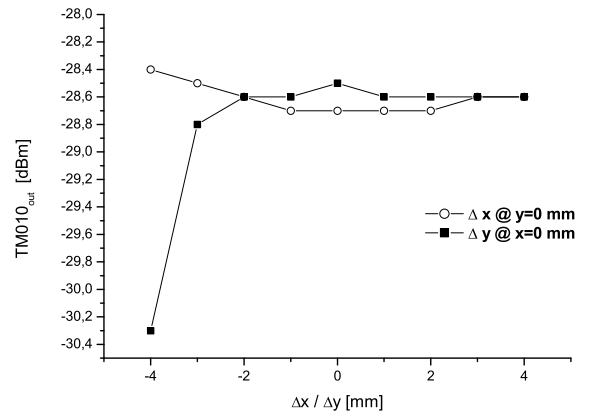
Fig. 3 Pickup signal vs. beam displacement.

The pickup output signals varied 0.3 dBm for ±3 mm beam displacement corresponding to an current measurement error of about 3.5%. At greater displacements we started to loose beam (see Fig. 3, Δy = -4 mm).

The RBCM has proven to be an accurate measuring tool which covers the whole range of beam currents used at ELBE.

[1]   R. Schurig, Beam Position Measurement for the ELBE-Linac, HTW-Dresden, Diploma thesis (2001)

[1] *FZ Rossendorf, FWF*

Design of a Secondary Electron Emission Beam Monitor

W. Neubert, K. Heidel, J. Hutsch, M. Langer, K.-H. Herrmann

For precise current measurements of low intensity CW-electron beams at ELBE the application of the standard strip-line beam-current monitors [1] is not feasible. For some types of experiments, e.g. the determination of the channeling radiation yields by means of photon counting detectors, such measurements are required. A commonly used instrument at electron accelerators in the MeV region is the secondary emission monitor (SEM) [2] consisting of metal foils which are traversed by the beam. The foils are alternatively phased in voltage. The secondary electrons ejected from the foils by the beam passage are collected onto the anode and the current is measured. In order to minimize the background radiation from the SEM we decided to test thin metalized Mylar foils. The power dissipation in such foils was simulated using the GEANT 3.2.1 code package. A 20 MeV electron beam with a Gaussian profile (FWHM=1.2 mm) passed through a $100\,\mu m$ diamond target (simulating the crystal for Channeling Radiation) and hits a foil of $3\,\mu m$ Mylar with 200 Å cover at one side. Fig. 1 shows the radial energy-loss distribution in the foil taking away $\simeq 9 \cdot 10^{-4}$ W/mm^2 in the region of a $1\,\mu A$ beam spot. The recommended maximum temperature of Mylar during permanent usage [3] is $\simeq 170\ ^oC$ which limits the beam current to ≤ 100 nA. Here we report on the mechanical construction of such a prototype detector and the corresponding electronical read-out. The device consists of a set of 3 stretched foils equally spaced by a distance of 3.9 mm using small glass spheres. The uncovered surface of the foil mounted as central electrode was ad-ditionally metalized by vacuum evaporation providing an Al layer of the same thickness. Since the yields of secondary electrons from surfaces of pure metals have nearly the same order of magnitude [4] we consider Al usefully. These foils were mounted on stainless steel support rings with a conical profile adapted to the counterpart. Teflon-insulated wires were soldered into the the steel rings to allow flexible electrical contact. The foil stacks were assembled under clean room conditions using frames of glass ceramics (VITRONIT) [5] with good insulator properties and suitability in ultra-high vacuum conditions (see Fig. 2). The described prototype will be mounted on a mechanical equipment which allows translations of $\simeq 80$ mm by means of a bellow mounted onto a flange. The current produced by the secondary electrons is fed into a current sensitive amplifier designed for a dynamical range from some nA to μA. The amplifier is based on the op-amp OPA 129 [6], which is equipped with an ultra-low bias current DiFET (typically 100 fA). The basic gain of this current-to-voltage converter amounts to $dV_{out}/dI_{in}=$ 100mV/10nA. The range of measurable currents can be changed by means of switching techniques and current scaling resistors. Response times from 1 ms are sufficient for an analog handling of the signals. Fig. 3 shows the result obtained by a transient simulation [7] for an alternating current source.

After completing the mechanical driving equipment this SEM prototype will be tested at the beam line of the electron accelerator ELBE.
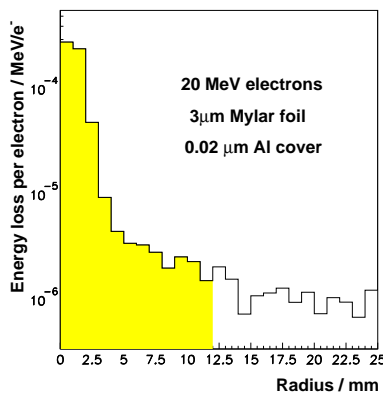
Fig. 1 *Simulated energy loss distribution deposited by the electron beam in one foil of the SEM. The hatched area corresponds to the SEM shown in Fig. 2.*
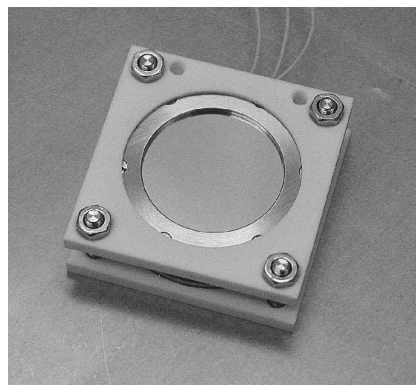
Fig. 2 *The assembled monitor (electrode planes embedded in VITRONIT spacers).*
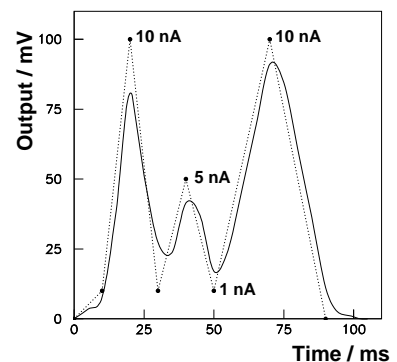
Fig. 3 *The simulated output signal of the current sensitive amplifier. An arbitrary current at fixed time was fed into the amplifier (black dots, connected by dashed lines). The response of the amplifier is shown by the solid line.*

[1] A. Büchner et al., FZ Rossendorf, Wiss.-Tech. Ber. FZR-319 (2001) 11
[2] V.J. Vanhuyse et al., Nucl. Instr. Meth. 15 (1962) 59
[3] http://www.goodfellow.com
[4] R. Kollath, Handbuch der Physik XXI (Electron emission and charge discharges I), Springer (1956) 232
[5] VITRON Spezialwerkstoffe GmbH, Otto-Schott-Str.13, 07745 Jena and http://www.vitron.de
[6] Burr-Brown Corporation 1994, http://www.burr-brown.com
[7] P.Spice Vers. 8.0, Cadence PCB System Division, http://www.cadence.com

Long Ionisation Chambers for Beam Loss Detection at ELBE

P. Michel, R. Schurig, U. Lehnert, J. Teichert, P. Evtushenko

In order to prevent the ELBE beam lines and other accelerator equipment from damage, an effective and reliable system for measuring beam loss is needed. The system has to fulfill two different functions. On one hand it generates a fast (~1ms) trigger signal when beam loss exceeds a preset value to shut off the beam current. On the other hand it gives online information about the origin (space along beam axis) and quantity of beam loss at relatively low beam loss values during operation. Latter function serves the operator to find optimal magnet settings for maximum beam transmission.

In order to find the most suitable detector for use at the ELBE accelerator three different systems were studied. These were photo multipliers with and without scintillators, Compton detectors [1] and long ionisation chambers (LIC) [2]. It turned out that long ionisation chambers are the optimal solution because of its adapted geometry, the linear signal characteristics over more than four orders of magnitude and the possibility to realize spatial resolution by segmenting the LIC. To set up a simple and inexpensive tube like ionisation chamber we used air filled HELIAX coaxial cable (5/8", air dielectric) [3]. The facing surfaces of the cable are bare copper spaced by a narrow spiral of polyethylene. To test the LIC under real conditions we produced a well-defined beam loss in a well-known place of the beam line. The chamber was installed parallel to the beam line at a distance of 20 cm. Fig. 1 shows the typical behaviour of an ionisation chamber with saturation of the signal with increasing the high voltage. At more than 300 V the signal height remains constant and the signal rise time approaches 0.6 ms, which was given by the integration time constant of the measurement.

Under these conditions we determined the minimum measurable beam loss of a 12 MeV electron beam to be 300 nA. Because of the high sensitivity of the detector, it can be used to find the best magnet settings during operation, without the risk of damaging any beam line components. Fig. 2 shows the detector signal when the beam was steered from one tube wall to the other one.
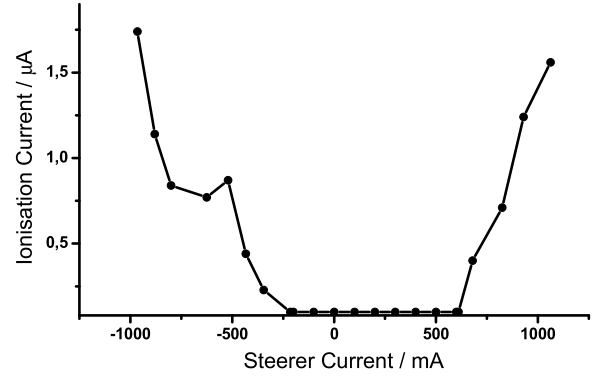
Fig. 2 *Beam loss distribution measured with LIC steered between beam tube walls.*

Investigations of the detector signal along the beam line axis showed that segmenting the ionisation chamber into 50 cm long sections is appropriate, since this corresponds to the width of the signal distribution at a detector distance of 20 cm, shown in Fig. 3. Presently the concept of data read out electronics is under development.
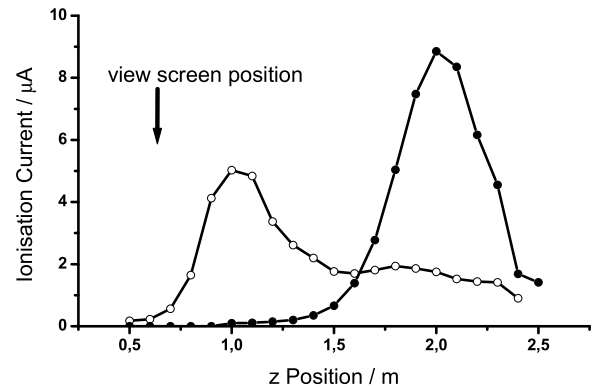
Fig. 3 *Longitudinal beam loss signal distribution produced at an inserted OTR beam viewer (open dots) and from a point source obtained by steering the beam to strike one side of the tubing (filled dots). Distributions were measured with a 20 cm long HELIAX cable moved parallel to the beam line at 20 cm distance.*

Fig. 1 *Measured ionisation current and signal rise time of 50 μA beam loss at 12 MeV electron beam energy.*

[1]   J. Teichert et al., This Report, p. 18
[2]   W.K.H. Panofski, SLAC Int. Rep. TN-63-57 (1963)
[3]   ANDREW HJ4.5-50 HELIAX specification

Experimental Study and Simulation of Compton Diodes for Use as Beam-Loss Monitors

J. Teichert, P. Evtushenko, H. Langenhagen[1], U. Lehnert, P. Michel, B. Naumann[2], B. Schweizer[3]

In a comparative study, Compton Diodes (CD) as well as other detectors [1] were tested as beam loss monitors. CDs are used routinely as gamma-ray detectors at high dose rates. They are rugged, inexpensive, require no external bias, possess good time resolution and have a linear response over a wide range of gamma-ray intensity where other detectors may tend to saturate. In the measurements, solid dielectric CDs which were designed at the Technical University of Darmstadt [2], were applied. They have a square cross-section and consist of a plexiglass (PMMA) dielectric, a Pb absorber, and an Al housing. Measurements were performed with a 12 MeV electron beam up to a few μA averaged current behind a Cu beam dump (8 cm) and near the beam line where the electrons were deflected to hit the stainless-steel tube. In case of the beam dump measurements the electron beam was completely absorbed in the Cu block. Fig. 1 shows the signal current as a function of the electron current for two CD positions.
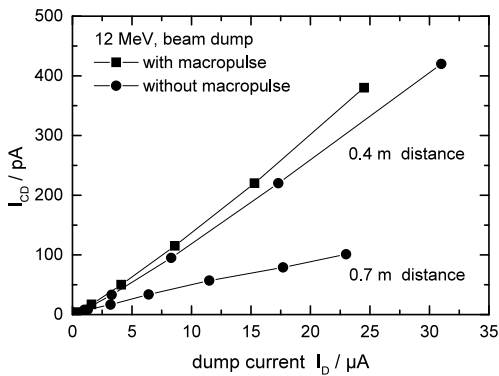
Fig. 1 *CD current versus e-beam current for different diode positions.*

As expected, there is a linear relation between dump current and CD current. At an electron current of 1 μA and distance of 0,7 m, where the dose rate was 1,5 Gy/h, a CD current of 3,7 pA was obtained which corresponds to a sensitivity of $8,9 \cdot 10^{-9}$ C/Gy (36 cm² CD cross-section area). The Monte Carlo simulation performed with the FLUKA [3] code give a CD current of 10 ± 3 pA. Fig. 2 represents results of beam loss measurements at the beamline about 1 m behind a switching magnet. At both sides of the stainless steel tube a CD was positioned. The correction coil of this magnet was used to deflect the electron beam. It is clearly visible whether the beam passes through the beam line (no signal from both CDs), or hit the right side, or the left one. The measured CD current level and rise time (1 ms) are sufficient for the ELBE machine interlock.
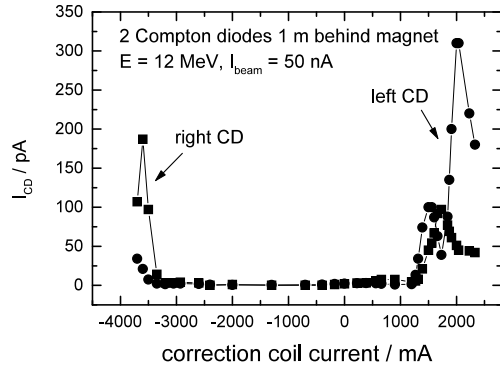
Fig. 2 *CD signals versus correction coil current. With the coil the beam was deflected to hit the right (< -3500 mA) or the left (> 1200 mA) tube wall.*

FLUKA simulation of the dependence of the CD current on the beam energy for an electron current of 1 μA are presented in Fig. 3 (Cu beam dump) and Fig. 4 (stainless steel tube). Whereas the CD current for the beam dump steadily increases there is a saturation of the CD current for the thin steel wall. A large fraction of the electrons penetrate through the wall, the radiative energy loss is nearly constant.
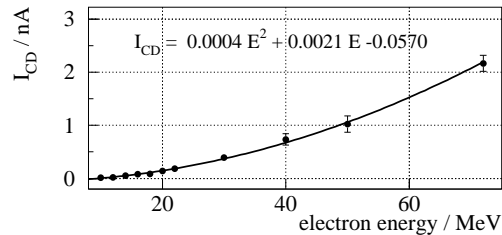
Fig. 3 *CU beam dump : simulated CD currents versus the beam energy; the distance between the dump and the CD amounts to 45 cm.*
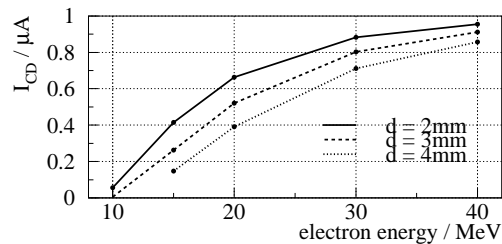
Fig. 4 *Steel tube : simulated CD currents versus the beam energy for three various steel thicknesses; the distance between the steel and the CD amounts to 1 cm.*

In summary, CDs are excellent with respect to linearity and dynamic range, provide sufficiently high signals, but a large number is required to monitor a long beam line.

[1] P. Michel et al., This Report, p. 17
[2] M. Brunken et al., Latest Developments from the S-DALINAC, FEL Conference, Hamburg, Germany (1999)
[3] A. Fasso, A. Ferrari and P.R. Sala, Proc. of the Monte Carlo 2000 Conference, Lisbon (2000)

[1] *FZ Rossendorf, FWF*
[2] *Institute of Nuclear and Particle Physics, TU Dresden*
[3] *Institute of Nuclear Physics, TU Darmstadt*

Electron Bunch Length Measurements at ELBE using Coherent Transition Radiation

P. Evtushenko, U. Lehnert, P. Michel, J. Teichert

The electron bunch length at ELBE is in the picosecond range. Such bunch length corresponds to a THz bandwidth. This makes direct electrical measurements impossible because the bandwidth of cables and waveguides is not high enough. During commissioning of the first ELBE acceleration module the electron bunch length was measured using a coherent transition radiation (CTR) technique. Here are the key issues of this technique.

The transition radiation is produced when electrons pass a boundary of two media with different dielectric constants. The response time of the transition radiation is zero. Due to this fact the longitudinal shape of the radiation pulse is a copy of the electron bunch shape. In the measurements a Martin-Puplett interferometer (MPI) [1] is used to measure the autocorrelation function of the CTR pulse (see Fig. 1). Than, the power spectrum of the electron beam can be calculated and compared with the spectrum of a beam of a suspected shape and size.

A 10 μm thick aluminum foil stretched over a frame was used to produce the CTR. The view screen is oriented 45° to the beam direction. Thus the backward CTR is propagating perpendicular to the electron beam. We have used crystal-quartz window for the output of the CTR from the beam line. An interferometric technique was already successfully used at TTF for the electron bunch length measurements [2]. We have modified the interferometer with the goal to use Golay cell detectors instead of pyro detectors, which are used in the original design. A video camera was also installed at the interferometer so that we could see the size and the position of the electron beam on the view screen.

Bunch length behavior was studied at different bunch charges as a function of RF field phase in the first accelerating cavity. The first cavity determines the bunch length since the electrons become relativistic there and then bunch length remains constant. The bunch length was measured to be minimum 2 ps RMS at 77 pC bunch charge. Fig. 2 shows the results of the measurements. The results are in good agreement with PARMELA simulations [3].
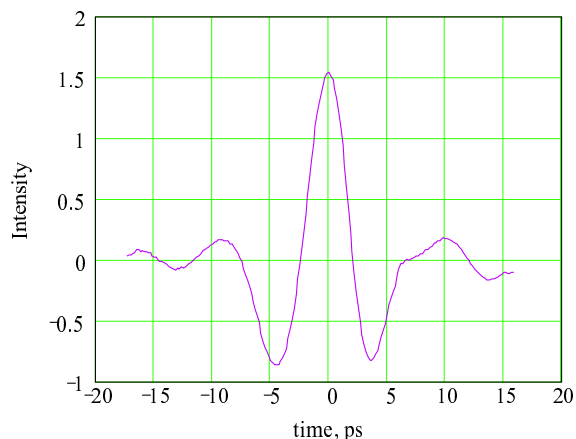
Fig. 1 *Interferogram obtained by scanning the time delay between the two optical paths of the interferometer.*
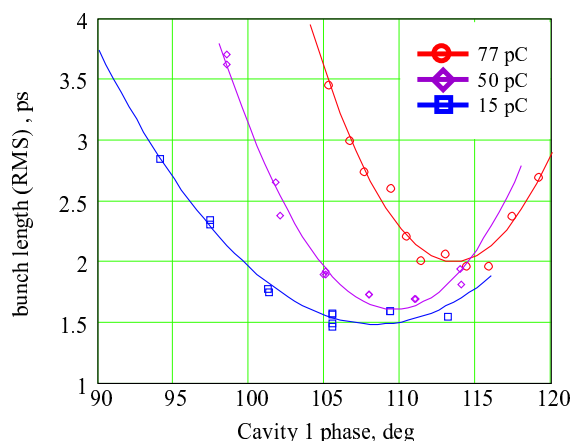
Fig. 2 *Bunch length vs. phase of the first cavity.*

[1]   P. Michel, P. Piot, FZ Rossendorf, Wiss.-Tech. Ber. FZR-217 (1999) 9
[2]   M. Geitz et al., Proceedings of the 1999 Particle Accelerator Conference, New York (1999) 2172
[3]   A. Buechner, Internal communication

The Transverse Emittance of the ELBE Electron Beam

U. Lehnert, P. Michel, J. Teichert

For many applications of the ELBE electron beam the transverse emittance is a crucial parameter. For radiation physics experiments a very low transverse emittance is required to allow as many electrons as possible to become trapped into channeling states when entering a crystal. The operation of free-electron lasers puts some requirements on the transverse emittance as well in order to achieve a good overlap between the electron beam and the optical mode over the whole length of the undulator.

Therefore, the transverse emittance of the ELBE electron beam was measured for typical bunch charges and for varying settings of the main accelerator controls. All measurements were done at 12 MeV beam energy using the quadrupole-scan method which is illustrated in Fig. 1. Basically, this method applies a variable lens (in this case a magnetic quadrupole) and detects the focal spot diameter on a viewscreen. From the dependence of the focal spot diameters on the strength of the lens the complete first-order parameter-set describing the transverse phase-space of the beam can be derived. So, Fig. 2 not only shows the measured emittance for varying RF-phase of the first accelerator cavity but also displays the estimated phase space ellipses to show correlations within the beam.

Such emittance measurements have been done for several bunch charges ranging from 1 pC to the FEL-mode at 77 pC. In all cases the measured values agree well to those previously measured at the ELBE injector using a pepper-pot mask. This indicates that the emittance growth during the beam capture into the RF-field of the first cells of the cavity is negligible. A normalized emittance of less than $3\ \pi$ mm mrad was measured at 1 pC bunch charge which could be cut down even further for radiation physics experiments using apertures in the injector. At full bunch charge the best measured values were below $8\ \pi$ mm mrad. However, for FEL operation the accelerator controls have to be set to meet some compromize between best transverse emittance and the requirements of a low energy spread and a short bunch length. In this case $10\ \pi$ mm mrad can be reached.

Fig. 1 *The basic principle of the quadrupole-scan method.*
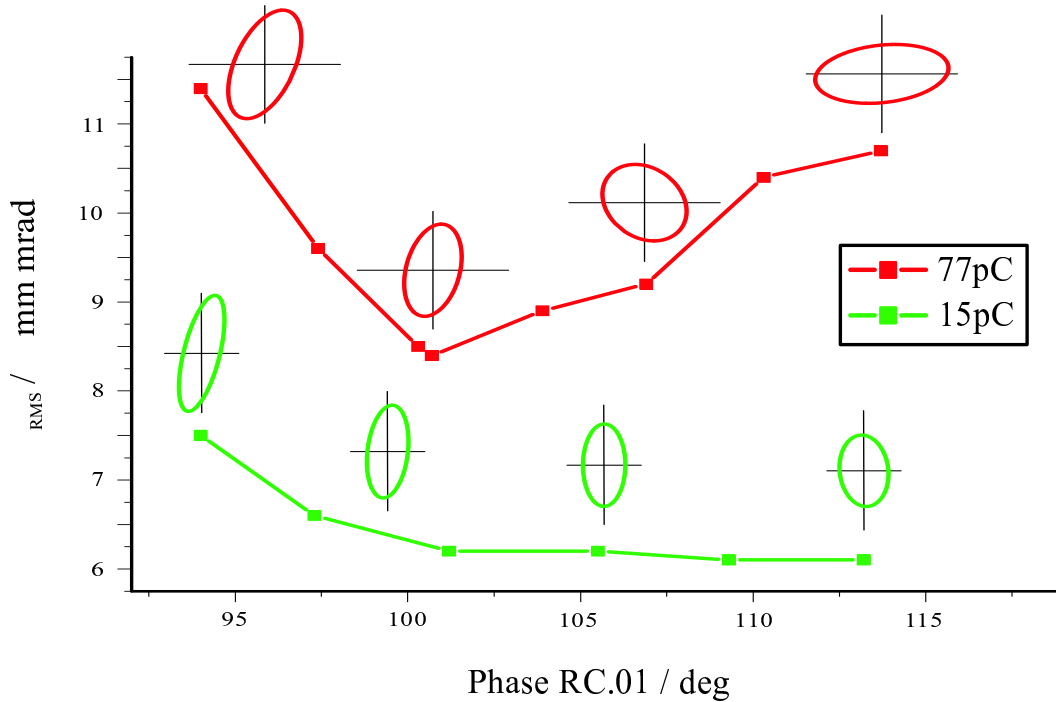
Fig. 2 *Normalized transverse emittance of the ELBE electron beam for two different bunch charges measured with the quadrupole scan method at 12 MeV beam energy for varying RF-phases of the first accelerator cavity.*

Study of Space Charge Effects at the ELBE Beam

K. Möller

To investigate the effect of Coulomb forces between the electrons on the behaviour of the ELBE beam a computer code has been developed which allows to study the expansion of electron bunches on the basis of microscopic calculations of any desired numerical accuracy. The calculations start from assumed initial distributions for position and velocity of the bunch electrons. The calculations are performed in the center of mass system (cms) because in this case nonrelativistic dynamics can be used and the time evolution of the charge distributions can simply be calculated by applying Newtons equation of motion with the static Coulomb interaction as driving force. This advantage however is paid for by the necessity of transforming the resulting time dependent space and velocity distributions from the cms to the laboratory system (lab) by Lorentz transformation. Since time and space coordinates are coupled in the Lorentz transform a "simultaneous" distribution in the lab originates from regions of cms distributions at different times. This causes some technical trouble but can be handled accurately. In order to keep computer memory requirements and calculation time within reasonable limits one starts with bunches of cylindrical shape. Then, due to the symmetry of the underlying dynamical equations the cylindrical symmetry is maintained throughout the time evolution of the bunch. Assuming this symmetry the general three-dimensional problem is reduced to an effective two-dimensional problem and the number of mesh points and computational time are less by orders of magnitudes as compared to the general solution of the Vlasov equations with comparable numerical accuracy. For maximum bunch charge at ELBE ($77\,pC \cong 4.8*10^8$ electrons) in the calculations every 500 electrons are grouped together to form a "heavy electron" with a charge of 500 times the electron charge. The error caused by this ap-

proximation is well under control by playing with the number of mesh points. It turned out to be of the order of 0.01% for the numerical calculations performed so far. Finally in the calculations one is left with about 1 million mesh points. In Fig. 1 results of the calculations are shown with bunch parameters corresponding to the ELBE injector, i.e., $\beta = 0.74$ and a bunch length of 600 ps (13.3 cm). Maximum bunch charge was assumed (77pC). The initial bunch radius was chosen to be 2 mm with the electrons distributed homogeneously in the cylindrical volume. The initial cms velocity of all electrons was set to zero. The quantity z_m in the figures denotes the position of the bunch center in the beam pipe (counted from the exit of the gun) and is equivalent to the time scale. The time evolution of the transverse phase space as well as the corresponding emittance values are shown in Fig. 2. Here, the emittance is defined in the conventional way as statistical emittance in the form $\varepsilon^2 = <x^2><(dx/dz)^2> - <x(dx/dz)>^2$ with the brackets $<>$ denoting summation over the distribution. There are mainly two conclusions which can be drawn from Figs. 1 and 2: i) for maximum bunch charge a considerable increase of the bunch radius can be observed, ii) due to strong correlations between position and direction values in the phase space the strong beam expansion is accompanied with only a small emittance growth. No straightforward explanation can be given for the emittance drop at $z_m = 67.41\,cm$ in Fig. 2. The numerical accuracy was checked and found to be about 0.01%. Therefore numerical errors cannot be responsible for the observed drop. The developed computer code has also been applied to calculate the Coulomb expansion for a variety of other situations , e.g., for compressed bunches as they are fed to the entrance of the accelerating cavities.
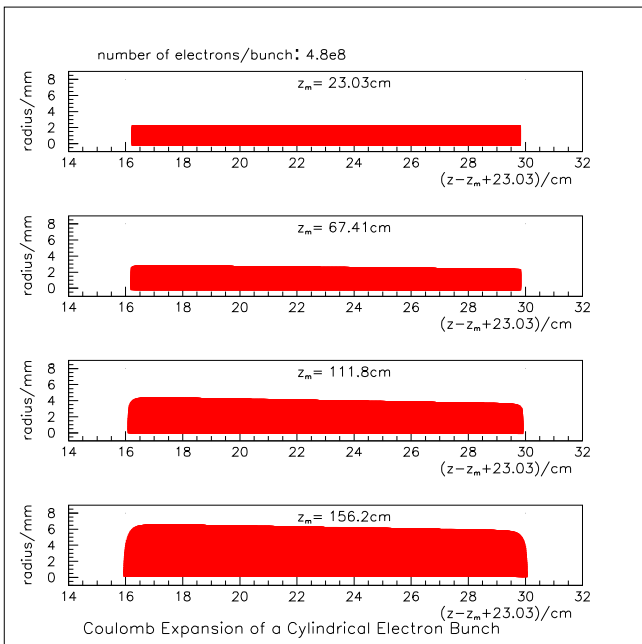
Fig. 1 *Coulomb expansion of an electron bunch.*
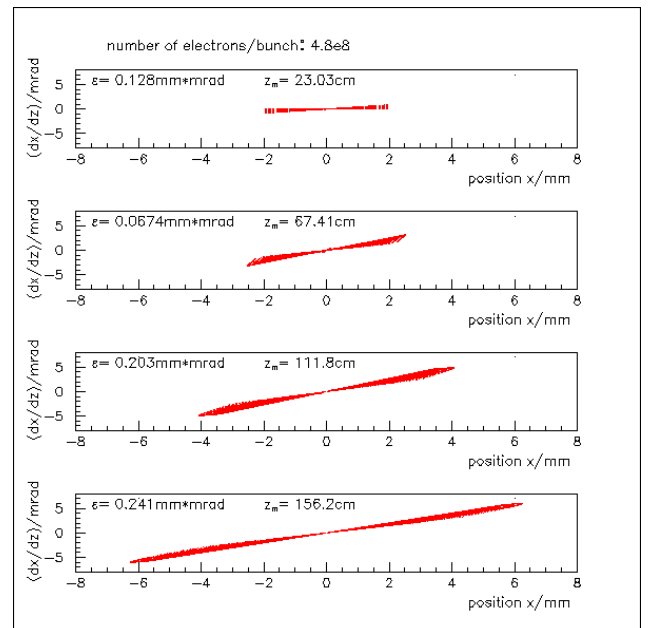
Fig. 2 *Time evolution of phase space corresponding to bunch expansion in Fig. 1.*

Preparation and Photo-Emission Measurements of Cs_2Te Cathodes for the Superconducting RF Gun

D. Janssen, S. Konstantinov[1], T. Quast[2], B. Reppe, J. Teichert

The superconducting RF electron gun [1], being under development, will use a caesium telluride photo cathode. For the formation of the Cs_2Te photo layers a preparation chamber was built. This chamber is connected to the cryostat and gun resonator cavity with a vacuum lock allowing the transfer of the prepared cathode under UHV conditions. The gold coated copper cathodes can be mounted with a thread in the cavity using a transfer rod. The circular front side of the cathode has a diameter of 10 mm. In the preparation chamber there are evaporators for Te and Cs, a deposition rate monitor, a cathode heater, and an aperture in front of the cathode which limits the deposition area to 5 mm in diameter.

For the photo emission measurements, the cathode was not mounted to the cavity but kept in the preparation chamber. A window allows to illuminate the cathode with the laser beam. The laser system, developed by the Max-Born-Institut, produces a 263 nm UV beam at a repetition rate (micropulse frequency) of 25.92 MHz, and a pulse duration of 5 ps. The laser is operated in a pulsed mode (macropulse) to reduce the average current and can be synchronized to the master oscillator of the RF system. The laser output power is greater than 1 W within the macropulse.

Great effort was done to obtain a vacuum of 10^{-10} mbar and particle free conditions in the preparation chamber.

The evaporators are heated up slowly to maintain a pressure better than 10^{-8} mbar during deposition. First, a layer of about 20 nm Te is deposited. Then the Cs is evaporated. During Cs deposition the laser beam is directed onto the cathode and the photo-current is measured. The Cs deposition is stopped when the photo-current reaches its maximum. During the photo-layer formation process, the cathode is held at about 120°C. The photo current was measured by collecting the electrons at an insulated aperture connected to a high-voltage power supply. The results of the photo-current measurements as a function of the aperture voltage for different laser conditions (power, macropulse duty factor) are shown in Fig. 1. Due to the adverse geometry and space charge, rather high collection voltages are needed. From the data, a quantum efficiency of about 0.4% can be obtained. It should be mentioned that this value is a lower limit. During the micropulse the peak current is about 6 A and should rather be space charge limited than restricted by photo emission. Within the RF cavity the electrical field-strength will be much higher which should lead to higher values of the quantum efficiency. Repeated measurements over several weeks after the photocathode preparation did not show any significant degradation of the quantum efficiency.
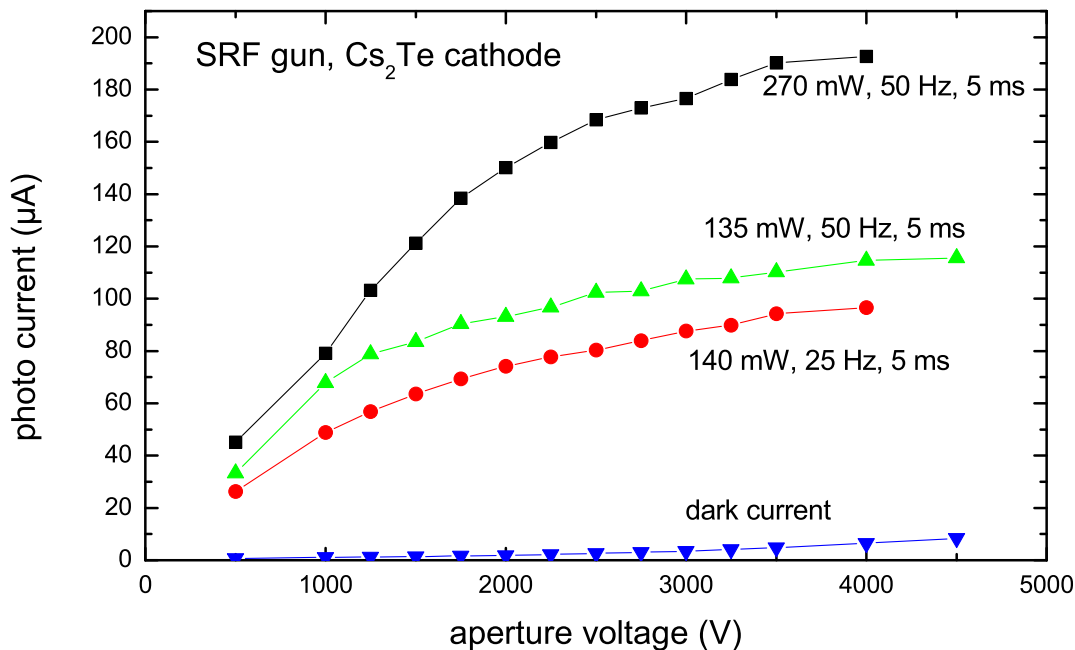
Fig. 1 *Photo-current measured at an aperture in front of the Cs_2Te coated cathode as a function of the aperture voltage for varying average laser power and macro-pulse frequency.*

[1] E. Barthels et al., Nucl. Instr. and Meth. A 445 (2000) 408

[1] *Budker Institute of Nuclear Physics, Novosibirsk, Russia*
[2] *Max-Born-Institut, Berlin*

Single-Drive Tuning Method of a Multicell Cavity Having One Nonstandard Cell

D. Janssen, V. Volkov[1]

We have done numerical simulations to investigate the tuning behavior of a multicell cavity, containing one special cell in addition to five TESLA cells. The special cell is designed for a superconducting RF Photoelectron gun and on the axis a photocathode is placed. The geometry of the cavity is schematically shown in Fig. 1.

All six cells have the same resonating frequency of 1.3 GHz. Now we would like to change the frequency of all cells by the same value, using a single drive only. In order to obtain this result, we have to determine the optimal diameter for the ring 2 at which the tuning force acts on the gun cell but also to modify the diameter of ring 1 that connects the gun cell and the first TESLA cell. (See Fig. 2).

The condition of uniform change of the frequencies of the gun cell, the first TESLA cell and the remaining TESLA cells defines a two dimensional optimization problem (see Fig. 3), which we have solved using the program ANSYS. The results are presented in Tab. 1.

The calculation shows, that for a given diameter of the tuning rings the resonating frequencies of the cells differ by less than 0.1%.

Choke Filter · Optimized 0.5 Cell · TESLA Cells · He Bath · Ring2 · Ring1 · Tuning force
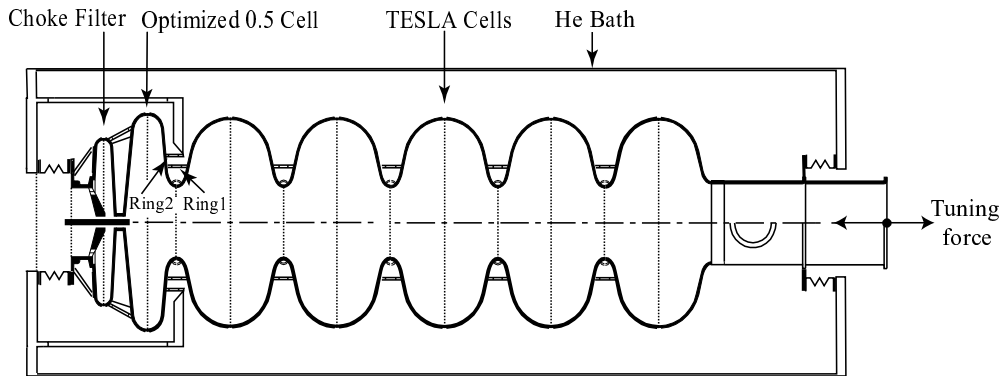
Fig. 1 *Tuning mechanism of the multicell cavity.*

Configuration/ Parameter	Half cell R1=5.5941 R2=6.5864 optimized	Midcup R1=5.5941 R2=6.5864 optimized	Middle cup of TESLA cell R=5.65 cm
Frequency/tuning force ratio, kHz/N	0.0923	0.0930	0.0924
Force/strain ratio, kN/mm	65.2	36.5	33.7
Frequency/strain ratio, MHz/mm	5.90	3.33	3.06
Elastic strain limit, mm($\sigma < 70$ N/mm^2)	0.074	0.279	0.298
Tuning force limit, N	4729	9986	9844
Tuning range, kHz	436	929	910

Tab. 1 *Results of the calculation.*

Midcup · Ring1 · Tuning · Ring2 · Half cell
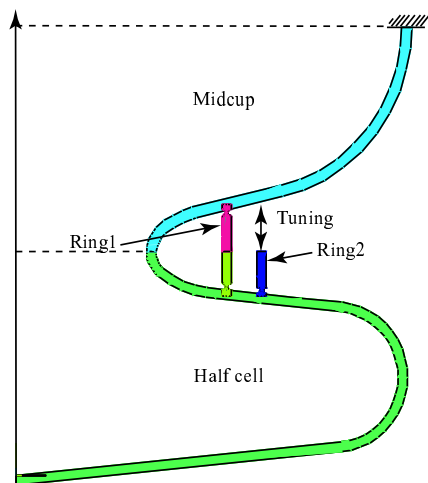
Fig. 2 *First part of the cavity.*

Crossing point of three planes · Half cell · Midcup · TESLA cell · Ring2 radius · Ring1 radius
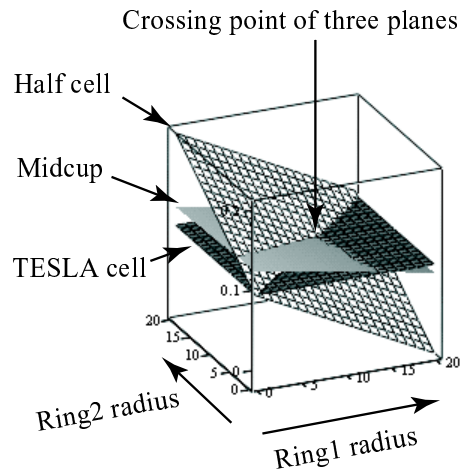
Fig. 3 *Two parameter optimization.*

[1]*Budker Institute of Nuclear Physics, Novosibirsk, Russia*

Production of Coherent Wiggler Radiation with Sub-Picosecond Electron Bunches

V. VOLKOV[1], D. JANSSEN, R. WÜNSCH

Sub-picosecond electron pulses have many scientific and industrial applications. One of them is the coherent enhancement of wiggler radiation. It requires injectors able to generate electron bunches with lengths of about 10 to 20 μm. A superconducting multi-cell photocathode rf gun may become the best variant of such an injector. The advantage of this scheme is its simplicity and compactness. A superconducting cavity limits the requirements of high power RF generation. The strong coupling between the cells makes this structure insensitive to mechanical errors and allows an operation at high acceleration gradient.

In the last years, our group has been working on the development of a superconducting RF gun injector [1]. Calculations of a $3\frac{1}{2}$-cell RF gun basing on TESLA structures show good beam quality [2] meeting the requirements of a free-electron laser. The same structure with a modified first cell (see Fig. 1) can be used to generate sub-picosecond bunches. The first cell must be shortened to about 0.3 wavelength. The number of cells was increased to 5 to obtain bunch energies of 10 MeV.
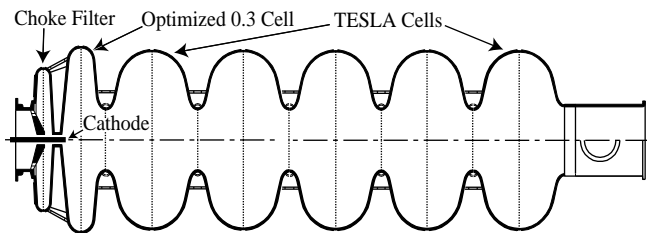
Fig. 1 *Superconducting 5.3 cell RF gun injector.*

In contrast to the well-known electron bunch compression method [3,4], where the bunch launches at small RF phase and compresses in the first $\frac{1}{2}$ cell, we propose a modification of this process. In this method, the beam is not launched at small RF phase but at rather high values (about 30 degree in our calculation). Bunch compression then occurs in the first full cell placed after the first 0.3 cell of the RF gun cavity.

Due to the shortened length of the gun cell the bunch enters the first full cell earlier, at negative RF phase. At the beginning of the first full cell the bunch partially decelerates and is then accelerated again. The tail of the bunch gains more energy than the head. The higher energy electrons then catch up with those at the head and reduce the bunch length before the beam becomes

relativistic. There exists an optimized entering phase at which the bunch length is at a minimum.

In the simulation presented here, a laser pulse duration (FWHM) of 3 ps with a Gaussian distribution is assumed as well as an instantaneous response of the cathode. The beam dynamics is simulated using the PARMELA code for bunch charges of 1 and 10 pC, respectively. The results are shown in Tab. 1.

bunch charge, pC	1	10
laser spot size, mm	2.0	2.72
injection RF phase, deg	30.7	27.8
beam energy, MeV	9.74	9.74
energy spread(rms), keV	7.25	6.76
norm. emittance, mm mrad	0.42	1.25
longitudinal emittance, mm keV	0.047	0.102
bunch length (rms), μm	7.2	15.4

Tab. 1 *Bunch characteristics of 5.3 cell rf gun (at a distance of 0.5 m from rf gun exit).*

The injection phase as well as the cathode radius are carefully adjusted to obtain a minimum bunch length. The sensitivity of the compressed bunch length δL to a change of the injection phase $\delta\varphi$ or a change of the cathode radius δR_C can be expressed as

$$\delta L[\mu m] = 2.8\,\delta\varphi^2[\text{deg}] \quad \text{and} \quad \delta\text{L}[\mu m] = 0.014\,\delta\text{R}_C^2\,[\mu m].$$

An electron bunch passing through a planar undulator spontaneously emits coherent electromagnetic radiation [5]. Table 2 shows the calculated radiation power and radiation wavelength, which could be obtained with the ELBE undulators U27 and U50 using an electron beam from the above presented electron gun.

	U27		U50	
undulator period, mm	27		50	
und. parameter K_{rms}	0.95		1.2	
bunch charge, pC	1	10	1	10
radiation wavelength, μm	64	64	152	152
radiation power, W	2.97	4.84	3.56	25.3

Tab. 2 *Characteristics of electromagnetic coherent radiation obtained from U27 and U50 undulators with average electron beam current of 1 mA.*

[1] D. Janssen et al., Nucl. Instr. and Meth. A445 (2000) 408

[2] D. Janssen, V. Volkov, Nucl. Instr. and Meth. A452 (2000) 34

[3] X.J. Wang, I. Ben-Zvi, PAC97, Vancouver/Kanada (1997) 2793

[4] L. Serafini, R. Zhang, C.Pelegrini, Nucl. Instr. And Meth. A387 (1997) 305

[5] H. Wiedemann, Particle Accelerator Physics, Springer-Verlag Berlin, Heidelberg (1993)

[1] *Budker Institute of Nuclear Physics, Novosibirsk, Russia*

Calculation of Dose Rate Source Terms around the Beam Dump Vessel

B. Naumann[1]

Beam dumps are incorporated into the experimental areas of the ELBE facility. Their purpose is to absorb the primary electron beam and the secondary radiation. It is planned to use a standardised beam dump design for the various experimental areas of the radiation source ELBE [1] except for the neutron time-of-flight facility. The beam dump consists of a purified graphite core contained within a water cooled stainless steel vessel. The beam dumps are aligned with the beam axis in each experimental area. The radiation shield surrounding the beam dump will be designed individually for each experimental area. In this context, dose rate calculations were carried out to estimate the dose rate source term around the stainless steel vessel of the beam dump. Detailed Monte Carlo simulations were carried out using the FLUKA code [2]. The energy dependent photon and neutron fluxes were obtained near the surface of the cylindrical steel vessel for a beam current of 1 mA and energies of 20 MeV and 50 MeV. Based on the electron beam transport and the scattering off the Be window that separates the dump from the beamline vacuum, the electron beam directed towards the cone-shaped hole of the beam dump has a radius of 4 cm. The geometrical configuration is shown in Fig. 1. For calculations, the steel vessel was surrounded with an imaginary cylinder, which was divided in 17 longitudinal and 9 radial segments. Radial segments were investigated in the planes before and behind the graphite core.
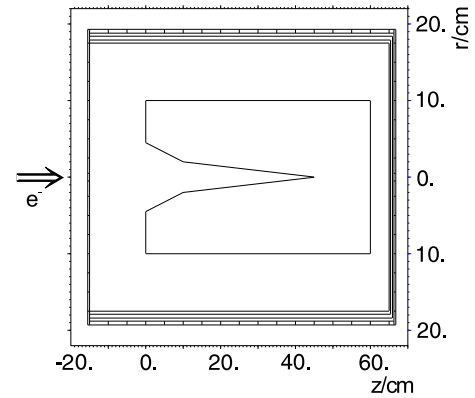
Fig. 1 *Cylindrical geometry of the beam dump consisting of the graphite core and the steel vessel with water cooling.*

In a next step, the energy dependent particle flux distributions have been converted to dose rate distributions by established conversion factors [3]. The energy integrated dose rate distributions around the steel vessel for E = 20 MeV and E = 50 MeV are shown in Fig. 2 and Fig. 3 respectively. The neutron dose rate increase with energy due to the photonuclear reactions in the graphite core and the steel vessel.
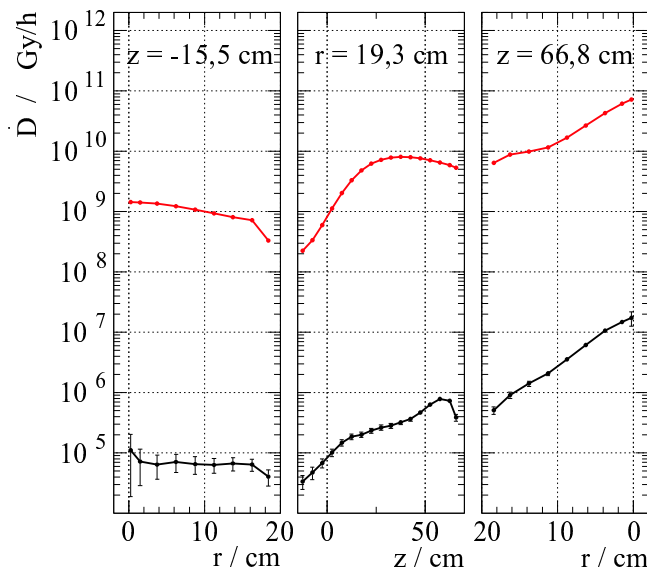
Fig. 2 *Dose rate distribution near the steel vessel for a beam energy of 20 MeV and a current of 1 mA. The abscissa follow a closed path along the surface of the vessel. The photon dose rate exceeds the neutron dose rate by about 4 orders of magnitude.*
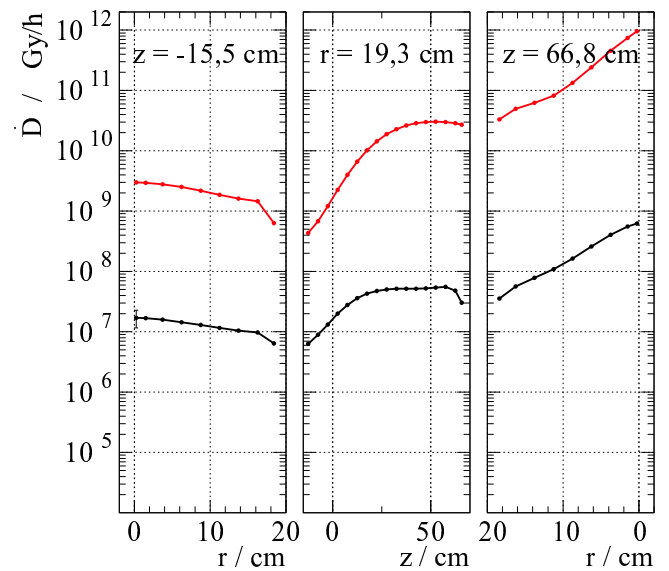
Fig. 3 *The same as for Fig. 2 for a beam energy of 50 MeV.*

[1] B. Naumann et al.,FZ Rossendorf, Wiss.-Tech. Ber. FZR-319 (2001) 23
[2] A. Fasso et al., Proc. of the III Spec. Meeting on Shielding Aspects, Sendai (1997) 61
[3] J.F. Briesmeister. Editor, MCNP Version 4A, LA 12625 M (1993)

[1] *Institute of Nuclear and Particle Physics, TU Dresden*

Status of the Optical Resonator for the ELBE-FEL U27

W. Seidel, E. Grosse[1], D. Oepts[2], B. Rimarzig, U. Wolf

We have started constructing the optical resonator for the U27 FEL. All components, including both mirror chambers, are in house and have been aligned by using optical methods. The optical cavity requirements are summarized in the following table.

Parameter	Requirement
Resonator	Stable, near-concentric, symmetric
Cavity length	11.53 m
Rayleigh range	1 m
Mirror radius	3.75cm
Mirror radius of curvature	5.94 m
Diameter of the out-coupling holes	1.5 mm; 2.0 mm; 3.0 mm; 4.5mm
Length stability	$< 0.5\ \mu$m, interferometer stabilized
Mirror tilt stability	$< 5\ \mu$rad
g^2	0.88

In view of their usually small bandwidth, the use of dielectric mirrors for coupling radiation out of the FEL cavity is not very attractive if a large spectral range is to be covered. The so-called hole coupling, using broadband metal mirrors with an on-axis aperture in one of the mirrors, is more attractive in our case. For the out-coupling, it is important to know the extraction ratio, i.e. the fraction of intra-cavity power that is coupled out of the cavity per roundtrip of the optical wave. It is obvious that this ratio should be smaller than the FEL gain per pass reduced by the intracavity losses in order to achieve laser oscillation. We have optimized the extraction ratio for the wavelength range of U27 by using different holes in different mirrors [1]. We have found out, that 4 holes of different size (see table) are sufficient.

The optical resonator will be equipped with Cu-mirrors especially Au-coated on a revolvable holder (wheel). Because of a small absorption in the mirrors the holder will be heated up to a definite temperature. We are testing a heating system for the mirror wheel, which stabilizes the mirror temperature at a level slightly above the laser heating temperature. The heat exchange is realized by thermal radiation into the vacuum only. Angular adjustment of the mirror wheel will be performed in vacuum with the aid of piezoelectric inchworm UHV motors, which provide both coarse and fine adjustments. To bring one of the mirrors in the right position for lasing, we shall use a high-precision rotation stage on which 5 out-coupling mirrors are mounted at most.

The downstream mirror is mounted in a small vacuum chamber [2]. Angular as well as longitudinal adjustment can be carried out by means of motorized micrometers and by a flexible bar for fine tuning. The mirror mount is coupled to the vacuum by means of a flexible bellow, while the DC-motors operate outside of the vacuum. The translation stage of this mirror will be used to adjust the cavity length.

The operation of an FEL will critically depend on the synchronism between the electron and light pulses controlled by the tuning of the optical cavity length. A Hewlett-Packard interferometer system will be used to monitor that length. The interferometer beam will pass through the same resonator chamber as the main laser beam and the electrons. However, constraints on the width of the vacuum chamber do not leave enough space in the cavity for a separate parallel interferometer beam. Therefore, the latter will pass diagonally from one side of the upstream cavity mirror to a retroreflector on the other side of the downstream mirror (see fig. 1). The control electronics for the interferometer include a servo system to control and stabilize the relative distance between the two cavity mirrors using the motorized micrometer drive on the translation stage of chamber 2.

At the upstream end, a vacuum tank will be used to install the mirror wheel and to leave space for alignment aids and for additional experiments concerning mode control, additional out-coupling, cavity dumping, etc. This tank is connected to the beam line via a vacuum valve such that replacement of optical parts can be performed without venting the rest of the vacuum system. The vacuum output window will be a CVD diamond window under Brewster's angle, with a useable aperture of 8 mm diameter. We note that diamond is the only material that is transparent from the visible to beyond 100 μm and has sufficient strength and damage resistance to be used as an output window.
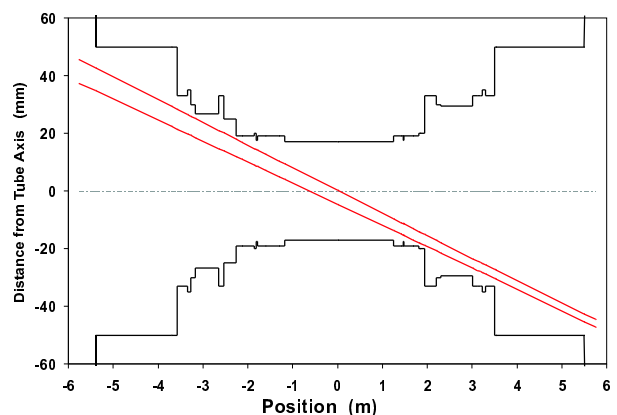
Fig. 1 *Top view of the interferometer beam envelope inside of the optical cavity with the inner contours of the vacuum pipe.*

[1] R. Wuensch, private communication
[2] B. Wustmann and A. Wolf, FZ Rossendorf, Wiss.-Tech. Ber. FZR-319 (2001) 34

[1] *also TU Dresden*
[2] *Institute for Plasma Physics Rijnhuizen, The Netherlands*

Field Measurements in the Undulator U27

P. Gippner, A. Schamlott, U. Wolf

At the Dresden Radiation Source ELBE an intense IR beam in the 3-30 μm range will be produced in the undulator U27 [1], which consists of two 34-pole sections mounted on two carriages. The distance between these sections is adjustable for phase matching. The magnetic structure has a period of λ_u=27.3 mm and consists of NdFeB permanent magnets and poles of decarborized iron. The gaps of both sections can be varied independently. For high-gain lasing one can introduce a tapering of the field. A magnetic chicane between the section would allow phase matching at a constant carriage distance[2]. Both sections were scanned and adjusted at DESY using a calibrated Hall-probe setup [3]. For a gap width of g=12 mm the results of these field measurements are shown in Fig. 1 (a). For an electron

of E=20 MeV the panels (b) and (c) present the angle with respect to the undulator axis and the displacement x, calculated from the 1st and 2nd field integrals, respectively. Auxiliary coils were inserted to get a minimum displacement at the exit sites of both sections. Only weak magnetic fields $B_{1,2}$ generated by these coils are necessary to keep the electrons within the optical beam. After the transportation of the undulator to the FZR and installation at the beam line the field was checked using the pulsed-wire method [4]. The measured 2nd field integrals are presented in Fig. 2. Minimal field aberrations in the second section eventually produced by shocks during the transportation will be corrected by a further measurement when the vacuum chamber is mounted.
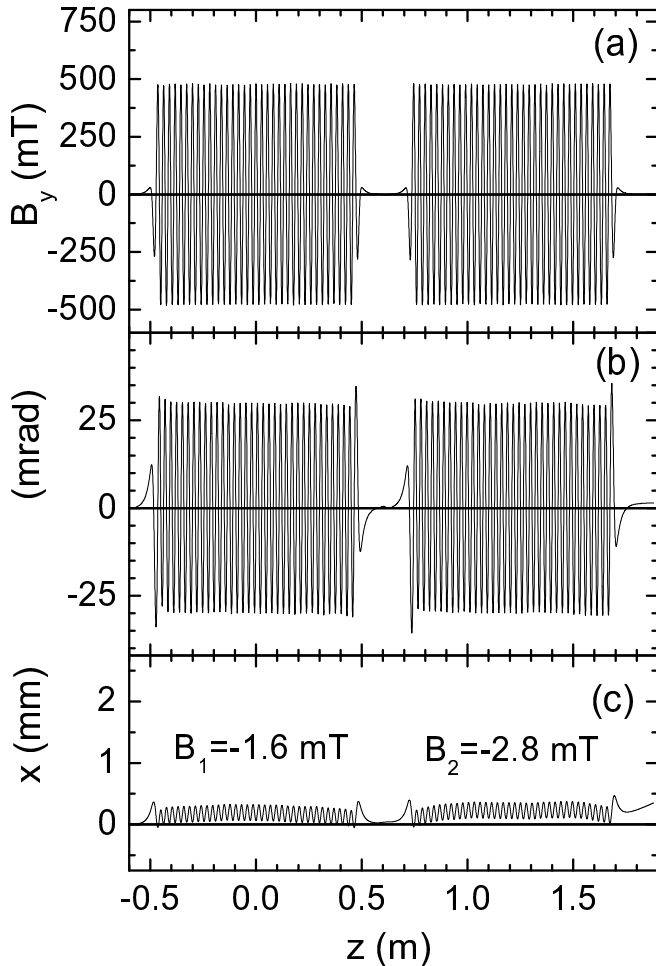
Fig. 1 *The measured vertical field component B_y of the undulator sections (a), electron angle (b) and displacement x (c) with respect to the undulator axis calculated for a reference electron of E=20 MeV and a gap width g=12 mm. For the auxiliary fields $B_{1,2}$ see text.*
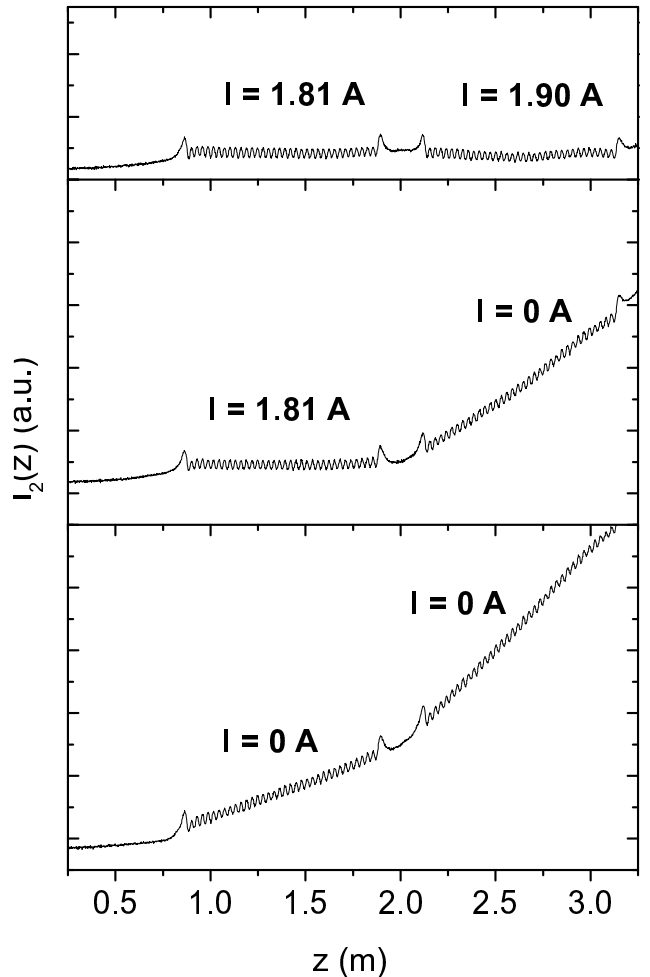
Fig. 2 *The 2nd field integrals as measured by the pulsed-wire method. The effect of correction coils width 100 windings and the exciting current values I are indicated.*

[1] P. Gippner et al., Contribution We-Pe-24 to the 23rd Int. Free Electron Laser Conf. Darmstadt, Germany, 2001, to be published in Nucl. Instr. Meth. A
[2] P. Gippner, This Report, p. 28
[3] B. Faatz, J. Pflüger et al., Nucl. Meth. A 375 (1996) 618
[4] P. Gippner et al., FZ Rossendorf, Wiss.-Tech. Ber. FZR-319 (2001) 28

A Magnetic Chicane for Phase Matching

P. Gippner

The undulator U27 consists of two separate sub-systems with a drift space d between them and individual mechanical drives for gap adjustment. Thus by variation of the gap width g the optical wave length is changed and consequently the phasing between the undulator sections has to be changed as well. This can be done by properly choosing the electron flight path between the sections by varying there distance. This method has extensively been described in [1].

To avoid the moving of the second section it was proposed to install a magnetic chicane [2, 3], which can vary continuously the electron flight path and hence ensure the phase matching for a constant separation space d at any undulator gap g. The design of a suitable chicane consisting of 3 dipoles is shown in fig. 1. The outer magnets have the same field B_0 and iron yokes of the same lengths l_m, whereas the center magnet requires double strength and is most easily made twice the iron length l_m.

The aim of these investigations is to study the influence of the superimposing fringe fields on the conditions for adjustment of the chicane. The necessary stability of

Fig. 2 *Field distributions(a) and corresponding electron trajectories within the chicane(b) for 3 different field strengths.*

the currents exciting the magnetic fields in the dipoles is a second point of interest. The corresponding calculations have been done using the code RADIA [4]. The fig. 2(a) indicates three typical field distributions within the whole setup when the chicane is adjusted. The trajectories of an electron of E=20 MeV for these different field strengths is shown in fig 2(b). As further calculations show the maximum magnetic strength required for electron energies E = 12 - 40 MeV and the corresponding wavelengths of the radiation amounts to 3.3 T*mm. This strength can be generated by excitation currents of I*N = 0.8 kA*turns in the dipole coils, far from nonlinearities of the hysteresis curve of ARMCO iron. The stability of the power supply should be 10^{-4}. More detailed investigations are necessary in the future.

Fig. 1 *The dipoles of the chicane between the undulator segments. The denounced parameters are:*
l_m=40 mm, l_0=25 mm, l_1=45 mm and d=300 mm.

[1] P. Gippner, J. Pflüger, FZ Rossendorf, Wiss.-Tech. Ber. FZR-319 (2001) 26
[2] R. Wünsch et al., Contribution We-P-24 to the 3rd Int. Free Electron Laser Conference, Darmstadt 2001, to be published in Nucl. Instr. Meth. A; C.A.J. van der Geer et al., This Report, p. 31
[3] J. Pflüger, M. Tischer, TESLA-FEL 2000-08, December 2000
[4] P. Elleaume, O. Chubar, J. Chavanne, J. Syn. Rad. 5 (1998) 481

Contributions of the 3rd and 5th Harmonics to the Measured Field of the Undulator U27

P. GIPPNER

The vertical component of the magnetic field distribution along the undulator axis (z - axis) can be described by

$$B_y(z) = B_0 cos(k_z * z), \qquad (1)$$

with $k_z = 2\pi/\lambda_u$ and the undulator period λ_u. In realistic cases the function (1) may be distorted by higher harmonics, which make the measured field $B_y(z)$ a bit more flat or more peaked than a pure cosine function is. In order to get an information about the intensities of the higher harmonic contributions to the measured field a Fast Fourier Transformation (FFT) was performed making use of the procedure CFT of the CERN Program Library.

The Fourier Transforms of the undulator U27 obtained from the measured field distribution $B_y(z)$ [1,2] are shown in figs. 1-2, which indicate for gap widths of g = 8 and 16 mm the absolute values $|f(n)|$ of the first, third and fifth harmonics of this function. The CFT subprogram delivers the wave numbers k_z as a multiple of the quantity k_0

$$k_0 = \frac{2\pi}{L}, \ k_z = n * k_0, \ n \quad integer, \qquad (2)$$

where L is the length of the interval used for the analysis. For each gap value a window of 1690 points and a length of L = 885.0 mm was employed containing 31 complete magnetic periods. The quantity k_0 is therefore equal to $k_0 = 0.007099 \, \text{mm}^{-1}$. Table 1 contains the wave numbers $k_z(\nu)$ found for the harmonics of the ν th order.

Tab. 1 *Wave numbers $k_z(\nu)$ evaluated by FFT of the measured field distribution $B_y(z)$ of the undulator U27. The quantities n_{cm} are the weighted mean values of n obtained from the corresponding peaks in the figures.*

$\frac{g}{mm}$	1st Harmonic		3rd Harmonic		5th Harmonic	
	n_{cm}	$\frac{k_z(1)}{mm^{-1}}$	n_{cm}	$\frac{k_z(3)}{mm^{-1}}$	n_{cm}	$\frac{k_z(5)}{mm^{-1}}$
8	32.0	0.2272	93.75	0.6869	155.5	1.1040
12	32.0	0.2272	93.46	0.6635	-	-
16	32.0	0.2272	93.37	0.6629	-	-
20	32.0	0.2272	92.84	0.6591	-	-

The magnetic period of U27 is $\lambda_u = 27.3$ mm resulting to $k_z(1)=0.2302$ mm^{-1} for the first harmonic. This is reproduced by the FFT results with a satisfying precision. As the contributions of the 3rd and 5th harmonics in f(n) exhibit always a positive sign they make $B_y(z)$ broader than a pure cosine function is. The width w_z of the poles in z-direction may be one of the reasons for the appearance of higher harmonics. As can be expected the intensities of these admixtures diminish with the decreasing ratio w_z/g .
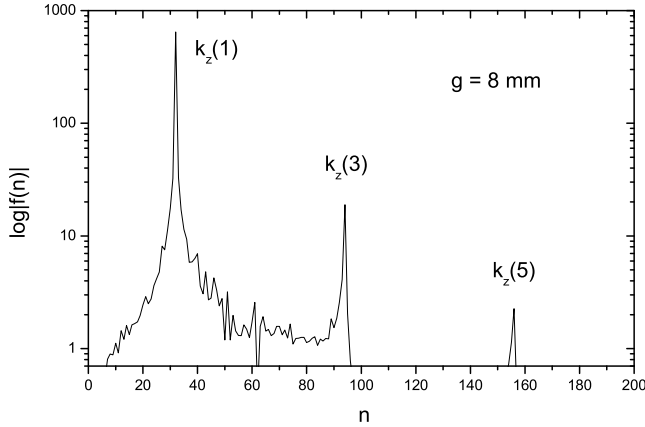
Fig. 1 *Fourier Transform of $B_y(z)$ for a gap width $= 8\,mm$*
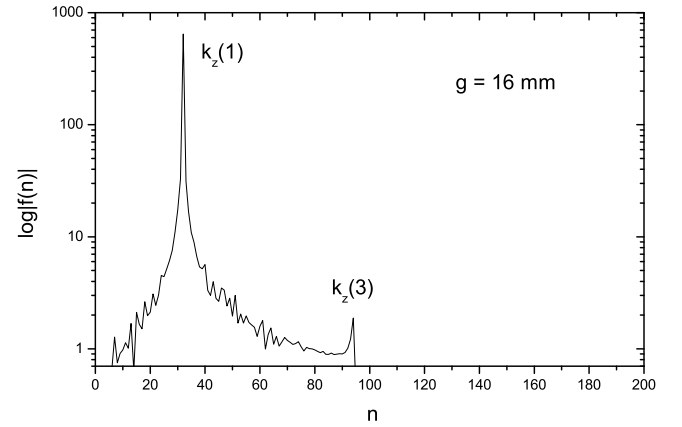
Fig. 2 *Fourier Transform of $B_y(z)$ for a gap width $= 16\,mm$*

[1] P. Gippner et al., FZ Rossendorf, Wiss.-Tech. Ber. FZR-319 (2001) 27
[2] P. Gippner et al., Contribution We-P-09 to the 23rd Int. Free Electron Laser Conference, Darmstadt 2001, to be published in Nucl. Instr. Meth. A

Contributions of the 3rd and 5th Harmonics to the Measured Field of the Undulator U50

P. GIPPNER

The Fast Fourier Transforms obtained from the measured field distribution $B_y(z)$ [1] of the undulator U50 are shown in the figs. 1-4, which indicate the absolute values $|f(n)|$ of the first, third and fifth harmonics of this function for gap widths of g = 16, 20, 25 and 30 mm. To evaluate the spectra f(n) the procedure CFT of the CERN Program Library was applied. This subprogram delivers the wave numbers k_z as a multiple of the quantity k_0:

$$k_0 = \frac{2\pi}{L}, \; k_z = n * k_0, \; n \;\; integer, \qquad (1)$$

where L is the length of the interval used for the analysis. For each gap value a window of 2048 points and a length of L = 2047.0 mm was employed. The quantity k_0 is therefore equal to k_0 = 0.0030695 mm^{-1}. Table 1 contains the wave numbers $k_z(\nu)$ found for the harmonics of the ν th order.

The magnetic period of U50 is λ_u = 50.0 mm resulting to $k_z(1)$ = 0.1257 mm^{-1} for the first harmonic.

Tab. 1 *Wave numbers $k_z(\nu)$ evaluated by FFT of the measured field distribution $B_y(z)$ of the undulator U50. The quantities n_{cm} are the weighted mean values of n obtained from the corresponding peaks in the figures.*

$\frac{g}{mm}$	1st Harmonic		3rd Harmonic		5th Harmonic	
	n_{cm}	$\frac{k_z(1)}{mm^{-1}}$	n_{cm}	$\frac{k_z(3)}{mm^{-1}}$	n_{cm}	$\frac{k_z(5)}{mm^{-1}}$
16	42.0	0.1289	124.2	0.3812	205.6	0.6311
20	42.0	0.1289	124.5	0.3821	205.5	0.6308
25	42.0	0.1289	124.0	0.3806	-	-
30	42.0	0.1289	-	-	-	-

This period is reproduced by the FFT results with satisfying precision. The contributions A3 and A5 of the 3rd and 5th harmonics in f(n) exhibit always a positive sign and make $B_y(z)$ a little broader than a pure cosine function is. In general, the ratios of the contributions A3/A1 and A5/A1 are lower than 1%. As expected these ratios decrease with increasing g.
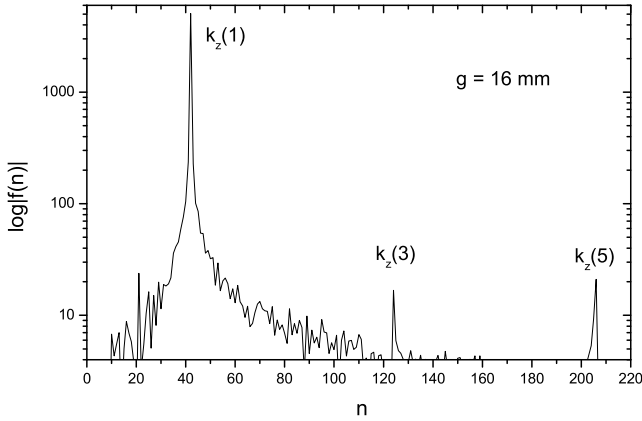
Fig. 1 *Fourier Transform of $B_y(z)$ for a gap width = 16 mm*
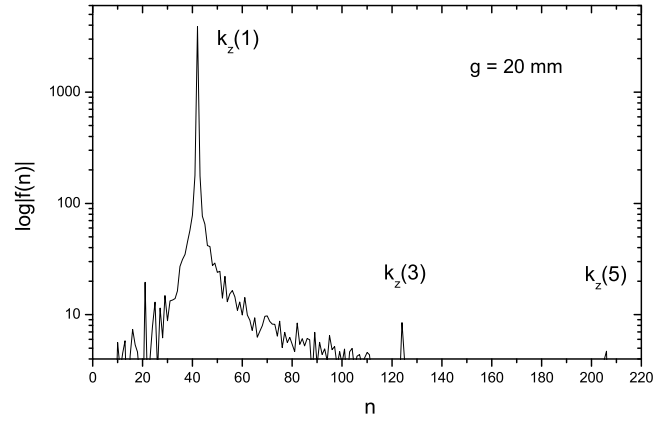
Fig. 2 *Fourier Transform of $B_y(z)$ for a gap width = 20 mm*
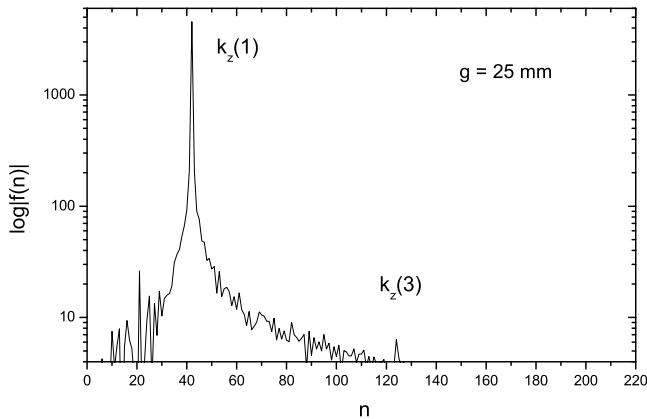
Fig. 3 *Fourier Transform of $B_y(z)$ for a gap width = 25 mm*
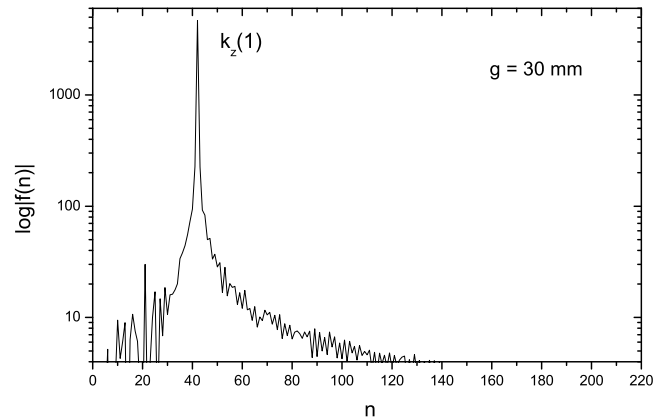
Fig. 4 *Fourier Transform of $B_y(z)$ for a gap width = 30 mm*

[1] P. Gippner et al., FZ Rossendorf, Wiss.-Tech. Ber. FZR-319 (2001) 28

An Optical Klystron for the ELBE-FEL-Undulator U27

C. A. J. van der Geer[1], E. Grosse[2], R. Wünsch

The U27 undulator consists of two independent sections with 34 magnetic periods of $\lambda_u = 2.73\,\text{cm}$. They are mounted on girders with carriages allowing the variation of the undulator parameter K_{rms} between 0.3 and 0.8. The drift section between the units can be varied between 25 and 35 cm.

To guarantee the constructive action of both units the distance d between the two units must be an integer multiple of the undulator period λ_u multiplied by a factor $1 + K_{\text{rms}}$ where K_{rms} is the undulator parameter which depends on the undulator gap g [1]. For that reason one has to move one of the undulator units when changing the gap.

To avoid moving an undulator section we propose to install a magnetic chicane in the drift space which can continuously modify the electron trajectory and hence ensure phase synchronism for any undulator gap. Fig. 1 shows the scheme of the proposed chicane. It consists of 3 dipole magnets. The outer magnets have field strength B and length l_m while the center magnet has the same strength but twice the length. The distances between the magnets are denoted by l_0 and l_1, respectively. Details of the magnetic layout are discussed in ref. [2].
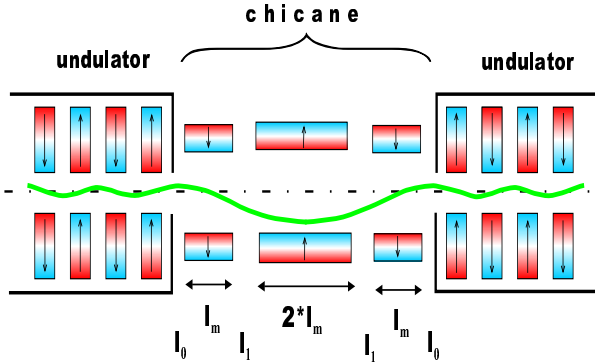
Fig. 1 *Setup of magnets in the chicane and in the neighboring parts of the undulator. Note that in reality the bending (curved line) is perpendicular to the plane of the paper.*

Fig. 2 displays the calculated [3] single-pass gain of the undulator with the chicane as a function of the magnetic field strength B. To achieve the constructive action of both units one has to fix the field strength to one of the peaks. A field up to 100 mT is sufficient continuously to match the optical phase for any undulator gap. The field strength has to be tuned with an accuracy of several mT.

Due to its dispersion the chicane enhances the microbunching of the electrons leading to a considerable in-

crease of the gain at a larger field strength. (Using a field of about 300 mT the gain is roughly 3 times larger than the gain without the chicane.) Effectively the chicane corresponds to a much longer drift space [4].
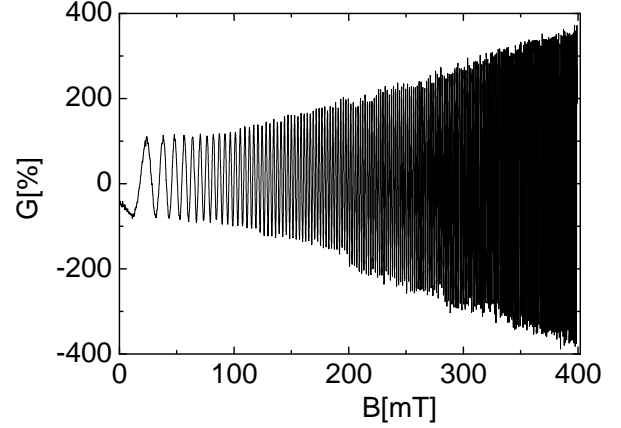
Fig. 2 *Rise in single-pass G gain due to a chicane calculated for a monoenergetic beam as a function of the field strength B. The first peak has been normalized to 100%.*

To take advantage of the higher laser gain the field has to exceed 200 mT. Here the spacing between the maxima of optimal matching is considerably smaller and the field has precisely to be fixed and stabilized within a few Gauss (0.1 mT). Moreover the electron energy spread affects the electron path in the chicane and disturbs the exact phase matching. Calculation have shown (fig. 3) that the gain can only be increased if the energy spread is lower than 0.1%. In contrast the simple phase matching around 50 mT can still be ensured for a beam with 0.4% energy spread.
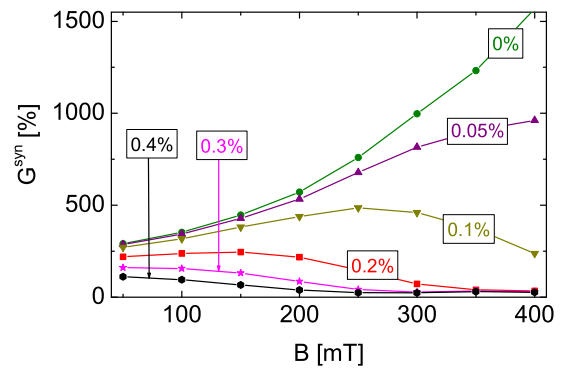
Fig. 3 *Gain G^{syn} in the case of phase synchronism as a function of the field strength B in the chicane for various values of the energy spread.*

[1] Ch.-Ch. Shih, M. Z. Caponi, Phys. Rev. A26 (1982) 438
[2] P. Gippner, This Report, p. 28
[3] S. B. van der Geer, M. J. de Loos, The General Particle Tracer Code, Thesis, TU Eindhoven (2001), ISBN 90-386-1739-9
[4] G. R. Neil, H. P. Freund, 22nd Int. FEL Conf. Duke University (2000)

[1] *Pulsar Physics, The Netherlands*
[2] *also TU Dresden*

Optical Beam Transportation from the Resonator to the Diagnostic Station

W. Seidel, D. Wohlfarth, R. Wünsch, E. Grosse[1], D. Oepts[2], B. Rimarzig, U. Wolf

Taking into account the broad tuning range of the FEL, the laser beam is transported by using broad-band metal mirrors in an evacuated light transport system to avoid light absorption by water vapour and carbon dioxide in the air. The U27-FEL radiation has to be transported 11 m to the diagnostic station and then further - depending on the location of the experiment- over distances of up to 24 m (see ref. [1]). Since infrared beams are prone to significant diffraction, a proper optical beam transport system must be installed in order to guide the light with minimum loss over such distances, at the same time keeping its size at reasonable dimensions.

We have designed and constructed a 4 mirrors optical transport system from the out-coupling hole of the resonator to the diagnostic station considering the building-related features. Because of the presence of high energy electrons, which also produce γ-rays and free neutrons, a strait transportation of the FEL-IR beam through the wall is excluded. The scheme of the system is shown in fig. 1. Now we are testing it in a separate experimental area. We use 3 toric (M11 - M13) and 1 flat (M14) mirror for beam transportation according to fig. 1.
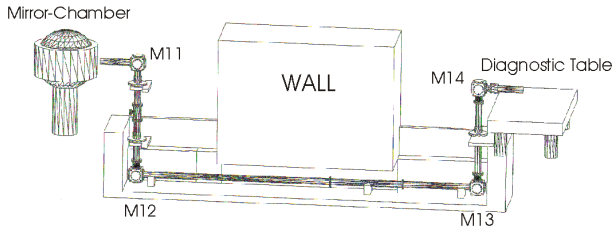
Fig 1 *Schematic layout of the optical beam transport system from the mirror chamber to the diagnostic station.*

The toroidal shape of the mirrors with radii of curvature in the ratio of 1:2 minimized the astigmatism at deflection angle of 90°. The 4 mirrors (Cu-mirrors coated with gold) are located at the building-related features for 90° deflection. The FEL output beam has a large divergence (scaled by $\Theta \sim \lambda/r$, where λ is the wavelength and r the radius of the hole) because a hole-coupled output mirror with small holes is used in the resonator [2]. This divergent beam passes through the CVD diamond window under Brewster's angle. The window separates the ultra-high vacuum system (10^{-8} mbar) of the mirror chamber from the vacuum environment of the transport system (about 10^{-3} mbar). Finally, the FEL beam comes out to the diagnostic table through a KRS-5 exit window under Brewster's angle. As a consequence of the divergent beam, the first mirror M11

is the only mirror with 10 cm diameter in the system, which is located 1.7 m away from the out-coupling hole. The remaining mirrors have 8 cm diameter.

The optics of the system will be aligned by monitoring the spatial intensity profiles of a He-Ne guide laser, which itself is aligned to the resonator axis . The same laser will be used for indicating the position of the IR beam in each laboratory [1]. Therefore, all optical components of the transport system have to be transparent for IR radiation and for 632 nm as well. The calculation for the optical system was carried out under the assumption of an equivalent Gaussian beam. In addition, we demanded an almost wavelength independent waist position at the diagnostic table. Fig. 2 shows the IR beam envelope from the hole in the resonator mirror up to a common beam waist on the diagnostic table for 4 different hole sizes. From fig. 2, it appears that a 10 cm beam pipe is sufficient for the transport system.
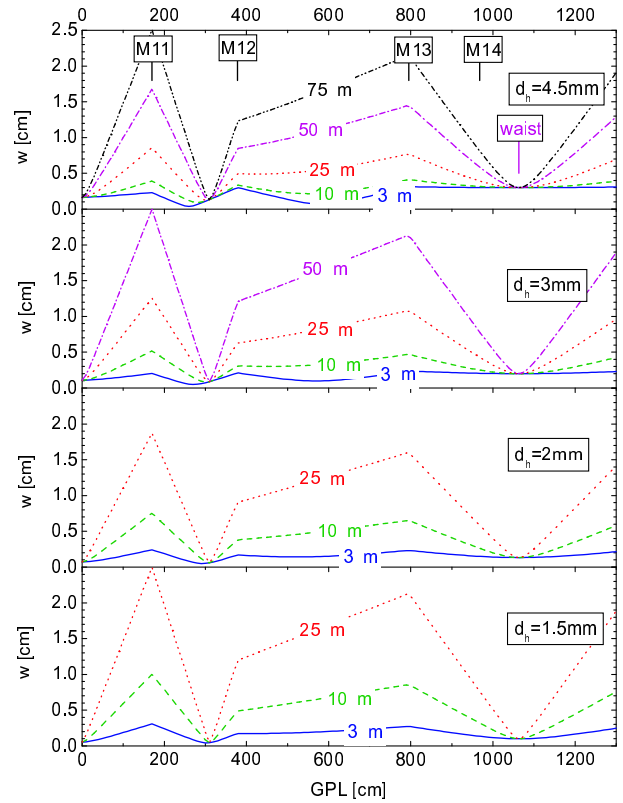
Fig 2 *Radius w of the optical beam as a function of the geometrical path length GPL from the out-coupling hole in the upstream resonator mirror to the beam waist on the diagnostic table calculated for different values of the hole diameter d_h and different wavelengths. Size and position of the second waist (diagnostic) are independent of the wavelength.*

[1] E. Grosse et al., This Report, p. 33

[2] W. Seidel et al., This Report, p. 26

[1] *also TU Dresden*

[2] *Institute for Plasma Physics Rijnhuizen, The Netherlands*

Design of the Infrared Beam Line from the Diagnostic Table to the Optical Laboratories

E. Grosse[1], D. Wohlfarth, R. Wünsch

Figure 1 illustrates the distribution of the infrared beam from the diagnostic table to the various optical laboratories by means of plane and focusing mirrors. The beam line has been designed for radiation with a wavelength from 3 to 150 μm with an average power not larger than 300 W. The position of the mirrors is determined by the physical conditions (position of walls and tables) and by the necessity to refocus the diverging IR beam after passing a distance of a few meters. In contrast to visible light mid and far infrared radiation undergoes a much stronger diffraction.

The large wavelength interval (almost two orders of magnitude) turned out to be a challenge for the design of the beamline and its components. To ensure a high reflectivity ($\approx$99%) in the whole wavelength range the mirrors are made of copper. To get a stigmatic transportation of the beam after a 90° deflection (the same waist in sagittal and tangential plane) the mirrors have a toroidal shape with radii of curvature with the ratio 1:2. Another restriction results from the technology of producing sufficiently accurate metal mirrors which limits the smaller radius of curvature to values below 3 m.

The calculations have been performed on the basis of equivalent Gaussian beams. A 10 cm beam pipe turns out to be sufficient for the beam transport.
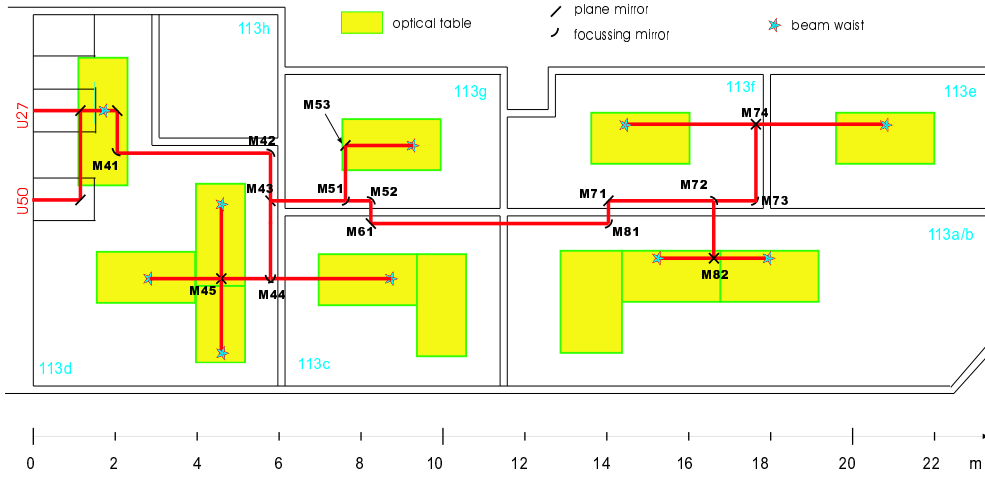
Fig. 1 *Floor plan of the optical laboratories of ELBE with the beam pipe (bold lines) for the IR beam. Mirrors and beam waist positions are indicated additionally.*

The layout complies with the following requirements of the users:

1. The beam has always a spherical cross section and is linearly polarized.

2. At a given nominal position close to the center of each laboratory the beam size is independent of the wavelength for a given outcoupling hole in the FEL resonator; it scales with the size of this hole. Although for short wavelength and thus large Rayleigh length may not lay at the nominal position the size there is still wavelength - independent.

3. The Rayleigh range of the beam on the optical tables exceeds 70 cm in all realistic cases.

4. At each nominal position the beam is between 3 and 6 times thicker than immediately behind the outcoupling hole. Its waist parameter varies between 3 and 11 mm in dependence on laboratory and hole size.

5. To switch the beam from one lab to an other a single mirror has to be moved without touching another one.

6. Within a range of 1 m around the nominal waist position 2-inch mirrors are sufficient for further manipulating the beam.

[1] *also TU Dresden*

Fig. 2 shows an example of the calculated beam envelopes beginning with the waist on the diagnostic table.
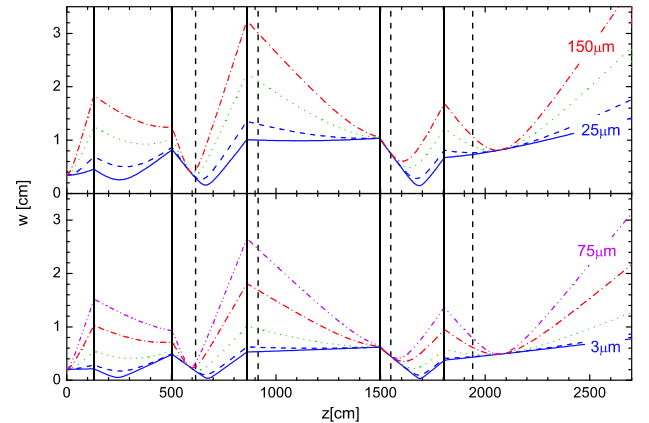
Fig. 2 *Envelopes of the beam to laboratory 113a/b calculated for the beam of the U27 undulator with a 3 mm resonator hole (lower part, wavelength: 3, 10, 25, 50, 75 μm) and for the U50 undulator with a 6 mm hole (upper part, wavelength: 25, 50, 100, 150 μm). Additionally the positions of the mirrors are indicated by vertical lines (solid lines: focusing mirrors, dashed lines: plane mirrors).*

Diagnostic Station for the ELBE-FELs

W. Seidel, E. Grosse[1], D. Wohlfarth

We are developing an optical beam diagnostic system (see fig. 1) properly to characterize and adapt the output of the two FELs (U27 and U50). The present system is compatible with a tuning range from 3 μm to 150μm, and can be extended beyond 150 μm if necessary.

The FEL beam from each undulator will be transported separately from the resonator to the diagnostic area through evacuated beam pipes using reflective optics. Both lines will be merged on the diagnostic table, which may be purged with dry nitrogen to avoid absorption in air if necessary. From the main beam, approximately 1-5 percent of the total power will be separated by different beam splitters for wavelength measurement and power monitoring. The FEL spectra will be measured with a Czerny-Turner type spectrometer which contains a turret with three different gratings to cover the wavelength range from 3 μm to about 200 μm. The monochromator will be equipped with a 48-channel pyroelectric linear array detector. For measurements with higher sensitivity we shall use the second side exit slit equipped with a single Hg-Cd-Te or Ge-Ga detector.

One of the most important features of our FEL will be the ability to select single pulses from the continuous optical pulse train by using plasma switching[1, 2]. To reduce heating problems of sensitive samples, the micropulse repetition rate can be changed from usually 13 MHz to the range from 2 kHz up to 1 Hz. The repetition rate can, in this way, be matched to the requirements of the experiment. For this purpose we shall focus the FEL beam across an additional by-pass to a high-purity silicon slab. We don't have any reflection for P-polarised FEL radiation if the silicon slab is exactly under Brewster's angle. The silicon slab will be illuminated with the focused output of the regenerative amplifier which is synchronized with the FEL. The laser generates a dense electron plasma in the slab, and thus making the slab reflective for several nanoseconds. The subsequent FEL micropulse will then be selected out of the 13 MHz pulse train, refocused to the waist parameters outside of the by-pass line and transported to the users.

With the advance of FEL applications the need arises to vary the radiation intensity over a large dynamic range. In an attenuator precisely fabricated metal grids diffract a calibrated percentage of power out of the beam. The rejected power is absorbed in the walls of the water-cooled housing. The mode structure and other properties of the transmitted beam including the divergence and the M^2 parameters are fully preserved, the polarisation as well.

To rotate the polarisation plane, we shall use a three-mirror arrangement as installed at FELIX [3]. The arrangement is based on the phase change of the electro-magnetic field components at reflection from a metal-coated mirror. A rotation of the arrangement along the axis by an angle α, with respect to the polarisation plane of the incident wave, results in a rotation by 2α of the polarisation of the exit beam.

The micropulse duration will be measured using an infrared autocorrelator. The underlying idea in autocorrelation is to split an incident pulse into two half-intensity pulses and to recombine them in a nonlinear medium. By measuring the second-harmonic intensity as a function of the delay between both pulses, we obtain the pulse length. Commercially available nonlinear crystals allow frequency doubling of wavelengths up to around 40 μm.

The variation in the peak power of each micropulse and in the average power will be detected with the corresponding detectors[4].

Apart from a well characterized and flexible laser beam it is also important to have a user-friendly interface to these items. We try to give any user as much control as possible over the important laser parameters, i.e., wavelength, scanning capabilities (without changing the electron energy), spectral width, pulse duration, attenuation, and polarisation direction.
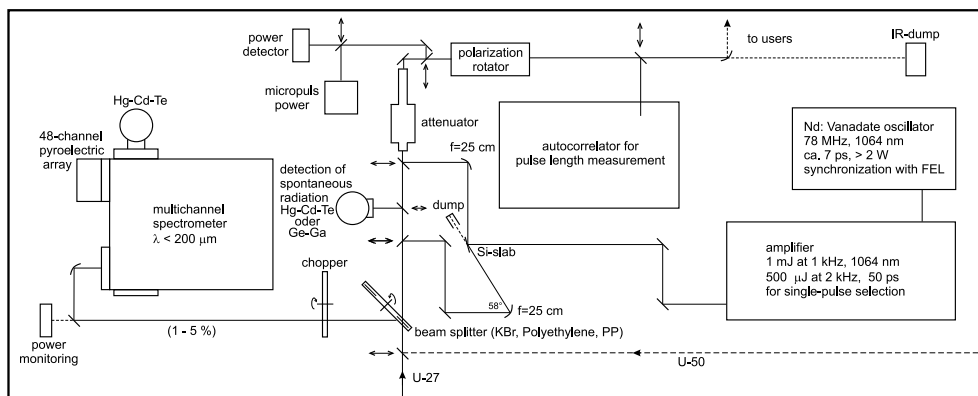
[1] E.H. Haselhoff et al., Nucl. Instr. and Meth. A358 (1995) ABS28

[2] P. Haar, Ph.D. thesis, Stanford University (1996)

[3] D. Oepts[2], FELIX, private communication

[4] Furlinski et al., This Report, p. 35

---

[1] also TU Dresden

[2] Acknowledgements: We would like to thank Dr. D. Oepts and Dr. A. van der Meer from FELIX, Institute for Plasma Physics Rijnhuizen, The Netherlands, for their helpful discussions and technical assistance.

Infrared Detectors for the Free-Electron Laser Beam Diagnostics

G.I. Furlinski, E. Grosse[1], W. Seidel, U. Wolf

For the characterisation of the Free-Electron Laser beam a number of IR detectors with different temporal, energetic and spectral performance are needed. The purpose of this investigation was to determine the features of the existing detectors compared with specifications of the manufacturers. The measurements and analyses of the results are in accordance with the methodology described by J. D. Vincent [1]. A CO_2 laser (MPB Technologies) at 11.14 μm, pulsed with a chopper arrangement, has been used as light source.

1. PC-16-1 is a Hg-Cd-Te photoconductive detector with preamplifier (PCA-500 with gain g=500) of the "Fermionics" Corp. company. The detector uses an active area of 1mm x 1mm = 1 mm^2, a ZnSe window, field of view 60^0 and works at temperature of 77 K. The cutoff wavelength is about 18 μm. The detector's responsivity has been measured with 1 kHz repetition rate pulses and the corresponding value obtained for responsivity is R = 2200 V/W (Fig. 1). Frequency response and noise spectral density have been obtained as well. The corner frequency has been derived at f_c = 260 kHz, which corresponding to a rise time of 960 ns.

2. PCI-L-2TE-3 is a Hg-Cd-Zn-Te photoconductive detector of the "VIGO Systems" company. The active area is 1mm x 1mm = 1mm^2 and the spectral range with antireflecting Ge window is 2 - 12 μm. The detector is cooled thermoelectrically to 230 K; its frequency range is 1 kHz - 100 MHz, which corresponds to 2.5 ns fastness. The signal-to-noise ratio is extremely high, and could not be determined due to the channel width of the measurement electronics. The detector's responsivity has been derived as 768 V/W (Fig 2); this value corresponds well with the 745 V/W specified by the manufacturer. The maximum power density threshold per peak is 10 W/mm^2.

3. The photon-drag detector is a Ge crystal doped with Au. There is a 0.95 cm^2 x 1.5 cm =1.43 cm^3 active volume and it works at room temperature. A fastness in the pico-second scale in a wild spectral range is inherent for this type of detectors. The detector's responsivity has been measured in a lock-in-amplifier scheme and estimated to be 57 mV/MW (Fig 3). This value is considerably lower than the theoretical estimation of 175 mV/MW obtained in accordance with paper [2] for ideal photon-drag detector. Possibly, the peak power of 6 W is out of its dynamic range of the detector.

4. P5-01 is a ultra-fast pyroelectric detector of the "Molectron" company. The active area of the detector has 1 mm diameter and works at room temperature in an extremely wide spectral range (from UV to FIR). The fastness is limited by the electronics; the values are in the pico-second range. Depending on the working conditions the detector is able to work in energy meter mode.

Due to the low laser power, the measurements have been performed close to the transition point between the two modes (detector mode and energy meter mode). As a consequence of that the maximal value derived for responsivity was 127 V/kW, which is above of the 16.1 V/MV mc specified by manufacturer. The detector's responsivity has been presented as drawing versus repetition rate (Fig 4).

In conclusion it can be said that the semiconductive photoconductive detectors are appropriate for applications, which require sensing of weak radiation. The photon-drag and pyroelectric detectors are suitable for applications requiring high fastness and resistance at large peak power density.

Fig. 1

Fig. 2

Fig. 3

Fig. 4
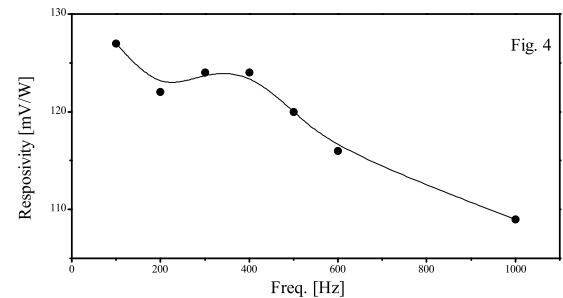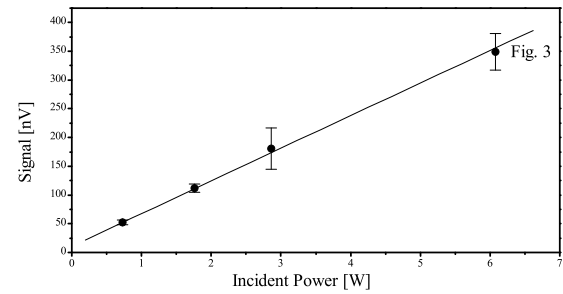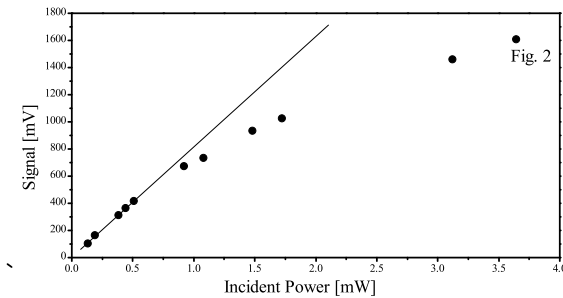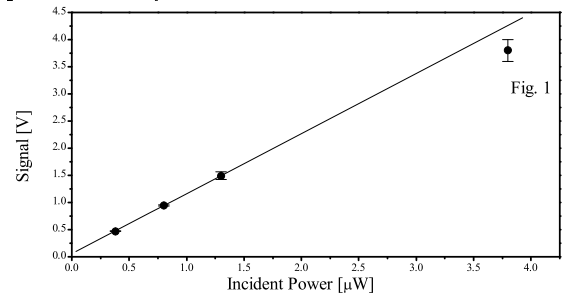
[1] J. D. Vincent, Fundamentals of infrared detector operation and testing, A Wiley-Interscience Publication (1990)
[2] J.G. Edward, A.G. Roddie, and P.A. Smith, J. Phys. E: Sci. Instrum., v. 16 (1983) 526

[1]also TU Dresden

Scanning Near Field Infrared Microscopy Using FEL Light

M. Sczepan, J. Martin[1], W. Seidel, E. Grosse[2]

The use as a light source in microspectrometry and microscopy is one application for the light generated by the FEL. Scanning near field microscopy and microspectroscopy allow the evaluation of samples with a spatial resolution beyond the Abbe limit, which, in classical microscopy, limits the resolution to $d_{min} = \lambda/NA$. With Numerical Apertures of $NA = 0.5 - 0.7$ for the reflective objectives used in conventional IR microscopy resolutions of about 1.4λ can be achieved. A common technique for near field microscopy is to illuminate the sample trough a small aperture of sub-wavelength diameter d (usually $d < \lambda/10$). For small distances between aperture and sample ($z < \lambda$) the width of the emitted light distribution is equal to the aperture size and thus the resolution of the instrument equals is limited only by the size of the aperture used. A part of the transmitted light is collected in the far field and focussed on a detector. An image is obtained by scanning the sample in x-y direction while a spectrum of a microscopic sample area can be obtained by varying the wavelength. For visible and infrared light metal-coated glass fibers with a small aperture on the tip are used to illuminate the sample. Other near field techniques employ small apertures for light gathering or light scattering from subwavelength sized metal tips [1].

The small light throughput is a major problem with the subwavelength apertures. Theoretical and experimental evaluation of light transmittance ([2] and [3]) revealed a d^6 behaviour for the central intensity of the transmitted light in the far field. For this reason the increase of resolution by using smaller apertures inevitably involves a strong reduction of the light throughput. Thus illumination sources for near field microscopy techniques must have a very high brightness. In order to perform microspectroscopy any choice of light source for near field microscopy must fulfill another requirement: the source should be either broadband or tunable to have access to a wide spectral range. The free electron laser with its high output power and easy tunability is an ideal light source for scanning near field microscopy.

A near field microscopy system has been set up in our laboratory using the fiber tip illumination scheme. In this scheme the sample is illuminated through a metal coated fiber tip with a sub-wavelength sized aperture which is placed close to the sample surface. The distance is controlled with a shear-force detection system. Small changes in the vibration frequency and phase of the fiber tip are used to detect the approach to the surface and to control the distance between sample and tip. A topografic image of the sample surface can be obtained from the distance control voltage. The transmitted light is detected in the far field yielding an infrared microscopic image. Fine tips on IR-transparent chalcogenide fibers (obtained from Amorphous Materials) have been produced using the etching technique described in ref. [4]. Sample scanning is realized using a xyz-piezomechanical translation stage which covers a scannable area of $100*100~\mu m^2$. The sample scanning and translation system as well as the probe-sample distance control systems have been tested. These tests have been performed with conventional drawn glass fiber tip as well as with an etched chalcogenide glass fiber tip. First topografic images of different samples have been obtained. An example of a topografic image (of a ca. 20 μm wide and 3 μm deep groove in a glass surface) is shown in Fig. 1.
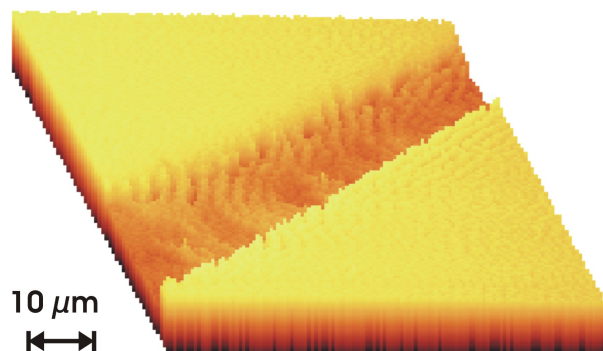
Fig. 1 *Topografic image of a test sample (groove in glass surface, ca. 20 μm wide and 3 μm deep) using a drawn quartz glass fiber tip*

[1] B. Knoll, F. Keilmann, Appl. Phys, Lett. 77 (2000) 3980

[2] H.A. Bethe, Phys.Rev. 66 (1944) 163

[3] T. Smith, 'The source issue in near-field IR microscopy', presentation in the WIRM 2001 workshop, Porquerolles, France (2001)

[4] M.A. Unger, D.A. Kossakovski, R. Kongovi, J.L. Beauchamp, D.V. Palanker, Rev. Sci. Instr. 69(8) (1998) 2988

[1] *Technical University Chemnitz, Institute for Physics, Germany*
[2] *also TU Dresden*

Bremsstrahlung Collimator for the NRF Set-Up at ELBE

K.D. Schilling, R. Schwengner, F. Dönau, L. Käubler, A. Wagner, W. Neumann[1], Th. Riedel[1], R. Schlenk[1]

The set-up for nuclear resonance fluorescence (NRF) experiments at the new ELBE accelerator recently described in [1,2] has been constructed and is now being installed. The bremsstrahlung photons produced in the radiator have to be collimated onto the NRF target located in the nuclear physics cave. This will be realized with the collimator displayed in Fig. 1.

As briefly outlined in [2], the overall length of the collimator is 2600 mm. It features a step-like construction consisting of 13 cylindrical segments of about 200 mm length each made of high-purity aluminium (Al99.5) with a gradually increasing aperture of 5 mm diameter at the collimator entrance and 24 mm at the collimator exit. This conically shaped aperture will strongly reduce small-angle scattering of the primary bremsstrahlung photons from the walls of the aperture. Aluminium has been chosen because of its high neutron separation energy ($S_n = 13.1$ MeV, cf. Table 1). Moreover, aluminium has an attenuation behaviour (e.g. tenth-value layer) comparable with that of the surrounding concrete wall (Table 1).

The casing tube of the collimator is welded together from three sub-tubes with step-wise increasing inner and outer diameters (for shielding reasons) and it consists of aluminium alloy with higher mechanical rigidity (AlMgSi1). This casing tube will be inserted into the heavy-concrete wall of 1.6 m thickness under an angle of 45° after having drilled a larger, cylindrical hole with accordingly step-wise increasing diameters. After careful adjustment of the tube, the remaining cylindrical gap will be filled with liquid concrete of the same composition as that of the surrounding wall.

Thus, the bremsstrahlung collimator in the chosen design will efficiently reduce undesired photon and, in particular, neutron background radiation in the nuclear physics cave positioned downstream of the collimator. The special flange construction at the collimator exit ensures the tight vacuum connection between the collimator and the beam tube in the nuclear physics cave. The collimator entrance is vacuum-tightly connected with the casing of the beam shutter and hardener [5].

By utilizing average beam currents in the order of $500\,\mu$A, photon fluxes of about 2×10^8 photons per MeV · s for 7 MeV photons at $E_{e^-} = 10$ MeV can be expected at the NRF target position.

element/ material	X_o (cm)	TVL (cm)	S_n (MeV)
C	18.8	(100)	18.7
Al	8.9	38	13.1
Fe	1.76	10.8	11.2
W	0.35	3.5	6.2
Pb	0.56	5.7	6.7
concrete (2.6 g/cm^3)	10.7	38	
heavy concrete (3.6 g/cm^3)	(6.0)	26	
polyethylene	47.9	(140)	18.7
water	36.1	(150)	15.7
air	30,400		10.6

Table 1. *Values of radiation length (X_o), tenth-value layer (TVL) and neutron separation energy (S_n) for different elements and composite materials [3,4] used in the NRF set-up at ELBE for electron energies up to 20 MeV. Isotopic abundances of less than 2.5 % have not been taken into account for the S_n-values. Values in parentheses have been extrapolated.*
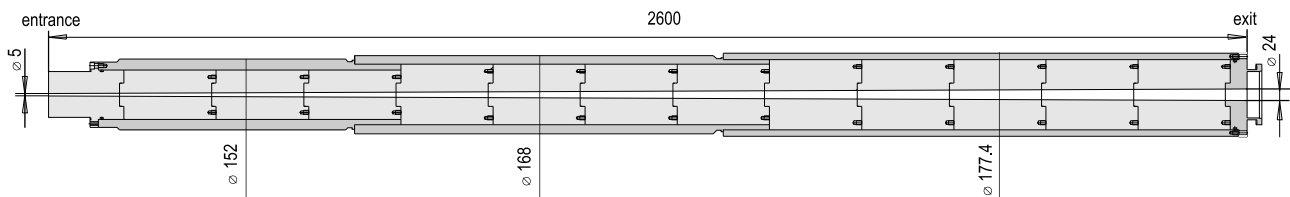
Fig. 1 *Cross-section of the collimator.*

[1] K.D. Schilling et al., FZ Rossendorf, Wiss.-Tech. Ber. FZR-217 (1999) 32
[2] K.D. Schilling, http://www.fz-rossendorf.de/ELBE/en/np
[3] W.P. Swanson, IAEA Report No. 188 (1979); DIN 6847, part 2 (1977)
[4] B. Dörschel et al., The Physics of Radiation Protection (Nuclear Technology Publishing, England, 1995)
[5] K.D. Schilling et al., This Report, p. 41

[1]*FZ Rossendorf, FWF*

Determination of the Spectral Distribution of the Bremsstrahlung Beam at ELBE

A. WAGNER, E. GROSSE[1], S. N. MALLION

Areas of research at the new ELBE facility of the FZR will include nuclear spectroscopic studies by means of nuclear resonance fluorescence (NRF) experiments utilizing polarized photons, and the spectroscopy of radioactive nuclei produced by photon-induced fission. For these experiments, it is mandatory to obtain detailed knowledge of the spectral distribution of the Bremsstrahlung that is produced by allowing the electron beam from ELBE to strike a target. In order to determine the flux and energy distribution of photons impinging on the NRF target we propose to detect the Compton-scattered photons emerging from the target at an angle of about 350 mrad with respect to the direction of the primary photon beam. With the energy of the outgoing photon E_γ^s determined by energy and momentum conservation as $E_\gamma^s = E_\gamma^i (1 + \frac{E_\gamma^i}{m_e c^2}(1 - \cos\theta))^{-1}$, where E_γ^i is the energy of the ingoing photon, we utilize the unambiguous direct correspondence between the energies of the in- and outgoing photons for a given scattering angle θ in order to recover the incident Bremsstrahlung spectrum.

The measurement of the energies of the scattered photons will be performed using a large NaI(Tl) scintillation detector [1] which is on loan from the Technical University of Dresden. This detector features an encapsulated cylindrical crystal of thallium-doped sodium iodide of 25.4 cm diameter and 25.4 cm length. The crystal is viewed by seven photomultiplier tubes (RCA 4900) which are attached by means of hollow light-guides. The active detector is surrounded by a 9.6 cm thick shell composed of a plastic scintillator, for suppressing cosmic-ray background in low-count-rate experiments. Both components are surrounded by a lead shield of 7.5 cm thickness. The detector is placed about 220 cm downstream from the target, close to the photon beam dump (see Fig. 1). A lead collimator having a thickness of 10 cm and an aperture of 5 cm diameter is fixed to the front of the crystal. The geometry of the collimator is such that the energy spread of the Compton-scattered photons across its aperture is comparable to the intrinsic energy resolution of the detector. The individual energy signals from the seven photomultiplier tubes are read out by charge-sensitive analog-to-digital converters in a list-mode data acquisition system. These signals are then added on an event-by-event basis, after first carrying out an energy calibration of each of the seven individual channels. This procedure facilitates compensation of drifts and gain changes which are due to variations of the temperatures of the NaI(Tl) crystal and the photomultiplier tubes.

Using the GEANT software package [2], we performed Monte-Carlo simulations of the detector response for a typical experimental situation in which the Bremsstrahlung impinges on a 5 mg molybdenum target.
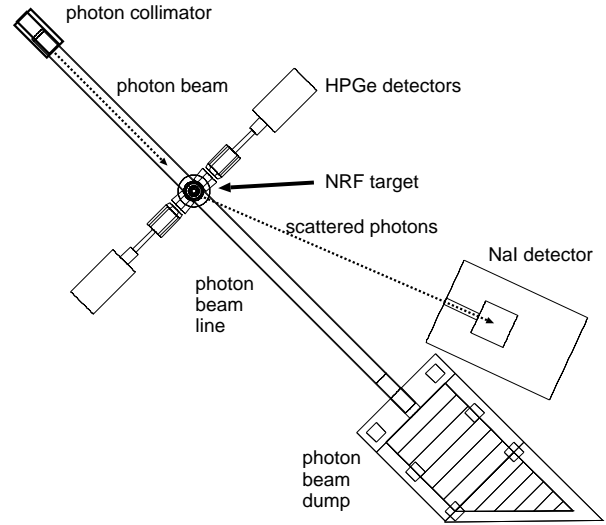
Fig. 1 *Set-up of the Bremsstrahlung measurement at ELBE.*

Fig. 2 displays the 2-dimensional correlation between the energies of the in- and outgoing photons for the conditions given above. Besides the strong correlation discussed above, a weaker background from pair-production can be seen below E_γ^s = 1 MeV. The response function which will be used in deriving the incident Bremsstrahlung spectrum will take account of this additional effect.
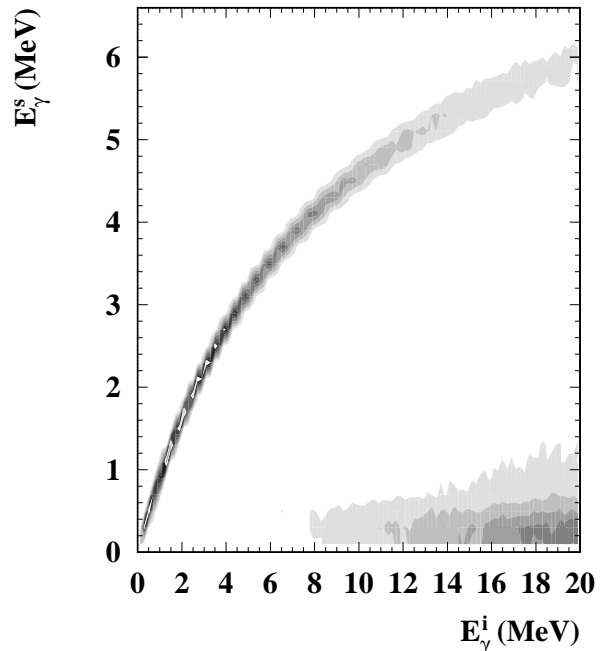
Fig. 2 *Correlation between the energy of photons scattered from a Mo target and the energy of the incident photons for a scattering angle of 350±5 mrad.*

[1] L. Ricken, Dissertation, Ruhr-Universität Bochum (1988)
[2] CERN Program Library Long Writeup Q121, CERN, Geneva (CH) (1994)

---

[1] *also TU Dresden*

A Polarisation Monitor for Experiments with Bremsstrahlung at ELBE [D]

R. Schwengner, H. Sharma, A. Wagner

The excitation of nuclear states by linearly polarised photons in connection with the measurement of the azimuthal asymmetry of the scattered photons is one method to distinguish between electric and magnetic dipole radiation at high photon energies ($E_\gamma > 5$ MeV) and, hence, to determine the parity of nuclear states. For this purpose, the production of linearly polarised photons is planned at the bremsstrahlung facility [1] being under construction at the ELBE radiation source. During long-time measurements it is important to monitor the degree of polarisation of the photons. This can be done via the photodisintegration of the deuteron. Because of predominant $E1$ absorption in this process the protons and neutrons are emitted preferentially in the direction of the electric field vector of the polarised bremsstrahlung. The energies of the incident photons correlate with the measured proton energies. The degree of polarisation can be deduced from azimuthal asymmetries of the intensities of the protons. This method has been applied in experiments with bremsstrahlung at the University of Gent [2].

We have designed a set-up of four silicon detectors positioned perpendicular to the photon beam at azimuthal angles of 0°, 90°, 180° and 270° in a cylindrical reaction chamber. A CD_2 foil of 40 μm thickness will be used as a target. A cross-section of the reaction chamber housing the detectors and the target is shown in Fig. 1.

The silicon detectors (type EURISYS LEC 200-4000) having sensitive areas of 200 mm^2 (diameter 16 mm) and useful thicknesses of 4.25 to 4.88 mm are mounted in cylindrical casings with a BNC connector at the rear side. To test the detectors we measured spectra of a mixed $^{239}Pu/^{241}Am/^{244}Cm$ α-particle source (internal line width of ≤ 20 keV) placed at the target position (cf. Fig. 1). In these measurements a ZfK-VV5 preamplifier in connection with an ORTEC 570 main amplifier at a shaping time of 0.5 μs were used. The counting rate was about 300 s^{-1}. The characteristics of the detectors are given in Table 1. An example of a measured spectrum is shown in Fig. 2.

Table 1. Characteristics of the silicon detectors.

Serial no.	U/V	$I/\mu A$	$FWHM/$keV at 5486 keV
9170	+500	2.9	35
9273	+450	1.3	25
9286	+450	3.1	34
9379	+510	4.9	29
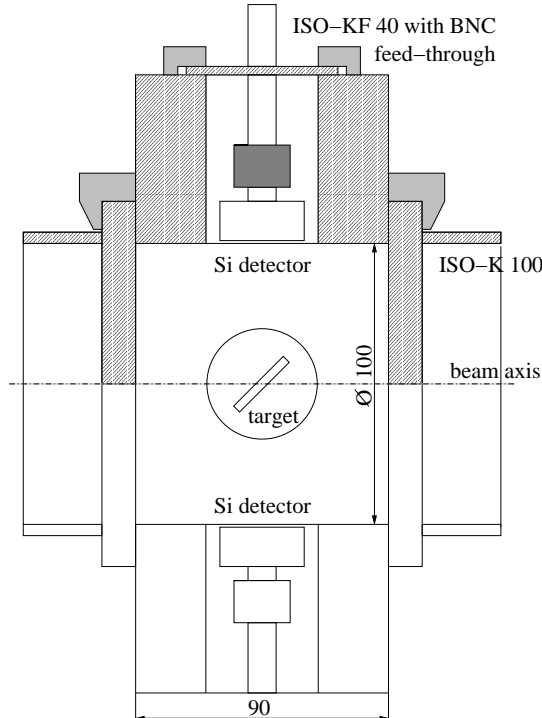
Fig. 1 *Cross-section through the vacuum chamber housing four Si detectors for monitoring the degree of polarisation of bremsstrahlung.*
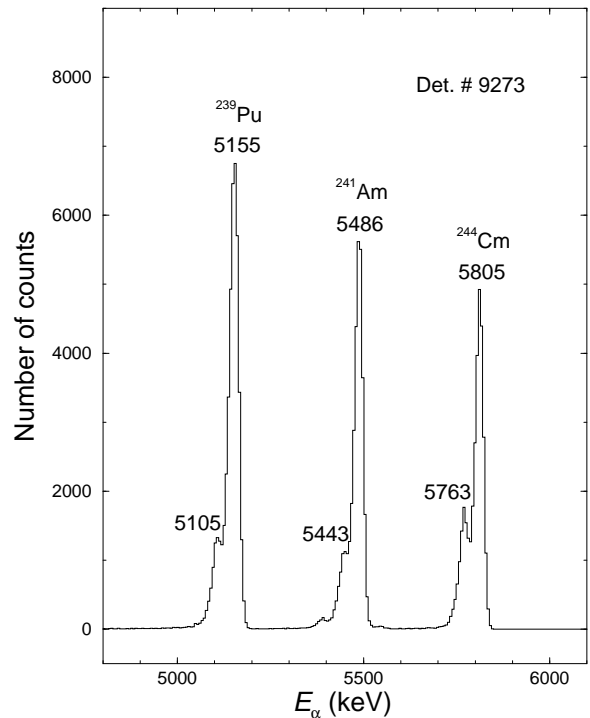
Fig. 2 *Spectrum of a mixed $^{239}Pu/^{241}Am/^{244}Cm$ α-particle source.*

[1] K.D. Schilling et al., FZ Rossendorf, Wiss.-Tech. Ber. FZR-217 (1999) 32
[2] K. Govaert et al., Nucl. Instrum. Methods in Phys. Res. A 337 (1994) 265

Calculation of the Photon Flux due to the Electron Beam Dump

S. N. Mallion

Nuclear Resonance Fluorescence (NRF) experiments utilising the ELBE radiation source require extremely low levels of background radiation. One potential source of such background is the electron beam dump. It is therefore desirable to know the background to which this beam dump gives rise in the experimental area, which is separated from the beam dump by a layer of iron having a thickness of 10 cm and a wall made from heavy concrete having a thickness of approximately 200 cm. For an electron beam current of 1 mA and an electron energy of 20 MeV, Naumann [1] used Monte Carlo techniques to calculate the photon flux per unit energy range at various points on the surface of an imaginary cylinder of 19.3 cm radius surrounding the electron beam dump. A sample of the data thus obtained is shown in Fig. 1. Utilising the flux data provided by the Monte Carlo calculations, whilst taking into account all pertinent geometrical factors as well as photon attenuation in both iron and concrete layers, the flux per unit energy range at a point inside the experimental area was calculated as a function of photon energy (Fig. 2). From Fig. 2, it is estimated that the rate at which photons in the energy range 0–20 MeV impinge on a detector having a surface area of 50 cm^2 is approximately 0.3 s^{-1}. During a recent experiment at the S-DALINAC of the TU Darmstadt [2], in which NRF was observed in ^{89}Y, the total background rate was found to be about 2300 s^{-1}. Assuming that, despite the different experimental conditions, the total background rate in our experiments at the ELBE facility will also be of the order of 10^3 s^{-1}, the contribution of the electron beam dump to the total background rate will be insignificant. Furthermore, in the experiment carried out at the S-DALINAC, a typical weak fluorescence line having a full width of 3 keV was found to give rise to an event rate of approximately 2.4 × 10^{-3} s^{-1}. Let us assume that a weak fluorescence line of the same width and intensity appears in an experiment at ELBE. In this case, the results of Fig. 2 indicate that photons which arise from the electron beam dump and which have energies within the 3 keV range spanned by the weak fluorescence line impinge on the detector at a rate which is only about 2% of the event rate corresponding to the line. Thus it is concluded that photons generated in the electron beam dump will not give rise to significant levels of background in the NRF experiments which are to be conducted at the ELBE facility.
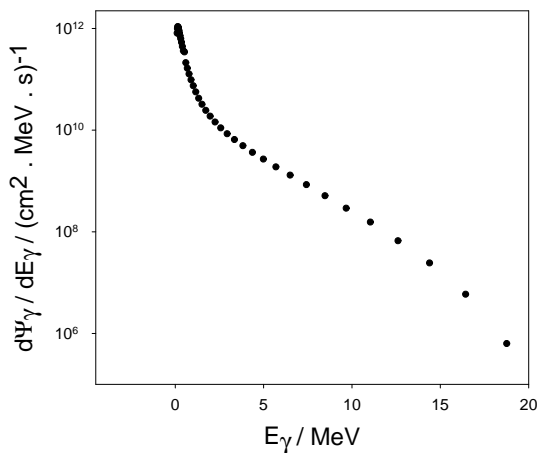
Fig. 1 *Flux per unit energy range as a function of energy at a point on the curved surface of the imaginary cylinder approximately half-way along its length.*
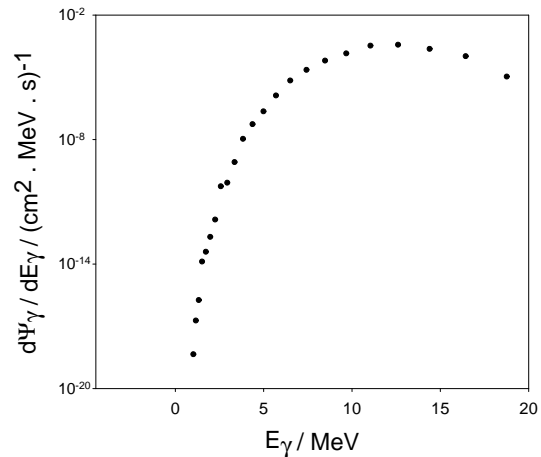
Fig. 2 *Flux per unit energy range at a particular point inside the experimental area as a function of photon energy.*

[1] B. Naumann, This Report, p. 25
[2] R. Schwengner et al., Nucl. Phys. A 620 (1997) 277

Beam Shutter and Hardener for the NRF Set-Up at ELBE

K.D. Schilling, A. Wagner, F. Dönau, L. Käubler, R. Schwengner, W. Neumann[1], R. Schlenk[1]

The beam shutter and hardener (BSH) is part of the radiation protection system of the ELBE accelerator, on the one hand, and it will influence the beam quality of the bremsstrahlung for the nuclear physics experiments, on the other hand. It will be positioned directly in front of the entrance aperture of the bremsstrahlung collimator [1]. A schematic view of the BSH is shown in Fig. 1. First considerations have been outlined previously in [2].
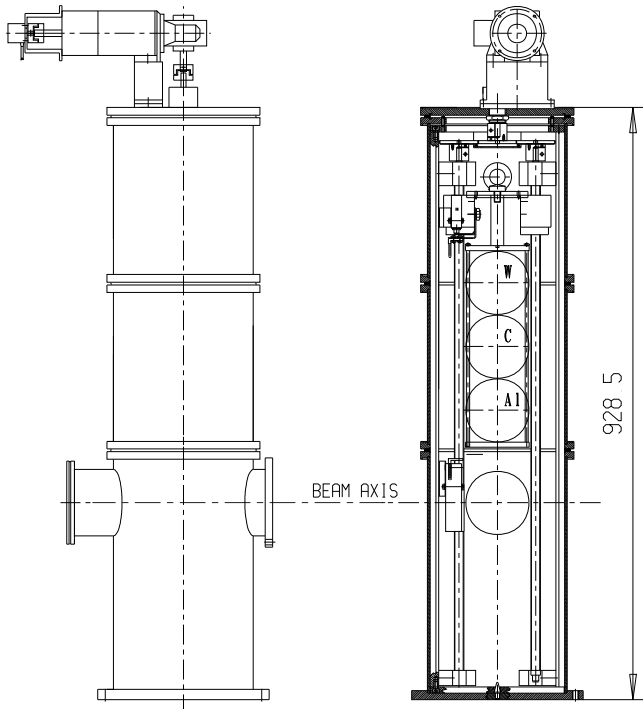
Fig. 1 *Cross-section of the beam shutter and hardener.*

The BSH will fulfil two requirements for the nuclear physics experiments at ELBE: (i) to shut the collimator entrance port against background radiation from the accelerator hall and, thus, to shield the nuclear physics cave when the accelerator is operating for other experimental caves; and (ii) to harden the spectral distribution of the bremsstrahlung photons (= attenuate the lower energies) for the NRF experiments by inserting appropriate absorbers into the photon beam, if desired.

In order to meet these requirements, four different settings of the BSH are available: three internal positions are equipped with different absorbers; the fourth position has no absorber providing an undisturbed photon beam (cf. Fig. 1). The three cylindrical absorbers of equal size (100 mm diameter, 100 mm length) are arranged on top of each other on a common frame that can be moved and positioned vertically by a remote-controlled stepping motor. The beam shutter is positioned at the top and consists of the heavy metal TRIAMET, a composite material made of 95 % W and 5 % Ni, Cu as binding phase resulting in a high density ($\rho = 18$ g/cm^3) and excellent shielding properties. Its photon attenuation is equivalent to that of 0.8 m of heavy concrete [3] satisfying the shielding requirements against background in the accelerator hall. The two absorbers for the beam hardening are made of electro graphite (impurity $< 10^{-2}$ %) and of high-purity aluminium (Al99.5), respectively. They attenuate the low-energy part of the photon spectrum as calculated in [2] using the GEANT software package [4].

The BSH is integrated into the interlock system of the accelerator. In case of emergency, the frame with the absorbers will be moved downwards to the lowest position to shut the collimator entrance with the TRIAMET absorber [case (i)]. The BSH is connected with the common vacuum system of the collimator and the beam tube in the nuclear physics cave, but, it is separated from the ultra-high vacuum in the accelerator and electron beam lines by a 1 mm thin, high-purity aluminium (Al99.5) window of 28 mm diameter.

[1] K.D. Schilling et al., This Report, p. 37
[2] A. Wagner, http://www/FWK/MITARB/wagnera/nrf/docu/en/NP-IS.01.html
[3] W.P. Swanson, IAEA Report No. 188 (1979)
[4] GEANT, CERN Program Library Long Writeup Q121, Geneva (1994)

[1] *FZ Rossendorf, FWF*

Design Studies of a Liquid Lead Neutron Radiator for TOF Experiments at ELBE [D]

E. Altstadt[1], S. Eckert[1], H. Freiesleben[2], V. Galindo[1], E. Grosse[3], B. Naumann[2], K. Seidel[2], F.-P. Weiss[1]

Radiator Design

Time of flight experiments with a pulsed neutron beam are planned at ELBE. The development of a technologically feasible radiator is an essential part of the operation of such neutron experiments. Simulations were carried out for rotational symmetric radiators (length $4.1\,mm$; radii $2.5\,mm$ and $5\,mm$) which consist of a solid material (Ta) [1]. For a beam energy range from $20\,MeV$ up to $50\,MeV$ and a current of about $1\,mA$ the energy deposition in the radiator would result in melting. Based on this fact, a new radiator concept was developed using liquid lead as a radiator. The material depth seen by the electron beam was chosen in the order of the radiation length X_0 (Pb; $X_0 = 6.3688\,g/cm^2$). Various materials for the radiator vessel were considered.

Simulation of the power dissipation

The power dissipation in the wall and the lead were obtained for an electron beam of $E = 30\,MeV$, $I = 1\,mA$ and $r = 1.5\,mm$. The Monte Carlo simulations were carried out using the FLUKA code [2].

	material and thickness [μm]		
	steel	beryllium	
	500	500	300
Pb	10.371	10.271	10.245
wall (beam in)	0.571	0.136	0.081
wall (beam out)	0.388	0.092	0.056
lateral walls	0.256	0.054	0.031
sum	11.586	10.553	10.413

Tab. 1 *Power dissipation in the lead and the wall given in kW after irradiation of the radiator with an electron beam of $E = 30\,MeV$ and $I = 1\,mA$.*

The results are shown in Tab. 1 for liquid lead ($\varrho = 10.5\,g/cm^3$) and structural parts of the wall consisting of stainless steel or beryllium.
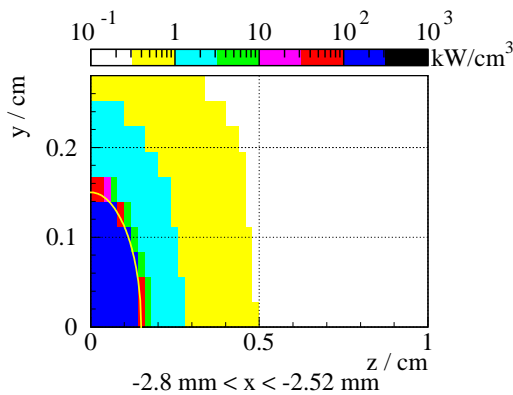
Fig. 1 *Power distribution in the liquid lead volume in the yz-plane normal to the beam in the first lead layer; the line describes the beam shape.*
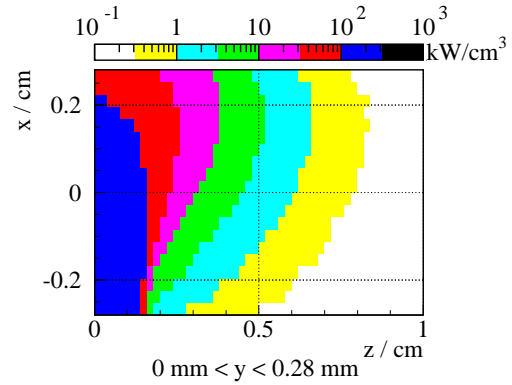
Fig. 2 *Power distribution in the liquid lead volume at the central xz-plane.*
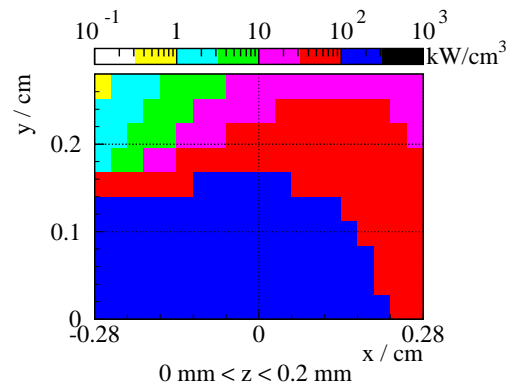
Fig. 3 *Power distribution in the liquid lead volume at the central xy-plane.*

The power density in the steel wall heated by the electron beam amounts to $162\,kW/cm^3$, which is four times more than in the $500\,\mu m$ thick beryllium wall and leads to an overheating of the steel. Hence a beryllium vessel was considered, the three-dimensional distribution of the power dissipation in the radiator was calculated.

In Fig. 1 the power distribution in the liquid lead volume is shown in the yz-plane. The beam hits the radiator at the Be wall at $x = -0.33\,cm$. The same is shown for the central regions in the xz-plane (Fig. 2) and the xy-plane (Fig. 3).

The liquid lead loop - Numerical flow and temperature simulation

The lead circulates inside a closed loop (Fig. 4). The liquid metal is exposed to the electron beam if it passes a target section with a cross sectional area of $5.6 \times 5.6\,mm^2$ and beryllium walls with a thickness of $500\,\mu m$.

Numerical calculations for the target section of $12\,cm$ length predict maximum values of the temperature of $530°\,C$ in the lead assuming a mean velocity of about $5\,m/s$ and a temperature of $400°\,C$ of the flowing lead at the inlet of the target section. A mean temperature of $450°\,C$ is obtained by averaging over the cross section at a distance of $6\,cm$ downstream of the position where the electron beam hit the lead.

[1] *FZR, Institute of Safety Research*
[2] *Institute of Nuclear and Particle Physics, TU Dresden*
[3] *also TU Dresden*
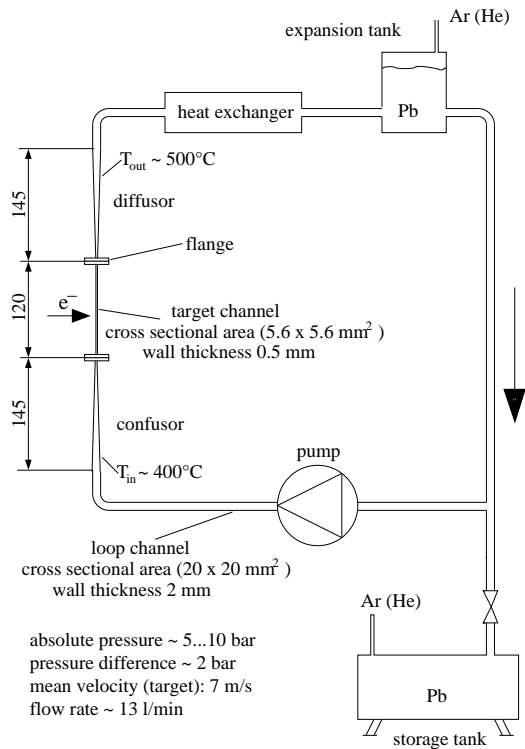
Fig. 5 shows the results of the numerical flow and heat transfer simulation using the commercial multi-purpose finite elements code FIDAP [3]. It shows, from the left to the right, the discretisation mesh, the temperature distribution at the beryllium wall, the temperature distribution in both wall and liquid lead, respectively. The flow is in z-direction.

A test loop will be set-up to validate the numerical calculations and to collect experience with respect to the behaviour of the materials as well as the handling and instrumentation of the loop. As shown in Fig. 4 the main components of the loop are an induction pump, a heat exchanger, an expansion tank and a storage tank. The loop is designed to operate at a pressure up to $6\,bars$ and a maximum flow rate of $0.2\,l/s$. The volume of the loop will be about $5\,l$.

The temperature field leads to mechanical loads in the wall of the Be-tube. The stresses and strains are evaluated using an finite element model based on the code ANSYS [4]. The mesh of the Be-wall is identical to that of the CFD model. Thus the nodal temperatures are taken from the FIDAP calculations.
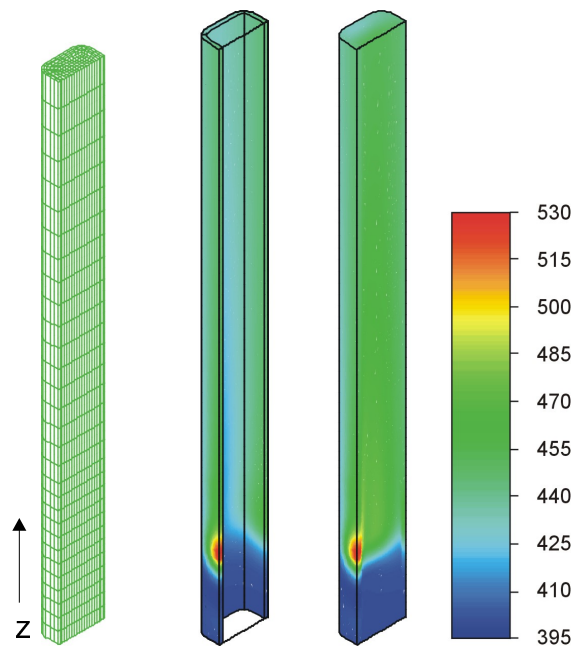
Fig. 5 *Temperature distribution. Mean Pb velocity: $5\,m/s$. Maximum temperature: $530°\,C$.*

Furthermore for reason of conservatism a static internal pressure of $10\,bars$ was assumed. An elastic-plastic material behavior is used. Beryllium is rather brittle at room temperature (plastic fracture strain 2%) whereas at higher temperatures $(300\text{-}700°\,C)$ it becomes more ductile (fracture strain up to 30%). Fig. 6 shows the plastic strain for a Pb velocity of $5\,m/s$. The plastic deformation in the Be-wall is limited to the vicinity of the electron beam. The maximum plastic equivalent strain is about 0.48% occurring at the wall which is hit by the beam. This is far below the fracture strain even at room temperature. However, considering a large number of temperature cycles (heat-up, cool down), material fatigue could be a problem.
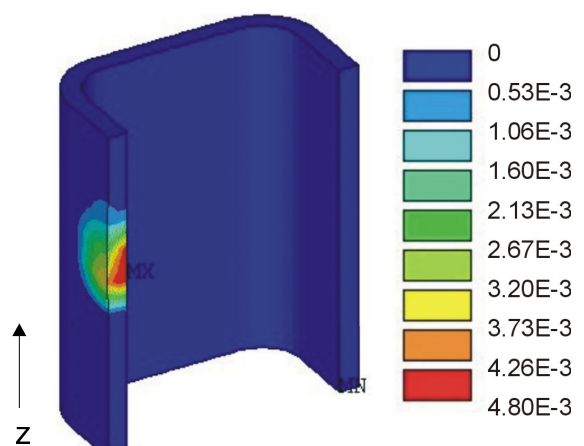
Fig. 6 *Plastic equivalent strain in the beryllium wall.*

[1] B. Naumann et al., FZ Rossendorf, Wiss.-Techn. Berichte FZR-271 (1999) 35
[2] A. Fasso, A. Ferrari and P.R. Sala, Proc. of the Monte Carlo 2000 Conference, Lisbon (2000)
[3] Fluent Inc.: *FIDAP 8 theory manual*, Lebanon, NH, USA (1998)
[4] ANSYS User's Manual for Rev. 5.6., Swansons Analysis Systems, Inc. (1999)

Induced Radioactivity in a Liquid Lead Neutron Radiator for TOF Measurements at ELBE [D]

B. Naumann[1], H. Freiesleben[1]

Time of flight experiments with neutrons produced by electrons are foreseen at the ELBE facility. Liquid lead was chosen as radiator. It is planned to include the lead in a rectangular beryllium tube (length $12\,cm$, quadratic base $6.6 \times 6.6\,mm^2$) with a Be-wall thickness of $500\,\mu m$ [1]. The nuclide production in such a neutron radiator was calculated with detailed Monte Carlo simulations using the FLUKA code [2]. In the simulations the electron beam had an energy of $E = 30\,MeV$ ($I = 1\,mA$) and a radius of $r = 1.5\,mm$. The irradiation direction is perpendicular to the length of the radiator. The total yield of radio-nuclides was scored and the result was written into output files which were combined in a post-processing step. The standard error was calculated for each isotope. Tab. 1 contains the calculated saturation activities of the radio-nuclides produced in the beryllium wall and in the liquid lead. In lead the main part of the activity stems from ^{203}Pb induced by the photo-nuclear reaction ^{204}Pb(γ,n). Since the results strongly depend on the included cross section data base, we checked the parameterization of the (γ,n)-reaction cross sections for the lead isotopes in FLUKA and found that in the case of ^{204}Pb the (γ,n)-reaction cross section is about a factor of 70 smaller compared with neighbouring nuclides, which is unreasonable. For first estimates we corrected the results for ^{203}Pb by this factor $F_c = 70$. Time dependent activities of each isotope obtained after $120\,h$ irradiation and $48\,h$ beam interruption are shown in Fig. 1 and 2. Activities of radio-nuclides with $T_{1/2} \leq 1\,h$ are marked only at the endpoint of the irradiation time.

nuclide	saturation activity $[Bq]$		$T_{1/2}$
beryllium wall $V_{Be} = 0.66 \times 0.66 \times 6\,cm^3 - V_{Pb}$			
^{6}He	$8.52 \cdot 10^8$	$\pm\quad 0.42\%$	0.8 s
^{7}Be	$8.07 \cdot 10^8$	$\pm\quad 1.36\%$	53.29 d
^{3}H	$3.49 \cdot 10^8$	$\pm\quad 2.08\%$	12.33 y
^{8}Li	$6.25 \cdot 10^7$	$\pm\quad 4.62\%$	0.84 s
^{10}Be	$8.25 \cdot 10^6$	$\pm\quad 1.54\%$	$1.51 \cdot 10^6$ y
liquid lead $V_{Pb} = 0.56 \times 0.56 \times 6\,cm^3$			
^{205}Pb	$1.41 \cdot 10^{12}$	$\pm\quad 0.03\%$	$1.53 \cdot 10^7$ y
^{203}Pb †	$4.31 \cdot 10^9$	$\pm\quad 0.62\%$	51.87 h
^{202}Pb	$6.15 \cdot 10^8$	$\pm\quad 1.60\%$	$5.25 \cdot 10^4$ y
^{207}Tl	$1.23 \cdot 10^8$	$\pm\quad 3.67\%$	4.77 m
^{206}Tl	$8.15 \cdot 10^7$	$\pm\quad 4.39\%$	4.20 m
^{209}Pb	$5.13 \cdot 10^7$	$\pm\quad 6.23\%$	3.253 h
^{201}Pb	$2.96 \cdot 10^7$	$\pm\quad 7.05\%$	9.33 h
^{204}Tl	$1.23 \cdot 10^7$	$\pm\quad 8.83\%$	3.78 y
^{3}H	$3.19 \cdot 10^6$	$\pm\quad 20.95\%$	12.33 y
^{202}Tl	$1.16 \cdot 10^6$	$\pm\quad 32.28\%$	12.23 d
^{205}Hg	$1.96 \cdot 10^4$	$\pm\quad 43.03\%$	5.2 m

Tab. 1 *Saturation activities for unstable nuclides in the neutron radiator at a beam energy of $30\,MeV$ and a beam current of $1\,mA$ calculated with FLUKA; † result without correction.*

The presented results are based on 43 FLUKA runs each with 10^7 events. On the 1.2 GHz Athlon Linux-Cluster of the IKH they required $\approx 650\,h$ CPU time.
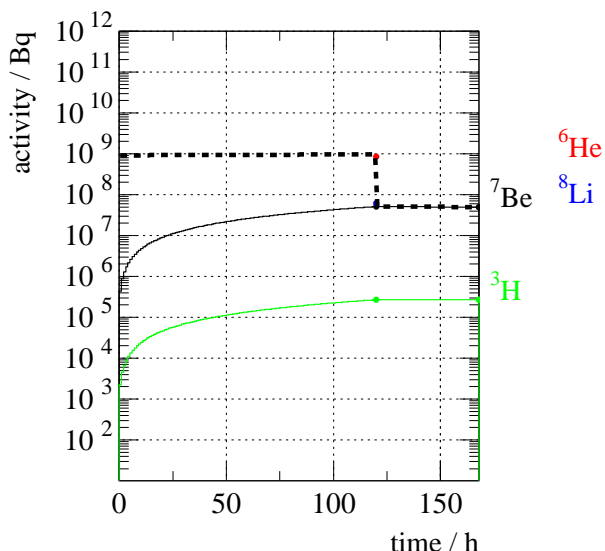
Fig. 1 *Time dependence of the activity from radio-nuclides produced in the beryllium wall during $120\,h$ irradiation and $48\,h$ pause; dotted line: total activity.*
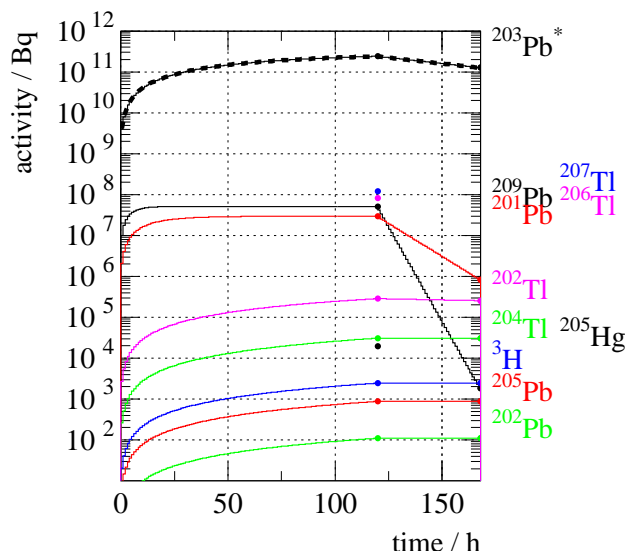
Fig. 2 *The same as Fig. 1 but for radio-nuclides produced in the liquid lead; * activity is scaled by a factor $F_c = 70$.*

[1] E. Altstadt et al., This Report, p. 42
[2] A. Fasso, A. Ferrari and P.R. Sala, Proc. of the Monte Carlo 2000 Conference, Lisbon, 23-26 Oct., 2000, Springer Verlag

---

[1] *Institute of Nuclear and Particle Physics, TU Dresden*

Shielding of Radioactivity Induced in a Liquid Lead Radiator [D]

B. Naumann[1], H. Freiesleben[1], K. Seidel[1]

For neutron time of flight experiments at ELBE the photo-neutrons will be produced by a radiator which will be hit by the electron beam. The radiator consists of a thin beryllium tube with streaming liquid lead [1]. During the exposure time the radiator materials are activated. The radioactivity increases with the current and the exposure time of the beam. The induced activities in the radiator were calculated for a beam energy of $30\,MeV$ with a current of $1\,mA$ [2]. The dominant activity in the neutron radiator stems from the ^{203}Pb nuclei which emit three gamma energies ($279.2\,keV$, $401.3\,keV$ and $680.5\,keV$). The radio-nuclides ^{205}Hg, ^{201}Tl, ^{202}Tl, ^{206}Tl and ^{207}Tl emit photons in the energy range from $30\,keV$ up to $1.7\,MeV$. A calculated gamma-ray energy spectrum for a irradiation time of $120\,h$ and $1\,h$ of decay is shown in Fig. 1.
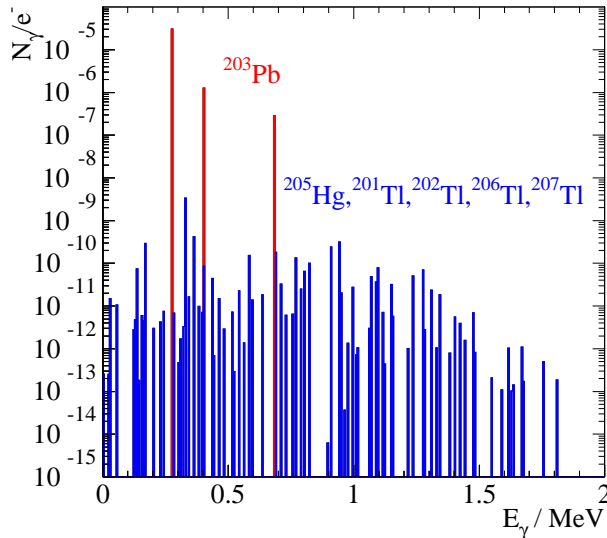
Fig. 1 *Discrete energy spectrum of gamma-rays emitted from radio-nuclei in lead after $120\,h$ of irradiation followed by $1\,h$ of decay normalized to one electron.*

It is planned to collect the liquid lead in a special vessel of about $5\,l$ volume at the end of the exposure. The dose rate distribution around such a vessel was obtained using the Monte Carlo code FLUKA [3]. Calculations were carried out for a cylindrical vessel with a radius of $8\,cm$ and a length of $25\,cm$. Isotropic gamma-ray sources were assumed to be homogeneously distributed in the tank volume. The discrete energy distribution shown in Fig. 1 was used. The dose rate at the tank surface amounts to about $40\,mGy/h$. Hence the lead tank vessel has to be shielded, in order to meet the radiation safety limit of $3\,\mu Gy/h$.
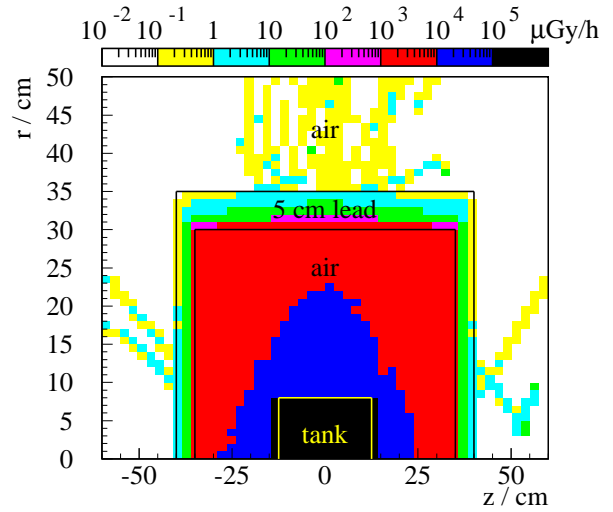
Fig. 2 *Dose rate distribution around a cylindrical lead tank with a $5\,cm$ thick lead shielding in cylindrical geometry.*

For first estimates a $5\,cm$ thick cylindrical lead shielding was considered in a distance of $22\,cm$ from the tank wall. The dose rate distribution in a cylindrical geometry is shown in Fig. 2. The result indicates the necessity to add some shielding material in the central regions above and sideways of the vessel. The energy dependent dose rate distributions at the lead shielding are shown in Fig. 3. At the inner and the outer shielding surface the averaged dose rates were found to be $(1045.7\,\pm\,0.7)\,\mu Gy/h$ and $(0.32\,\pm\,0.02)\,\mu Gy/h$, respectively.
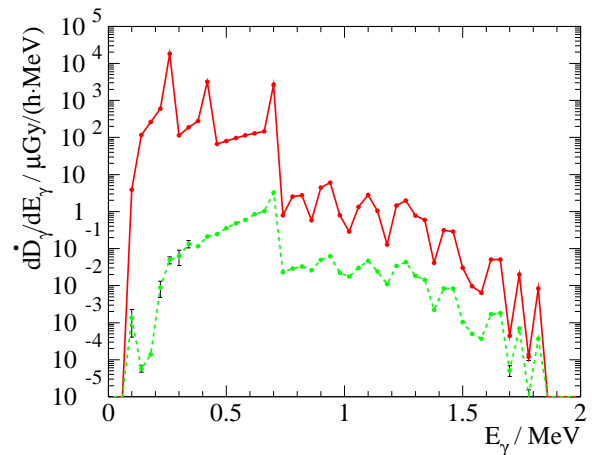
Fig. 3 *Energy dependent dose rate distributions averaged over the inner (full line) and the outer surface (dashed line) of a $5\,cm$ thick lead shielding in a distance of $22\,cm$ from the tank wall.*

[1] E. Altstadt et al., This Report, p. 42
[2] B. Naumann et al., This Report, p. 44
[3] A. Fasso, A. Ferrari and P.R. Sala, Proc. of the Monte Carlo 2000 Conference, Lisbon, 23-26 Oct. 2000, Springer-Verlag

---

[1]*Institute of Nuclear and Particle Physics, TU Dresden*

Hadron Physics

The _h_igh-_a_cceptance _d_ielectron _s_pectrometer HADES at the heavy-ion synchrotron SIS in GSI/Darmstadt is by now largely completed. Among the subdetector systems are the large multi-wire drift chambers of the third plane built and tested in our detector laboratory in FZ Rossendorf; four of them are already mounted in HADES, and the remaining two ones will be shipped to HADES in 2002.

HADES is the main future experimental device for the Hadron Physics Department. The starting experiments at HADES are aimed at studying in-medium modifications of the light vector mesons ρ, ω and ϕ. Resting on chiral symmetry as governing principle of strong interaction, chiral symmetry breaking and partial restoration in dense nuclear matter, various models predict noticeable in-medium modifications of hadrons when embedded in strongly interacting matter. While HADES is a dedicated detector system for vector meson spectroscopy via the dielectron decay channel, also pure hadronic observables are accessible. HADES is expected to have a large scientific potential for various investigations with pion, proton und ion beams, delivered from SIS, impinging on nuclear and proton targets.

Focusing our experimental activities on the HADES project marks a new era in the work of the Hadron Physics Department. The previous activities were centered on investigations of strange hadrons in heavy-ion collisions, hadron reactions and electroproduction. For instance, in a series of experiments of the KaoS and FOPI collaborations at SIS, the kaon and antikaon production in heavy-ion collisions has been studied. The result has been interpreted by means of in-medium modifications in the context of chiral symmetry restoration. The improved data basis and theoretical understanding point to a rather subtle interplay of various effects. In this respect the measurements of kaon and antikaon production in proton-nucleus collisions represent the missing link for systematically understanding the details of strangeness production. The experiments by the KaoS collaboration at SIS and the ANKE collaboration at the cooler synchrotron COSY in FZ Jülich are expected to offer new insights into this topic.

Hidden strangeness, e. g. in ϕ mesons, represents another facet of strangeness degrees of freedom. While ϕ production is presently a hot topic in hadron reactions with respect to the strangeness sea in nucleons and OZI rule violations, the ϕ multiplicity in heavy-ion collisions appears puzzling. The current analysis of data taken previously with the FOPI detector points to a large ϕ production probability thus challenging transport models.

An important lesson of the last decade of heavy-ion experiments is that the interpretation within transport models was hampered by lacking knowledge of elementary hadron reaction cross sections. During the last years the COSY-11 and TOF collaborations at COSY enlarged substantially the data basis for strangeness production in elementary hadron reactions. Especially important for future HADES experiments is the precise knowledge of the ω production cross section in pp collisions. Here, the TOF collaboration at COSY succeeded in completing the needed data.

The theory group in the hadron physics department is accompanying these experimental activities. Predictions and interpretations of selected topics in the field of strange and rare electromagnetic probes are provided. Most of these calculations refer to the energy range covered by the experiments performed with FZR participation (see collaboration list below), others deal with various phenomenological aspects of deconfined matter, as a state with chiral symmetry restoration in the strongly interacting medium, produced in high-energy heavy-ion reactions. Whereas the investigations of dense and hot hadronic matter, produced in medium-energy collisions, are of strong interest for the understanding of astronomical objects like supernovae and neutron stars, the studies of deconfinement effects are of relevance for more violent scenarios like the big bang.

Collaborations

ANKE: Univ. Münster, FZ Jülich, Univ. Giessen, Univ. Bonn, Univ. Köln, Univ. Erlangen-Nürnberg, Fachhochschule München, FZ Rossendorf, JINR Dubna (Russia), Univ. Tbilisi (Georgia), Petersburg Nuclear Physics Institute (Russia), ITEP Moscow (Russia), Russian Academy of Science Moscow (Russia), ECN-Nuclear Energy (Netherlands), Jagellonian Univ. Cracow (Poland), Moscow State University (Russia), Univ. College London (England), Soltan Institute for Nuclear Studies (Poland),
spokesperson: M. Büscher

FOPI: Univ. Heidelberg, GSI Darmstadt, FZ Rossendorf, IPNE Bucharest (Romania), KFKI Budapest (Hungary), LPC and Univ. Blaise Pascal Clermont (France), ITEP Moscow (Russia), Kurchatov Institute Moscow (Russia), Korea Univ. Seoul (South Korea), IreS Strasbourg (France), Univ. Warsaw (Poland), RBI Zagreb (Croatia),
spokesperson: N. Herrmann

HADES: Univ. Frankfurt, TU München, Univ. Giessen, GSI Darmstadt, FZ Rossendorf, Institute of Physics Bratislava (Slovakia), LNS Catania (Italy), LPC and Univ. Blaise Pascal Clermont (France), Jagellonian Univ. Cracow (Poland), JINR Dubna (Russia), Univ. degli Studi di Milano (Italy), ITEP Moscow (Russia), INR Moscow (Russia), MEPhI Moscow (Russia), Univ. of Cyprus (Cyprus), Institute de Physique Nucleaire d'Orsay (France), Nuclear Physics Institute Rez (Tschechia), Univ. of Santiago de Compostela (Spain), Univ. of Valencia (Spain),
spokesperson: J. Friese

JLab E 91916: JLAB E91-016: Argonne National Laboratory, Argonne (USA), California Institute of Technology, Pasadena (USA), College of William and Mary, Williamsburg (USA), Duke University, Durham (USA), Florida International University, Miami (USA), FZ Rossendorf, Juniata College, Huntingdon (U0SA), Kent State University, Kent (USA), North Carolina A&T State University, Greensboro (USA), Northwestern University, Evanston (USA), Ohio University, Athens (USA), Southern University at New Orleans, New Orleans (USA), The George Washington University, Washington DC (USA), Thomas Jefferson National Accelerator Facility, Newport News (USA), Tohoku University, Sendai (Japan), University of Houston, Houston, (USA), University of Maryland, College Park (USA), University of Minnesota, Minneapolis (USA), University of Virginia, Charlottesville (USA), Yerevan Physics Institute, Yerevan, (Armenia),
spokespersons: B. Zeidman, J. Reinhold

KaoS: TU Darmstadt, Univ. Frankfurt, Univ. Marburg, GSI Darmstadt, Jagellonian Univ. Cracow (Poland), FZ Rossendorf,
spokesperson: P. Senger

TOF: Univ. Bochum, FZ Jülich, Univ. Bonn, TU Dresden, Fachhochschule Jülich, Univ. Tübingen, Univ. Erlangen-Nürnberg, FZ Rossendorf, IUCF Bloomington (USA), INFN Torino (Italy), SINS Warsaw (Poland),
local organizer: E. Roderburg

Status Report of the Dilepton Spectrometer HADES at SIS/GSI Darmstadt [B,G]

F. Dohrmann, R. Dressler, W. Enghardt, E. Grosse[1], K. Heidel, J. Hutsch, B. Kämpfer, K. Kanaki, R. Kotte, L. Naumann, A. Sadovski, J. Seibert, M. Sobiella and the HADES collaboration

The HADES collaboration performed first physics studies, aimed at measuring electron-positron pairs produced in relativistic reactions of carbon on carbon. Previous measurements by the DLS and the CERES collaborations have shown an enhancement of dielectron production in the region of low invariant masses. An explanation of the enhancement might be a reshaping of the vector meson strength.

The HADES spectrometer allows a measurement of the dilepton mass spectrum with an invariant mass resolution of about one percent. In the November/December 2001 beam time a 2 GeV/nucleon carbon beam with an intensity of 1.2×10^6 particles per spill hit a carbon target. The spill length amounted to 9.5 s. The target was 8 mm in diameter and had an interaction length of 4-5 %. A fast hardware selection of central collisions reduced the data to 26,000 reaction triggers per spill. Using this trigger, most of the detected reaction products were protons and pions. Future runs require therefore a trigger system which is able to reduce the event rate up to a factor of 10^{-4} by preselecting leptons. During the beam time we took 884 runs with 2×10^8 events; these included 306 runs with high magnetic field ($I = 2500\,A$).
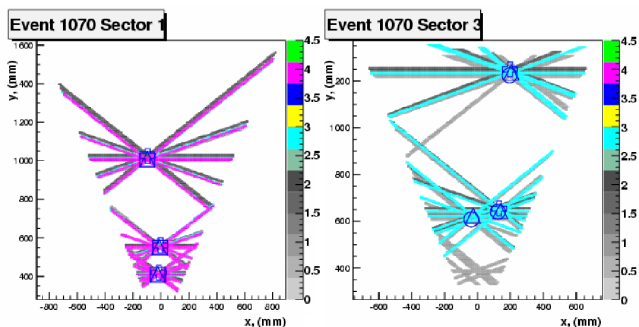
Fig. 1 *Coincidental prongs of one event in the MDC's of two sectors. Each prong is characterised by the intersection point of all fired signal wires. The MDC plane numbers have been labeled at the right edges of the plots.*

The HADES setup includes the most detector units, read-out, data-acquisition and trigger electronics. The ring imaging Cherenkov counters (RICH), the inner multiwire drift chambers ($MDC-I, MDC-II$), the time of flight scintillation hodoscopes (TOF, TOFINO) and the pre-shower modules were completely installed [1]. A typical event of charged particles in two sectors of HADES is shown in Fig. 1. Up to now four large-area drift chambers $MDC-III$, produced at FZ Rossendorf, and one $MDC-IV$ prepared at IPN Orsay for the outer tracking planes were installed.

[1] http://www-hades.gsi.de
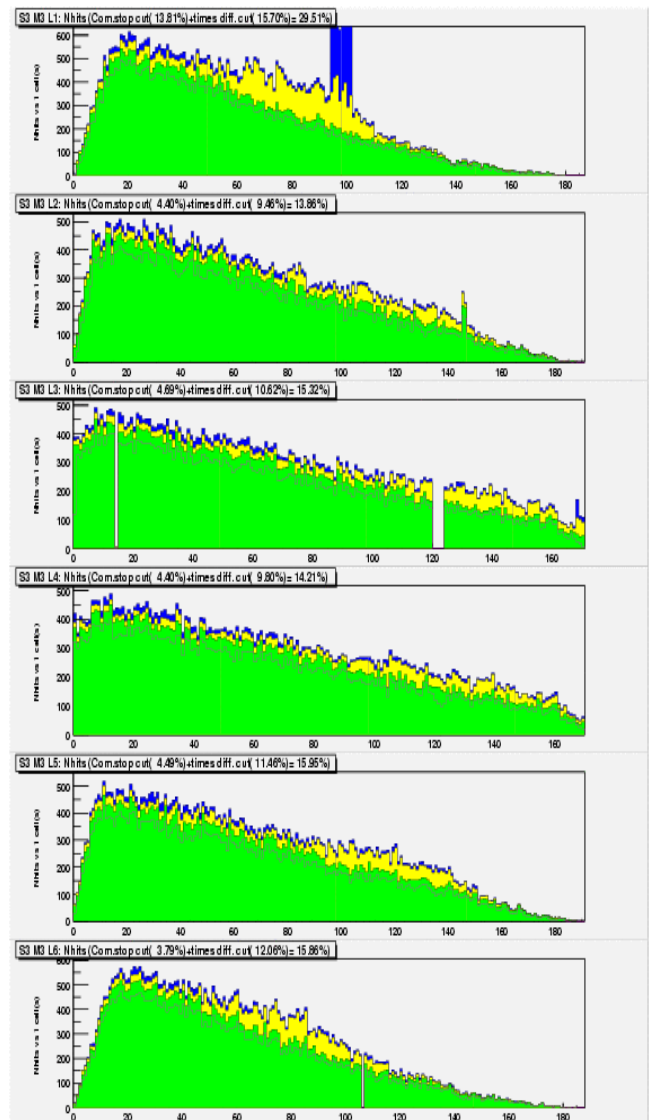
Fig. 2 *Distribution of the number of hits vs. drift cell number (wire) for the six layers of the $MDC-III$ in sector 3. The wire numbers increase with azimutal angle θ. Green: noise cuts with defined drift time intervall and time above threshold signals; Yellow: noise cut with common stop signal; Blue: no noise cuts.*

One sector of the spectrometer is now fully equipped with an angular acceptance of $\phi = 0° - 60°$ and $\theta = 18° - 85°$. The performance of the drift chambers as well as all other detectors were controlled online. Fig. 2 shows the hit distribution in all six layers of one driftchamber. The two remaining chambers of the third tracking plane are under construction at FZ Rossendorf and will be delivered in spring 2002.

---

[1] *also TU Dresden*

Electric Field and Drift Characteristics Studies for the Multiwire Drift Chambers of the Third Plane of HADES

K. Kanaki, F. Dohrmann, R. Dressler, E. Grosse[1], B. Kämpfer, R. Kotte, L. Naumann, A. Sadovski, J. Seibert

The starting experiments with the High Acceptance Di-Electron Spectrometer (HADES) at GSI/Darmstadt provide the possibility for electron-positron pair spectroscopy in heavy-ion collisions at incident energies up to 2 AGeV. For this purpose, a momentum resolution of about 1% is required, i.e. the determination of the particle tracks should be done with a precision better than 100 μm. The tracking is accomplished by Multiwire Drift Chambers (MDC). Electrons produced by the incoming charged particle migrate along the electric field lines with velocity v and reach the high electric field strength region at a distance of a few wire radii from the anode where avalanche multiplication starts. It is obviously very convenient to have a linear space-time relationship between the coordinate of the track and the drift time of the electrons, and this can be obtained in structures with uniform electric field. In order to find the optimum potential configuration that will provide this linear relationship, simulations of the third plane drift chambers with two- and three-dimensional programs were performed.

As a first step, two-dimensional simulations were done with Garfield [1]. The program gives the user the possibility to apply electric potentials on the wires and then to calculate the electric field with a high precision. The user is also given the possibility to set trajectories of charged particles from which Garfield drifts electrons calculating their arrival time distributions and distance-drift time relations.

The electrons on their way to the anodes drift with a variable drift velocity. The distribution of the isochrones inside the drift cell directly evidences the linearity of the forementioned distance-time relationship. If the time contours are not homocentric with constant radii differences, then non-linearities are operational. In particular, the rectangular form of the drift cells (8×12 mm^2) might cause a non-uniform distribution of drift velocites. One can further conjecture that a higher potential on the field wires compensates for the asymmetry of the cell dimensions. Our calculations show that indeed, a linear distance-time relationship is achieved, in a larger part of the drift cell (see Fig. 1).

Nevertheless, despite of this fact, there are regions at the border of the cells, where the drift velocity is obviously not constant. For a more extensive study of these areas, a three-dimensional field map is needed. Such a map was produced with Opera [2], one of the commercially available finite element programs. The idea is to use the field map in combination with Garfield, so as to calculate the drift properties of the electrons in three dimensions. The obtained potential distribution of the middle layers of the chambers is depicted in Fig. 2.

To obtain more realistic comparisons between 2d- and 3d-simulations, the Opera fieldmaps should be incorporated in Garfield, in order to study the drift behaviour of the electrons in the volume of the drift cell.
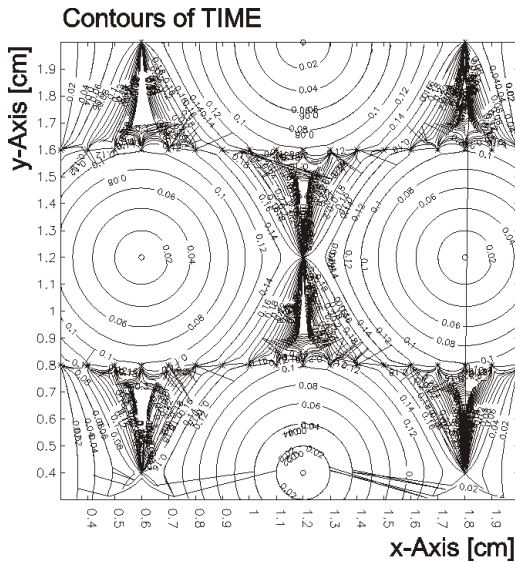
Fig. 1 *In this simulation shown are two sequences of cathodes (∗), and a sequence of alternating anode (○) and field wires (∗) in between. The time contours are calculated for $V_c = -2000V$ and $V_f = -2400V$. With this potential configuration the isochrones are homocentric with equal spacing.*
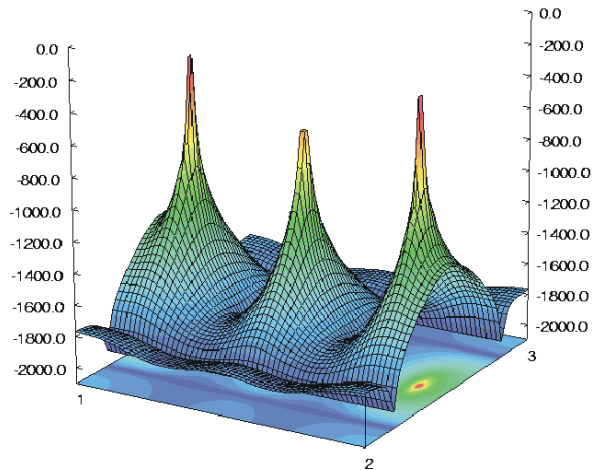
Fig. 2 *Potential distribution for $V_c = V_f = -2000V$. The peaks represent the anode wires, while the two "valleys" are the cathode wires. Between the anode wires there are also two field wires.*

[1] Simulation of gaseous detectors, http://garfield.web.cern.ch/garfield
[2] http://www.vectorfields.co.uk/software.htm

---

[1] *also TU Dresden*

Track Fitting Applications Using Single HADES MDC Cluster Information

A. Sadovski, F. Dohrmann, R. Dressler, E. Grosse[1], B. Kämpfer, K. Kanaki, R. Kotte, L. Naumann, J. Seibert

The designed HADES Multiwire Drift Chamber (MDC) resolution should be on the order of 100 μm. This can be achieved using a set of sense wire positions and the corresponding time informations from six layers contributing to a hit cluster and a subsequent fit procedure. As a result of a cluster finding algorithm [1] in the HYDRA package [2], we get clusters. A cluster is a set of wires with time information of the electron cloud drifting from the track to the sense wire in the corresponding drift cell. Assuming a certain functional dependence, one can transform the drift time into the minimal distance from a track to a wire. Using the time information of all wires of a cluster and the drift-time-to-distance dependence, one can fit track parameters in coordinate space to improve the cluster position. Only coordinates of the single MDC and of the preliminary target position are required. Several extensions of the method were applied. First, in an iterative procedure one can estimate a time vs. distance dependence (for details see [3]). Starting from a linear dependence as a first approximation, a nonlinear one is achieved after 2 - 3 steps of fitting procedure (see Fig. 1). This procedure improves the position resolution by 15 - 20% in comparison to the pure linear case for the MDC-III.

A second useful application of the fit was the investigation of the dependence of the position resolution on different High Voltage (HV) settings. During the April 2001 beam time several combinations of the cathode and field wire HV of MDC-III were tested. According to GARFIELD calculations [4] the choice $HV_{field} > HV_{cath}$ would improve the radial symmetry of the isochrones of MDC-III and therefore the linearity of the time-to-distance dependence, allowing a simpler functional approximation. For the case with radially unsymmetric isochrones the number of iterations to find the approximation is greater, and the function becomes nonlinear. It was found that in first order the resolution does not depend on the linearity of the function but on the reconstruction quality of the function. Thus we do not need to apply different HV settings for Cathode and Field wires in order to achieve better resolution.

Finally, a multicluster fit procedure for a single MDC has been developed, extending the single cluster fit to fitting of several clusters, formed by tracks originating from the same vertex. As a result, we can estimate the distance between the chamber and the target or (having a setup of aligned chambers) we can estimate the alignment agreement for individual chamber in an independent way. Some results are illustrated in Fig 2. The method is described in [3].
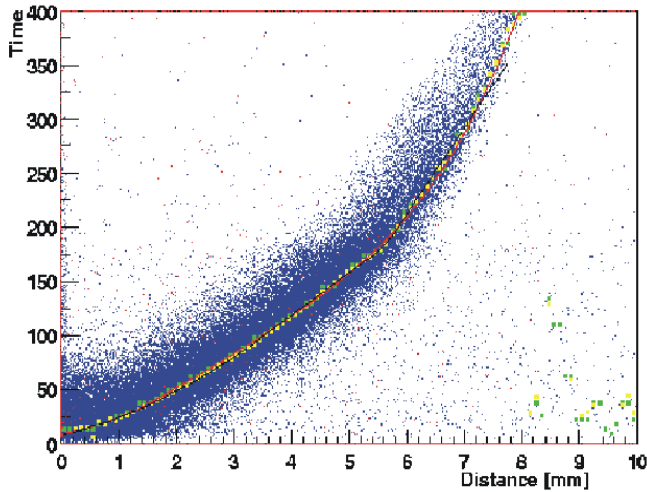
Fig. 1 *Reconstruction of the function* **time-vs.-distance** *for MDC-III drift cell. scatter points are measured times vs. the obtained distances after the fit procedure (in a track cluster fit). Bright points in the middle of the distribution indicate times obtained after the fit of the measured time vs. the distance obtained from the first fit. The black curve indicates a time vs. distance functional approximation for the next iteration of the fitting procedure. The maximum distance between sense wire and track is 7.2 mm.*
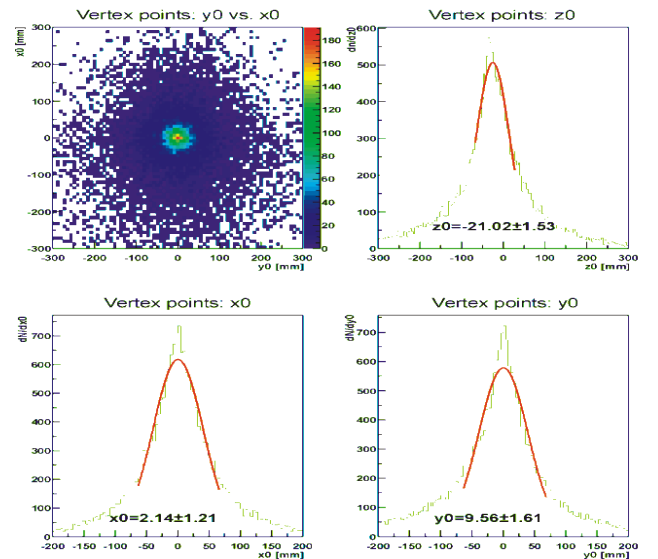
Fig. 2 *The relative target position reconstruction respectively the ideal position of MDC-II sector 1 when applying event-wise the multicluster fit. Upper pictures: target reconstruction in x − y projection and z-target reconstruction distribution. Lower pictures: x-target and y-target reconstruction distributions. The errors given are only statistical.*

[1] G.N. Agakichiev et al., Part. and Nucl., Lett. 4[101] (2000) 54

[2] http://www-hades.gsi.de/computing/

[3] http://www.fz-rossendorf.de/FWK/MITARB/sadovski/mdc/analysis/analysis.html

[4] K. Kanaki at al., This Report, p. 50

---

[1] *also TU Dresden*

Antikaon Production in Au+Au Collisions at 1.5 AGeV [B,G]

M. Ploskon, A. Förster, E. Grosse[1], P. Koczoń, B. Kohlmeyer, L. Naumann, H. Oeschler, P. Senger,
W. Scheinast, E. Schwab, Y. Shin, H. Ströbele, C. Sturm, F. Uhlig, A. Wagner, W. Waluś

(KaoS collaboration)

Flow effects of varius ejectiles in heavy-ion collisions are known to be sensitive to the equation of state. In former experiments the emission pattern of light fragments, protons, pions and kaons were studied. It was found, that the directed flow and squeeze-out of protons and light fragments are in agreement with predictions based on hydrodynamical models. Pions are preferentially emitted out-of-plane, because they are shadowed by spectator matter. The pattern of the kaon emission, which is peaked perpendicularly to the reaction plane, can be reproduced by transport calculations, which assume a repulsive in-medium kaon-nucleon potential.

Various theoretical considerations predict the influence of an attractive in-medium potential on the azimuthal emission pattern of antikaons. Both the yields and azimuthal emission pattern are important to understand the modification of kaon and antikaon properties in dense nuclear matter.

Up to now precise data on antikaon flow were lacking. In June/July 2001 the KaoS collaboration performed an experiment on K^- production in Au + Au collisions using the Kaon Spectrometer [1] at SIS/GSI. The experiment was designed on such a way that the measurement delives yields and azimuthal emission pattern

of antikaons.

The highest available beam energy of 1.5 AGeV for ^{197}Au was obtained in a two stage acceleration cycle. The beam intensity amounted 2×10^8 per spill with a spill length up to 12 s. The target thickness was 0.5 mm. The small angle hodoscope with about 400 scintillation counters was upgraded, which allowed us to increase the trigger rates up to 1 kHz. K-mesons were measured in the momentum range $p_{lab} = 200 - 1200$ MeV/c at polar angles $\Theta_{lab} = (40° \pm 4°); (48° \pm 4°); (72° \pm 4°)$ and at magnetic field strength B= $\pm 0.6; \pm 0.9; \pm 1.4$ T (Tab. 1). The phase space covered by the measurement is shown in Fig. 1. An example for raw spectra of antikaons obtained online during data taking is given in Fig. 2. The analysis of the data is still in progress.

Tab. 1 *Estimates of the obtained antikaon and kaon statistics.*

Θ_{lab}	B	± 0.6 T	± 0.9 T	± 1.4 T
40°	K^-	–	2200	2300
40°	K^+	750	10000	13000
48°	K^-	–	1800	2600
48°	K^+	600	7400	6200
72°	K^+	+	+	+
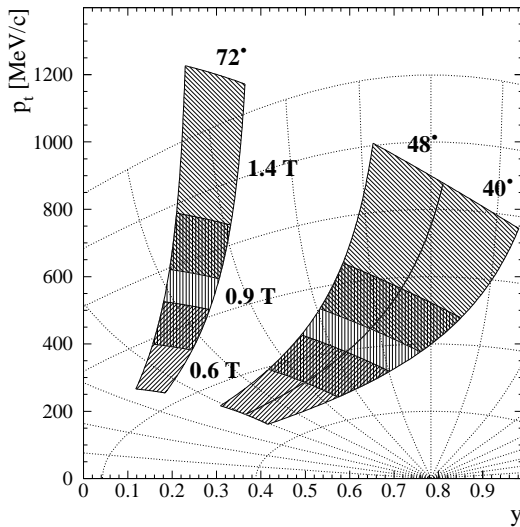
Fig. 1 *The Kaon Spectrometer phase space coverage for charged K-mesons. The plot shows the transverse momentum versus rapidity. Antikaons were measured around midrapidity in the upper right hatched areas (40° − 48° and 0.9 T − 1.4 T).*
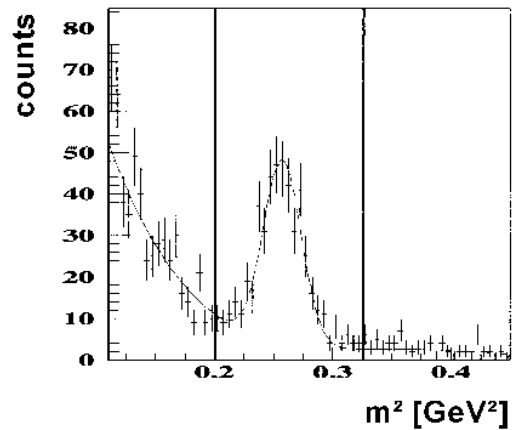
Fig. 2 *Raw mass spectrum obtained for $B = -1.4$ T at $\Theta_{lab} = 48°$.*
The peak in the range $\Delta m^2 = 0.2 - 0.32 (GeV/c^2)^2$ is due to antikaons.

[1] http://www-kaos.gsi.de

---

[1] *also TU Dresden*

First Measurements of Antikaons in Proton-Nucleus Collisions at SIS [B,G]

W. Scheinast for the KaoS Collaboration:

I. Böttcher[3], M. Dębowski, F. Dohrmann, A. Förster[2], E. Grosse[6], B. Kamys[5], P. Koczoń[1], B. Kohlmeyer[3], F. Laue[1], M. Menzel[3], L. Naumann, H. Oeschler[2], F. Pühlhofer[3], Ch. Schneider, E. Schwab[1], P. Senger[1], Y. Shin[4], H. Ströbele[4], Ch. Sturm[2], G. Surówka[5], F. Uhlig[2], A. Wagner, W. Waluś[5]

The first systematic experimental investigation of K^- production in proton-nucleus collisions at SIS energies has been performed using the Kaon Spectrometer at SIS/GSI. Au and C targets were bombarded with proton beams at energies of 1.6, 2.5, and 3.5 GeV. K mesons and pions were measured at laboratory angles of 32°, 40°, 48°, and 56°. In total, 350000 K^+ and 35000 K^- have been recorded. Fig. 1 shows the inclusive invariant production cross sections for K^+ (open symbols) and K^- (full symbols) as function of transverse mass (minus rest mass).

The spectra measured at different angles can be described by a Boltzmann distribution with a normalization factor, a temperature, and a longitudinal source velocity as free parameters. By integrating the Boltzmann distribution we estimate the total production cross sections σ_K. The resulting multiplicity $M_K = \sigma_K/\sigma_R$ with σ_R the geometrical reaction cross section is shown in fig. 2.

A detailed comparison of the data to results of transport model calculations is in progress.
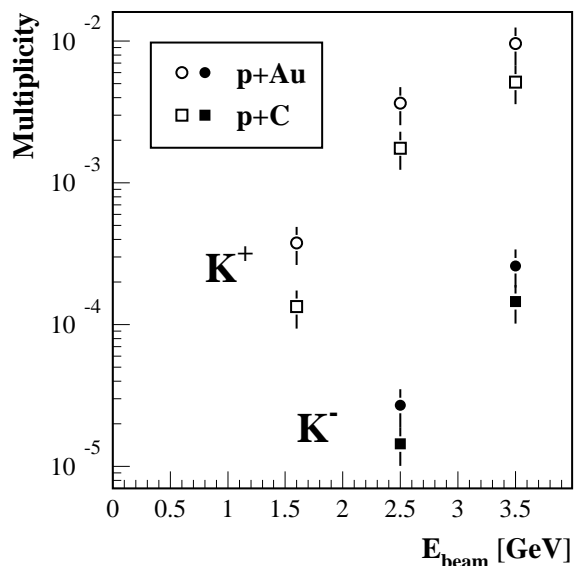
Fig. 2 *Multiplicity of K^+ and K^- mesons in $p + C$ and $p + Au$ collisions as function of beam energy (preliminary).*
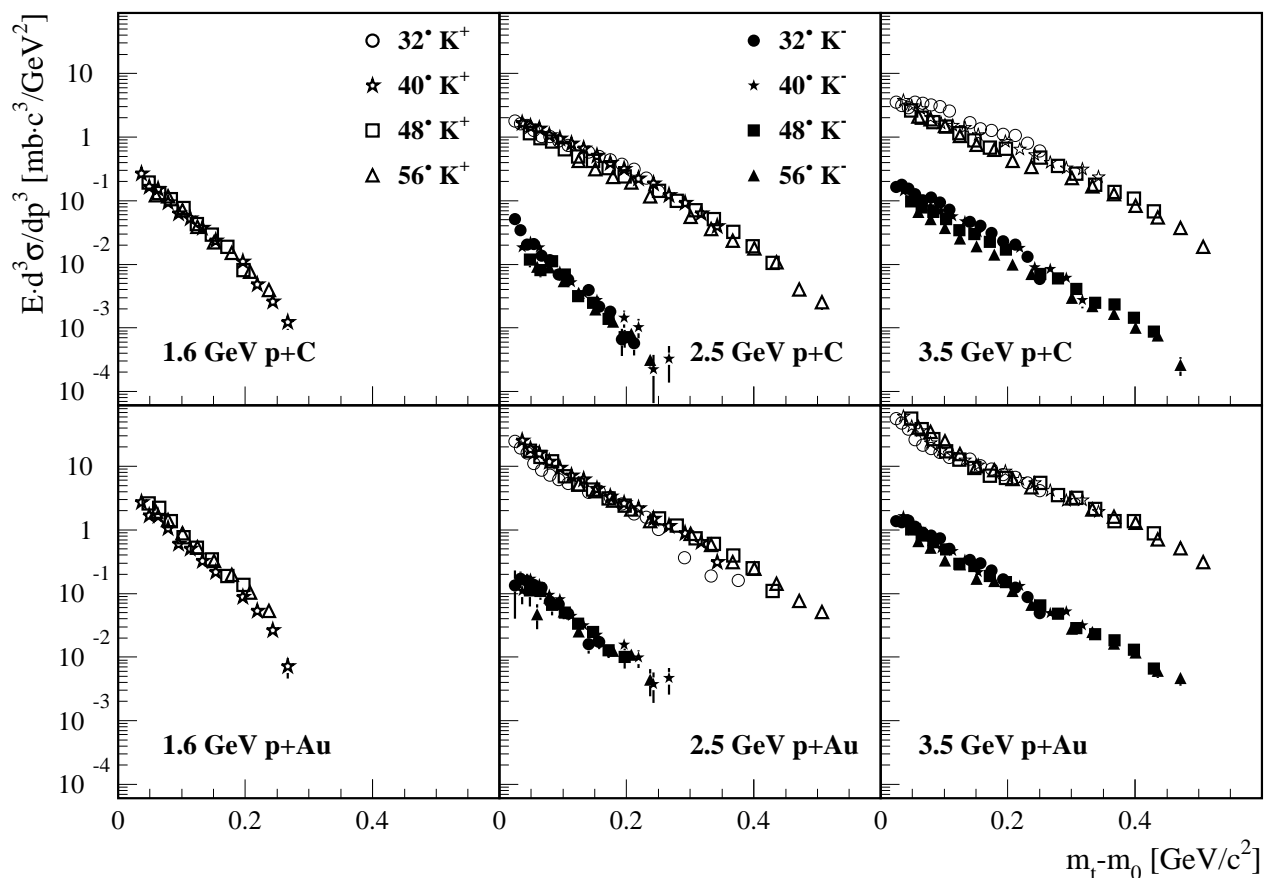
Fig. 1 *Inclusive invariant production cross sections for K^+ (open symbols) and K^- (full symbols) measured in proton-nucleus collisions (preliminary).*

---

[1] *GSI Darmstadt,* [2] *TU Darmstadt,* [3] *Univ. Marburg,* [4] *Univ. Frankfurt,* [5] *Univ. Cracow,* [6] *also TU Dresden*

Measurement of Deep Subthreshold K^+ Production in pA Reactions at ANKE and Prospects for K^- Experiments [J]

V.I. Dimitrov, J. Seibert for the ANKE collaboration

The ANKE spectrometer was originally designed for investigating K^+ meson production at forward angles in proton–nucleus collisions near and below the nucleon–nucleon threshold of $1.58\,GeV$. A detailed description of the experiment, installed in a straight section of the COSY ring at Jülich, can be found in [1]. So far, measurements for projectile energies $T = 1$, 1.2, 1.5, 1.75, 2 and $2.3\,GeV$, and target nuclei C, Cu, Ag and Au have been performed, resulting in differential cross-sections $d^3\sigma_K/dpd\Omega$ in the momentum range $150\ldots600\,MeV/c$ of the produced kaons. Deep subthreshold kaon production in pA collisions requires a certain degree of short range correlations in the target nucleus. A comparison of the measured invariant cross-sections for kaon production with the ones from the phase-space approximation reveals that, on the average, 4 to 6 nucleons have to participate in the process [2]. This is consistent with the tendency of the nucleons in nuclei to form α-clusters, which in their turn show further short range correlations among themselves. Another possible explanation of the deep subthreshold kaon production may be the involvement of multi-step processes. Should such processes dominate, a strong dependence of the production cross-section on the mass of the target nucleus is to be expected. Data taken and analysed up to now do not provide clear evidence for the alleged change of the dominant reaction mechanism between direct and two-step processes; the observed target mass dependence of the cross-section is close to the purely geometrical $\sim A^{2/3}$, which points to a direct reaction mechanism. In order to clarify the situation, further data at forward angles are needed [3]. It is possible to study Kp and Kd correlations with protons and deuterons from one- or two-step reactions. The Kd final state can be observed in case of two-step reactions only, while protons can occur in both cases; further correlations with a third particle can provide the required criteria to identify πN and pN channels [4][1]. During the last ANKE beam time in October 2001 the feasibility of such correlation measurements at ANKE has been demonstrated. The ANKE spectrometer is unique in its ability to deal with kaon momenta down to $150\,MeV/c$. At such low momenta the Coulomb and nuclear potentials play a significant rôle for the shape of the kaon production cross-sections. In particular, the outgoing kaon momenta are shifted to higher values for target nuclei with larger Z and A. This effect is clearly observed in the recent data. It turns out that, along with the Coulomb potential, an additional repulsive kaon potential of about $20\,MeV$ is needed in order to describe the observations [5].

Recently an additional detector system (Fig.1) for negatively charged ejectiles has been installed partially inside the low-field area $(0-200\,mT)$ of the C-shaped magnet D2. With its help negatively charged particles with momenta of $120\ldots1000\,MeV/c$ can be registered at maximal magnetic field $1.59\,T$. The system comprises thin $(2\,mm)$ start scintillators, two MWPC for momentum reconstruction, two groups of stop scintillators and a group of bent Čerenkov counters for kaon–pion discrimination for momentum values where TOF differences are too small [6]. It will be fully operational in early spring 2002, and will be used for studying a_0/f_0-resonance production in pn interactions, ϕ-meson production in pp as well as charged kaon–antikaon production in pp, pn and pA collisions, at the maximal COSY beam energy [7][1]. Recent KaoS data [8] indicate that the inclusive differential cross-section for antikaon production in pA at a proton energy $2.5\,GeV$ is about 0.5% of that for kaon production, in wide range of target masses and momenta. These data have been taken at angles from 32^0 to 56^0; in forward direction near threshold one expects this ratio to be somewhat larger. Monte Carlo simulations for the acceptances of the negative and positive particle ANKE detector systems, taking into account the decay in flight of kaons, and antikaons, yield a factor of about 2 in favour of the negative detector; another factor of 2 results from the low efficiency of the positive detector's telescopes. Thus, for pA collisions at $2.5\,GeV$ one can estimate a lower limit of the antikaon counting rate as 2% of the kaon counting rate of the positive detector.
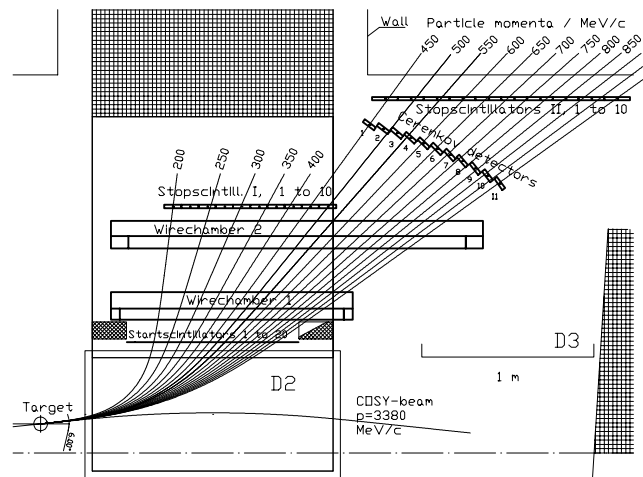
Fig. 1 *The ANKE detection system with trajectories for negative ejectiles with momenta of $200\ldots950\,MeV/c$.*

[1] S. Barsov et al., *NIM* A462 (2001) 364
[2] V. Koptev et al., *Phys.Rev.Lett.* 87 (2001) 022301
[3] M. Büscher et al., *Phys.Rev.* C65 (2002) 014603
[4] V. Koptev et al., *COSY* beam-time request #70 (2001)
[5] M. Nekipelov et al., FZJ Annual Report (2001)
[6] H.R. Koch et al., *FZJ Annual Report* (1999) 28
[7] M. Büscher et al., COSY proposals #97,#104 (2001)
[8] W. Scheinast (KaoS collaboration), This Report, p. 53

[1] *ANKE proposals are available at http://ikpd15.ikp.kfa-juelich.de:8085/doc/Proposals.html*

Electroproduction of Strangeness on Light Nuclei

F. DOHRMANN FOR THE JEFFERSON LAB E91016 COLLABORATION

Jefferson Lab experiment E91016 recently studied the electroproduction of kaons, $A(e, e'K^+)$, on targets of H_2, D_2, ^3He, ^4He, C and Al. The incident electron energy was $E = 3.245$ GeV, the virtual photon energy $W = 1.91$ GeV. The scattered electron e' and emergent K^+ were detected in coincidence with the use of the HMS and SOS spectrometers, respectively, in Hall C of Jefferson Laboratory. Angular distributions for the $(e, e'K^+)Y$ reactions were measured at forward angles with respect to the virtual photon for $Q^2 \simeq 0.35$ GeV^2. The measurements on $^{3,4}He$ are the first performed. Quantitative descriptions of the missing mass spectra for targets with mass number $A \geq 2$ need to take into account hyperon-nucleon (YN) final state interactions (FSI) that are sensitive to YN potentials. An effective range Ansatz for the FSI together with the simulation of the possible quasifree distributions for the different hyperons, $A(e, e'K^+)YX$, where $Y = \Lambda, \Sigma^0, \Sigma^-$, gives a decent description of the data for $A = 2, 3, 4$ (Fig. 1). Moreover, we see clear evidence for the $^4_\Lambda H$ bound state in the $A = 4$ data (Fig. 2) for which we present an angular distribution (Fig. 3). Dividing out the elementary cross section on the proton, $H(e, e'K^+)\Lambda$, measured in the same experiment, the distribution falls steeply. Following [1] this may be interpreted as a measurement of the nuclear form factor. In addition we see evidence for the $^{12}_\Lambda B$ bound state in reactions on carbon.
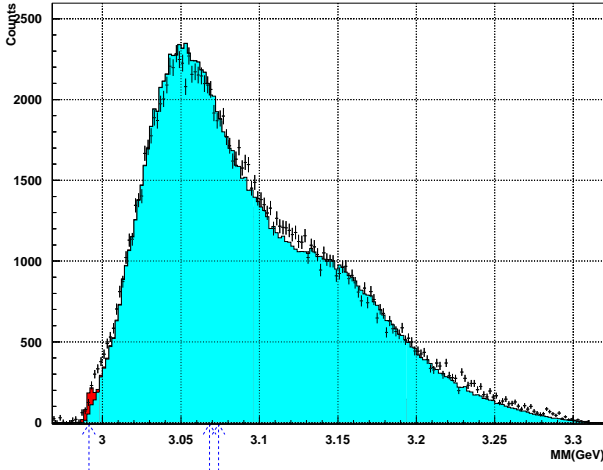
Fig. 1 *Combined fit (blue) of missing mass distributions for $^3He(e, e'K)\Lambda X$, $^3He(e, e'K)\Sigma^0 X$, $^3He(e, e'K)\Sigma^- X$, including FSI, to the data (black). The evidence for a bound state for $A = 3$ (red) is only weak. The arrows indicate the quasifree thresholds for Λd, $\Sigma^0 d$, and $\Sigma^- pp$.*
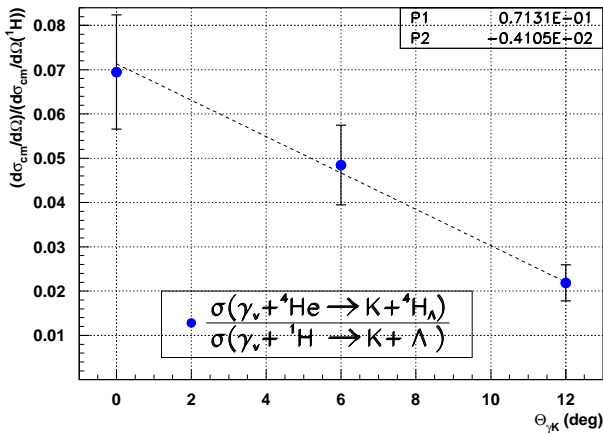
Fig. 3 *Cross section for the $^4_\Lambda H$ boundstate, divided by the elementary cross section on the proton.*
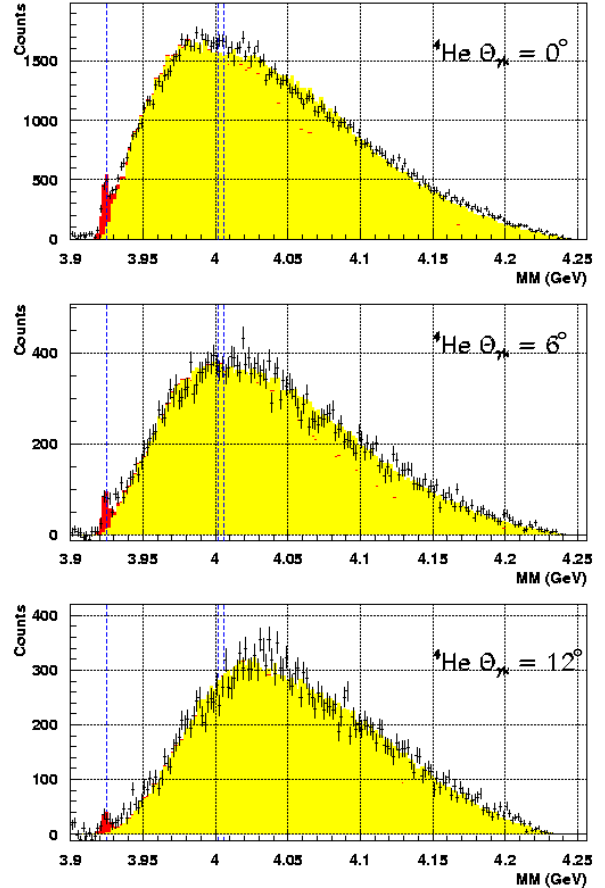
Fig. 2 *Combined fit of quasifree missing mass distributions for $^4He(e, e'K^+)$ (yellow) and a $^4_\Lambda H$ bound state (red). The evidence is strong for all measured angles $\theta^{lab}_{\gamma K} = 0, 6, 12$ deg (i.e. also at higher momentum transfer t). The dashed lines indicate the quasifree thresholds for Λt, $\Sigma^0 t$, and $\Sigma^- {}^3He$.*

[1] T. Mart et al., Nucl. Phys. A640 (1998) 235

Production of ω Mesons in Proton-Proton Collisions [B,J]

K.-Th. Brinkmann[1] for the COSY-TOF collaboration

Data taken with the TOF spectrometer, an experimental setup located at one of the external beam lines of the COoler SYnchrotron COSY at the Forschungszentrum Jülich, during an experiment in early 2000 were evaluated with respect to a signal for ω meson production [1]. The beam momenta of 2950 and 3200 MeV/c correspond to excess energies of $\epsilon = 92$ and 173 MeV, respectively, above the threshold for pp $\to$ ppω.

Events with a characteristic topology in the TOF detector were selected from the data sample for further inspection. This pattern includes two hits at small angles associated with the protons from the pp $\to$ ppX reaction, and an additional pair of hits at angles larger than that allowed for protons. The latter were assumed to be decay pions from, e.g., $\rho^0 \to \pi^+\pi^-$ (BR 100%) or $\omega \to \pi^+\pi^-\pi^0$ (BR 89%) decay. ρ^0 and 2π production contribute appreciably to the background. The missing mass of particle X and its momentum were calculated using the mass assignment of the two proton candidates and their measured velocity vectors. An additional cut on the coplanarity of the decay pions was used to reject events that meet the condition that the charged pions were emitted back to back in the center-of-momentum frame defined by X ($X \to \pi^+\pi^-$). The remaining spectrum of ω candidates is shown in figure 1.

A clean signature of ω production is visible at $M_X^2 = M_\omega^2$. The hatched peak at the same position shows the simulated response function of the TOF detector. It nicely agrees in shape with the ω signal above background, as demonstrated by the shaded area that is a sum of the parametrized background as indicated and the Monte Carlo ω signal. Using the simulated detector acceptance for events of the chosen type and a luminosity calibration extracted from elastic proton-proton scattering events, total cross sections for ω production were deduced. These are shown in figure 2 together with data from the literature [2, 3, 4].

The present data nicely fill the gap between the SPES3 measurements [2] below $\epsilon = 30$ MeV and the DISTO result [3] at $\epsilon = 320$ MeV. The DISTO experiment not only measured ω production but also took data on the production of ϕ mesons. According to the SU(3) mixing scheme, the quark content of the ϕ meson is almost exclusively $s\bar{s}$, while the ω wave function contains $u\bar{u} \oplus d\bar{d}$. Hence, ϕ meson production should be suppressed by $\sigma_\phi/\sigma_\omega \approx 0.4\%$, as predicted by the OZI rule [5]. The DISTO result [3] suggested a violation of this rule by one order of magnitude, but the finding relied on an extrapolation for the ω cross section to $\epsilon = 85$ MeV. The present work gives a value for the cross section at an energy closeby, so that the ratio can now be determined without further assumptions. We find $\sigma_\phi/\sigma_\omega = (2.5\pm1.0)\%$, which is about a factor of 7 above the naive SU(3) expectation.
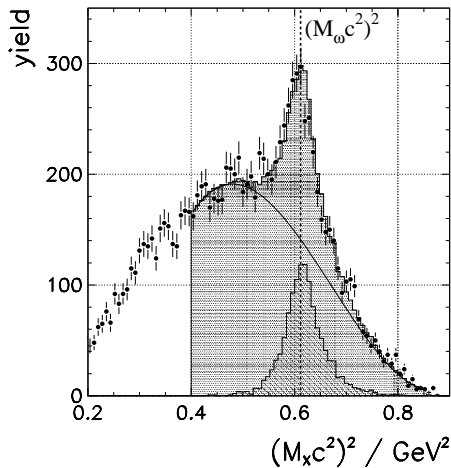
Fig. 1 *Spectrum of the squared missing mass deduced from the two detected proton candidates. The ω peak at $(M_X c^2)^2 \approx 0.6$ GeV^2 is clearly visible.*
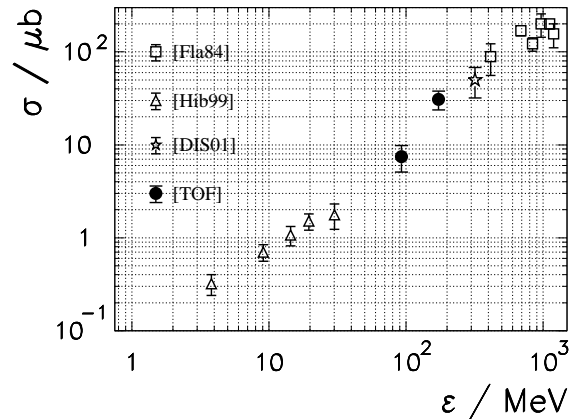
Fig. 2 *Excitation function of pp $\to$ ppω. The filled circles are the present data, while the open triangles are from [2] and the star is from [3]. The open squares represent data adopted from a compilation of cross sections [4].*

[1] COSY-TOF collaboration, Phys. Lett. B 522 (2001) 16
[2] F. Hibou et al., Phys. Rev. Lett. 83 (1999) 492
[3] DISTO collaboration, Phys. Rev. Lett. 81 (1998) 4572 *and* Phys. Rev. C 63 (2001) 024004
[4] V. Flaminio et al., Compilation of Cross-Sections, CERN-HERA 84-10 (1984)
[5] S. Okubo, Phys. Lett. 5B (1965) 165; G. Zweig, CERN Report No 8419/Th 412; I. Iizuka, Prog. Theor. Phys. Suppl. 37-38 (1966) 21

[1] *Institut für Kern- und Teilchenphysik, TU Dresden*

Simulation of Neutron Detector Efficiencies for COSYnus [B,J]

B. Jakob[1], B. Naumann[1] for the COSY-TOF collaboration

Different codes for the calculation of efficiency corrections for neutron detectors in the energy range up to $500\,MeV$ exist. For the neutron detector COSYnus [1] at COSY-TOF, results obtained with the three different codes Modeff [2], FLUKA [3] and LasVegas [4] were compared. All these programs have their advantages and shortcomings. Modeff is a widely used and tested code in the lower energy region $(1 - 20\,MeV)$, but only extrapolations from the low energy regions are used to remedy the lack of experimental cross sections for neutron interactions at higher energies. With the FLUKA code, neutron interactions in the energy range from thermal neutrons up to $E_n \approx 20\,TeV$ can be simulated, but implementing the full TOF geometry in FLUKA would be very complicated. In the LasVegas code, which is a Monte Carlo code designed for TOF, neutron interac-

tions can only be incorporated through the use of the INC-Code of Cloth [5] which is based on the INtranuclear Cascade model of Bertini [6]. The results of the calculations are shown in Figures 1 and 2. They were obtained for three different detection thresholds requiring a light deposit of at least $E_{th} = 2, 5$, and $7\,MeV_{pe}$ in the scintillator. Obviously, the LasVegas results for energies less than about $100\,MeV$ are too low, since at these energies nuclear reactions play an important role, which are not well described in cascade type models. Experimental data, in particular for the high energy region, are needed but are not yet available. First results obtained with COSYnus [7] show large statistical uncertainties and do not allow to distinguish between different simulations.
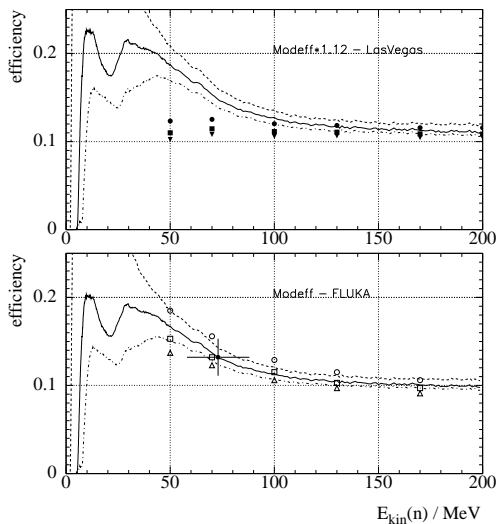
Fig. 1 *Comparison of neutron detection efficiencies obtained with Modeff (lines), LasVegas (filled symbols) and FLUKA (open symbols). The results are shown for the threshold energies $E_{th} = 2\,MeV_{pe}$ (dotted lines or circles), $E_{th} = 5\,MeV_{pe}$ (dashed or squares) and $E_{th} = 7\,MeV_{pe}$ (dash-dotted or triangles). Upper plot: LasVegas results in comparison with Modeff simulations, scaled by a factor $1, 12$ [9]. Lower plot: good agreement between FLUKA and Modeff (not scaled in this case); the experimental value for neutrons with a kinetic energy of $(73 \pm 16)\,MeV$ was obtained by measuring all three particles of the reaction $pp \rightarrow pn\pi^+$ at a beam energy of $T = 300\,MeV$ $(E_{th} = 5\,MeV_{pe})$ [8].*
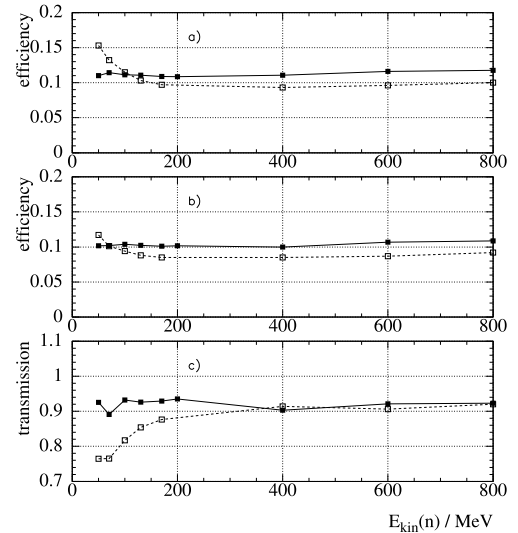
Fig. 2 *Comparison of detection efficiencies obtained with LasVegas (filled symbols) and FLUKA (open symbols) for high neutron energies using $E_{th} = 5\,MeV_{pe}$: a) without the influence of the vacuum vessel, b) with vacuum vessel (i.e. $1.5\,cm$ Fe) and c) the transmission through the iron wall.*

For the time being, LasVegas can be used for simulations of the TOF detector but a systematic uncertainty of 10% for the neutron efficiency should be taken into account in absolute normalizations. For a more detailed discussion see also [8].

[1] A. Böhm, Dissertation, TU Dresden, 1998
[2] R. A. Cecil et al., Nucl. Instr. and Meth. 161 (1979) 439
[3] A. Fasso et al., Proc. of the III Spec. Meeting on Shielding Aspects, Sendai, 12 - 13 May 1997, 61
[4] U. Zielinski, Dissertation, Ruhr-Universität Bochum, 1998
[5] P. Cloth, Programm INC77, Version 1.0, FZ Jülich 1992
[6] H. W. Bertini, Phys. Rev. 131 (1963) 1801, Phys. Rev. 188 (1969) 1711
[7] L. Karsch et al., Nucl. Instr. and Meth. A 460 (2001) 362
[8] B. Jakob, Dissertation, TU Dresden, 2001
[9] K. Knoche, Dissertation, Universität Hamburg, 1994

[1] *Institute of Nuclear and Particle Physics, TU Dresden*

Evaluation of QCD Sum Rules for HADES [B]

S. Zschocke, O.P. Pavlenko[1], B. Kämpfer

The in-medium modifications of the light vector mesons (ρ, ω, ϕ) receive recently growing attention both from theoretical and experimental sides. On the theoretical side there are various indications concerning an important sensitivity of vector mesons to partial restoration of chiral symmetry in a hot and dense nuclear medium. In particular, at finite temperature vector and axial-vector correlation functions, which are related to the meson spectral densities, undergo mixing in accordance with in-medium Weinberg sum rules. At low temperature this mixing can be expressed directly via vacuum correlators in a model independent way. Additionally, as shown within lattice QCD and various effective model calculations, the chiral quark condensate as order parameter decreases with increasing temperature and baryon density. Being interrelated via QCD sum rules with the vector meson spectral density, all mentioned approaches predict considerable in-medium modifications of vector mesons even at normal nuclear matter density.

We have evaluated the QCD Borel sum rule for finite baryon density _and_ temperature

$$M^{-2} \int_0^\infty ds\, \rho_{\mathrm{had}}(s) \mathrm{e}^{-s/M^2} = C_0 + \sum_{n=1}^{3} \frac{C_n}{(n-1)!\, M^{2n}}$$

which emerges from the Fourier transformed longitudinal retarded current-current correlation function $\Pi_L^R(q^0; \mu_N, T)$ by employing a truncated operator product expansion and a dispersion relation; C_n denote the Wilson coefficients including temperature and density dependent condensates and moments of the parton distributions in nucleons and pions (for the explicit form cf. [1]), and M stands for the Borel mass. Using the pole

+ continuum + Landau damping ansatz for the spectral density $\rho_{\mathrm{had}}(s; \mu_N, T) = \frac{1}{\pi} \mathrm{Im}\Pi_L^R(s; \mu_N, T)$ the pole mass parameter m_V is determined by

$$\frac{m_V^2}{M^2} = \left\{ C_0 \left(1 - [1 + \frac{s_0^V}{M^2}]\mathrm{e}^{-s_0^V/M^2}\right) - \frac{C_2}{M^4} - \frac{C_3}{M^6} \right\}$$
$$\left\{ C_0 \left(1 - \mathrm{e}^{-s_0^V/M^2}\right) + \frac{C_1 - \rho_{\mathrm{scatt}}^{V,N+\pi}}{M^2} + \frac{C_2}{M^4} + \frac{C_3}{2M^6} \right\}^{-1},$$

where s_0^V stands for the continuum threshold; the Landau term is $\rho_{\mathrm{scatt}}^{V,\pi+N}$. Instead of the often used saturation hypothesis we introduce suitable parameters to control a deviation from the factorization of the four-quark condensate.

Requiring maximum flatness of $m_V(M^2)$ within the Borel window (0.75 - 1.5 GeV^2 for ρ and ω mesons, 0.75 - 3.0 GeV^2 for ϕ meson) we get the following results:

(i) ρ meson: according to some cancellations of the coefficients, the four-quark condensate determines essentially the in-medium mass; m_ρ drops with increasing density (see Fig. 1, left panel);

(ii) ω meson: the Landau damping term is numerically important; the in-medium behavior depends sensitively on the strength parameter κ_N for the density dependence of the four-quark condensate (see Fig. 2, middle panel);

(iii) ϕ meson: the chiral strangeness condensate determines the dropping of m_ϕ (see Fig. 3, right panel), however, its strength depends decisively on the strangeness content in the nucleon.

Temperature effects are, in accordance with the mixing theorem, rather week.
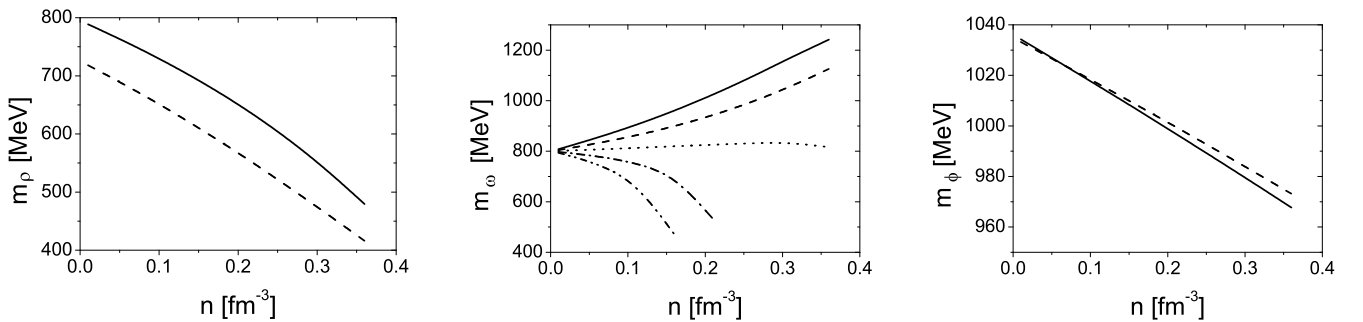
Fig. 1 _The ρ, ω, ϕ meson masses as a function of the density. Full (dashed) curves in the left and right panels are for $T = 20$ (140) MeV. In the middle panel we have chosen $T = 20$ MeV and the various curves are for $\kappa_N = 0 \cdots 4$ (from top to bottom), where the density dependence controlling parameter κ_N appears in the four-quark condensate $q_4 = -\kappa_0 \langle \bar{u}u \rangle_0^2 \left[1 - \frac{\kappa_N}{\kappa_0} \frac{4M_N \sigma_N}{m_q(-\langle \bar{u}u \rangle_0)} I_1^N\right]$ entering the coefficient C_3. κ_0 controls the vacuum saturation of the chiral condensate $\langle \bar{u}u \rangle_0$, σ_N denotes the nucleon sigma term, and M_N is the vacuum nucleon mass; the term I_1^N depends on density and temperature, cf. [1]._

[1] S. Zschocke, O.P. Pavlenko, B. Kämpfer, XL Internat. Winter Meeting on Nucl. Phys., Bormio 2002, (Ed.) I. Iori

[1] _Institute for Theoretical Physics, Kiev, Ukraine_

BUU Studies of Dilepton Production in Heavy-Ion Collisions at HADES [B]

Gy. Wolf[1], B. Kämpfer, O.P. Pavlenko[2], S. Zschocke

QCD sum rules and various hadronic models predict substantial in-medium modifications of ρ and ω mesons. While the predictive power of QCD sum rules is restricted to mass changes or vector–axial-vector mixing either in zero-width approximation or as interrelation of width broadening vs. mass shift, more detailed hadronic models point to strong broadening effects in dense nuclear matter.

We have recently shown [1] that for conditions expected in the forthcoming heavy-ion experiments at HADES the broadening of the ρ meson might be so strong that it disappears as distinctive peak in the invariant mass spectrum. However, multidimensional spectra, e.g. the rate as a function of the invariant mass M and transverse mass $M_\perp$ still carry the wanted information on the ρ peak. This result was obtained within a simple fire ball model. To make more detailed predictions of the dilepton spectra we now use the BUU transport code [2] to study various background sources and multidifferential spectra in central collisions of Au(1 AGeV) + Au.

Fig. 1 exhibits the background sources pn bremsstrahlung, and Δ and η Dalitz decays as well. The contributions from pion annihilation $\pi^+\pi^- \rightarrow \rho \rightarrow e^+e^-$ overcomes both these background sources and the dilepton decays of so-called direct ρ mesons stemming from baryon resonance decays in the region $M > 400$ MeV. Clearly visible is the ρ peak when selecting $M_\perp = 850 \cdots 950$ MeV.

Fig. 2 displays the ω decay contribution. A selection of dielectrons with small transverse momentum $Q_\perp$ enhances the yield of in-medium decays.
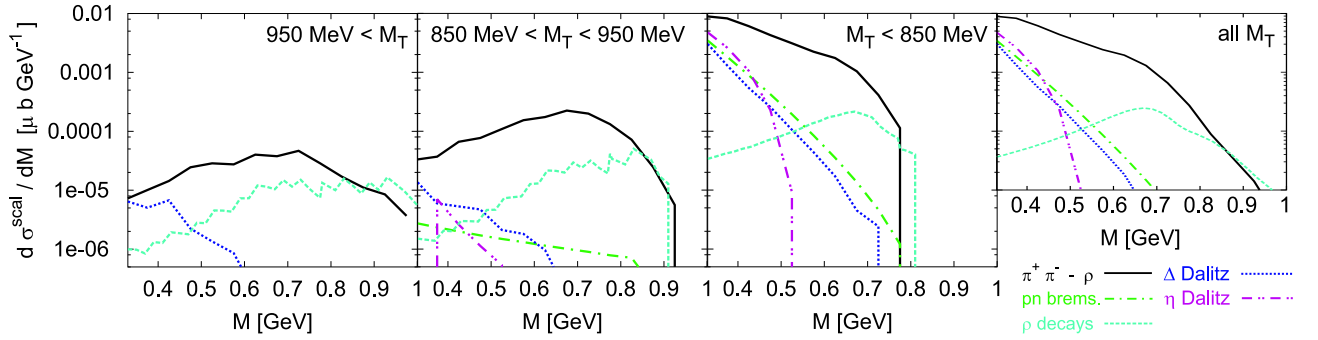
Fig. 1 *Dilepton spectra as a function of invariant mass for several $M_\perp$ bins. A ρ broadening by a factor 3 is assumed, no mass shift. The ω and ϕ contributions are not shown.*
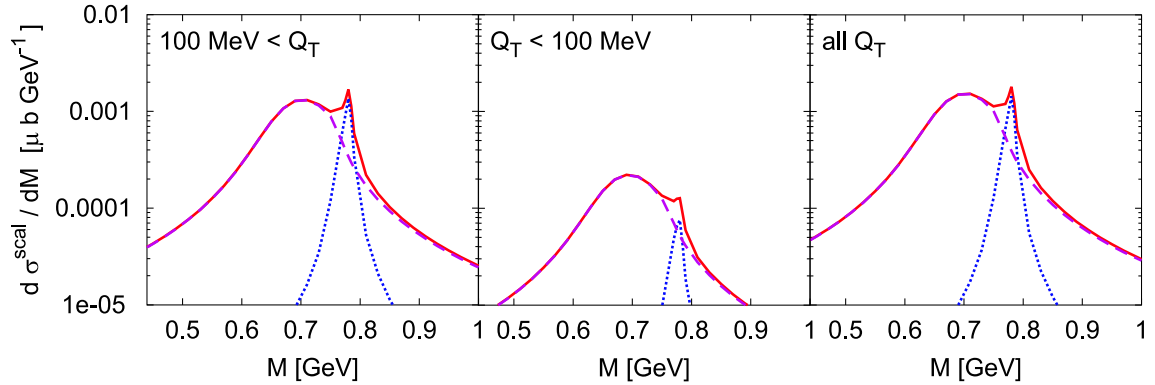
Fig. 2 *Dilepton spectra from ω decays as a function of invariant mass for several $Q_\perp$ bins. The density dependent mass and width are parametrized as $m_\omega = m_\omega^0 - \delta m_\omega n/n_0$ and $\Gamma_\omega = \Gamma_\omega^0 - \delta\Gamma_\omega n/n_0$ with $\delta m_\omega = 70$ MeV and $\delta\Gamma_\omega = 50$ MeV. The sharp peak structure depicts the vacuum decay contribution.*

[1] B. Kämpfer, O.P. Pavlenko, Eur. Phys. J. A10 (2001) 101
[2] Gy. Wolf et al., Nucl. Phys. A 517 (1990) 615, A 552 (1993) 549

[1] *KFKI-RKMI Budapest, Hungary*
[2] *Institute for Theoretical Physics, Kiev, Ukraine*

The Role of ρ Meson Channels for ϕ Meson Production in Heavy-Ion Collisions [A,B]

H.W. Barz, Gy. Wolf[1], M. Zétényi[1], B. Kämpfer

Meson production in heavy-ion collisions is considered a sensitive probe of the reaction dynamics. Particularly interesting is the production of heavy mesons at such a kinetic energy which is insufficient to create the respective meson in a free nucleon-nucleon collision. Their study provides valuable information on the equation of state of dense and hot nuclear matter and the properties of the participating particles. Recently, the ϕ meson production was measured in reactions of Ni+Ni and Ru + Ru at energies of 1.93 and 1.69 A·GeV, respectively [1]. Extrapolations from the limited phase space available point to a larger cross section than standard Boltzmann-Ühling-Uhlenbeck (BUU) calculations [2]. The discrepancy of these calculations with the data inspired us to study whether further elementary channels might essentially contribute to the ϕ meson production. Especially collisions of ρ mesons and baryons have rather large production cross sections which have been neglected in the past. Therefore we include in transport calculation of the BUU type [3] the new reaction channels $\rho N(\Delta)$, $\pi N(1520)$ and $\pi\rho$. In this model resonances up to 2 GeV are included together with $\pi, \eta, \rho, \sigma, \omega, K^+$ and K^0 mesons and hyperons. A momentum dependent soft mean field for baryons and a weak mean field for the ϕ mesons have been employed (for details cf. [4]).

In table 1 we list the contributions to ϕ production from the elementary reactions for central Ni+Ni collisions at 1.93 A·GeV. The new included channels (lines 3 - 5) increase the ϕ meson production by about a factor of three.

yields from	Ni + Ni (1.93 A·GeV)
B + B	$3.5 \cdot 10^{-4}$
π + B	$2.9 \cdot 10^{-4}$
ρ + B	$8.9 \cdot 10^{-4}$
$\pi + \rho$	$1.6 \cdot 10^{-4}$
π + N(1520)	$0.5 \cdot 10^{-4}$
total yield	$1.7 \cdot 10^{-3}$
in HELITRON	$1.2 \cdot 10^{-5}$
in CDC	$2.7 \cdot 10^{-5}$
experiment [1]	$(8.7 \pm 3.6) \cdot 10^{-3}$

Table 1 *Contributions to the ϕ yield.*

It is interesting to observe that the different channels provide very different angular distributions. The ϕ mesons which are created in BB collisions have a nearly isotropic angular distribution. However, in the πB and ρB channels the resulting angular distributions are significantly forward-backward peaked. This anisotropy caused by the meson channels determines the total momentum distribution as can be seen in Fig. 1. This leads to the fact that the yield in the backward lying CDC detector is larger than that in the HELITRON detector which is sensitive at midrapidity. This finding seems to be in contradiction to the preliminary analysis by the FOPI group. Results by Aichelin and Hartnack [5] within a quantum molecular dynamic transport code support this behaviour of the different channels.
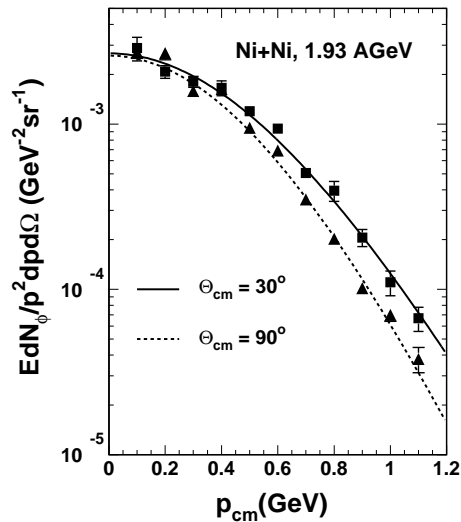
Fig. 1 *Predicted momentum distributions of ϕ mesons in the centre-of-mass system for central Ni + Ni collisions for two centre-of-mass angles Θ. The error bars on the symbols reflect the statistical uncertainty in our Monte-Carlo calculation. The smooth curves show fits to a thermal model with temperature values of 120 MeV for $\Theta_{cm} = 30°$ and 100 MeV for $\Theta_{cm} = 90°$, respectively.*

In spite of a substantial increase of the ϕ multiplicities by the newly included channels the results stay below the tentative numbers extracted from experimental data. We like to mention that we have not considered a possible change of the decay width of the ϕ meson which is poorly known at present and would reduce the measured ϕ multiplicity since the created K^- would scatter with a large probability and reduce the K^+K^- correlation. Therefore the branching ratio between the electromagnetic and the hadronic decay will be sensitive to the in-medium properties of mesons. Measurements of this ratio will become accessible via the e^+e^- decay channel in the HADES detector and the up-graded FOPI apparatus.

[1] R. Kotte (FOPI collaboration), Proc. Int. Workshop XXVIII, Hirschegg, Austria (2000) 112
[2] W.S. Chung, G.Q. Li, C.M. Ko, Nucl. Phys. A 625 (1997) 347
[3] Gy. Wolf, W. Cassing, U. Mosel, Nucl. Phys. A 552 (1993) 549
[4] H.W. Barz, M. Zétényi, Gy. Wolf, B. Kämpfer, nucl-th/0110013, Nucl. Phys. A (2002) in print
[5] J. Aichelin, Chr. Hartnack, private communication

[1] *KFKI Budapest, Hungary*

Estimates of Sub-Threshold Phi Meson Production for HADES and FOPI [B]

R. Kotte, B. Kämpfer

The ϕ meson acceptance of two large detector installations, the 4π detector FOPI [1] and the dilepton spectrometer HADES [2] at SIS/GSI, has been calculated [3] for the reaction C $(2\,A\cdot\text{GeV})$ + C. These setups allow to measure either exclusively the decay products of the hadronic channel $\phi \rightarrow K^+K^-$ (FOPI) or both the products of the hadronic and leptonic $\phi \rightarrow e^+e^-$ channels (HADES). Maximum luminosities compatible with the data-acquisition times and taping rates are assumed. The available phase-space regions and the spectral shape of the mother ϕ mesons (i.e., an isotropic source with effective inverse slope T_ϕ) have been varied in order to be flexible with respect to reliable predictions of both the beam time necessary for a certain ϕ yield and the size of the corresponding event sample which has to be processed. In the following the results achieved for $T_\phi = 70$ MeV are summarized.

The largest geometrical acceptance $(30 - 40\,\%)$ is achieved with HADES when measuring the $e^\pm$ pairs from the ϕ decay, see Fig. 1a. This channel would allow for the reconstruction of almost the full triple-differential momentum distribution of the ϕ mesons. About 400 ϕ mesons are expected after a beam time of two weeks. Due to the small branching ratio of $\Gamma_{\phi\rightarrow e^+e^-}/\Gamma_{\phi,total} = 2.9 \cdot 10^{-4}$ a fast and efficient 2nd level trigger is mandatory.

Concerning the hadronic channel $(\Gamma_{\phi\rightarrow K^+K^-}/\Gamma_{\phi,total} = 0.49)$, the HADES spectrometer with an upgraded TOF subdetector will provide a geometrical acceptance of only $6\,\%$ only (Fig. 1b). But it will still allow for reliable reconstruction of the ϕ distribution and the corresponding total production probability. About 2200 ϕ mesons are expected within two weeks. In case of the upgraded FOPI setup, the overall geometrical acceptance of all involved subdetector combinations amounts to $4\,\%$, see Fig. 1c. There, about 750 ϕ meson are expected after two weeks of beam on target.

If there would be some change of ϕ inverse slope, beam intensity, collision system, detection efficiencies or expected ϕ cross section, the beam-time estimates can be easily rescaled with the help of the systematics summarized in ref. [3]. Further details are provided there, such as the change of the acceptance when imposing different momentum cuts.
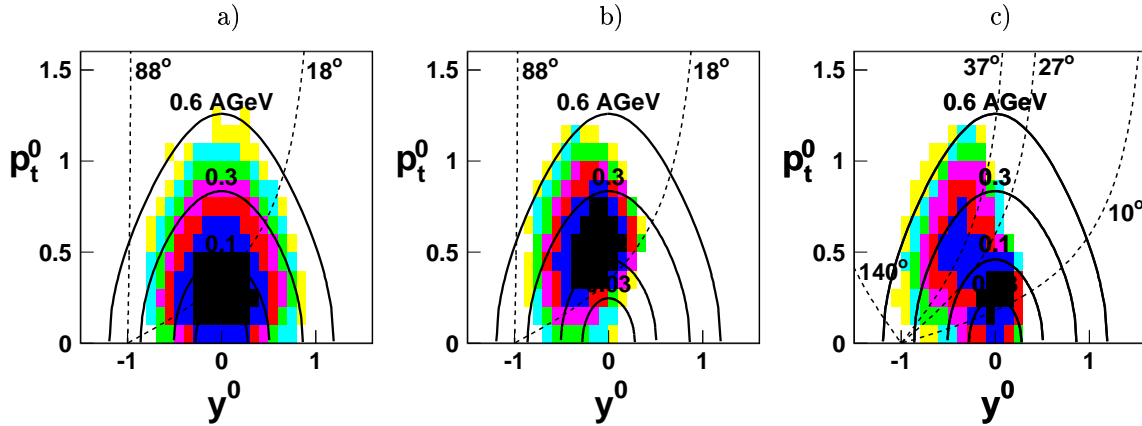
Fig. 1 *Phase-space distribution $d^2N/dp_t dy$ of reconstructed ϕ mesons within the acceptance regions of HADES (a: e^+e^- channel, $18^o < \theta_e < 88^o$; b: K^+K^- channel, $18^o < \theta_K < 88^o$, $p_K < 1$ GeV/c) and FOPI (c: K^+K^- channel, all possible subdetector combinations involved; CDC with upgraded TOF Barrel, $37^o < \theta_K < 140^o$, 0.1 GeV/c $< p_K < 1$ GeV/c; Helitron/Plastic Wall, $10^o < \theta_K < 27^o$, 0.2 GeV/c $< p_K < 0.8$ GeV/c). Here, $p_t^0 = (p_t/A)/(p_{proj}/A_{proj})_{cm} = (\beta_t\gamma)/(\beta\gamma)_{cm}^{proj}$ and $y^0 = (y/y_{proj})_{cm} = (y/y_{cm} - 1)$ are the normalized transverse momentum and rapidity, respectively, and $A = m/m_p$ is the particle mass number. Both quantities are related to the corresponding projectile quantities in the center-of-mass (c.m.) frame of the colliding nuclei (with $y_{cm} = 0.904$ and $(\beta\gamma)_{cm}^{proj} = 1.032$ for 2.0 $A\cdot$GeV beam energy). The dashed and full lines indicate the polar angle limits and constant c.m. kinetic energies per nucleon, respectively. A logarithmic intensity scale is used.*

[1] A. Gobbi et al. (FOPI collaboration), Nucl. Instr. Meth. A 325 (1993) 156;
J. Ritman for the FOPI collaboration, Nucl. Phys. (Proc. Suppl.) B 44 (1995) 708
[2] J. Friese for the HADES collaboration, Nucl. Phys. A 654 (1999) 1017c; Progr. in Part. and Nucl. Phys. 42 (1999) 235;
C. Garabatos for the HADES collaboration, Nucl. Phys. B 61 (1998) 607
[3] R. Kotte and B. Kämpfer, FZ Rossendorf Technical Report, FZR-339 (2002)

Model Calculations of Meson Production in Proton-Nucleus Collisions

H. Müller

In a recent experiment at SIS/GSI a comprehensive set of kaon and pion production data in proton-nucleus reactions has been measured [1] at energies near the kaon production thresholds of the relevant elementary processes. Part of these data are analyzed here within the Rossendorf Collision (ROC) model [2, and references therein]. Contrary to BUU [3] calculations, the ROC model does not need parameterizations of the elementary hadronic interactions as input. Thus, there is no limitation for higher energies caused by the rapidly increasing numbers of elementary channels, which must be considered in BUU calculations. The ROC model aims at a unified description of both hadronic and nuclear interactions. In [2] the applicability of the model for pp interactions up to ISR energies has been demonstrated. A nuclear reaction is described on the basis of the participant-spectator picture. A proton-participant interaction is treated in a similar manner as a hadron-hadron interaction with slight modifications of the relevant parameter values. Hereby the participating nucleons are considered as a single entity. The internal momentum of the participant groups is taken as a Gaussian distribution having a width $\sigma_a = \sqrt{a(A-a)/5(A-1)}\, p_F$ with a being the number of participants within the nucleus A. For the Fermi momentum a value of $p_F = 0.23$ GeV is taken in case of carbon $A = 12$.

The partial cross sections for the interaction of a participant group consisting of a definite number of nucleons are calculated on the basis of a probabilistic interpretation of the Glauber theory. The cross sections for particle production are taken as the incoherent sum over the contributions from the various participant groups. Below and near the threshold of the considered ejectile the contributions from multi-particle groups are essential, while far above the threshold the quasi-free collisions with single nucleons give the main contributions.

In a proton-participant interaction translational energy is converted into internal excitation energy of a varying number of subsystems emerging from the collision. Also the excitation of the residual nucleus caused by the collision is taken into account. The valence quarks of the interaction partners and additional produced quark-antiquark pairs recombine in a second stage to hadrons. Primarily produced resonances decay during the final stage into stable particles.

The model is implemented as a Monte Carlo generator, which samples complete events. Therefore a comparison with experimental data is not restricted to selected final channels. Thus, a comparison of both the pion and the kaon spectra calculated with the same parameter set at all energies is possible.

In Fig. 1 the experimental data are compared with the results of ROC model calculations. The overall agreement between data and calculations is satisfactory. Only in case of the K^- spectrum at 3.5 GeV a slight overestimation of the data is observed. This may be due to the fact, that no final state interactions are implemented in the model calculations. Because of the larger K^-N cross section compared to the K^+N one a stronger attenuation of the K^- spectra can be expected.

To summarize, both the pion and the kaon spectra are well reproduced within the framework of the ROC model. No special assumptions concerning in-medium effects like reduced masses of the produced mesons or high-momentum components of the nuclear wave function are needed for the description of the observables considered. Only the inclusion of the interaction with multi-particle groups is to a certain degree equivalent to multi-step processes with intermediate particles as considered in BUU calculations.

$$p + C \rightarrow (\pi, K)(40°) + X$$
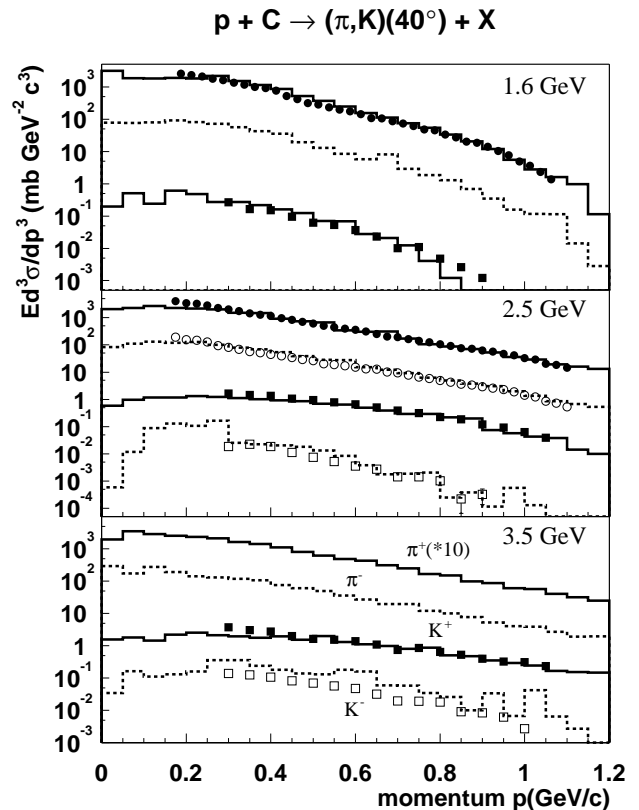
Fig. 1 *Invariant differential cross sections for the production of charged pions and kaons. Full points are π^+, open points π^-, full squares K^+ and open squares K^- data [1]. The full (for positive) and dashed histograms (for negative mesons) depict the ROC results. Data and histograms for π^+ mesons are multiplied by 10.*

[1] W. Scheinast, Acta Physica Polonica B 31 (2000) 2305
[2] H. Müller, Eur. Phys. J. C 18 (2001) 563
[3] Gy. Wolf et al., Nucl. Phys. A 552 (1993) 549

Production of ω and ϕ Mesons in Near-Threshold πN Reactions: Baryon Resonances and Okubo-Zweig-Iizuka Rule [B]

A.I. TITOV[1], B. KÄMPFER, B.L. REZNIK[1]

The present interest in a combined study of the ω and ϕ meson production in different elementary reactions is mainly related to the investigation of the hidden strangeness degrees of freedom in the nucleon. Since the ϕ meson is thought to consist mainly of strange quarks, its production should be suppressed according to the Okubo-Zweig-Iizuka (OZI) rule if the entrance channel does not possess a considerable admixture of strangeness. The standard OZI rule violation is described by the deviation from the ideal $\omega - \phi$ mixing by the angle $\Delta\theta_V \simeq 3.7^0$, which is a measure of the small contribution of light $u, \bar{u}$ and $d, \bar{d}$ quarks in the ϕ meson, or strange $s, \bar{s}$ quarks in the ω meson. Thus, the ratio of ω to ϕ production cross sections is expected to be $R^2_{\omega/\phi} \simeq \mathrm{ctg}^2 \Delta\theta_V \simeq 2.4 \times 10^2$.

The recent experiments on the proton annihilation at rest point to a large apparent violation of the OZI rule, which is interpreted as a hint to an intrinsic $s\bar{s}$ component in the proton. However, the data can be explained as well by modified meson exchange models without introducing any strangeness component in the nucleon or OZI rule violation mechanisms. On the other hand, the analysis of the πN sigma term suggests that the proton might contain a strange quark admixture as large as 20%. Thus this issue remains controversial. Therefore it is tempting to look for other observables which are sensitive to the strangeness content of the nucleon. Most of them are related to a possible strong interference of delicate $s\bar{s}$ knock-out (or shake-off) amplitudes and the "non-strange" amplitude which is caused by OZI rule allowed processes, or by processes wherein the standard OZI rule violation comes from the $\phi - \omega$ mixing.

A detailed analysis of the current status of the OZI rule in πN and NN reactions has been presented recently [1]. It is shown that existing data for the ω and ϕ meson production in πN reactions give for the ratio of averaged amplitudes the value $R_{\omega/\phi} = 8.7 \pm 1.8$, which is much smaller than the standard OZI rule violation value of $R^{OZI}_{\omega/\phi} = 15.43$ and may be interpreted as a hint to non-zero strangeness components in the nucleon.

Obviously, reliable information on a manifestation of hidden strangeness in the combined study of ϕ and ω production processes can be obtained only when the conventional, i.e. non-exotic, amplitudes have been understood quantitatively.

The resonance contribution to vector meson production has its own interest because it might affect significantly in-medium polarization operators and the corresponding dilepton emissivity of hadronic matter. Therefore its detailed study in elementary πN processes is another important issue.

Our analysis of the reaction $\pi N \rightarrow VN$ is based on interaction Lagrangians from [2] with $\omega\rho\pi$ $\phi\rho\pi$, ρNN, πNN^*, ωNN^* and ϕNN^* vertices. We include the

resonances $P_{11}(1440)$, $D_{13}(1520)$, $S_{11}(1535)$, $S_{11}(1650)$, $D_{15}(1675)$, $F_{15}(1680)$, $D_{13}(1700)$, $P_{13}(1720)$.

It is found [3] that the resonance contributions can influence significantly the total and the differential cross sections at small energy excess as well as the ratio of the averaged amplitudes of ω and ϕ production. For this ratio we get the value 8.7 ± 1.5 which is much smaller than the value based on the standard OZI rule violation. The dominant contributions are found to stem from the nucleon resonances $N_{\frac{1}{2}-}(1535)S_{11}$, $N_{\frac{1}{2}-}(1650)S_{11}$, and $N_{\frac{1}{2}+}(1440)P_{11}$. The total cross section is exhibited in fig. 1, while fig. 2 displays individual contributions to the ω production.
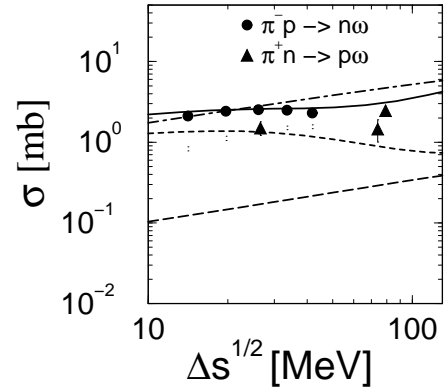
Fig. 1 *Total cross sections for the reaction $\pi N \rightarrow N\omega$ (left panel) as a function of the energy excess $\Delta s^{1/2}$. The meaning of the curves is: meson exchange - dot-dashed, direct and crossed nucleon terms - long-dashed, N^* resonances - dashed, full amplitude - solid.*
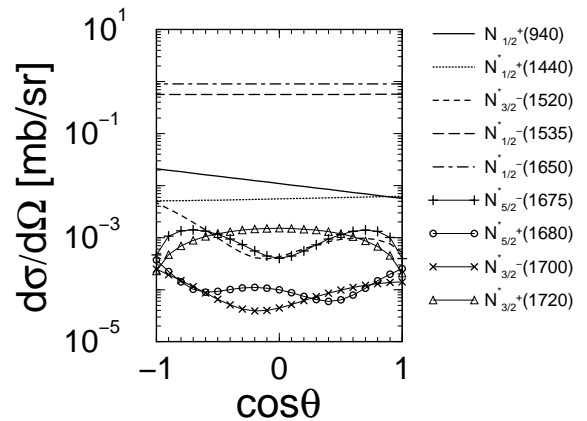
Fig. 2 *Individual contributions of nucleon resonances to the angular differential cross section of ω production at $\Delta s^{1/2} = 20$ MeV.*

[1] A. Sibirtsev, W. Cassing, Eur. Phys. J. A 7 (2000) 407
[2] D.O. Riska, G.E. Brown, Nucl. Phys. A 679 (2001) 577
[3] A.I. Titov, B. Kämpfer, B.L. Reznik, nucl-th/0102032

---

[1]*Bogoliubov Laboratory of Theoretical Physics, JINR, Dubna, Russia*

The Reactions $pn \to pn\phi$, $pn \to d\phi$ and $pd \to d\phi p_{\mathrm{spec}}$ [B]

L.P. Kaptari[1], B. Kämpfer

Meson production is presently studied in experiments at UICF, CELCIUS and COSY to elucidate the precise behavior of the amplitudes near threshold. The threshold-near vector meson production in elementary hadron reactions is of particular interest for the starting HADES experiments at SIS. While the pp and πp reactions are directly accessible, reactions with a neutron in the entrance channel need special emphasis. Recently, the spectator technique has been proposed to study the quasi-free meson production at the deuteron by selecting a special kinematics with tagging the spectator proton p_{spec} from the deuteron. In such a way one can investigate, e.g., the reaction $pn \to pn\phi$. As shown in [1], within an effective interaction Lagrangian approach, due to different interferences the ratio of cross sections $\sigma_{pp \to pp\phi}/\sigma_{pn \to pn\phi}$ is a non-monotonic function of the energy. Isospin effects, therefore, can not be absorbed in simple factors. It should also be stressed that the final state interaction depends on the relative state of the proton p and the neutron n. Here the situation simplifies considerably if p and n are in a unique state, namely the deuteron d.
In [2] we have studied the quasi-free reaction $pn \to d\phi$. Results for the energy dependence of the total cross section, following from

$$\frac{d\sigma}{dt} = \frac{1}{16\pi s(s - 4m^2)} \frac{1}{4} \sum_{spins} |\mathcal{T}_{pn \to d\phi}(s,t)|^2 \qquad (1)$$

with s, t as usual Mandelstam variables, are displayed in fig. 1. Parameters of the elementary amplitudes are adopted from [1]. Our calculations are based on the use of a numerical solution of the Bethe-Salpeter (BS) equation describing the deuteron wave function. Also polarization observables are studied in detail in [2].
Recently, we extended the study in [2] to the complete reaction $pd \to d\phi p_{\mathrm{spec}}$ to check the validity of the spectator mechanism assumption. The process is diagrammatically depicted in fig. 2. The cross section reads in the system, where the target deuteron is at rest,

$$2E_d' \frac{d^5\sigma}{d^3p_d' \, d\Omega_p'} = \frac{1}{8(2\pi)^5 \sqrt{\lambda}} \frac{1}{6} \frac{|\vec{p}_p{}'|^2}{|B|\vec{p}_p{}'| - CE_p'|}$$
$$\times \sum_{spins} |\mathcal{T}_{pd \to d\phi p_{\mathrm{spec}}}|^2 \qquad (2)$$

with $\lambda = 4M_d^2 |\vec{p}_p|^2$ $B = M_d + E_p - E_d'$, $C = |\vec{p}_p| \cos\theta_p' - |\vec{p}_d{}'| \cos\theta_{dp}'$, and $p_p = (E_p, \vec{p}_p)$, $p_d = (M_d, \mathbf{0})$ as initial momenta of the proton and deuteron, $(p_p' = (E_p', \vec{p}_p{}')$, $p_d' = (E_d', \vec{p}_d{}'))$, and $p_\phi = (E_\phi, \vec{p}_\phi)$. Strictly speaking,

a factorization of the complete reaction into two parts can be obtained only on the amplitude level. However, due to spin selection rules near the threshold the cross section of the reaction $pd \to d\phi p_{\mathrm{spec}}$ can be factorized in a part containing only the subprocess $pn \to d\phi$ and a remaining part depending on the target deuteron wave function. Farer above threshold one can neglect the D wave component in the deuteron wave functions and gets also a factorization. Despite of huge differences of the final state phase space for the reactions $pd \to d\phi p_{\mathrm{spec}}$ and $pn \to d\phi$ (compare eqs. (1) and (2)) we were able to show numerically for selected kinematical situations that factorization holds indeed in a wide energy range.
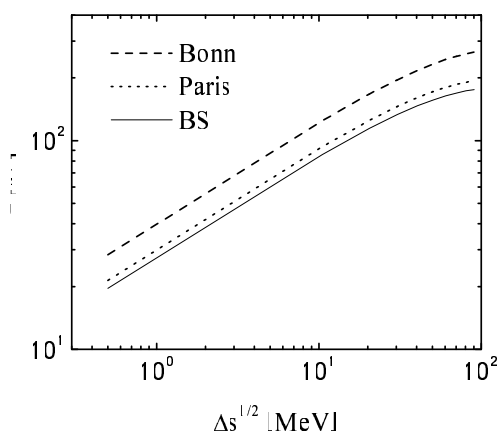
Fig. 1 *Total cross section for the reaction $pn \to d\phi$ as a function of the excess energy $\Delta s^{1/2} = \sqrt{s} - M_d - M_\phi$ for various deuteron wave functions. The elementary amplitude $pn \to pn\phi$ is taken from [1].*
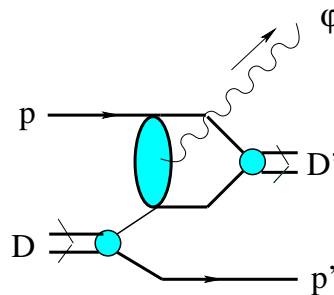
Fig. 2 *Diagrammatic representation of the complete reaction $pd \to d\phi p_{\mathrm{spec}}$.*

[1] A.I. Titov, B. Kämpfer, B.L. Reznik, Eur. Phys. J. A 7 (2000) 543
[2] L.P. Kaptari, B. Kämpfer, nucl-th/0102026

[1] *Bogoliubov Laboratory of Theoretical Physics, JINR, Dubna, Russia*

Isoscalar-Isovector Interferences in $\pi N \to N e^+ e^-$ Reactions as a Probe of Baryon Resonance Dynamics [B]

A.I. Titov[1], B. Kämpfer

For an understanding of dielectron spectra in hadron-nucleus and heavy-ion collisions the elementary hadronic reaction channels must be under control. Here the reactions $NN \to X e^+ e^-$ and $\pi N \to X e^+ e^-$ occupy a highly important place in the dielectron physics. These reactions serve as a necessary input for kinetic approaches. But on the other hand, they are interesting for themselves because they are mainly related to the baryon resonance dynamics. Different facets of the manifestation of baryon resonances in πN collisions have already been analyzed. Particularly interesting are such recent theoretical approaches which attempt a unifying description of meson-nucleon interactions. The quantum interference in $e^+ e^-$ decays of intermediate ρ and ω mesons produced in the exclusive reaction $\pi^- p \to n\rho(\omega) \to n e^+ e^-$ has been first discussed in [1], and the first round of HADES experiments will experimentally address this problem.

Here, we would like to emphasize that the $\rho - \omega$ interference in dielectron production has also an another interesting aspect: The interference may be used as a tool for studying the isoscalar part of the electromagnetic current in the resonance region, what is rather difficult to do by another methods. Varying the dilepton invariant mass M one can test low-lying baryon resonances which are deeply subthreshold for on-shell omega production. Of course, the contribution of the isoscalar part (i.e., the virtual ω production) is much smaller than the dominant isovector (i.e., virtual ρ production) at $M \neq m_\omega$ but it may be clearly seen in the $\rho - \omega$ interference which is proportional to the difference of the $e^+ e^-$ cross sections in $\pi^- p$ and $\pi^+ n$ collisions.

Indeed, since the electromagnetic current is the sum of isoscalar and isovector components, the invariant amplitude of the reaction $\pi^- p \to n e^+ e^-$ may be expressed as $T^{\pi^- p \to n e^+ e^-} \propto T^{\text{scalar}} + T^{\text{vector}}$, where, according to the vector dominance model, the isoscalar (isovector) contributions may be identified with ω (ρ) meson intermediate states, i.e. $T^{\text{scalar}} \propto T^\omega$ and $T^{\text{vector}} \propto T^\rho$. A rotation by 180° around the y-axis in isospin space leads to the transformations $|p\rangle \to -|n\rangle$, $|n\rangle \to |p\rangle$, $|\pi^-\rangle \to -|\pi^+\rangle$, $|\omega\rangle \to |\omega\rangle$, $|\rho^0\rangle \to -|\rho^0\rangle$ and, therefore, one gets $T^{\pi^+ n \to p e^+ e^-} \propto T^{\text{scalar}} - T^{\text{vector}}$. That means, the quantum interferences in the reactions $\pi^- p$ and $\pi^+ n$ are different, and these differences might be well observable in the vicinity of the ω resonance peak.

Our approach, described in detail in [2], is based on the effective interaction Lagrangians from [3] with $\pi N B^*$, $\omega N N^*$ and $\rho N B^*$ vertices, where we include in the isoscalar amplitudes the contributions of the nucleon (N) and the 8 resonances (N^*) $P_{11}(1440)$, $D_{13}(1520)$, $S_{11}(1535)$, $S_{11}(1650)$, $D_{15}(1675)$, $F_{15}(1680)$, $D_{13}(1700)$,

$P_{13}(1720)$ ($P_{11}(1710)$ is neglected due to a weak coupling) and in the isovector amplitudes these states and additionally the 4 Δ states up to 1700 MeV (all together B^*) $P_{33}(1232)$, $P_{33}(1600)$, $S_{31}(1620)$, $D_{33}(1700)$. Examples of interference patterns are exhibited in fig. 1 for a dilepton emission angle of 30^0 in the πN center-of-mass system. As shown in [2], multidifferential cross sections and excitations functions are needed to disentangle the dynamics of the various resonance contributions.
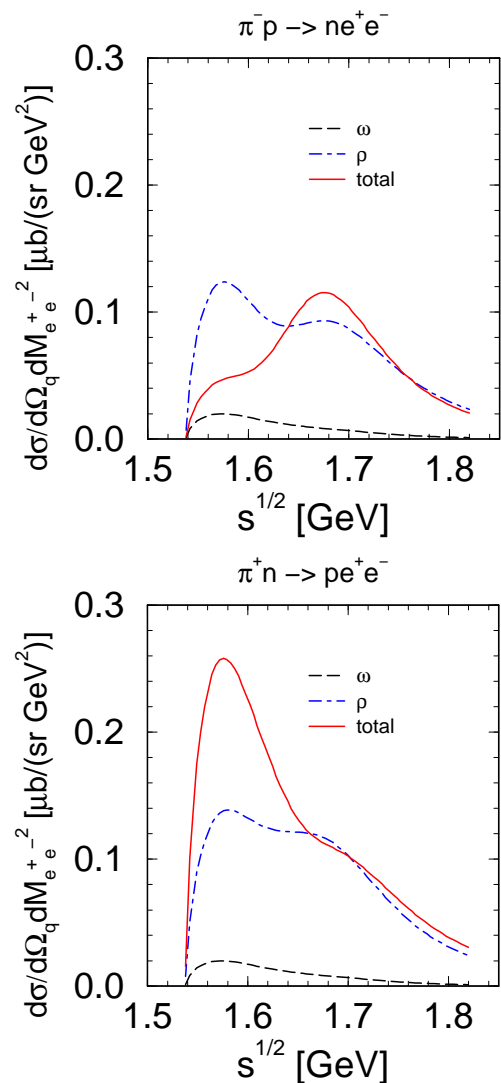
Fig. 1 *Differential cross sections of dielectron production as a function of $s^{1/2}$ for $M_{e^+ e^-} = 0.6$ GeV for the reactions $\pi^- p \to n e^+ e^-$ (upper panel) and $\pi^+ n \to p e^+ e^-$ (lower panel).*

[1] M. Soyuer, M. Lutz, B. Friman, nucl-th/0003013
[2] A.I. Titov, B. Kämpfer, Eur. Phys. J. A 12 (2001) 217
[3] D.O. Riska, G.E. Brown, Nucl. Phys. A 679 (2001) 577

---

[1]*Bogoliubov Laboratory of Theoretical Physics, JINR, Dubna, Russia*

Some Remarks on the Concept of Final State Interaction in Hadron Reactions [B,J]

K. MÖLLER FOR THE COSY-TOF COLLABORATION

In the present paper some problems are discussed which appeared in connection with the interpretation of spectra of proton-proton reactions measured recently at the COSY-TOF spectrometer [1,2]. Owing to the lack of theoretical calculations in many cases the interpretation of spectra measured in hadronic reactions is restricted to a mere comparison with phase space. The phase space distribution however does not contain any dynamics. It is completely determined by kinematics. In a first step of sophistication often the final state interaction (FSI) is taken into account to include at least a minimum of dynamics. The FSI concept goes back to Watson [3] and Migdal [4] who proved that a spectrum of a three-particle reaction in certain kinematical regions may reveal an enhancement which is mainly determined by the dynamics of one of the two-particle subsystems. In more detail this means, that a resonance or a resonance-like state (e.g., the virtual state of the singlet NN-interaction) in a two-particle subsystem will dominate also the form of the three-particle spectrum in the corresponding energy region with the rest of the dynamics contributing only a smooth behaviour.

Although the existence of the FSI mechanism was proven decades ago even today sometimes questions arise among experimentalists with respect to FSI. Some of these questions are: i) what are the conditions to observe an enhancement in the spectrum due to FSI, ii) how is FSI embedded in the three-particle reaction and how can FSI be interpreted in terms of the reaction mechanism of the three-particle reaction, iii) how can the effect of Coulomb interaction be incorporated and iv) how must the FSI enhancement term be combined with the phase space expression.
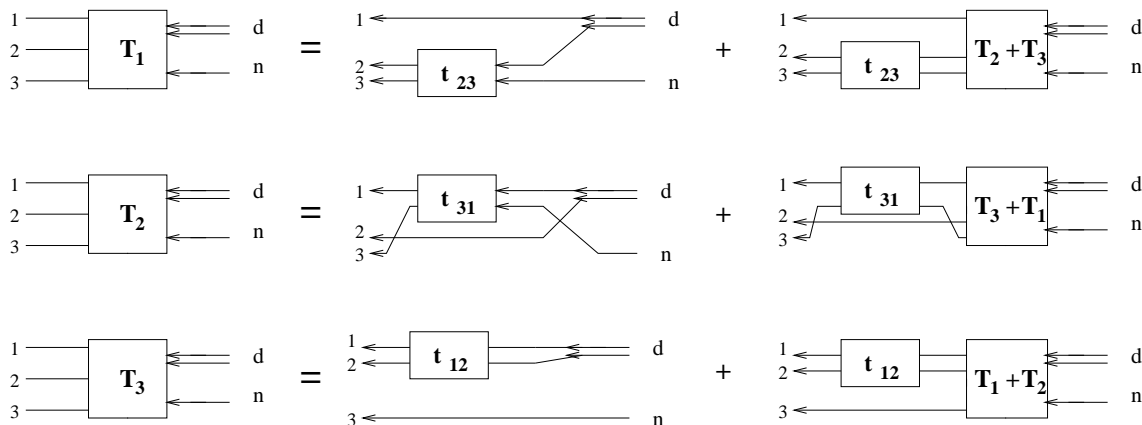
Fig. 1 *Faddeev integral equation system for the calculation of the n-d break-up.*

In the present paper a contribution is presented to answer the second question. It can be shown that the validity of the FSI mechanism for three particle reactions can be derived in a rigorous way from the Faddeev equations which are the exact equations for the description of three-particle reactions [5,6]. Here, rather than giving the full derivation only a few arguments are outlined on how the result was obtained. In Fig. 1 the Faddeev integral equation system is depicted for the calculation of the deuteron break-up by neutrons. The differential cross section for this process is given by $\sigma = \rho \mid T \mid^2$ with the phase space factor ρ and the three-particle T-matrix given by $< \vec{f}, \vec{k} \mid T_1 + T_2 + T_3 \mid \vec{k}_0 \varphi_d >$. Here $\vec{f}$, $\vec{k}$ and $\vec{k}_0$ are the momenta in conventional Jacobian coordinate notation. $\vec{f}$ denotes the momentum in the corresponding subsystem. The energy in the subsystem is given by $E_r = (h^2/m)f^2$. The crucial feature for the derivation of the FSI mechanism is the observation in Fig. 1 that all terms entering the three-particle T-matrix are terminated in the exit channel by a two-particle scattering process t_{ik}. The FSI approximation now is based on the fact that any two-particle t-matrix can be decomposed into a sum of separable terms (Hilbert-Schmidt decom-

position) [7] and that in the vicinity of a two-particle resonance E_{res} only one separable term of the sum survives. It has the form $t_{ik}(\vec{f}, \vec{f'}, E_r) \approx g(\vec{f})g(\vec{f'})/(E_r - E_{res})$. Inserting this expression into the integral equation in Fig. 1 one ends up with a three-particle T-matrix of the form $T \approx C_1/(E_r - E_{res}) + C_2$. This means, the two-particle energy denominator $(E_r - E_{res})$ is factored out in the three-particle T-matrix. In general the coefficients C_1 and C_2 will have a much weaker dependence on the kinematic variables than the energy denominator. The energy E_r is just the experimentally measured energy of the corresponding subsystem. For the singlet NN interaction we have $E_{res}=$ -67 keV thus reproducing the well known Watson-Migdal denominator, but this time exactly embedded in the three-particle "environment".

[1] R. Bilger et. al.: Phys. Lett. B 429 (1998) 195

[2] K.T. Brinkmann et. al.: Phys. Lett. B 522 (2001) 16

[3] K.M. Watson: Phys. Rev. 88 (1952) 1163

[4] A.B. Migdal: Zh. Eksperim. i Teor. Fiz. 28 (1955) 3

[5] L.D. Faddeev: Soviet Physics JETP 39 (1960) 1459

[6] S. Weinberg: Phys. Rev. 131 (1963) 440

[7] K. Möller et. al.: Z. Physik A 315 (1984) 325

Analysis of Dileptons in Relativistic Heavy-Ion Collisions at CERN-SPS [B]

K. Gallmeister[1], B. Kämpfer, O.P. Pavlenko[2]

Recently, we have proposed [1,2] a unique parameterization of dilepton data in central collisions Pb(158 AGeV) + Au, Pb as measured by the CERES and NA50 collaborations. Our model is based on the "hadron–quark duality" according to which the emission rates of hadron matter and deconfined parton matter are equal at a given temperature. The vector–axial-vector mixing theorem supports this duality: The empirical information on the cross sections of the reaction $e^+e^- \to hadrons$ can be used, within the mixing theorem, to obtain a dilepton emissivity which coincides with the lowest-order $\bar{q}q$ annihilation rate.

In [2] we have shown that also other data, such as from the HELIOS-3, CERES and NA38 collaborations, in the reactions S(200 AGeV) + Au, Pb, W can be well described, too. The outcome is that in these central collisions a thermal source, characterized by a space-time averaged temperature of 170 MeV, is operative. This extracted temperature is in the range of the chiral transition temperature of QCD. The full observed spectrum consists of the thermal component superimposed to hadronic decay contributions (including $\bar{D}D$ decays) and the Drell–Yan yield.

To pursue the approach further and to check the sensitivity of our model to variations of the beam energy, we have analyzed the recent data of the CERES collaboration [3] for central collisions Pb(40 AGeV) + Au. The results are displayed in fig. 1. Adding the thermal source, described by the rate

$$\frac{dN}{d^4Q} = \frac{5\alpha^2}{36\pi^4} N_{\mathrm{dil}} \exp\left\{ -\frac{M_\perp \cosh(Y - Y_{\mathrm{cms}})}{T} \right\},$$

where N_{dil} is a space-time normalization factor, $M_\perp$ denotes the transverse dilepton mass and Y the pair rapidity, with the hadronic decay cocktail and applying the acceptance of the CERES apparatus via Monte Carlo simulations for leptons with four-momentum Q, we reproduce the data by $T = 145$ MeV. This demonstrates the sensitivity of our parameterization and let us interpret T as the physically relevant scale characterizing the average temperature of the produced matter. Interestingly, this temperature parameter agrees with the chemical freeze-out temperature.

As matter of fact we mention that, in the same spirit as the above dilepton spectra at CERN-SPS energies, also BUU calculations of dilepton spectra in heavy-ion collisions in the 1 AGeV range can be parameterized by a formula based on one essential temperature parameter. Relying on the reaction $\pi^+\pi^- \to \rho \to e^+e^-$ with appropriate Breit-Wigner distribution of the ρ form factor, an averaged temperature of 70 MeV is needed to reproduce the BUU results. This finding might be useful in analyzing the forthcoming dilepton spectra from HADES.
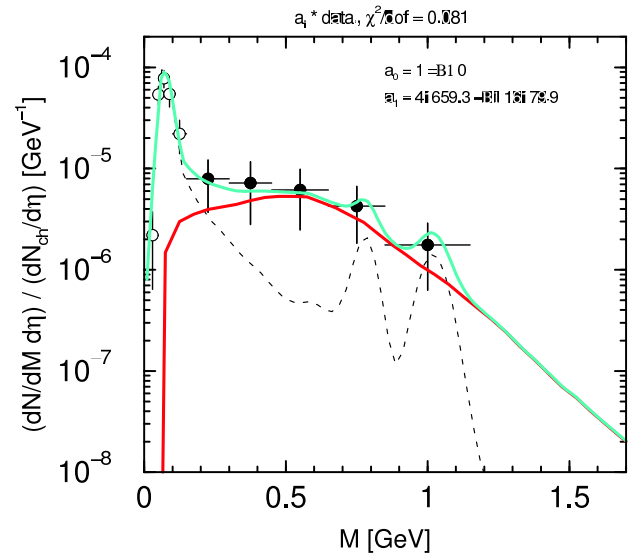
Fig. 1 *Comparison of the CERES data [3] with our model. The fat curve is the thermal contribution, while the thin dotted curve depicts the hadronic cocktail; the uppermost curve is for the sum of these contributions.*

[1] K. Gallmeister, B. Kämpfer, O.P. Pavlenko, Phys. Lett. B 473 (2000) 20
[2] K. Gallmeister, B. Kämpfer, O.P. Pavlenko, C. Gale, Nucl. Phys. A 688 (2001) 939,
     B. Kämpfer, K. Gallmeister, O.P. Pavlenko, C. Gale, Nucl. Phys. A 698 (2002) 424
[3] K. Filimonov et al. (CERES collaboration), nucl-ex/0109017,
     S. Damjanovic et al. (CERES collaboration), nucl-ex/0111009

[1] *Institut für Theoretische Physik, Universität Giessen*
[2] *Institute for Theoretical Physics, Kiev, Ukraine*

Centrality Dependence of Thermal Parameters in Heavy-Ion Collisions at CERN-SPS [B]

J. Cleymans[1], B. Kämpfer, S. Wheaton[1]

The abundances of different hadronic species in the final state of relativistic heavy-ion collisions can be well described by statistical-thermal models. In such a way, the observed multiplicities of a large number of hadrons can be reproduced by a small number of parameters. Such a description can be justified for multiplicities measured over the whole phase-space, since many dynamical effects cancel out in ratios of hadron yields. It is the subject of the present note to pursue this idea and to analyze the centrality dependence of the thermal parameters describing hadron multiplicities. This will provide further information about the effects of the size of the excited strongly interacting system and help in the systematic understanding of the experimental data. We show here that the thermal model is able to describe the available data for various centrality classes at one beam energy.

For not too small number of participants one can use the grand canonical partition function $\mathcal{Z}(V, T, \mu_i) = \mathrm{Tr}[\exp\{-(\hat{H} - \sum_i \mu_i Q_i)/T\}]$, where $\hat{H}$ is the statistical operator of the system, T denotes the temperature, μ_i and Q_i stand for the chemical potentials and corresponding conserved charges; V is the volume. The net-zero strangeness and total electric charge constrain the μ_i. The particle numbers are accordingly $N_i^{\mathrm{prim}} =$

$V(2J_i + 1) \int \frac{d^3 p}{(2\pi)^3} \, dm_i \, \frac{1}{\gamma_s^{-|S_i|} e^{\frac{E_i - \mu_i Q_i}{T}} \pm 1} \mathrm{BW}(m_i)$, where we include phenomenologically a strangeness suppression factor γ_s for hadrons with total strange charge $|S_i|$ to account for incomplete equilibration in this sector; $E_i = \sqrt{\vec{p}^2 + m_i^2}$; BW is the Breit-Wigner distribution. The final particle numbers are $N_i = N_i^{\mathrm{prim}} + \sum_j \mathrm{Br}^{j \to i} N_j^{\mathrm{prim}}$ due to decays of unstable particles with branching ratios $\mathrm{Br}^{j \to i}$.

We have analyzed the NA49 4π multiplicities of $\pi^\pm$, $K^\pm$, N_{part} (taken as sum over all baryons) and $\bar{p}$ [1]. It should be emphasized that protons are not included in our analysis as they due not belong to participants in non-central collisions. Results of our fits are displayed in figs. 1 (upper panel) and 2. The parameters T and $\mu_B \approx 250$ MeV are fairly independent of the centrality, while the strangeness factor γ_s and the size increase significantly with centrality.

Since the number of hadron species to be analyzed is rather small, we use our gained parameters to predict other hadrons, as exhibited in the lower panel in fig. 1. Only for central collisions (bin 1) data from NA49 are at our disposal; they give confidence in the present analysis. For more details consult [2].
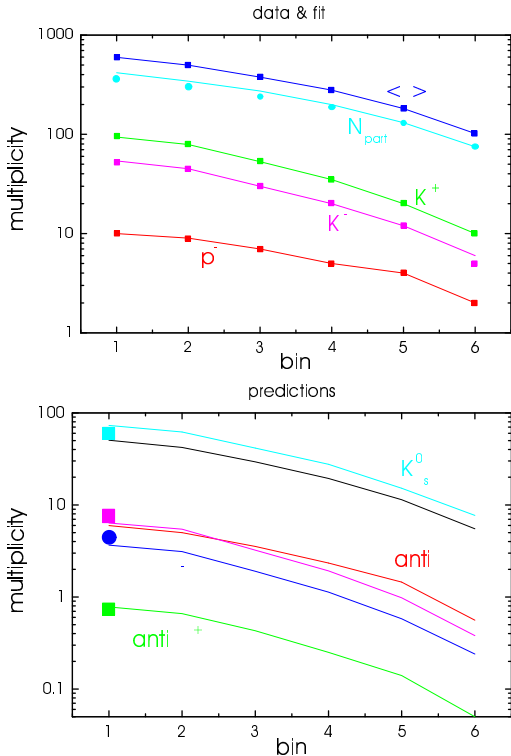
Fig. 1 *Comparison of the data [1] (symbols) with our fits (lines). The impact parameters for bins 1 - 6 are estimated in [1] as 2.2, 4.3, 6.0, 7.4, 8.9, 10.7 fm.*
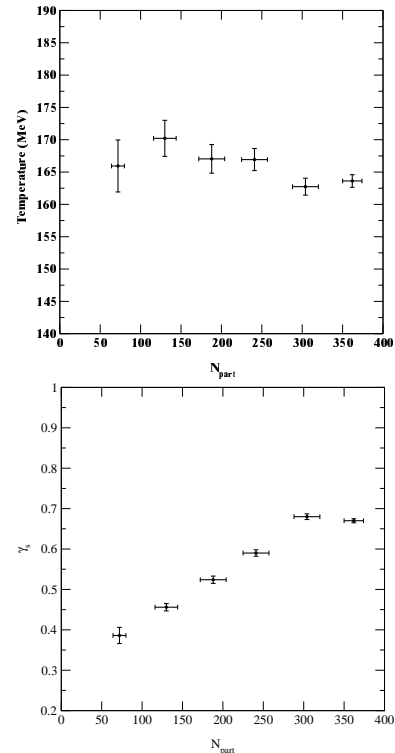
Fig. 2 *The dependence of temperature T (upper panel) and strangeness suppression γ_s (lower panel) on the participant number N_{part}.*

[1] F. Sikler (for the NA49 collaboration), Nucl. Phys. A 661 (1999) 45c
[2] J. Cleymans, B. Kämpfer, S. Wheaton, Phys. Rev. C 65 (2002) 027901

[1] *University of Cape Town, South Africa*

HBT Radii for an Opaque Source at RHIC Energies [B]

H. W. Barz

Recent measurements of the two-pion correlation at the RHIC accelerator at energies of $\sqrt{s_{NN}} = 130$ GeV have revealed surprisingly small values of the of the outward radius compared to the sideward radius of the collision zone for large pair momenta [1]. However as has been shown in ref. [2] the rescattering of the pions make the source opaque and pions only from the surface region can be detected.

To investigate this effect in more detail we use a simple analytical solution which covers the main features of hydrodynamics after freeze-out, namely longitudinal Bjorken scaling and transverse expansion. Pion density and velocity field are given by

$$n(r,\tau) = \frac{\tau_0}{\tau}\frac{R_0^2}{R^2}\frac{1}{\gamma_\perp}\exp\left(-r^2/(2R^2)\right), \qquad (1)$$

$$v_\perp = v_0\frac{r}{R}, \quad R = R_0 + v_0(\tau - \tau_0). \qquad (2)$$

with τ_0 being the emission time and $\gamma_\perp = 1/\sqrt{1 - v_\perp^2}$. The source function $S(\mathbf{K}, x)$ for pions emitted with momentum $\mathbf{K}$ from space-time point x is proportional to the density $n(r,\tau)$ and the Bose-Einstein distribution f_{BE}. Now, opacity is considered by assuming that only those particles can interfere that have not suffered any collision. Therefore the source function is reduced by an absorptive factor:

$$S(\mathbf{K}, x) = n(r,\tau)f_{BE}(K_\mu u_1^\mu) \times \qquad (3)$$

$$\exp\left[-\int\frac{dt'}{\gamma_1}\sum_k\left\langle\sigma_{\pi k}u_{rel}n_k(t',\mathbf{r} + \mathbf{v}_1(t' - t))\right\rangle\right].$$

assuming that the scaterring processes add incoherently. The exponent describes the scattering of the pion on particles of type k of density n_k with cross sections $\sigma_{\pi k}$ times relative flux factors u_{rel} when traversing the expanding and cooling matter with four-velocity u_1. From the source function (3) the correlation function and the HBT radii R_{long}, R_{side} and R_{out} are derived by a standard Hanbury-Brown-Twist (HBT) analysis [3].

We apply the model to the situation of central heavy ion collisions at $\sqrt{s_{NN}} = 130$ GeV RHIC energies. The measured charged particle density dN/dy amounts roughly to 700. In Eq. (3) we take into account the scattering of the pions with themselves, kaons and baryons. The scattering cross sections are obtained essentially from from the s-wave $\pi\pi$ scattering and the ρ, K^* and Δ resonances. In Fig. 1 we show the HBT radii compared with data taken from ref. [1]. As an appropriate break-up configuration we choose $R = 8$ fm, $\tau_0 = 10$ fm/c, $< v_\perp > = 0.5c$ and $T = 150$ MeV. The temperature only marginally

influences the sideward and outward radii. The effect of the rescattering diminishes drastically the ratio of the outward to the sideward radius. A small duration time $\Delta\tau$ of 3 fm/c (dash-dotted lines) is also compatible with the data.
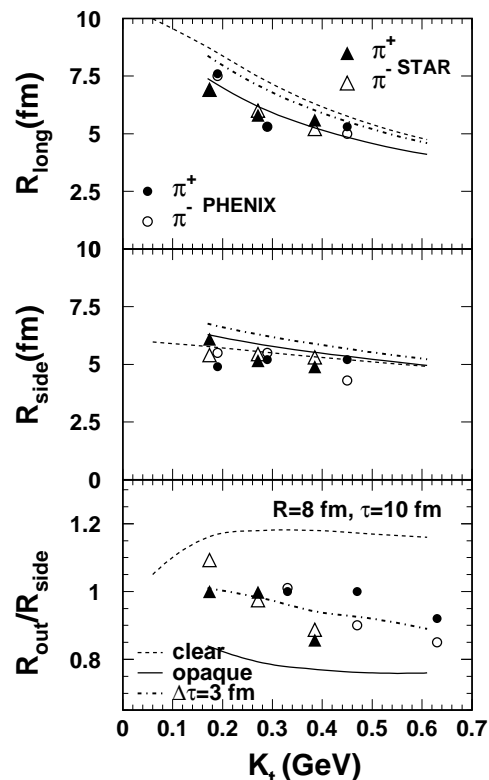
Fig. 1 *HBT radii R_{long}, R_{side} and the ratio R_{out}/R_{side} for central collisions at RHIC energies as a function of the mean pion momentum K_t. The effect of the rescattering is seen comparing the dashed and the full lines.*

The calculations shown here are in contrast to the calculations applying a transport model [4]. In those calculations a large time duration for pion emission of about 15 fm/c has been found. The square of the outward radius R_{out}^2 is given by the average of the space-time emission points $(r_i - v_i t_i)^2$ which provides large values if there is only a weak space-time correlation. Obviously a sufficiently strong correlation is absent in the transport model. In the simple approach considered here the repeated absorption and reemission processes are simulated by an absorption along the straight line trajectories of the pions. An improved treatment is needed to estimate the consequences of the reemission processes.

[1] STAR collaboration, Phys. Rev. Lett. 87 (2001) 082301; PHENIX Collaboration, Nucl. Phys. A 698 (2002) 603
[2] H. Heiselberg, A.P. Visher, Eur. Phys. J. C 1 (1998) 593
[3] G. Bertsch, M. Gong, M. Toyama, Phys. Rev. C 37 (1988) 1896
[4] S. Soff, S. Bass, A. Dimitru, Phys. Rev. Lett. 86, (2001) 3981

Nuclear Physics

The first electron beam to be delivered to users from the radiation source ELBE will be the bremsstrahlung photon beam for nuclear physics experiments. Accordingly many activities of the nuclear physics department concentrated on the completion of the beam line as well as on the preparation of the experimental set-up and data acquisition system. ELBE will provide us with the possibility of measuring the nuclear response in photo reactions with photon energies ranging from below the particle decay thresholds up to the energy region of giant resonances. The investigation of nuclear structure effects in the energy region of reaction channels with particle emission demands an efficient detection system for both photons and particles. It is further extremely important to keep the background radiation level as low as possible. In order to achieve good experimental conditions the following special measures were taken.

The photon collimator is manufactured from high-purity aluminum in order to diminish the neutron production. To minimize photon scattering within the long collimator its hole is conically shaped supposing a geometrical beam transport from the nearly pointlike radiator to the rather extended target. Absorber blocks in front of the collimator aperture facilitate so-called beam hardening i.e. stronger attenuation of the undesired low photon energies. The electron beam dump which is a source of perturbing photon background, is situated outside the experimental cave and is shielded by an iron housing. Further, an additional lead shielding wall was installed in front of the concrete wall between the electron beam dump and the cave. The elements of the photon beam line and the detector supports are made of aluminum and are designed to be as light as possible in order to avoid production and scattering of neutrons. Generally, we attempted to avoid heavy lead detector shielding. Instead, active shields such as escape-suppression shields or electronic vetoes using the beam pulse structure are applied. The entire photon beam line, including the collimator, is evacuated. A special photon beam dump consisting of a large polyethylene block, covered by cadmium foils and lead shielding, was designed for low background contribution. Details of these developments are presented in the first section of this report, which is devoted to the radiation source ELBE.

Recently, in photon scattering experiments on ^{98,100}Mo which were carried out at the DYNA-MITRON in Stuttgart, several strong dipole excitations were observed. These nuclei shall also be studied in our experiments at ELBE, but at higher photon energies. Concerning the photo-induced fission experiments which will be performed at ELBE, three of the 'state of the art' models (i.e. shell-correction, relativistic mean field and Skyrme Hartree Fock methods) were compared with respect to the predicted shapes of very neutron-rich nuclei. It transpires that the different approaches do indeed predict rather different shapes.

The discovery of chiral rotation as a novel feature of spontaneous symmetry breaking in nuclei has attracted public interest. Extensive articles on this phenomenon appeared in "Science", "Physics World" and the scientific part of the German newspaper "FAZ". As a new result in this area a quasi-classical description of the chiral symmetry breaking is presented here.

Using the GASP spectrometer at the Laboratori Nazionali di Legnaro the neutron-rich nuclei ^{90}Y and ^{89,90}Sr have been investigated. Extensive shell model calculations were performed in order to interpret experimental level schemes and transition rates. The proximity to the Z=38 and N=50 shell closures in these nuclei causes a dominance of few-particle excitations and the absence of pronounced collective structures.

Several remarkable experimental achievements were realised by participating in international collaborations. The quadrupole moment of an isomeric state in ^{196}Pb has been measured at the cyclotron in Louvain-la-Neuve by using the newly developed LEMS method. We took part in a series of experiments at the On-Line Mass Separator at GSI exploring the properties of proton-rich nuclei with N≤Z. Such properties are of fundamental importance in the understanding of the astrophysical rp-process and complement those of neutron-rich nuclei.

Collaborations

As in previous years we were substantially benefitting from the successful and permanent cooperation with the spectroscopy groups from the German universities at Stuttgart, Bonn, Köln and Darmstadt as well as with the ISOL group of the GSI Darmstadt. We acknowledge also the fruitful cooperation with the Italian colleagues who were experimenting with us at the GASP spectrometer at Legnaro, with the colleagues from the INRNE and the University of Sofia and from the University of Leuven. Furthermore we are also grateful to the common work done with our colleagues at the University of Tennessee, USA and with the Joint Institute of Nuclear research at Dubna, Russia.

Quasi-Classical Description of the Chiral Rotation

F. Dönau, S. Frauendorf[1], Jing-ye Zhang[2], L.L. Riedinger[2], P.B. Semmes[3]

The Tilted Axis Cranking (TAC) model predicted the possible existence of chiral sister bands in rotating triaxial nuclei as a result of the spontaneous breaking of the chiral symmetry [1, 2]. Indeed candidates for the described structures, i.e. pairs of almost degenerate $\Delta I = 1$ rotational sequences with the same parity, were found in odd-odd N=75 isotones in the A=130 mass region [3-6]. These nuclei satisfy the conditions for the appearance of chiral symmetry breaking as formulated by the TAC model: (i) a triaxial shape of nearly $\gamma \approx 30°$ and (ii) high-j odd quasiparticles which align their angular momenta perpendicular on to each other. In this situation the favored rotational axis of the nucleus is outside of any of the three principal planes of the triaxially deformed density distribution.

Since within the TAC model the angular momentum (a.m.) is only conserved in average it is worthwhile to investigate the chiral symmetry breaking also in models where the angular momentum is treated in a quantum-mechanically correct manner. The quasiparticle plus rotor (PR) models possess the angular momentum I as a good quantum number. This advantage enables one also to account the electromagnetic ($M1$ and $E2$) transition probabilities without problems which is important for the comparison with experimental data. On the other hand, one should note that PR models need to take the deformation and the inertial mass parameters as an empirical input coming e.g. from the TAC model. In practice, the description of chiral bands in terms of the triaxial PR model with two high-j odd quasiparticles [7, 8] turns out to be an extensive diagonalisation problem. The resulting PR wave functions may have thousands of components which makes a physical analysis quite ambiguous. Based on the PR concept we found a much simpler way to understand the dynamics of the chiral rotation when implementing directly also the condition (ii) into the PR Hamiltonian.
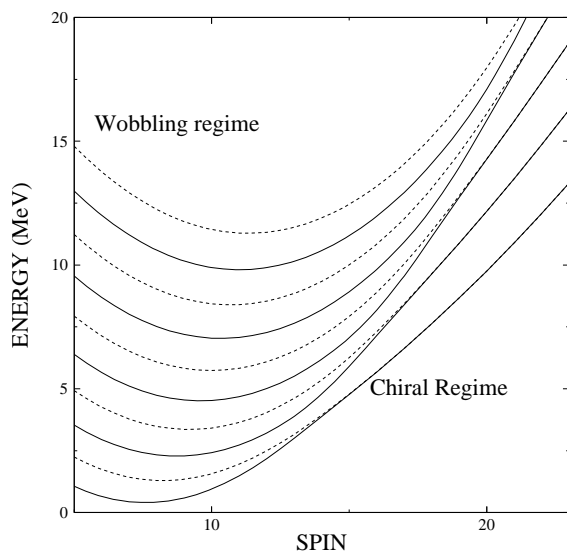
Fig. 1 *Energies E vs. spin I for the lowest ten bands for the frozen alignment model.*

Fig. 2 *B(E2) values $[e^4b^2]$ for the lowest two bands. Solid lines: inband transitions, dashed lines: interband transitions.*

Such a simplified PR version is called below the frozen alignment model. The corresponding PR Hamiltonian considered for the chiral case (i.e. $\gamma = 30°$ triaxility and hydrodynamical values of the moments of inertia [9]) simplifies as follows

$$H = h_{qp} + \frac{\hbar^2}{2\mathcal{J}_c}\left[4(J_1 - j)^2 + J_2^2 + 4(J_3 - j)^2\right], \quad (1)$$

where $J_{k=1,2,3}$ denote the a.m. components along the principal axes (k) and $\mathcal{J}_c$ is the core moment of inertia. In the frozen alignment approximation the quasiparticle angular momenta form a constant vector $\vec{j}_{qp} = (j, 0, j)$

in which the odd quasiparticles contribute the perpendicular components $j_1 = j$ and $j_3 = j$, respectively. Under this assumption the quasiparticle energy h_{qp} becomes a constant. The band energies and B(E2) values obtained with the frozen alignment approximation are shown in Figs. 1,2. We mention that for the lowest bands they almost quantitatively agree with the results of the full PR model. Considering the lowest two bands one notices the formation of the chiral doublets above spin $I = 15\hbar$. Treating the Hamiltonian (1) as classical energy function, $H = E$, and adding the angular momentum conservation as as classical condition, i.e.

[1] *On leave of absence at Department of Physics, University of Notre Dame, USA*
[2] *Department of Physics and Astronomy, University of Tennessee, USA*
[3] *Physics Department, Tennessee Technological University, Cookville, USA*

73

$$J^2 = J_1^2 + J_2^2 + J_3^2 = I(I+1) \qquad (2)$$

one obtains a quasi-classical PR model of the triaxial rotor plus quasiparticle system. There, for given values E and I, the components of the total a.m. vector $\vec{J} = (J_1, J_2, J_3)$ are the unknowns which can be geometrically determined as intersections between the energy surface (1) and a.m. sphere surface (2) which then emerge as closed "orbitals" of the a.m. vector on the sphere (2). In Figs. 3,4 some selected orbitals are shown for two spin values $I = 6\hbar$ and $I = 18\hbar$ taking the quantal energies given in Fig. 1. The energetically lowest orbitals correspond to the smallest enclosed area. Generally, at low spin all those orbitals are centered about the planar a.m. direction defined by the spherical angles $\vartheta = \pi/2$ and $\phi = \pi/4$ measuring these angles with respect to the intermediate and long principal axis, respectively. Above the spin $I = 15\hbar$, where in Fig. 1 the lowest two energy branches do merge, the topological character of the orbitals changes such that one gets two equivalent orbitals centered at $(\vartheta, \phi = \pi/4)$ and $(\pi - \vartheta, \phi = \pi/4)$ with polar angles $\vartheta \neq \pi/2$ thus marking the chiral transition to the aplanar a.m. direction. Obviously, the two equivalent orbitals at ϑ and $\pi - \vartheta$ correspond to the left and right handed configuration of a chiral rotation. The different orbitals at given spin I correspond to the series of bands displayed in Fig. 1. The smallest orbital visualizes the zero-point oscillation of the a.m. vector whereas the excited states belong to the known wobbling excitations of a triaxial system.
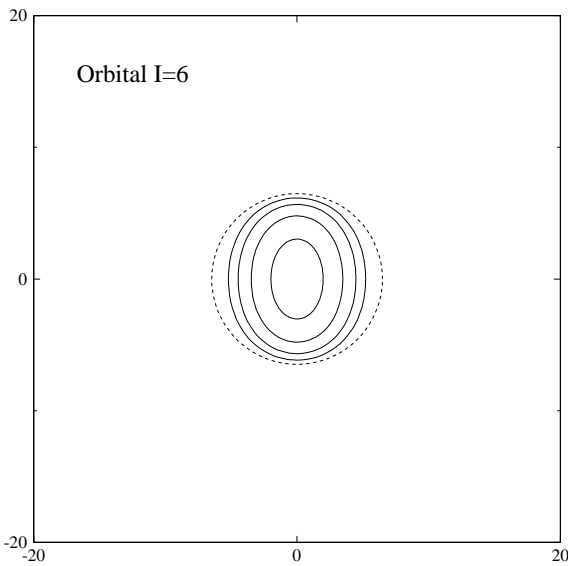
Fig. 3 *Classical orbitals (solid lines) of the a.m. vector for the spin $I = 6\hbar$ seen from the direction $\vartheta = \pi/2$ and $\phi = \pi/4$ defining these angles with respect to the intermediate and long axis, respectively. The a.m.sphere is indicated by a dashed line within the frame with units $\hbar$.*
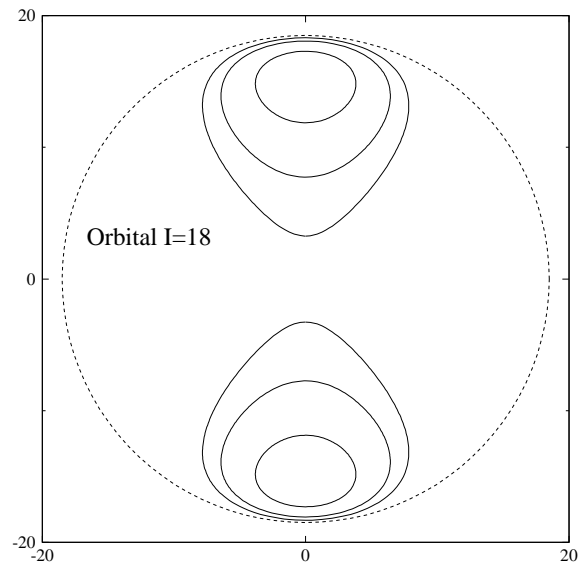
Fig. 4 *Classical orbitals for the spin $I = 18\hbar$ of the lowest six states. Upper and lower part in the a.m.sphere correspond to right and left handed chirality. Notations as in Fig. 3.*

Classically one easily derives for the stretched $E2$ inband transitions a relation $B(E2, I \to I-2) \propto \cos^4(\vartheta)$. Accordingly the $B(E2)$ strength measures the value of the polar angle. In Fig. 2 this $BE2$ strength stays at zero below the critical spin $I = 15\hbar$ in agreement with the orbitals centered at $\vartheta = \pi/2$ for this spin region. Above the value of the polar angle decreases giving rise to steep increase of the $B(E2)$ strength. This finding agrees very well with the result of the full PR calculation. Since such a critical behaviour of the $E2$ strength within the band indicates the transition to chiral rotation it might be taken as a helpful signal in order to identify chiral band structures in experiment.

[1] S. Frauendorf and J. Meng, Nucl. Phys. A617 (1997) 131

[2] V.I. Dimitrov, S. Frauendorf and F. Dönau, Phys. Rev. Lett. 84 (2000) 5732

[3] C.M. Petrache et al., Nucl. Phys. A597 (1996) 106

[4] K. Starosta et al., Phys. Rev. Lett. 86 (2001) 971

[5] R.A. Bark et al. Nucl. Phys. A 691 (2001) 577

[6] D.J. Hartley, L.L. Riedinger, M.A. Riley, D.L. Balabanski, F.G. Kondev, R.W. Laird, J. Pfohl, D.E. Archer, T.B. Brown, R.M. Clark, M. Devlin, P. Fallon, I.M. Hibbert, D.T. Joss, D.R. LaFosse, P.J. Nolan, N.J. O'Brien, E.S. Paul, D.G. Sarantites, R.K. Sheline, S.L. Shepherd, J. Simpson, R. Wadsworth, Jing-ye Zhang, P.B. Semmes and F. Dönau, Phys. Rev. 64 (2001) 031304(R)

[7] S.E. Larsson, G. Leander and I. Ragnarsson, Nucl. Phys. A307 (1978) 189

[8] I. Ragnarsson and P.B. Semmes, Hyp. Int. 43 (1988) 425

[9] A. Bohr and B.M. Mottelson, Nuclear Structure, Vol. 2

Magnetic and Collective Rotation in ^{79}Br [B]

R. Schwengner, F. Dönau, T. Servene, H. Schnare, J. Reif, G. Winter, L. Käubler, H. Prade, S. Skoda[1],
J. Eberth[1], H.G. Thomas[1], F. Becker[1], B. Fiedler[1], S. Freund[1], S. Kasemann[1], T. Steinhardt[1], O. Thelen[1],
T. Härtlein[2], C. Ender[2], F. Köck[2], P. Reiter[2], D. Schwalm[2]

We investigated excited states of the nucleus ^{79}Br via the reaction ^{76}Ge(^{7}Li,4n) at a beam energy of 35 MeV. Coincidence data of emitted γ rays were measured with an arrangement of six EUROBALL CLUSTER detectors. A magnetic dipole ($M1$) band starting with a 15/2$^-$ state at 2.6 MeV known from previous work [1,2] was extended up to $J = (29/2)$ at $E = 6.4$ MeV. Cross-over $E2$ transitions within this band were observed for the first time and mean level lifetimes were deduced using the Doppler-shift-attenuation method. Results of this study were given in Ref. [3] and Refs. therein.

Here we focus on a new interpretation of the $M1$ band in the framework of the hybrid version of the TAC model [4] in connection with the shell-correction method. The equilibrium values for the deformation parameters (ϵ_2, γ) are determined from the minimum in the Total-Routhian Surface (TRS) in conjunction with a stable rotational axis that is in general tilted with respect to the principal deformation axes. The TRS for the lowest-lying three-quasiparticle ($3qp$) configuration, $(\pi g_{9/2})\ \nu(g_{9/2})\ \nu(fp)$, is shown in Fig. 1. The rotational axis is found to be tilted by an angle of $\theta \approx 60°$ relative to the 3-axis within the principal plane (1,3) for the whole frequency range up to $\hbar\omega = 0.7$ MeV. The equilibrium shape is relatively stable in the ranges of $\epsilon_2 = 0.18 - 0.17$ and $\gamma = 27° - 24°$ up to $\hbar\omega = 0.6$ MeV, i.e. the triaxial deformation is important for describing the $M1$ band.

Experimental and calculated $B(M1)$ transition strengths within the $M1$ band are compared in Fig. 2. The experimental strengths are somewhat underestimated by the calculations at low frequencies. However, the TAC model provides a qualitatively reasonable description of the data. We see that the calculated $B(M1)$ strength stays almost constant at a relatively large value over the whole considered frequency range, i.e., it does not show the typical decline with increasing frequency as expected for magnetic rotation. This behaviour displays that the perpendicular coupling of the two $g_{9/2}$ quasiparticles in the configuration $\pi(g_{9/2})\ \nu(g_{9/2})\ \nu(fp)$ can not be realised because of the substantial triaxial deformation of $\gamma > 20°$. Moreover, the collective angular momentum does not have a definite orientation (perpendicular to the symmetry axis) as in an axially symmetric system, because its orientation can change with the spin. For the considered situation all this leads to the resulting constancy of the $B(M1)$ values as well as of the $B(E2)$ values. Based on these properties the $M1$ band in ^{79}Br is considered as a band including components of both, magnetic and collective rotation.
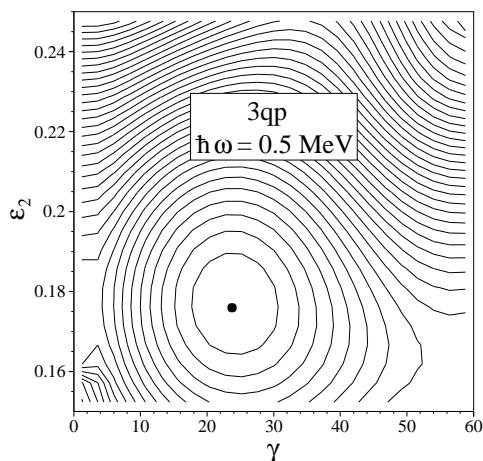
Fig. 1 *Total routhian surface for the 3qp configuration $\pi(g_{9/2})\ \nu(g_{9/2})\ \nu(fp)$ in ^{79}Br as a function of the quadrupole deformation ϵ_2 and the triaxial deformation γ at a rotational frequency of $\hbar\omega = 0.5$ MeV. The distance between the contour lines is 25 keV.*
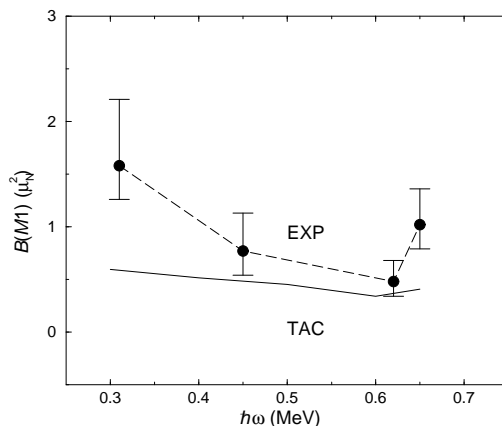
Fig. 2 *Experimental and calculated $B(M1)$ values of the $M1$ band in ^{79}Br as a function of the rotational frequency.*

[1] R. Schwengner et al., Nucl. Phys. A 486 (1988) 43
[2] I. Ray et al., Nucl. Phys. A 646 (1999) 141
[3] T. Servene at al., Annual report 1997, FZR-215 (1998) 50
[4] V.I. Dimitrov, F. Dönau and S. Frauendorf, Phys. Rev. C 62 (2000) 24315

[1] *Institut für Kernphysik, Universität zu Köln, Germany*
[2] *Max-Planck-Institut für Kernphysik, Heidelberg, Germany*

The Quadrupole Moment of the 11^- Intruder Isomer in ^{196}Pb and its Implications for the 16^- Shears-Band Head

K. Vyvey[1], S. Chmel[2], G. Neyens[1], H. Hübel[2], D.L. Balabanski[1], D. Borremans[1], N. Coulier[1], R. Coussement[1], G. Georgiev[1], N. Nenoff[2], S. Pancholi[3], D. Rossbach[2], R. Schwengner, S. Teughels[1], S. Frauendorf[4]

Magnetic rotation, a novel rotational mode in nuclei, occurs in nearly spherical nuclei in contrast to the conventional collective rotation. The nuclear deformation has, however, not been measured very accurately for states of magnetic-dipole (shears) bands. Information about the deformation in such bands can be obtained from both, static and transition quadrupole moments. An accurate determination of transition quadrupole moments from lifetime measurements and intensity branching ratios is difficult, because the $E2$ crossover transitions are very weak as compared to the strong $M1$ transitions in these bands. An alternative is the direct measurement of the spectroscopic quadrupole moments of the band heads, which is, however, also difficult due to the short lifetimes of the states. To overcome this difficulty we tried an indirect approach. It is possible to measure the spectroscopic quadrupole moments of the long-lived states which couple to the configurations of the shears bands. Therefore, we have measured the quadrupole moment of the $\pi(3s_{1/2}^{-2}1h_{9/2}1i_{13/2})11^-$ isomer in ^{196}Pb, which has the same proton configuration as the $\{\pi(3s_{1/2}^{-2}1h_{9/2}1i_{13/2})_{11^-} \otimes \nu(1i_{13/2}^{-2})_{12^+}\}16^-$ shears band head in this nucleus [1, 2]. The quadrupole moment of the $\nu(1i_{13/2}^{-2})12^+$ isomer, which has the same neutron configuration as the 16^- state, has been measured previously [3]. These two quadrupole moments will be used to constrain the parameters of the theoretical description of the shears bands.

The quadrupole moment of the 11^- isomer ($T_{1/2} = 72(4)$ ns) in ^{196}Pb has been measured using the level-mixing spectroscopy (LEMS) method [4]. The experiments were performed at the CYCLONE cyclotron in Louvain-la-Neuve. The ^{196}Pb($I^\pi = 11^-$) isomer was populated in the ^{nat}Re(^{14}N,$5n$) reaction at 87 MeV. The 50 μm thick Re foil served as target, LEMS host, and beam stopper at the same time. The main experimental result of the experiment is the LEMS curve. This curve shows the anisotropy of the γ rays measured at 0° and 90° with respect to the beam axis as a function of the external magnetic field oriented parallel to the beam axis. The LEMS curve is at intermediate strengths of the magnetic field sensitive to the ratio ν_Q/ν_μ of the quadrupole interaction frequency, $\nu_Q = eQV_{ZZ}/h$ and to the magnetic interaction frequency, $\nu_\mu = \mu B/h$, where μ is the magnetic moment of the isomer. If the magnetic moment μ and the electric field gradient V_{ZZ} are known, a value for the quadrupole moment can be extracted [4, 5]. The LEMS curve obtained for the 498 keV transition depopulating the 11^- isomer is shown in Fig. 1. Using the experimental magnetic moment $\mu(11^-) = 10.56(88)\mu_N$ [6], the analysis of this curve results in a quadrupole interaction frequency of $\nu_Q(11^-) = 199(32)$ MHz. A similar analysis for the 12^+ isomer results in $\nu_Q(12^+) = 38(3)$ MHz. The quoted uncertainties include the uncertainties of the corresponding magnetic moments as well. From the ratio $\nu_Q(11^-)/\nu_Q(12^+)$ a value of $Q_s(11^-) = (-)3.41(66)$ b has been extracted. Assuming an axially symmetric deformed nucleus, this value corresponds to a quadrupole deformation of $\beta_2(11^-) = (-)0.156(28)$.

Calculations in the tilted-axis cranking (TAC) model reproduce the experimental quadrupole moments of the 11^- and the 12^+ isomers with deformation parameters of $\beta_2^{\mathrm{TAC}}(11^-) = -0.127$ and $\beta_2^{\mathrm{TAC}}(12^+) = 0.044$, respectively. Using the same model parameter as for the 11^- and 12^+ isomers, the TAC model predicts for the 16^- shears band head a quadrupole moment of $Q_s(16^-) = -1.2$ b, which corresponds to a deformation of $\beta_2 = -0.13$. This indicates that the $M1$ band is, at least near the band head, moderately oblate deformed. The results of this study are published in Ref. [7].
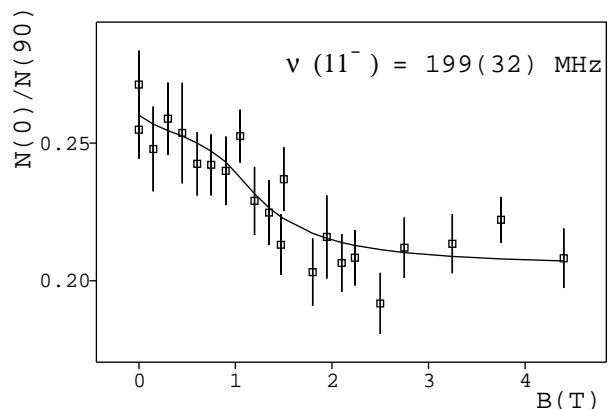
Fig. 1 *LEMS curve obtained for the 498 keV ($E1$, $11^- \rightarrow 12^+$) transition.*

[1] J.R. Hughes et al., Phys. Rev. C 47 (1993) R1337
[2] G. Baldsiefen et al., Z. Phys. A 355 (1996) 337
[3] S. Zywietz et al., Hyperfine Interact. 9 (1981) 109
[4] F. Hardeman et al., Phys. Rev. C 43 (1991) 130
[5] F. Hardeman et al., Hyperfine Interact. 59 (1990) 13
[6] J. Penninga et al., Nucl. Phys. A 471 (1987) 535
[7] K. Vyvey et al., Phys. Rev. Lett. 88 (2002) 102502

[1] *Instituut voor Kern- en Stralingsfysica, University of Leuven, Belgium*
[2] *Institut für Strahlen- und Kernphysik, Universität Bonn*
[3] *Department of Physics and Astrophysics, Delhi University, India*
[4] *On leave of absence at Department of Physics, University of Notre Dame, USA*

A Nuclear Resonance Fluorescence Experiment on ^{98}Mo

G. Rusev[1], R. Schwengner, F. Dönau, L. Käubler, S. N. Mallion, K. D. Schilling, A. Wagner, H. von Garrel[2], U. Kneissl[2], C. Kohstall[2], M. Kreutz[2], H. H. Pitz[2], M. Scheck[2], F. Stedile[2]

We present the results of the first photon-scattering experiment on the nuclide ^{98}Mo. The experiment was performed at the bremsstrahlung facility of the Stuttgart Dynamitron accelerator at an electron energy of 3.8 MeV. A sample of ^{98}Mo was used as a target with a mass of 1998 mg, enriched to 98.55%. The target was combined with 756.7 mg ^{27}Al and 102 mg ^{13}C for photon flux calibration. The scattered photons were detected with three HPGe detectors placed at 90°, 127° and 150°, respectively, to the beam. A part of the spectrum measured at 150° in the energy range from 2800 to 3750 keV is shown in Fig. 1.
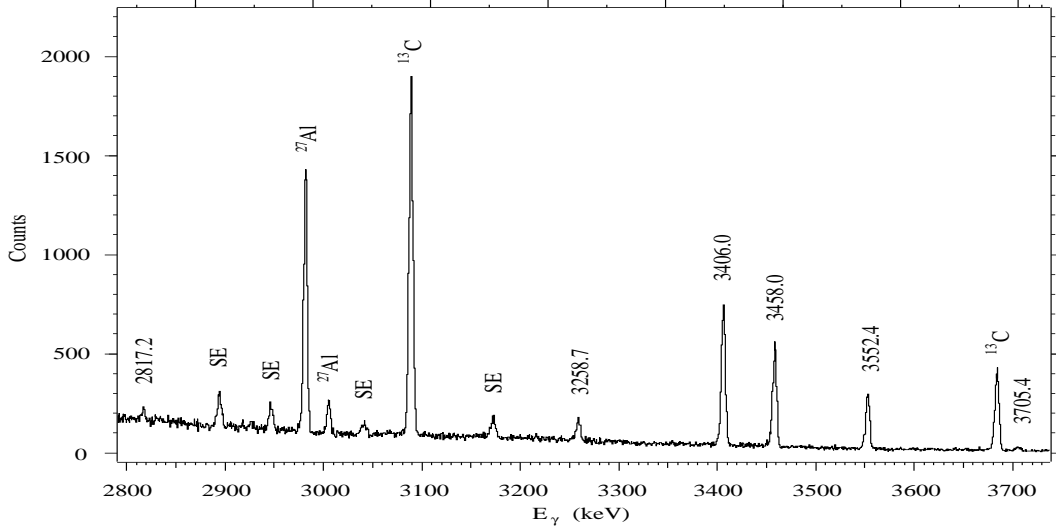
Fig. 1 *Partial photon scattering spectrum from ^{98}Mo at 150° relative to the beam axis. The peaks labelled with their energies in keV correspond to dipole transitions assigned to ^{98}Mo.*

We observed six new transitions in ^{98}Mo with energies marked in Fig. 1. We analysed the angular distribution of the observed transitions by comparing the ratio of the γ-ray intensities observed at 90° and 127° with the expected values for dipole and quadrupole transitions [1]. The ratios shown in Fig. 2 are normalised such that the ratio calculated for the 2981.8 keV transition in ^{27}Al is reproduced.

The state at 2817.2 keV may be a candidate for the $[2^+\otimes 3^-]_{1^-}$ two-phonon excitation while the remaining five states may be considered as $J^\pi=1^+$ states of mixed-symmetry.

The analysis of this experiment is in progress. In addition, we plan a measurement of the linear polarisation of the scattered photons at the Dynamitron to deduce parities of nuclear states, and an experiment at higher electron energies at the ELBE accelerator to investigate nuclear excitations in ^{98}Mo for $E > 4$ MeV.
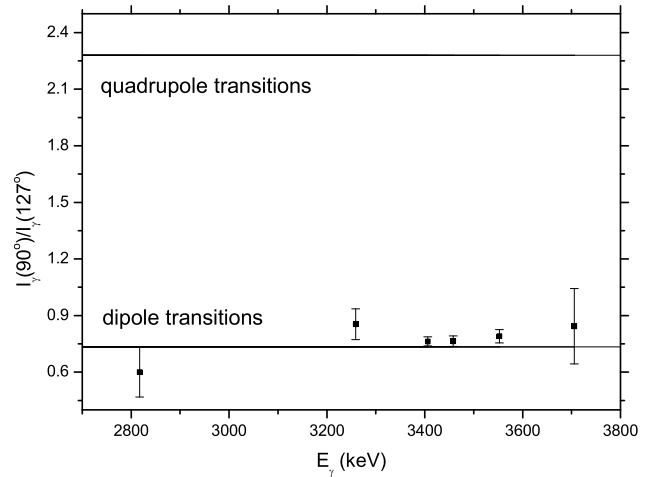
Fig. 2 *Ratio of the γ-ray intensities observed at 90° and 127°. The theoretical values for pure dipole and quadrupole photons scattered from even-even nuclei are 0.734 and 2.28, respectively.*

[1] U. Kneissl, H.H. Pitz and A. Zilges. Prog. Part. Nucl. Phys. 37 (1996) 349

[1] *FZR and INRNE, Sofia, Bulgaria*
[2] *Institut für Strahlenphysik, Universität Stuttgart, Germany*

The Structure of Electric Dipole Excitations in the $N = 50$ Nucleus ^{87}Rb [D,S]

L. Käubler, K.D. Schilling, R. Schwengner, D. Belic[1], P. v. Brentano[2], F. Dönau, C. Fransen[2], M. Grinberg[3],
E. Grosse[4], U. Kneissl[1], C. Kohstall[1], A. Linnemann[2], P. Matschinsky[2], A. Nord[1], N. Pietralla[2], H.H. Pitz[1],
M. Scheck[1], F. Stedile[1], V. Werner[2]

The properties of the semimagic N=50 nuclei between ^{86}Kr (Z=36) and ^{92}Mo (Z=42) are essentially determined by the proton subshell closures at Z=38, 40 and 50 due to the successive filling into the $p_{3/2}$, $p_{1/2}$ and $g_{9/2}$ orbitals, complicating the structure of that nuclei [1]. An important question is whether N=50 core excitations contribute to the structure of low-spin states.

Dipole excitations in the semimagic N=50 nucleus ^{87}Rb were investigated at the Stuttgart Dynamitron facility using bremsstrahlung with an endpoint energy of 4.0 MeV [2]. The observed magnetic dipole excitations are well reproduced in the framework of the shell model [3, 4]. However, these calculations cannot describe the observed strength of the electric dipole excitations from the $3/2^-$ ground state to the $1/2^+$ states at 3060 and 3837 keV, respectively [4].

The weak coupling model is a possible way to describe these $1/2^+$ states in ^{87}Rb [4]. This model may be used, if there is no strong overlap between the coupling particle and the core state. In this sense, the following couplings of protons with the first 2^+ or 3^- states in ^{88}Sr are allowed and enable the generation of electric dipole excitations in ^{87}Rb:

(i) $2^+ \otimes g_{9/2}$ giving a $5/2^+$ state at about 3400 keV,

(ii) $3^- \otimes p_{1/2}$ giving a $5/2^+$ state at about 3600 keV,

(iii) $3^- \otimes p_{3/2}$ giving $3/2^+$ and $5/2^+$ states at about 2700 keV,

(iv) $3^- \otimes f_{5/2}$ giving $1/2^+$, $3/2^+$ and $5/2^+$ states at about 3100 keV. Thereby, the following energies have been used: $E_x(2_1^+,^{88}\text{Sr})$=1836 keV, $E_x(3_1^-,^{88}\text{Sr})$=2734 keV, and the experimental proton single-particle energies $E_x(f_{5/2})$ = 403 keV, $E_x(p_{1/2})$ = 845 keV and $E_x(g_{9/2})$ = 1578 keV observed in ^{87}Rb. Only the coupling (iv) results in an $1/2^+$ state. Therefore, the first $1/2^+$ state at 3060 keV may be tentatively explained by the weak coupling of a proton $f_{5/2}$ hole to the 3^- octupole vibrational state in the core ^{88}Sr, giving a $1/2^+$ state at 3137 keV.

The experimental value $B(E1)\downarrow$=6.2×10^{-4} e^2fm^2 of the 3060 keV g.s. transition in ^{87}Rb agrees approximately with that of the $3_1^- \rightarrow 2_1^+$ transition observed in ^{88}Sr ($B(E1)\downarrow$=7.67×10^{-4} e^2fm^2 [5]). Therefore, we assume that both $E1$ transitions take place between similar configurations.

The experimental $3_1^- \rightarrow 2_1^+$ $B(E1)\downarrow$ value in ^{88}Sr is well reproduced by calculations within the quasiparticle-phonon model (QPM), which is explained in more detail in Ref. [6]. The values $B(E1,3_1^- \rightarrow 2_1^+)$=3.2×10^{-4} e^2fm^2, $E_x(2_1^+,^{88}\text{Sr})$=1852 keV and $E_x(3_1^-,^{88}\text{Sr})$=2640 keV result from this model in good agreement with the experimental values. The QPM wave functions are constructed out of quasiparticle RPA-phonons and the wave function of an excited state is taken as a superposition of one-, two- and three-phonon components. The QPM wave function of the first 2^+ state in ^{88}Sr consists to 91% of the first 2_1^+ RPA phonon, which contains to 11% the two-quasiparticle configuration $\nu(0g_{9/2}1d_{5/2})$. The first 3^- state consists to 92% of the first 3_1^- RPA phonon containing to 8% the two-quasiparticle configuration $\nu(0g_{9/2}0h_{11/2})$. Thus, according to the QPM calculations, the $3_1^- \rightarrow 2_1^+$ $E1$ transition in ^{88}Sr is a $\nu h_{11/2} \rightarrow \nu g_{9/2}$ transition, since it is the only allowed $E1$ transition in the considered configuration space.

Regarding the possible $3^-(^{88}\text{Sr}) \otimes \pi f_{5/2}$ structure of the $1/2^+$ level at 3060 keV in ^{87}Rb, this state should contain also small $\nu h_{11/2}$ components to allow $E1$ transitions to the ground state. The shell model wave function of the $3/2^-$ g.s. in ^{87}Rb contains to 1.3% the configuration $\pi(0f_{5/2}^{-1}1p_{3/2}^{-1}1p_{1/2}^1)\nu(0g_{9/2}^{-1}1d_{5/2}^1)_2$. Thus, $\nu h_{11/2} \rightarrow \nu g_{9/2}$ transitions are possible also for the $1/2^+(3060$ keV) $\rightarrow 3/2^-$g.s. transition in ^{87}Rb, which gives a qualitative explanation for this electric dipole transition as well as for the similarity with the $3_1^- \rightarrow 2_1^+$ transition in ^{88}Sr.

It is well known that strong $E1$ transitions may be realized even by very small admixtures to the wave functions. The above discussion shows that the breakup of the $N = 50$ core and the excitation of one neutron to the $h_{11/2}$ shell are crucial points for the description of electric dipole excitations in the $N = 50$ nucleus ^{87}Rb. The weak coupling of an $f_{5/2}$ proton to the first 3^- state in the $N = 50$ nucleus ^{86}Kr at 3099 keV would give a $1/2^+$ state at about 3500 keV, which could be a possible candidate for the $1/2^+$ state in ^{87}Rb at 3837 keV. Unfortunately, the strength of the $3_1^- \rightarrow 2_1^+$ transition in ^{86}Kr is unknown and the question remains open whether such a weak coupling is able to reproduce the very strong $E1$ excitation to the 3837 keV state in ^{87}Rb.

[1] J. Reif et al., Nucl. Phys. A 620 (1997) 1
[2] L. Käubler et al., Inst. f. Strahlenphysik, Uni Stuttgart, Annual Report (1999) 22
[3] L. Käubler et al., FZ Rossendorf, Wiss.-Tech. Ber. FZR-319 (2001) 79
[4] L. Käubler et al., Phys. Rev. C, in press
[5] H.-W. Müller, Nucl. Data Sheets 54 (1988) 44
[6] M. Grinberg and Ch. Stoyanov, Nucl. Phys. A 573 (1994) 231

[1] Institut für Strahlenphysik, Universität Stuttgart, Germany
[2] Institut für Kernphysik, Universität zu Köln, Germany
[3] Institute of Nuclear Research and Nuclear Energy, Sofia, Bulgaria
[4] also TU Dresden

Structure of Neutron-Rich Nuclei Produced by Photon-Induced Fission

A. Afanasjev[1], V.I. Dimitrov, S. Frauendorf [2]

Understanding the structure of very neutron-rich nuclei is essential for a reliable description of astrophysical processes. Since the relevant nuclei are not experimentally accessible and will not be in near future, the nuclear input into astrophysical calculations relies completely on theoretical extrapolations.
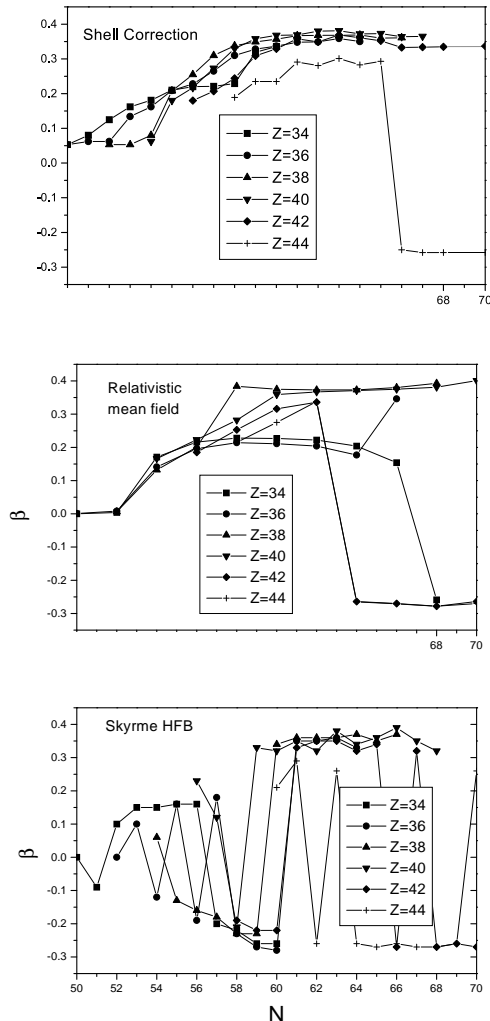
Fig. 1 *Deformation parameter (> 0 prolate, < oblate) as predicted by the three different types of mean field calculations.*

Not only the binding energies, also shapes, pair correlations and other nuclear structure characteristics influence the astrophysical output. Except for very light nuclei, different versions of mean field calculations are used, which substantially differ in their predictions. Fig. 1 shows the deformation parameters predicted by shell-correction method (SCM) [1], the relativistic mean field theory (RMF) [2], and the Skyrme HFB theory (SHF)[3] for nuclei with $Z \approx 38$ and $N \approx 60$. SCM predicts mostly prolate shapes, SHF a pronounced coexistence of prolate and oblate shapes, and RMF lies in between. The new ELBE facility will study these nuclei by means of photon-induced fission. The γ spectroscopy of low spin states will permit discrimination between prolate and oblate shapes. Testing the theoretical models, such experiments will improve the reliability of theoretical predictions for very neutron rich nuclei, where the mutual discrepancies are stronger. The predicted richness of shapes makes the region interesting from the nuclear structure point of view as well. Moreover, the tilted axis cranking calculations [4] that we carried out predict the appearance of triaxial shapes and chirality around $A = 104$.
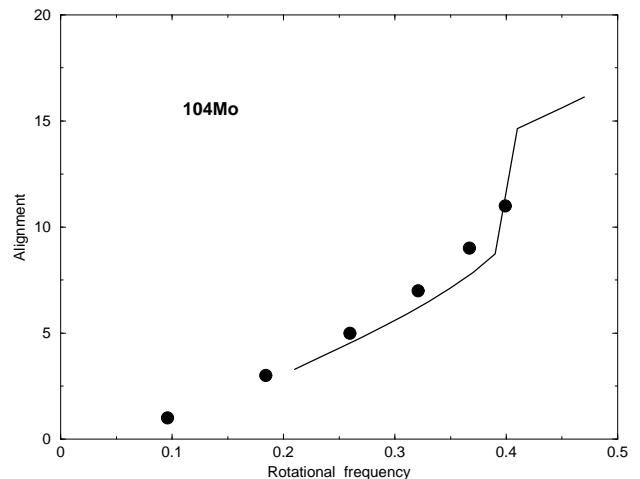
Fig. 2 *Experimental (dots) and calculated (line) angular momentum as functions of the rotational frequency for ^{104}Mo.*

We consider the RMF as most promising for exploring the virgin region of neutron rich nuclei because of its fundamental basis (meson exchange). Using the CRMF [5] code, we calculated the yrast levels for the few nuclei in $Z \approx 38$ and $N \approx 60$ region that have been experimentally studied. Fig. 2 shows that $^{104}_{42}Mo_{62}$, which has a prolate shape, is well reproduced. This indicates that the recently discovered overestimate of the pair correlation by the CRMF [6] is restricted to heavy nuclei. The agreement between the calculated and experimental moments of inertia for $^{108}_{42}Mo_{66}$ is consistent with the predicted oblate shape but does not exclude the prolate alternative. More systematic spectroscopic experiments (in particular for odd mass nuclei) on the ELBE facility will permit more stringent tests of the theory.

[1] P. Moeller et al., Atomic Data Nucl. Data Tables 66 (1997) 131

[2] G. Lalazissis et al., Atomic Data Nucl. Data Tables 71 (1999) 1

[3] S. Goriely et al., Atomic Data Nucl. Data Tables 77 (2001) 311

[4] V. Dimitrov et al., Phys. Rev. Lett. 84 (2000) 5732

[5] A. Afanasjev et al., Nucl. Phys. A608 (1996) 107

[6] A. Afanasjev et al., in preparation

[1] *Department of Physics, University of Notre Dame, Indiana, USA*
[2] *On leave of absence at Department of Physics, University of Notre Dame, Indiana, USA*

Few-Particle Excitations in the $N = 51$ Nucleus ^{90}Y [E,S]

G. Rainovski[1], R. Schwengner, K.D. Schilling, A. Wagner, A. Jungclaus,[2] E. Galindo[3], O. Thelen[4], D.R. Napoli[5], C.A. Ur[6], G. de Angelis[5], M. Axiotis[5], A. Gadea[5], N. Marginean[5], T. Martínez[5], Th. Kröll[6]

Nuclei with few protons above $Z = 38$ and few neutrons above $N = 50$ provide good testing grounds for nuclear models. High-spin states in these nuclei can be generated by aligning the spins of the unpaired particles and by lifting them into orbitals with higher angular momentum. At high spin and high excitation energy, the breakup of the $N = 50$ core contributes considerably to the generation of angular momentum. The study of the odd-odd nucleus ^{90}Y with one proton above the subshell closure at $Z = 38$ and one neutron above the shell closure at $N = 50$ may therefore improve our understanding of the mechanisms of coupling the angular momenta of active nucleons to generate high-spin states.

Excited states in ^{90}Y were populated in the ^{82}Se(^{11}B,3n) reaction at a beam energy of 37 MeV using the XTU tandem accelerator of the Laboratori Nazionali di Legnaro. Gamma rays were detected with the spectrometer GASP [1]. A total of 2.5×10^9 γ-γ coincidence events were sorted off-line into E_γ-E_γ matrices and about 3.8×10^8 γ-γ-γ events into an E_γ-E_γ-E_γ cube.

The level scheme of ^{90}Y resulting from the present experiment is shown in Fig. 1.
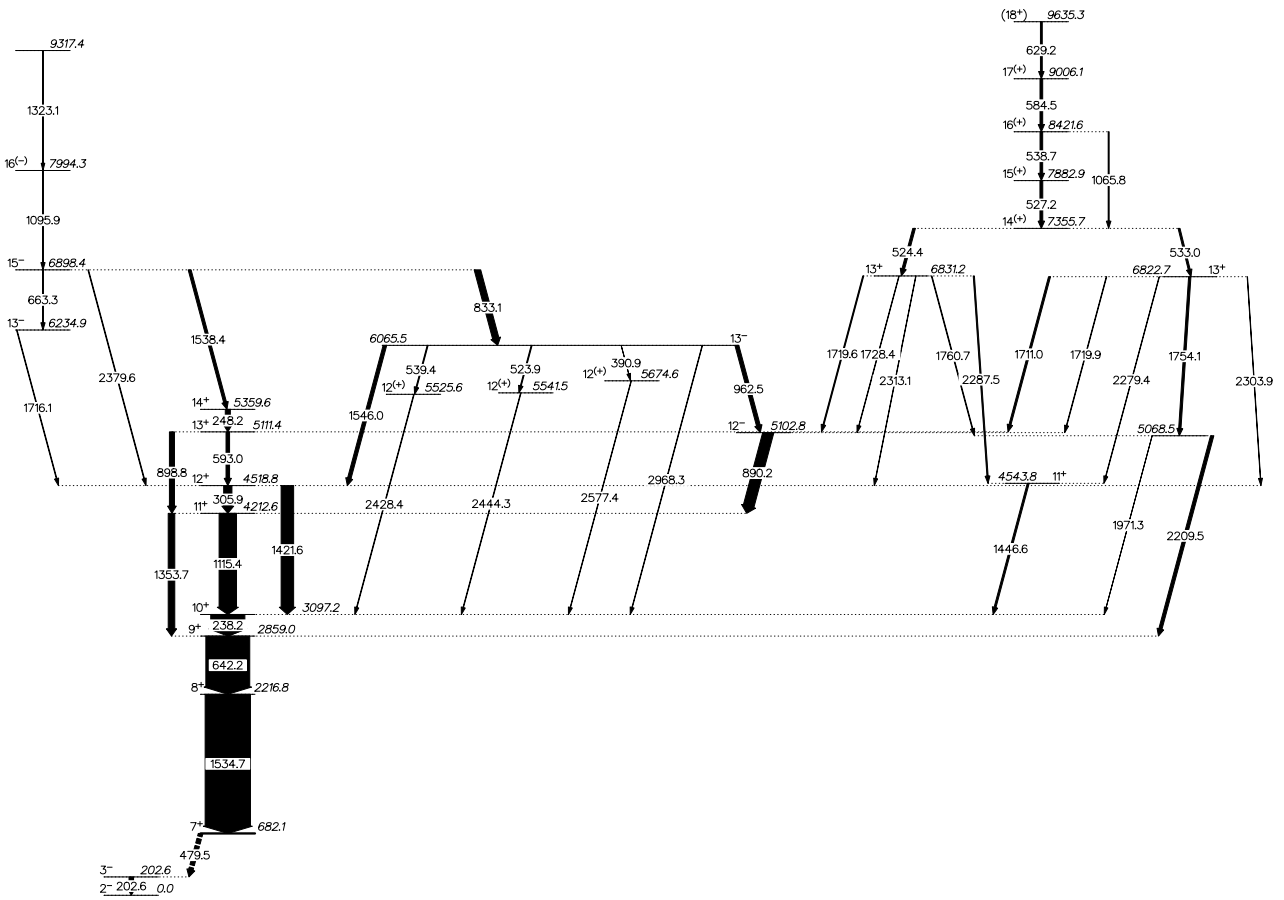
Fig. 1 *Level scheme of ^{90}Y deduced from the present experiment. All states above the 12^+ yrast state have been observed for the first time. The energies of the γ transitions and of the levels are given in keV. Spins and parities in parentheses are assigned tentatively. The thicknesses of the arrows are proportional to the γ-ray intensities.*

[1] *FZR and University of Sofia, Bulgaria*
[2] *Universidad Autónoma de Madrid, Spain*
[3] *Universität Göttingen, Germany*
[4] *Universität zu Köln, Germany*
[5] *INFN, Laboratori Nazionali di Legnaro, Italy*
[6] *INFN and Dipartimento di Fisica dell'Università di Padova, Italy*

All states above the 12^+ yrast state have been observed for the first time. Mean lifetimes of four levels were determined using the method of Doppler-shift attenuation. The results are given in Table 1.

Table 1. Lifetimes of levels in ^{90}Y.

E_i (keV)	E_γ (keV)	τ (ps)
7882.9	527.2	0.16(4)
8421.6	538.7	0.82(11)
9006.1	584.5	0.54(8)
9635.3	629.2	0.55(9)

The errors of the lifetimes include the statistical error, uncertainties of feeding times, feeding intensities and a 10% uncertainty of the nuclear and electronic stopping power.

The structure of ^{90}Y was interpreted in terms of the shell model. The calculations were performed in the model space $\pi(0f_{5/2}, 1p_{3/2}, 1p_{1/2}, 0g_{9/2})$ $\nu(1p_{1/2}, 0g_{9/2}, 1d_{5/2})$ relative to a hypothetic ^{66}Ni core (model space I), and in an extended space (model space II), which includes in addition the $\nu(0g_{7/2})$ orbital while the $\nu(1p_{1/2})$ orbital is not active, i.e., this space is relative to a ^{68}Ni core. The calculations in model space I reproduce the low-lying positive-parity states up to $J^\pi = 9^+$, but neither describe adequately the positive-parity states with higher spin nor the negative-parity states.

Excited states predicted by the calculations in model space II are compared with experimental states in Fig. 2. The calculated states with $J^\pi \geq 9^+$ are generally predicted higher than the experimental ones. The wave functions of the 9^+ to 12^+ states show that the coupling of a $0g_{7/2}$ neutron to states in the $N = 50$ core nucleus ^{89}Y is important.

The experimental positive-parity states with $14 \leq J \leq 18$ form an almost regular sequence including strong $M1$ transitions (cf. Fig. 1). In order to find appropriate shell-model states we combined the lowest states of each spin that reproduce roughly the experimental $M1$ transition strengths. These states are displayed in Fig. 2. The large $B(M1)$ values of 0.2 to 1.3 Weisskopf units within this sequence can be attributed to the excitation of a neutron from the $0g_{9/2}$ to the $0g_{7/2}$ orbital.

The differences between experimental and calculated levels found for ^{90}Y are more pronounced than in our shell-model studies of nuclei with $Z \leq 38$ and $N = 48$

[2,3], $N = 49$ [4,5], $N = 50$ [4,6], and $N = 51$, 52 [7]. Even the description of the $Z = 39$ isotope ^{89}Y with $N = 50$ [8] was more successful. This may suggest that the specific combination of $Z > 38$ and $N > 50$ realised in ^{90}Y needs another set of matrix elements for the effective interactions in order to describe the level structure in such nuclei. To investigate this problem in more detail, further experimental studies of nuclei with $Z \geq 39, N \geq 51$ as well as improved information about empirical effective interactions between the relevant orbitals are needed.
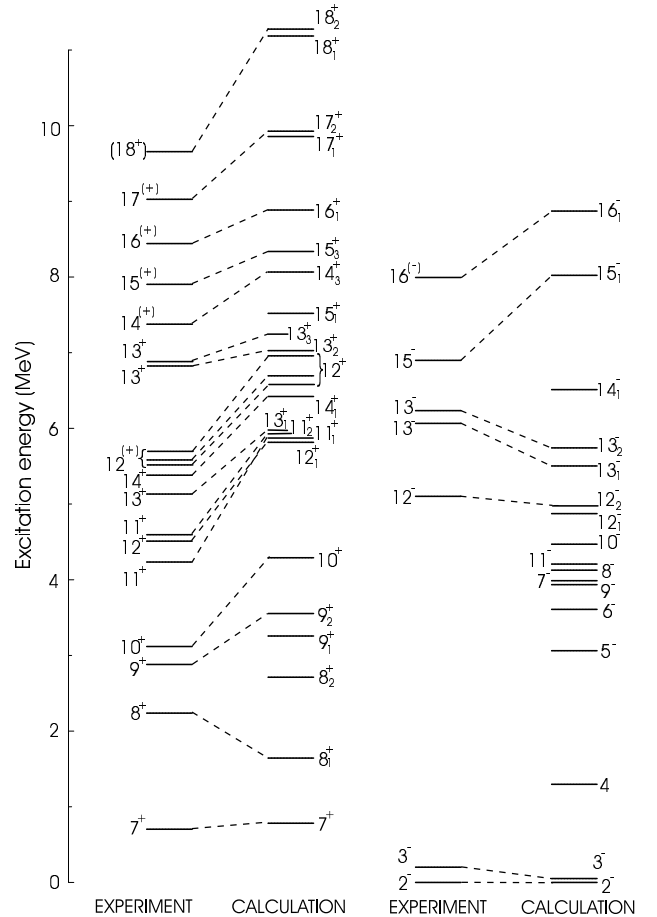
Fig. 2 *Comparison of experimental excitation energies in ^{90}Y with shell-model predictions in model space II, where the $\nu 0g_{7/2}$ orbital is included.*

[1] D. Bazzacco, in *Int. Conf. on Nuclear Structure at High Angular Momentum*, Ottawa 1992, Chalk River Report (AECL 10613) 386
[2] R. Schwengner et al., Nucl. Phys. A 584 (1995) 159
[3] R. Schwengner et al., Phys. Rev. C 57 (1998) 2892
[4] G. Winter et al., Phys. Rev. C 48 (1993) 1010
[5] G. Winter et al., Phys. Rev. C 49 (1994) 2427
[6] E.A. Stefanova et al., Phys. Rev. C 62 (2000) 054314
[7] E.A. Stefanova et al., Phys. Rev. C 63 (2001) 064315
[8] J. Reif et al., Nucl. Phys. A 587 (1995) 449

Structure of the Neutron-Rich Isotopes ^{89}Sr and ^{90}Sr [E,S]

E.A. Stefanova[1], R. Schwengner, G. Rainovski[2], K.D. Schilling, A. Wagner, F. Dönau, E. Galindo[3],
A. Jungclaus[3], K.P. Lieb[3], O. Thelen[4], J. Eberth[4], D.R. Napoli[5], C.A. Ur[6], G. de Angelis[5], M. Axiotis[5],
A. Gadea[5], N. Marginean[5], T. Martínez[5], Th. Kröll[6], T. Kutsarova[1]

The even-even nuclei $^{88-96}$Sr as well as $^{90-98}$Zr form the region of lowest collectivity of known nuclides between ^{56}Ni and the spherical Pb isotopes. These nuclei are therefore of interest for studies of the properties of multi-particle excitations and testing the shell model. Having started with the $N = 50$ nucleus ^{88}Sr [1], we continued our study of Sr isotopes with ^{89}Sr and ^{90}Sr, which have one and two $1d_{5/2}$ neutrons, respectively, outside the shell closure at $N = 50$.

Excited states of ^{89}Sr and ^{90}Sr were populated via the reactions ^{82}Se(^{11}B,$p3n$) and ^{82}Se(^{11}B,$p2n$), respectively, at a beam energy of 37 MeV. The ^{11}B beam was delivered by the XTU tandem accelerator of the Laboratori Nazionali di Legnaro. Gamma rays were detected with the GASP spectrometer [2] consisting of 40 escape-suppressed HPGe detectors and an inner ball containing 80 bismuth germanate elements. A total of 2.5×10^9 prompt $\gamma - \gamma$ coincidence events were recorded in this experiment. As an example, the level scheme of ^{90}Sr deduced from the present study is shown in Fig. 1.
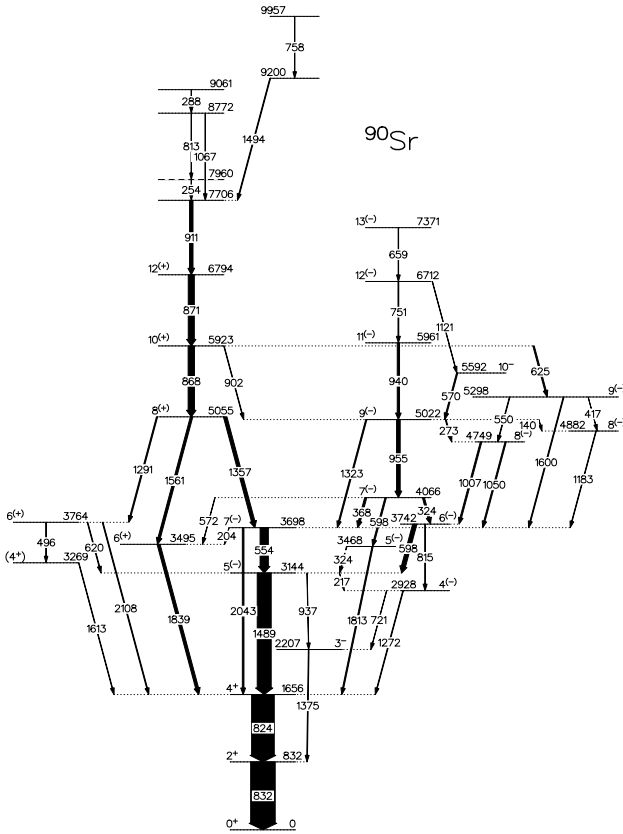
The level structures in ^{89}Sr and ^{90}Sr were interpreted in terms of the shell model. The calculations were performed in the configuration space $\pi(0f_{5/2}, 1p_{3/2}, 1p_{1/2}, 0g_{9/2})$ $\nu(1p_{1/2}, 0g_{9/2}, 1d_{5/2})$. Experimental and calculated level energies in ^{90}Sr are compared in Fig. 2. The calculations give a good overall description of the observed states. A special feature of the structure of ^{90}Sr is the occurrence of an equidistant $\Delta J = 2$ level sequence of 8^+, 10^+ and 12^+ states, which resembles a vibrational-like structure similar to the 0^+, 2^+ and 4^+ states. This sequence above the 8^+ state is described in the calculations by the configuration $\pi[(0f_{5/2}^{-2})(0g_{9/2}^2)]\nu(1d_{5/2}^2)$ that energetically favours even spins (cf. Fig. 2). The results of this study have been published in Ref. [3].

Fig. 1 *Level scheme of ^{90}Sr deduced from the present study.*
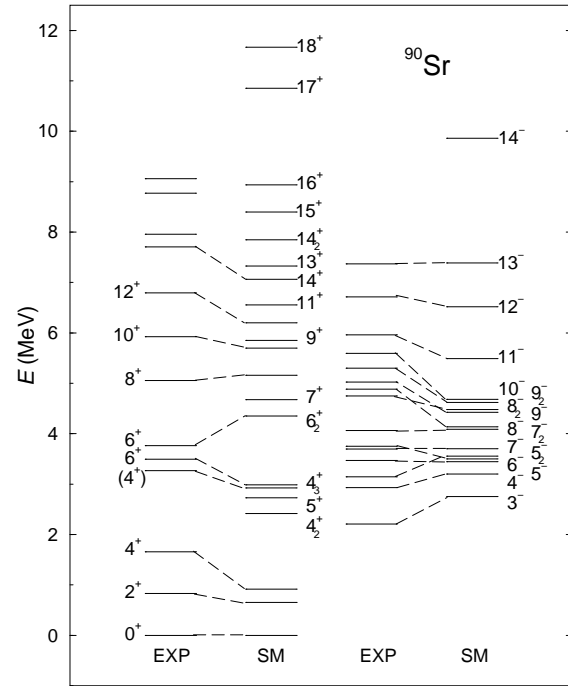
Fig. 2 *Comparison of experimental with calculated level energies in ^{90}Sr.*

[1] E.A. Stefanova et al., Phys. Rev. C 62 (2000) 054314

[2] D. Bazzacco, in *Int. Conf. on Nuclear Structure at High Angular Momentum*, Ottawa 1992, Chalk River Report (AECL 10613) 386

[3] E.A. Stefanova et al., Phys. Rev. C 63 (2001) 064315

[1]*FZR and INRNE Sofia, Bulgaria*
[2]*FZR and University of Sofia, Bulgaria*
[3]*Universität Göttingen, Germany*
[4]*Universität zu Köln, Germany*
[5]*INFN, Laboratori Nazionali di Legnaro, Italy*
[6]*INFN and Dipartimento di Fisica dell'Università di Padova, Italy*

First Measurement of β-Decay Properties of the Proton Drip-Line Nucleus ^{60}Ga

C. Mazzocchi[1][2], Z. Janas[1][3], J. Döring[1], M. Axiotis[4], L. Batist[5], R. Borcea[1], D. Cano-Ott[6] E. Caurier[7], G. de Angelis[4], E. Farnea[4], A. Fassbender[1], A. Gadea[4], H. Grawe[1], A. Jungclaus[8] M. Kapica[1], R. Kirchner[1], J. Kurcewicz[1], S.M. Lenzi[9], T. Martínez[4], I. Mukha[1], E. Nácher[10], D.R. Napoli[4], E. Roeckl[1], B. Rubio[10], R. Schwengner, J.L. Tain[10], C.A. Ur[9]

The decay properties of $N = Z - 2$ ($T_Z = -1$) odd-odd nuclei in the pf shell are of special interest for many disciplines as (i) nuclear-structure physics, where effects related to the occupation of identical orbits by neutrons and protons in the vicinity of the proton drip-line may be studied, (ii) fundamental physics, where the standard model of weak interaction may be tested by precision measurements of superallowed $0^+ \rightarrow 0^+\beta$-decays, and (iii) astrophysics, for which the understanding of processes like electron-capture cooling of supernovae or the astrophysical rp-process is crucial.

We have studied the decay-properties of the $T_Z = -1$ nucleus ^{60}Ga for the first time. ^{60}Ga nuclei were produced in the ^{28}Si(^{36}Ar,$p3n$) fusion-evaporation reaction, induced by a 4.71 MeV·A, 85 particle-nA ^{36}Ar beam impinging on a natural-silicon target. The targets of thicknesses ranging from 2.1 to 2.5 mg/cm^2 in the various measurements were mounted close to the ion source of the GSI On-Line Mass Separator in two separate experiments which are described in detail in Ref. [1]:

1) A FEBIAD-E [2] ion source was used, which yielded a mass-separated beam intensity of 1.8 ions/s for ^{60}Ga, based on the decay data obtained in this work. The A = 60 beam contained, however, strong isobaric contaminants of ^{60}Cu ($T_{1/2} = 23.7$ min) and ^{60}Zn ($T_{1/2} = 2.38$ min).

2) A TIS [2,3] ion source was employed to strongly suppress the A = 60 contaminants compared to the values obtained during experiment 1. A suppression factor of 700 for the strongest contaminant ^{60}Cu and an even larger one for ^{60}Zn were reached, while the separation efficiency for ^{60}Ga was reduced by only a factor of 6 ($\approx$ 5% with TIS compared to $\approx$ 30% with FEBIAD).

Using various set-ups, we measured β-delayed γ rays and protons. As a result of the measurement of $\beta\gamma$ coincidences, the decay scheme of ^{60}Zn following the β decay of ^{60}Ga has been deduced as shown in Fig. 1. The γ rays at 1555, 2293 and 2559 keV have been newly assigned to the decay of ^{60}Ga and led us to establish a level at 2559 keV with a tentative spin and parity assignment of (2^+). This (2_2^+) state is about 400 keV higher than the corresponding state in ^{62}Zn and in heavier even-even isotopes.

From a semi-empirical Coulomb-energy estimate, a proton separation energy of $S_p = 40(70)$ keV was deduced for ^{60}Ga. As this is compatible with zero, ^{60}Ga can indeed be considered to be a proton drip-line nucleus. The S_p values of neutron-deficient gallium isotopes are of crucial importance for the rp-process as they determine at which zinc isotope (i) a captured proton is not removed right away by strong photodisintegration of the weakly proton-bound gallium isotone and (ii) the rp-process can proceed to heavier elements via fast proton captures. In particular, they determine to which degree the β-decay of the potential long-lived waiting-point nucleus ^{60}Zn can be bypassed by proton captures on ^{59}Zn or ^{60}Zn. Recent calculations [4] assuming an S_p value of 30(150) keV [5] for ^{60}Ga in agreement with the result obtained in this work have shown that only a small fraction of 10^{-4} [6] of the rp-process flow runs through ^{60}Ga, while its dominant part involves the β-decay of ^{59}Zn. This is is due to the small S_p value of ^{60}Ga.

The results of this work have been published in Ref. [1].
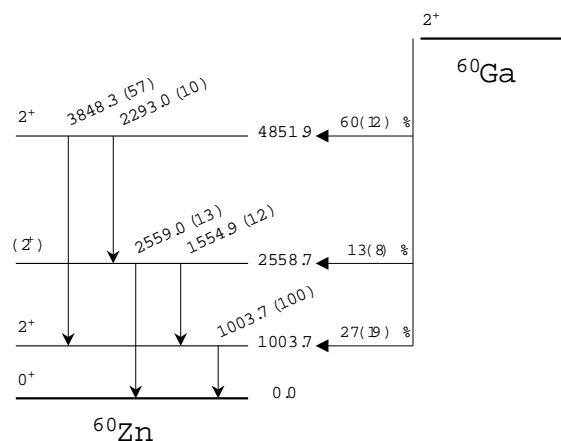
Fig. 1 *Level scheme of ^{60}Zn following the decay of ^{60}Ga as obtained in the present work.*

[1] C. Mazzocchi et al., Eur. Phys. J. A 12 (2001) 269
[2] R. Kirchner et al., Nucl. Instr. Meth. 186 (1981) 295
[3] R. Kirchner, Nucl. Instr. Meth. A 292 (1990) 203
[4] H. Schatz et al., Phys. Rev. Lett. 86 (2001) 3471
[5] G. Audi et al., Nucl. Phys. A 624 (1997) 1

[1] *GSI, Darmstadt, Germany*
[2] *Università degli Studi di Milano, Italy*
[3] *University of Warsaw, Poland*
[4] *INFN, Laboratori Nazionali di Legnaro, Italy*
[5] *St. Petersburg Nuclear Physics Institute, Gatchina, Russia*
[6] *CIEMAT, Department of Nuclear Fission, Madrid, Spain*
[7] *Institut de Recherches Subatomiques, Strasbourg, France*
[8] *Departamento de Fisica Teórica, Universidad Autónoma de Madrid, Spain*
[9] *INFN and Dipartimento di Fisica dell'Università di Padova, Italy*
[10] *Instituto de Fisica Corpuscular, CSIC-Universidad de Valencia, Spain*

Beta-Decay Study of the Self-Conjugate Odd-Odd Nuclei ^{62}Ga and ^{70}Br

J. Döring[1], C. Plettner[1], M. Axiotis[2], R. Borcea[1], J. Eberth[3], A. Gadea[2], M. Górska[1], H. Grawe[1], Z. Janas[14], R. Kirchner[1], M. La Commara[1], C. Mazzocchi[15], E. Nácher González[1], A. Płochocki[4], E. Roeckl[1], K. Schmidt[1], R. Schwengner, T. Steinhardt[3], J. Zylicz[4]

Nuclei in the mass 70 region exhibit a variety of nuclear structure effects such as rapid shape changes and shape coexistence. Whereas the nuclei around the doubly-magic nucleus ^{56}Ni are considered to be spherical in shape, oblate-deformed ground states have been found in a region around ^{69}Se ($Z = 34$) [1], and prolate-deformed ground states in the proton-rich Sr ($Z = 38$) isotopes [2]. The deformed shapes are well-stabilized by the competing $Z = 34$, 36, and 38 gaps in the single-particle energies. To explore the evolution of the nuclear shape along the $N = Z$ line and their influence on the competition of $T = 0$ and $T = 1$ isospins in odd-odd nuclei, the β-delayed γ-ray emission of the self-conjugate nuclei ^{62}Ga and ^{70}Br has been investigated. The measurements were performed at the On-line Mass Separator of GSI Darmstadt. Experimental details were reported earlier [3], and preliminary results of the data analysis have been communicated at several conferences [4, 5].

In the experiment on the β^+ decay of ^{62}Ga, an intense 511 keV annihilation peak originating from the $0^+ \to 0^+$ Fermi ground-state decay [6] and the much weaker 954 keV $2^+ \to 0^+$ yrast transition in ^{62}Zn have been identified as is shown in Fig. 1. If a coincidence gate is set on this 954 keV line, weak γ transitions at 1388 and 2225 keV show up. Thus, the transitions may depopulate levels at 2342 and 3179 keV in ^{62}Zn. From a previous (p, t) reaction study [7], levels at 2330 (0^+) and 3160 keV (2^+) are known in ^{62}Zn which are close in energy to the levels populated in β decay. However, due to limited statistics, no reliable half-life for the β-delayed 954 keV γ ray could be deduced.

The occurrence of the 954, 1388, and 2225 keV transitions can result from two different scenarios: (i) from the β decay of a low-lying isomeric state in ^{62}Ga or (ii) from a non-analog decay branch of the 0^+ ground state in ^{62}Ga to higher-lying 0^+ and/or 1^+ states in ^{62}Zn which are deexcited by the emission of γ rays. If we assume that the observed 954 keV line intensity results from a non-analog decay branch, then a branching ratio of $(0.106 \pm 0.017)\%$ can be estimated. This ratio agrees quite well with a previously reported value of $(0.120 \pm 0.021)\%$ [8]. Since almost the same ratio has been obtained in two very different measurements, the interpretation as a non-analog branch is favoured.

In the study of the lightest proton-bound bromine isotope, ^{70}Br, extensive β-γ-γ coincidences were measured [3, 4, 5] for the decay of the known $T_{1/2} = 2.2(2)$ s isomer [9]. The analysis reveals a complex decay scheme with about 74% of the β feeding populating the 4606 keV level in ^{70}Se which is known as a (8,9$^+$) state from

previous in-beam work [10]. This level was found to be depopulated by transitions of 569.0 and 690.2 keV. However, we observe additional γ rays of 958 and 1604 keV which link this level further to the yrast 6^+ and the 6_2^+ states in ^{70}Se, and thus restrict spin and parity to $I^\pi = 8^+$. Furthermore, the yrast sequence in ^{70}Se has been observed up to the 10^+ state at 5207 keV for the first time in β decay. The deduced apparent β feeding of the 10^+ level is about 1.2(2)%. Thus, the β-decaying isomeric state in ^{70}Br must have a high spin, and we propose spin and parity of 9^+, the only assignment being consistent with all experimental results. The high spin of the isomer is interpreted as arising from the Nilsson configuration ($\pi 9/2^+[404]$, $\nu 9/2^+[404]$) at an oblate deformation of $\beta_2 \approx -0.3$. Our findings are in agreement with conclusions drawn from another experiment [11] where also a 9^+ assignment is proposed. However, this is at variance with the earlier assignment of 5^+ given by the same group [12].
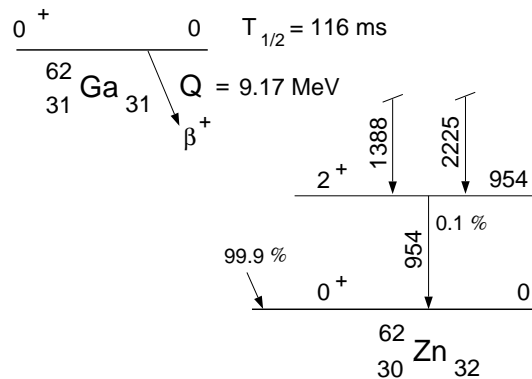
Fig. 1 *Beta decay of the self-conjugate nucleus ^{62}Ga.*

[1] M. Wiosna et al., Phys. Lett. B 200 (1988) 255

[2] C.J. Lister et al., Phys. Rev. Lett. 49 (1982) 308

[3] J. Döring et al., GSI Scientific Report 2000, 14

[4] E. Roeckl et al., Nucl. Phys. A (in press).

[5] J. Döring et al., Proc. Int. Workshop Pingst2000, Lund Uni., Sweden, LUIP 0003 (2000) 131

[6] C.N. Davids et al., Phys. Rev. C 19 (1979) 1463

[7] R.A. Hinrichs et al., Phys. Rev. C 10 (1974) 1381

[8] B.C. Hyman et al., Cyclotrone Inst., Texas A&M Univ., Progress in Research (1999) I-28

[9] B. Vosicki et al., Nucl. Instrum. Meth. 186 (1981) 307

[10] T. Mylaeus et al., J. Phys. G 15 (1989) L135

[11] A. Piechaczek et al., Phys. Rev. C 62 (2000) 054317

[12] A. Piechaczek et al., Proc. Conf. on Perspectives in Nucl. Phys., World Scientific, Singapore (1999) 201

[1]*GSI, Darmstadt, Germany*
[2]*INFN, Laboratori Nazionali di Legnaro, Italy*
[3]*Institut für Kernphysik, Universität zu Köln, Germany*
[4]*University of Warsaw, Poland*
[5]*Università degli Studi di Milano, Italy*

Beta Decay of ^{56}Cu

R. Borcea[1], J. Äystö[2], E. Caurier[3], P. Dendooven[2], J. Döring[1], M. Gierlik[4], M. Górska[1], H. Grawe[1],
M. Hellström[1], Z. Janas[4], A. Jokinen[2], M. Karny[4], R. Kirchner[1], M. La Commara[1], K. Langanke[5],
G. Martínez-Pinedo[5], P. Mayet[1], A. Nieminen[2], F. Nowacki[6], H. Penttilä[2], A. Płochocki[4], M. Rejmund[1],
E. Roeckl[1], C. Schlegel[1], K. Schmidt[1], R. Schwengner, M. Sawicka[4]

Beta-decay studies of proton-rich isotopes near the doubly closed-shell nucleus ^{56}Ni are of interest as (i) nuclei with a few nucleons outside a doubly-magic core are expected to represent comparatively simple configurations and thus be useful for testing nuclear shell-model predictions, and (ii) the large decay-energy window permits to experimentally access a sizeable fraction of the strength of the allowed β decay. Moreover, nuclear-structure properties of proton-rich $N \approx Z$ isotopes are of astrophysical interest.

The β decay of ^{56}Cu was studied at the GSI On-line Mass Separator by using a 5.5 MeV·A ^{32}S beam of the UNILAC to induce ^{28}Si(^{32}S,$p3n$)^{56}Cu fusion-evaporation reactions. The reaction products were stopped in a catcher inside an ion source, released as singly-charged ions, accelerated to 55 keV and mass-separated in a magnetic field. The $A = 56$ beam was implanted into a movable tape and investigated by means of a β-γ-γ detector array consisting of a plastic scintillator and two composite high-purity germanium detectors. The ^{56}Cu decay to the doubly-magic nucleus ^{56}Ni was investigated for the first time at the On-line Mass Separator in 1996 [1]. At that time, four γ transitions were observed, corresponding to the β feedings of three excited ^{56}Ni states, and a half-life of (78 ± 15) ms was determined. In the present experiment [2], the quality of the data was considerably improved due to the more efficient detector set-up and a longer measurement time. In particular it was possible to observe β-gated γ-γ coincidences. Six γ transitions were identified in addition to the four known ones. Three states were added to the level scheme of ^{56}Ni, and the half-life was determined more accurately to be (93 ± 3) ms. The level scheme of ^{56}Ni following the decay of ^{56}Cu as deduced from the present experiment is shown in Fig. 1.

By using the newly established level scheme and the half-life, β feedings and reduced Gamow-Teller transition probabilities (B(GT)) were deduced with higher accuracy. The experimental B(GT) values were confronted with predictions of five different shell-model calculations. It was found that the experimental GT-strength distribution over states in ^{56}Ni between 3.9 and 6.6 MeV qualitatively agrees with the predictions (see [2]). We consider this to be a valuable test of shell-model calculations, including their ability to predict the higher-lying GT strength reliably. Moreover, the identification of hitherto unobserved low-spin states in ^{56}Ni is important for a further improvement of data from in-beam spectroscopy as well as for further tests of nuclear models. Finally, it was shown [2] that the new experimental data do not imply a revision of the calculated stellar weak-interaction rates of $A = 56$ nuclei [3].
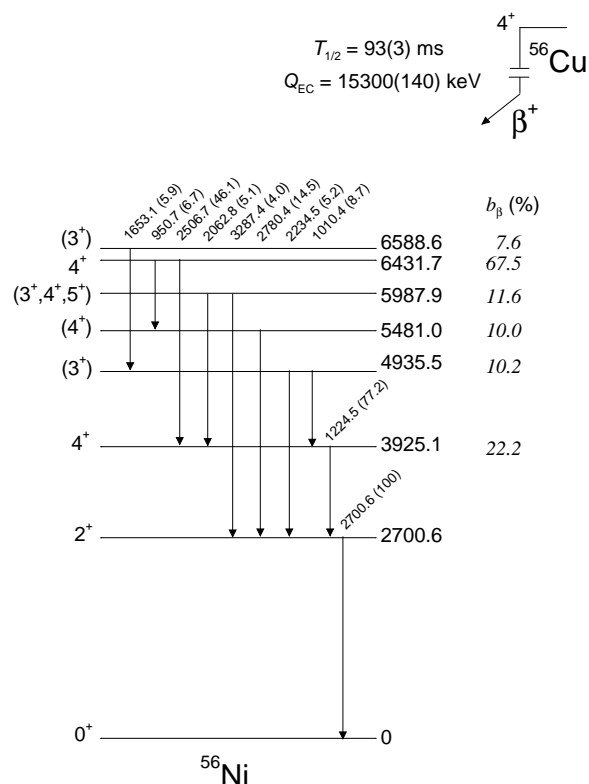
Fig. 1 *Level scheme of ^{56}Ni following the decay of ^{56}Cu as obtained in the present work.*

[1] M. Ramdhane et al., Phys. Lett. B 432 (1998) 22
[2] R. Borcea et al., Nucl. Phys. A 695 (2001) 69
[3] K. Langanke and G. Martinez-Pinedo, Nucl. Phys. A 673 (2000) 481

[1] *GSI, Darmstadt, Germany*
[2] *University of Jyväskylä, Finland*
[3] *Institut de Recherches Subatomiques, Strasbourg, France*
[4] *Institute of Experimental Physics, University of Warsaw, Poland*
[5] *Institut for Fysik og Astronomi, Aarhus Universitet, Denmark*
[6] *Laboratoire de Physique Théorique de Strasbourg, France*

Biomedical Research

The research of the institute on the application of radiation and nuclear physics techniques to the fields of biology and medicine concentrates on two topics: Cell radiobiology with quasi-monochromatic X-rays and positron emission tomography (PET) for quality assurance of charged hadron tumour therapy.

While the PET-method is in routine clinical operation at the experimental heavy ion therapy facility at GSI Darmstadt, the radiobiology equipment at the radiation source ELBE is under preparation. The first research activity will be aimed at measurements of the relative biological effectiveness (RBE) for photon energies between 10 and 100 keV. Since such X-rays are widely used in diagnostic radiology (e. g. mammography) and since it has been recently shown by means of soft X-ray tubes that the RBE for cell death as well as for the induction of genomic defects is photon energy dependent, a precise knowledge of these RBE values is highly desirable for radiation protection purposes. Furthermore, these data are relevant for treatment planning in radionuclide or brachytherapy, if isotopes emitting low-energy photons or the recently developed miniature X-ray tubes are applied. In a common project together with the Institute of Bioinorganic and Radiopharmaceutical Chemistry of the FZR the energy dependent increase of the RBE of photons caused by the accumulation of molecules containing atoms of high atomic number within the radiation sensitive structures of the cells will be investigated. The basis for this research are quasi-monochromatic X-rays which will be produced at ELBE by means of channeling relativistic electrons through crystalline matter (diamond). The preparations of radiobiological experiments at ELBE comprised in 2001:

- *the completion of a cell culture laboratory in the ELBE building;*
- *experiments on the determination of RBE of photons from conventional soft X-ray tubes;*
- *on-line dosimetry at well as off-line dose measurements in volumes of subcellular scale;*
- *the design of an X-ray monochromator of highly oriented pyrolythic graphite;*
- *radiation transport calculations with special emphasis to radiation protection and experimental setups at the ELBE source as well as to the dosimetry in subcellular structures. Furthermore, these methods have been applied to the design of an industrial facility for product irradiations (polymer cross linking and sterilization of medical disposals).*

The department supplies the service of quality assurance of heavy ion tumour therapy by means of PET for the German Heavy Ion Therapy Project. In 2001 during 3 therapy beam times 39 patients have been treated, 35 of them with head and neck tumours, and, as a new development, 4 patients suffering from chordoma in the pelvic region. 23 patients were exclusively treated with ^{12}C ion beams, whereas to 16 patients a combined photon/carbon treatment was applied. Considering the irradiations within the pelvic region it is interesting to note that, despite of the high γ-ray attenuation, PET images of good quality could be taken with sufficient significance for reliable particle range and field position determination. For a total number of 1419 treatment fractions PET data have been acquired. As a result of the recent improvements of the physical beam model, which has been mainly induced by PET observations, the particle range for head and neck irradiations is precisely predicted by the treatment planning. Therefore, the PET data evaluation is increasingly focused onto the quantification of local deviations between planned and applied dose. Such deviations are caused by slight patient mispositioning or, even more important, by local changes of the tissue density distribution. The tomographic reconstruction was considerably improved by integrating a scatter correction into the iterative algorithm. Further research activities on PET are aimed at the development of an improved in-beam positron camera for the large clinical charged hadron therapy facility at Heidelberg, whose construction will be started in the year 2002. They comprise:

-   the design of a large solid angle positron camera in combination with a rotating ion beam delivery (gantry);
-   the evaluation of new concepts of position sensitive γ-ray detectors with regard to their suitability for being operated in-beam;
-   a feasibility study of proton therapy monitoring by means of PET;
-   investigating the time microstructure of the γ-radiation as a condition for the layout of an efficient data acquisition system;
-   the measurement of tissue dependent activity washout in order to improve the reliability of predicting β^+-activity distributions from the treatment plans.

Collaborations

Heavy Ion Tumour Therapy

- GSI Darmstadt
- Radiologische Klinik der Universität Heidelberg
- Deutsches Krebsforschungszentrum Heidelberg
- Institute for Bioinorganic and Radiopharmaceutical Chemistry (FZ Rossendorf)
- Soltan Institute for Nuclear Studies, Otwock-Swierk, Poland

Cell Radiobiology at ELBE

- Klinik für Strahlentherapie und Radioonkologie, TU Dresden
- Institut für Strahlenschutzphysik, TU Dresden
- Institut für Zoologie, TU Dresden
- Institute for Bioinorganic and Radiopharmaceutical Chemistry (FZ Rossendorf)

Establishment of a Cell Culture Laboratory at ELBE

A. Panteleeva, J. Pawelke, E. Lessmann

Measurement of RBE values of photons in the energy range 10 - 100 keV are planned to be performed using the quasi-monochromatic channeling radiation source at the ELBE accelerator [1]. In order to study radiation effects on living cells, minimizing of side effects coming from the time consuming preparation procedures and transportation of the cell cultures is necessary. Therefore, a cell culture laboratory was established in the ELBE building to allow the straight preparation of the samples for irradiation and as fast as possible processing after it. Equipment for cell culture growth (two CO_2 incubators), for handling in sterile environment (a laminar flow box) and a cooled centrifuge are provided. The cell growth as well as the radiation induced effects can be observed with the help of an ordinary light microscope as well as of an inverse fluorescent microscope. The sterilisation of instruments and media is performed by hot air or hot steam and pressure sterilisation. There is equipment for water deionisation as well as chemical neutralisation of the disposed liquids. In the future, possibilities for the determination of radiation damage using radioactively labelled cells as well as growth of cells in different gas environment (N_2, O_2) are allowed in the laboratory. Furthermore, the laboratory is prepared for later use of genetically modified samples (genetic class S2).

The cell culture work started in May 2001. As biological endpoints for the first experiments at the ELBE photon source, clonogenic survival and micronuclei formation assays are chosen [2]. Preparation of the future experiments includes establishment of conditions for cell growth for different cell lines, optimisation of both assays in use and tests of cell carrier materials, which can be used in practicable irradiation unit. The cell lines under research in our laboratory up to now are NIH/3T3 (mouse fibroblasts, ATCC) and HH4dd (human skin fibroblasts, provided by Prof. Rodemann, Tübingen University).

In order to measure the RBE of X-rays at the horizontal ELBE beam, some requirements to the irradiation setup have to be fulfilled: (i) in order to minimise the attenuation of X-rays, the thickness of the cell substrate has to be in the order of ≤ 100 μm; (ii) the cell vessel has to be closed and to contain sufficient amount of medium (Fig. 1). The material of the substrate has to provide good attachment and cell proliferation. The growing conditions of the two cell lines were optimized for different substrate materials, and the properties of the most suitable are shown in Table 1. Capability of the cells to form colonies (plating efficiency), the control level of micronuclei formation and the cell proliferation by means of dye-exclusion assay were compared after the cells were growing on the studied substrates and standard material (polystyrene culture dish). The results are presented in Table 2, showing that the parameters of growth and proliferation are not changed by the studied substrate materials. However, the commercially available tissue culture insert PetriPerm, based on the Biofolie membrane (Sartorius, Göttingen) was chosen (thickness 25 μm), mainly because the transparent membrane allows observation of growth and performing of the micronucleus test directly on the membrane.

The future cell culture work at ELBE cell lab includes introducing of more cell lines (e.g. AG-01522 human fibroblasts, human mammary epithelial cells).

Fig. 1 *Design of the irradiation setup.*

Tab. 1 *Main membrane properties.*

Membrane material	additional treatment	growth of cells as a monolayer	transparent
Isopore [a] (polycarbonate)	poly-L-lysine	good	not
Biofolie [b] (Teflon)	not required	good	yes

Producers: [a]Millipore, Eschborn   [b]Sartorius, Göttingen

Tab. 2 *Control levels of cell proliferation parameters - comparison of conventional cell culture vessels and membrane materials for the two cell lines.*

Cell line	3T3			HH4dd	
cell substrate	Plating efficiency [%]	BNC+MN [a] [%]	MN/ BNC+MN [b]	BNC+MN [a] [%]	MN/ BNC+MN [b]
Biofolie	35.9±1.7	2.2±0.2	1.10±0.06	3.4±0.4	1.09±0.04
Isopore	36.2±1.4	not possible, membrane not transparent			
polystyrene (culture flask)	33.0±1.6	1.7±0.3	1.02±0.02	3.3±0.5	1.04±0.03

[a] Fraction of binucleated cells with micronuclei   [b] Number of micronuclei per binucleated cell with micronuclei

[1] W. Neubert et al., FZ Rossendorf, Wiss.-Tech. Ber. FZR-319 (2001) 41
[2] A. Panteleeva et al., This Report, p. 90

Determination of RBE of 25 kV X-Rays for Cell Survival and Chromosomal Damage

A. Panteleeva, K. Brankovic[1], W. Dörr[1], C. Hoinkis[1], J. Pawelke, D. Slonina[2], K. Spekl[1]

The determination of RBE of X-rays in the energy range 10 - 100 keV is important because of their wide application in radiology (e. g. mammography) and radiotherapy. Lately it was shown that the RBE value of X-rays from a 29 kV X-ray tube for neoplastic transformation of the human hybrid cell line CGL1 (HeLa/skin fibroblasts) is 3.4, whereas for survival it was 1.1 - 2.0 (reference radiation 200 kV X-ray tube) [1].

At the Medical Department of Dresden University the RBE value of X-rays from a 25 kV X-ray tube was determined for cell survival [2] and chromosomal damage (formation of micronuclei). The irradiation was performed with a tungsten anode therapy unit Darpaq 150-MC (operated at 25 kV, 20 mA, dose rate 1.7 Gy/min) and a conventional tungsten anode X-ray tube Isovolt 320/13 (operated at 200 kV, 20 mA, dose rate 1.2 Gy/min). The cell lines in use were: mouse fibroblasts NIH/3T3 (ATCC, USA), hamster fibroblasts V79 (ATCC, USA), primary neonatal human keratinocytes HEKn (TEBU, Germany), primary human skin fibroblasts HFIB (Biochrom, Germany).

The HFIB fibroblasts were not used in the survival assay because of lacking colony formation. A strong cell line dependence of the survival was found in the experiments. Applying the linear-quadratic model fit to the survival curves, the α and β values displayed in Table 1 were obtained. The 3T3 fibroblasts showed a strong decrease in survival after irradiation with 25 kV X-rays compared to the irradiation with 200 kV at high doses, which was not observed for the other cell lines. The RBE was calculated at 10 % survival and it was found to be not significantly different from 1 for all cell lines.

The second endpoint investigated was the induction of micronuclei which is a manifestation of cytogenetic damage. After irradiation, the cells are incubated in culture medium with cell line dependent concentration of cytochalasin B, which blocks the cytokinesis without blocking the karyokinesis. This allows to select the cells which have passed exactly one division after irradiation (binucleated cells). The micronuclei are chromosome fragments (or even whole chromosomes) closed by a nuclear membrane, which are formed during the cell division due to DNA damage. The severity of damage is determined by the number of binucleated cells with micronuclei; the number of micronuclei per binucleated cells with micronuclei is an indication of the quality of the damage. The V79 fibroblasts were not used in this assay, because of a lacking responsiveness to cytochalasin B. The fraction of binucleated cells was found to decrease with the increase of the dose, which shows the diminished division capability after irradiation. This effect is equally expressed for both radiation qualities. The frequency of binucleated cells with micronuclei, as well as the number of micronuclei per binucleated cell were found to be linearly dependent on the dose up to ~ 5 Gy for all cell lines. Significantly higher induction of micronuclei was observed after irradiation with 25 kV X-rays in comparison to 200 kV X-rays (Fig. 1). The RBE-values for the different cell lines were found to be between 1.1 and 1.3.

Further experiments with monochromatic sources will allow detailed study of the X-ray energy dependence of the RBE. Such experiments are in preparation at the photon source at ELBE.

Tab. 1 *Parameters of the cell survival of fibroblasts (3T3, V79) and keratinocytes (HEKn) after irradiation with 25 kV and 200 kV X-rays.*

cell line	radiation quality	$\alpha(\pm\text{SEM})$ $[Gy^{-1}]$	$\beta(\pm\text{SEM})$ $[Gy^{-2}]$
3T3	25 kV	0.10 ± 0.05	0.070 ± 0.010
	200 kV	0.24 ± 0.02	0.022 ± 0.002
V79	25 kV	0.11 ± 0.04	0.035 ± 0.014
	200 kV	0.08 ± 0.02	0.032 ± 0.005
HEKn	25 kV	0.40 ± 0.10	0.048 ± 0.054
	200 kV	0.31 ± 0.03	0.048 ± 0.011
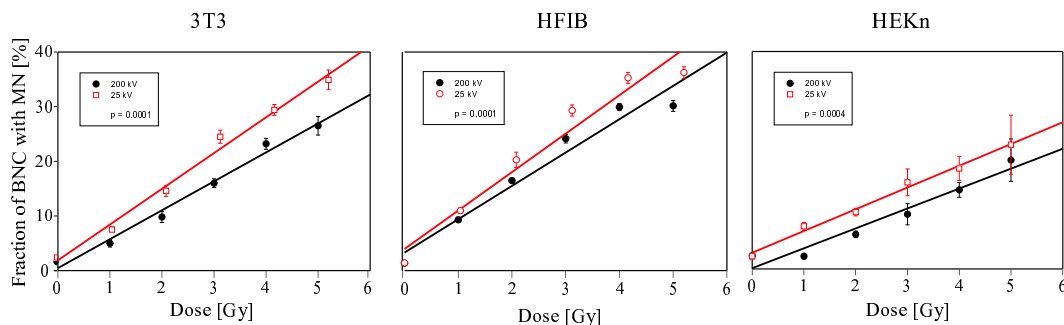
Fig. 1 *Dose dependence of the fraction of binucleated cells with micronuclei after irradiation with 25 kV (grey lines, open symbols) and 200 kV X-rays (black lines, closed symbols).*

[1] D. Frankenberg et.al., Stahlenbiologie und Strahlenschutz, Band I, TÜV-Verlag, Köln (ISBN 3-8249-0618-X) (2000) 27
[2] K. Brankovic et.al., Exp. Strahlenther. Klin. Strahlenbiol. 10 (2001) 71

[1] *Dept. Radiotherapy, Medical Faculty, TU Dresden*
[2] *Radiobiology Laboratory, Centre of Oncology, Krakow, Poland*

Design of an X-Ray Monochromator for the Channeling Source at ELBE

J. Pawelke, B. Beckhoff[1], B. Kanngiesser[2], M. Palm[3], A. Panteleeva, B. Stoevesandt[3]

One topic of research at the ELBE facility is the realisation of an X-ray source for radiobiological investigations. In a first project, quasi-monochromatic X-rays will be produced by electron channeling in diamond crystals which will be applied to determine the energy dependent relative biological effectiveness of photons in the range of $10 - 100$ keV. The channeling radiation (CR) source has been optimised in order to reduce the bremsstrahlung background to the unavoidable contribution from the diamond crystal. In a given energy interval, the intensity of the quasi-monochromatic CR dominates over the polychromatic bremsstrahlung background by more than one order of magnitude. However, the integral dose of bremsstrahlung is comparable to the CR dose [1].

Therefore, a first X-ray monochromator has been designed for CR of 19.4 keV maximum energy, assuming a cut of the channeling cone of 10 % FWHM energy spread to be used. This X-ray energy chosen is of relevance for mammography. It will be obtained by channeling of electrons of 15.5 MeV at the (110) plane (1→0 transition). Bragg reflection at the (002) plane of highly oriented pyrolytic graphite (HOPG) crystals was selected to achieve highest intensity of monochromatic radiation [2]. The determination of crystal curvature requires consideration of the Bragg reflection condition, the angular dependent intensity and energy distribution of the CR (calculated following the formalism given in [3]) as well as the practical limitations at the ELBE beamline such as CR source to monochromator distance of 1 m and fo-

cusing the reflected beam to a cell target of ≈ 3 cm^2 size at a distance of 2 m from the source (Fig. 1). Furthermore, aspects of the experimental HOPG design and the interaction of the X-rays with the crystals by use of a ray tracing code based on Monte Carlo methods [2] were also considered.

An optimal design was found to be a monochromator consisting of 15 steps (Fig. 2). The toroidal basic shape (cf. Fig. 1, rotation about a line which is parallel to x-axis passing Z_0) results in optimal focusing whereas the logarithmic shape of each step (approximated by a sector with radius R_M, cf. Fig. 1 left) fulfills optimal reflection condition. For this geometry with 0.5 mm thick HOPG crystals of 0.8° mosaicity, a transmission from CR source to cell target of 21.2 % is calculated. Neither moving the source a few mm along x- or z-axis nor changing the crystal mosaic spread within $0.6 - 1.0°$ will strongly change the reflected radiation. However, moving the source by 2 mm along y-axis reduces the total transmission to 18.6 %. The intensity of the reflected photons varies at cell target by ≈ 50 % which has to be further considered in cell irradiation procedure.

Currently, the best material and best production technology for manufacturing the monochromator mould which will be coated with the HOPG crystals is under investigation. Here, radiation hardness of the mould in combination with high precision of the final curvature is necessary.
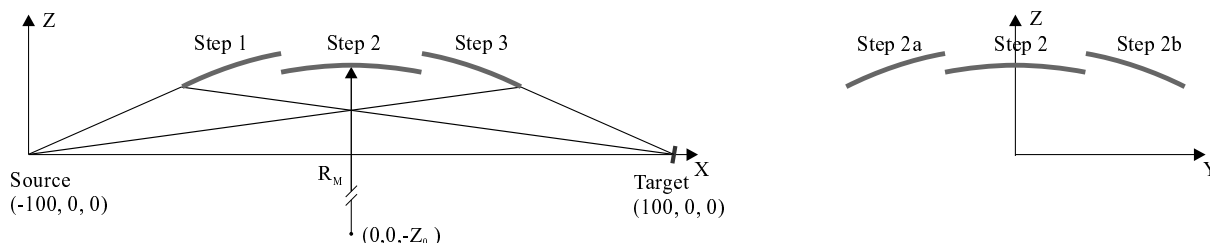
Fig. 1 *Schematic outline of the input geometry for monochromator design in meridional (left) and sagittal (right) direction.*
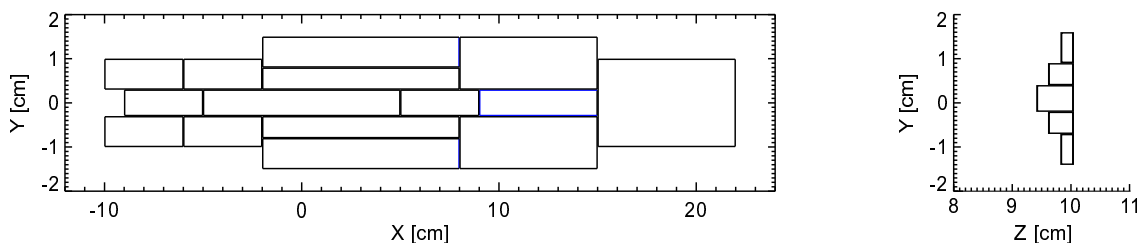
Fig. 2 *Geometry of the stepped monochromator design. Each step has a corresponding value of R_M and Z_0. The range of R_M and Z_0 is $955.3 - 1051.0$ cm and $945.2 - 1041.4$ cm, respectively, whereby $R_M > Z_0$.*

[1] W. Neubert et al., Proc. of the Int. Conf. Monte Carlo 2000, Lisbon, Portugal, Springer Berlin Heidelberg (2001) 123
[2] B. Beckhoff, PhD thesis, University of Bremen, signature DS-1732 (1995)
[3] A. Panteleeva et al., FZ Rossendorf, Wiss.-Tech. Ber. FZR-271 (1999) 95

[1] *Physikalisch-Technische Bundesanstalt, Berlin*
[2] *Technische Universiät Berlin*
[3] *Universität Bremen*

Considerations on Dosimetry for Measuring the RBE of Soft X-Rays at ELBE

J. PAWELKE, A. PANTELEEVA, C. HOINKIS[1]

For determining relative biological effectiveness (RBE) of soft X-rays a quasi-monochromatic channeling source ($E_\gamma \approx 10 - 100$ keV) is being developed [1]. In preparation of RBE measurements at ELBE, experiments were performed with a conventional X-ray tube at TU Dresden. Several cell lines were irradiated with photons from a 25 kV soft X-ray tube and a 200 kV reference X-ray tube. Although the RBE values obtained show the enhanced damage from soft X-rays [2], there is a demand to determine it more precisely. Besides the irradiation with monochromatic soft X-rays, accurate determination of absolute dose delivered to the cell target is a crucial point for this.

Standard dosimetric technique is obtaining direct values for absorbed dose by air filled ionisation chambers (IC) which are optimised with respect to dose and energy dependence of response. A small soft X-ray chamber (23342) and a tube chamber (31003, PTW Freiburg) were used to measure the dose rate at target position before cell irradiation for the 25 kV and 200 kV X-ray tube, respectively. The dose delivered to cell is controlled by exposure time. However, ICs are integrating over photon energy and sensitive chamber volume.

Therefore, the dose was also calculated after determination of spectral photon flux density by considering the energy dependent energy absorption coefficient for water and integrating over energy range. For the measurement of the flux density of the 25 kV X-rays (Fig. 1), the necessary flux reduction was achieved by 25 μm slit tungsten collimator. Due to pratical limitations in reducing the flux density by using collimator or increasing the distance from the vertically emitting tube, a 200 kV X-ray model spectrum was calculated (Fig. 2). The comparison of the 25 kV and the 200 kV X-ray tube revealed that in the first case the main contribution to the dose

(76 %) is coming from photons of energy $10 - 20$ keV and a minor one (20 %) by energies ≤ 10 keV, whereas in the second case, only 4 % of the dose is contributed by photons of $10 - 20$ keV but 61 % by photons of $20 - 60$ keV. Although useful in understanding the RBE energy dependence, the dose calculated in this way is less accurate than that one measured by IC. Here, the high dynamic range of ELBE beam intensity will allow more precise flux measurements without the use of any collimator. Furthermore, dose control by monitoring the ELBE electron beam intensity will be studied.

A suitable way to sample the depth dose distribution in a cell monolayer ($\approx 5\,\mu$m thick) seems to be the use of TSEE detectors, because they have a sensitive layer of the order of ~ 10 nm and show stable response [3]. If the detectors are irradiated in water or propanol (Table 1), the detector reponse remains stable and is only reduced due to attenuation in the liquid layer. In the presence of cell culture medium with its ingredients such as sugar, salts and proteins an unstable response with shift and change of the shape of the glow curve is observed. Therefore, TSEE detectors allow to sample the dose delivered to the cell approximating real conditions.

Tab. 1 *TSEE response of detectors covered with propanol or air after irradiation with low energy X-rays from ^{55}Fe source and high energy photons from ^{22}Na source.*

Detector type	Sensitive area [mm^2]	Spacing^a [mm]	Response ratio air to propanol^b ^{22}Na	^{55}Fe
I	43.0	1.0±0.1	1.0±0.1	28±2
II	146.4	1.0±0.1	1.0±0.1	68±6
III	146.4	2.4±0.2	1.4±0.3	112±4

^{a}) Detector to source distance, filled up with air or liquid

^{b}) Average of 5 repeated measurements
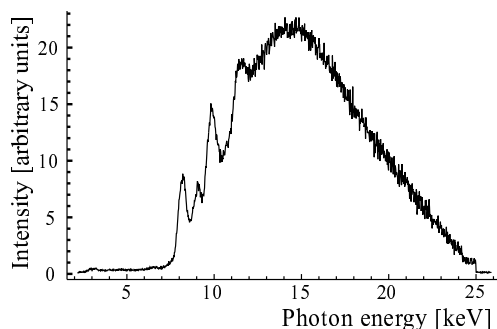
Fig. 1 *Energy distribution of the soft X-ray tube intensity (25 kV, tungsten anode, 0.3 mm Al filter), measured with a low-energy detector (XR100-CR, AmpTek, USA), corrected for the detection efficiency in the region $10 - 25$ keV.*
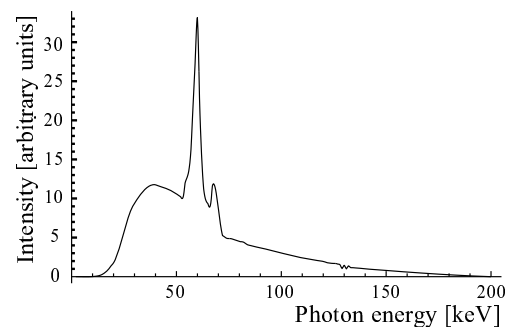
Fig. 2 *Energy distribution of the reference X-ray tube intensity (200 kV, tungsten anode, 0.5 mm Cu filter), calculated following the formalism given in [4].*

[1] W. Neubert et al., FZ Rossendorf, Wiss.-Tech. Ber. FZR-319 (2001) 41

[2] A. Panteleeva et al., This Report, p. 90

[3] J. Pawelke and A. Panteleeva, FZ Rossendorf, Wiss.-Tech. Ber. FZR-319 (2001) 102

[4] J.M. Boone and J.A. Seibert, Med. Phys. 24 (1997) 1661

[1] *Dept. Radiotherapy, Medical Faculty, TU Dresden*

Influence of Auger Electrons on Dose Distributions Simulated by PENELOPE

W. Neubert, W. Enghardt

It is well recognised that Auger emitters exhibit high-LET type radiotoxicity. The simulation of such processes requires reliable tools for radiation transport at very low energies. The updated code package PENELOPE [1] is capable of describing the transport of electrons and photons in arbitrary media down to energies as low as 100 eV and $\simeq$ 1 keV, respectively. PENELOPE considers the relaxation process of an atom, excited by photon or electron impact, in which characteristic X-rays, photo- and Auger electrons are taken into account.

Table 1 *Auger electron radiation spectrum of ^{55}Fe [2].*
The first column gives the Auger process, where the first letter denotes the shell with the vacancy before the Auger transition, the second and third letters indicate where the new vacancies are created, where X or Y denote shells above the specified ones. The last column gives the range in water.

Transition	Energy/keV	Yield/decay	Range /μm
KLL	5.13	0.487	0.874
KLX	5.77	0.120	1.06
KXY	6.42	0.0082	1.27
LMM	0.56	1.41	0.0291
LMX	0.61	$\simeq$0.02	0.0341
MXY	0.049	0.23	0.00325

Iron was chosen since the code exactly treats the inner atomic electron shells up to the M subshells. Characteristics of Auger electrons emitted from ^{55}Fe [2] are given in table 1. The advantage of Fe is that by photon impact more than 60% of the photons are converted into K-shell Auger electrons [3] and about 90% of the electrons given in table 1 are tracked by PENELOPE. This way, the response of most of the components of the Auger electron spectrum can be studied separately. If the energy (e.g. for MXY Auger electrons) is below the above thresholds the dose will be deposited locally thus preventing a distinction of different transitions. In the next step we studied the track length distributions of selected Auger electron energies (see fig. 1). These data reproduce the ranges given in table 1. This reproduction is a necessary condition to apply PENELOPE for microdosimetric applications since related quantities are sensitive to the small-scale spatial distribution of the energy deposits along a track. The corresponding distributions (lower part of Fig. 1) show a regular behavior as low as 0.1 nm. Dose calculations were performed for a 2 μm thick layer of water. 15 keV photons impinging on a 0.1 μm Fe layer in front of this phantom generate flourescent X-rays, photoelectrons (7.87 and 8.62 keV) and Auger electrons the latter one's are stopped within the phantom thickness. The depth dose distribution in Fig. 2 shows a pronounced enhancement at low distances from the entrance. This effect cannot be asigned to characteristic flourescense radiation and photoelectrons which show another dose profile.
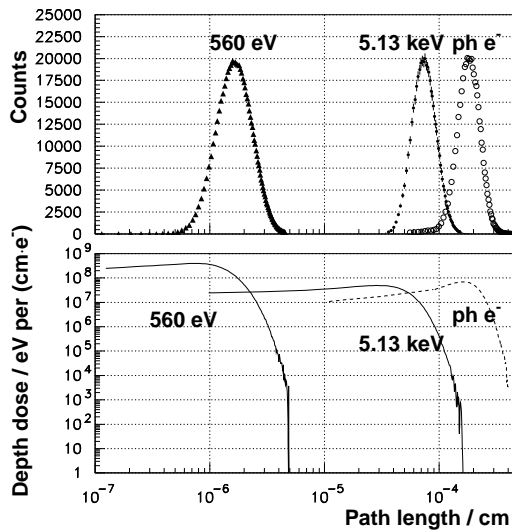
Fig. 1 *Upper part: Normalized track length distributions of low energy electrons corresponding to LMM and KLL Auger transitions, ph e$^-$ denotes photoelectrons from 15 keV photon impact on Fe as calculated by PENELOPE. Lower part: corresponding depth dose distributions.*
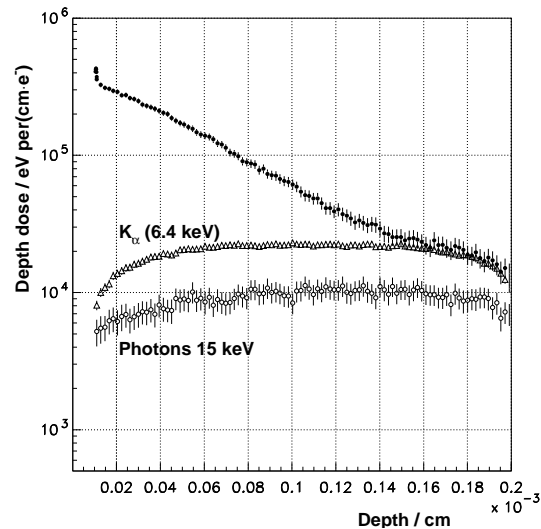
Fig. 2 *Depth dose distributions in water. Dots: 15 keV photons impinging on a 0.1 μm Fe foil in front of the specimen. Triangles: 6.4 keV Fe-K$_\alpha$ in water. Open circles: response of 15 keV photons in water.*

[1] F. Salvat et al., PENELOPE, A code System for Monte Carlo Simulations of Electron and Photon Transport, Proc. Workshop/Training Course OECD/NEA, 5-7 Nov.2001, NEA/NSC/DOC (2001) 19, ISBN: 92-64-18475-9
[2] R.W. Howell, Med. Phys. 19 (1992) 1371
[3] J. Stepanek, Med. Phys. 27 (2000) 1544

Electromagnetic Interactions Simulated by PENELOPE, FLUKA and GEANT4

H. Müller, B. Naumann[1], W. Neubert

The construction of setups at the experimental areas of the superconducting electron accelerator ELBE with respect to requirements of radiation protection are based on comprehensive calculations. In order to find optional solutions one has to be sure that the used codes reproduce experimental data related to the basic electromagnetic interactions within the necessary accuracy, especially at low energies. The incident energy of $20\,MeV$ which is typical for ELBE was chosen for an intercomparison of three code packages available in the public domain.

The code system PENELOPE [1] performs Monte-Carlo simulations of coupled electron-photon transport in arbitrary materials from $100\,eV$ for electrons and $1\,keV$ for photons to about $1\,GeV$. Electron and positron histories are generated on the basis of a mixed procedure which combines detailed simulation of hard events with condensed simulation of soft interactions.

The code FLUKA [2] originally written as hadron event generator handles now electromagnetic processes too. Differences concerning stopping power and bremsstrahlung production in electron and positron interactions are considered. The angular distribution of bremsstrahlung photons correlated with the energy are taken into account. FLUKA simulates the transport of all these radiation components and their reciprocal interactions at the same time. The lower thresholds for particle and photon propagation are $1\,keV$ limited by an upper energy of about $1000\,TeV$.

GEANT4 [3] is a toolkit for the simulation of the passage of particles through matter. Its application areas include high energy physics and nuclear experiments, medical, accelerator and space physics studies. Due to its object oriented design different processes and models can be easily implemented. The user decides which processes are relevant for his problem and which models to be used. In the present paper the standard package for energies down to $10\,keV$ and the low energy package for energies down to $250\,eV$ have been employed. The use of evaluated data files allows the application up to the GeV region.

In order to compare the results of the available codes a simple test arrangement was used. A disk of iron ($1\,cm$ in diameter and $1\,mm$ thick) was chosen as target arranged perpendicularly to the point-like incident beam of $20\,MeV$ electrons and photons. In the following we compare the energy spectra of electrons and photons emitted at the downstream side of the disk as calculated with the available codes.

The results for photon induced processes are shown in Fig. 1, that for electron induced ones in Fig. 2. There is a good agreement in case of incident photons. Only at the highest energies of the secondary electrons GEANT4 yields a bump, which is not observed in the PENELOPE and FLUKA results. For incident electrons a remarkable agreement was obtained (i.e. within the line widths) between the curves from PENELOPE, FLUKA and the standard version of GEANT4, while the results from the low energy package show distinct deviations up to a factor of about 4 in the high-energy part of the bremsstrahlung photons and about $50\,\%$ for the scattered electrons at energies around $5\,MeV$.
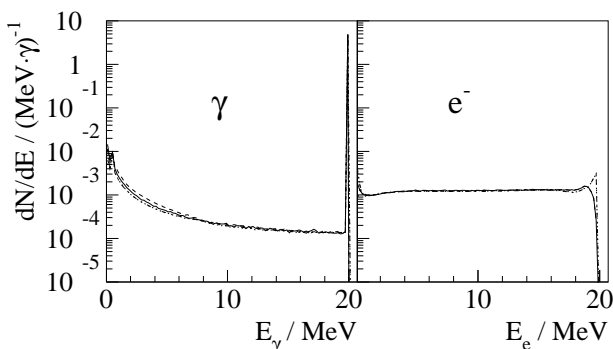
Fig. 1 *20 MeV incident photons: distributions of scattered photons and secondary electrons calculated with PENELOPE (full lines), FLUKA (dashed lines) and GEANT4 (dotted lines for standard, dashed-dotted lines for low energy package). The spike at 20 MeV in the left panel belongs to transmitted photons.*
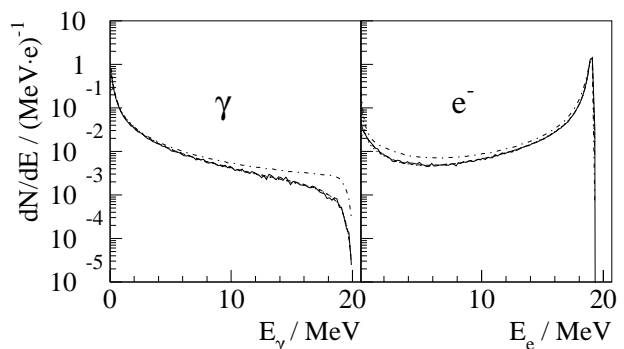
Fig. 2 *20 MeV incident electrons: distributions of bremsstrahlung and scattered electrons calculated with PENELOPE (full lines), FLUKA (dashed lines) and GEANT4 (dotted lines for standard, dashed-dotted lines for low energy package). Fluctuations in the PENELOPE distributions are due to lower statistics.*

[1] F. Salvat et al., PENELOPE, A code System for Monte Carlo Simulations of Electron and Photon Transport, Proc. Workshop/Training Course OECD/NEA, 5-7 Nov.2001, NEA/NSC/DOC (2001) 19, ISBN: 92-64-18475-9

[2] A. Fasso, A. Ferrari and P.R. Sala, Proc. of the Monte Carlo 2000 Conference, Lisbon, 23-26 Oct., 2000

[3] The GEANT4 Collaboration, http://wwwinfo.cern.ch/asd/geant4/geant4.html, Version 4.0

[1]*Institute of Nuclear and Particle Physics, TU Dresden*

Neutron Production by Photons and Electrons Simulated by FLUKA, MCNP4C2 and GEANT4-4.0

C. Beckert[1], H. Müller, B. Naumann[2], K. Noack[1]

Neutron production at the electron beam of ELBE proceeds as a two-step process via Bremsstrahlung with subsequent photo-neutron production. Envisaged research with neutrons concerns the interaction of neutrons with materials used for fission or fusion reactors [1]. Neutrons might also turn out to be a rather disturbing background for planned radio-biological studies [2]. Therefore, efforts are necessary to understand neutron production at ELBE.

In FLUKA the cross sections of photo-nuclear interactions in the region of the Giant Dipole Resonance are taken from tables or from parameterizations. Since the nuclear de-excitation is similar to that of a compound nucleus, the energy dissipation is treated by the PEANUT preequilibrium-evaporation module [3] of FLUKA.

MCNP is a general purpose Monte Carlo transport code for neutrons up to $20\,MeV$ and for photons and electrons between $1\,keV$ and $100\,MeV$. Photo-nuclear physics is implemented on the basis of evaluated data both for the photo-nuclear cross sections as well as for the distributions of the secondary particles [4].

GEANT4 takes parameterizations of available data for the calculation of the probability of photo-nuclear interactions. Final states are generated on the basis of the Chiral Invariant Phase Space model [5]. For the present considerations the standard package for electromagnetic interactions is used together with the low-energy package for neutron propagation, which is applicable from thermal energies up to about $20\,MeV$.

For a comparison of the above mentioned codes a test arrangement similar to that of the previous contribution [6] was used. The thickness of the iron disk is increased to $1\,cm$ to get enough neutrons within reasonable computer times. Again, incident beams of $20\,MeV$ photons and electrons interact with the target and the energy spectra of neutrons at the downstream side of the disk are calculated. The spectral distribution of photon induced neutrons is shown in Fig. 1, that of electron induced ones in Fig. 2. The results of the various codes show distinct differences. The most prominent discrepancy is the strong population of the ground state of the final nucleus of the (γ, n) reaction (the peak around $9\,MeV$) in case of the GEANT4-4.0 calculation, a feature not observed for the other codes. Experimental data are rather scarce, thus an independent verification is difficult. Also around $1\,MeV$ the neutron yield differs between FLUKA and GEANT4-4.0 by nearly a factor of 4.

The neutron spectra from incident electrons (Fig. 2) reflect to a certain degree the properties of the (γ, n) reaction, because the electrons produce a broad distribution of Bremsstrahlung-photons (see Fig. 2 in [6]) which, in turn, are responsible for neutron production. The GEANT4-4.0 (γ, n) spectrum exhibits the largest intensity at high energies, and consequently also the neutrons from the two-step process, $e^- \rightarrow \gamma \rightarrow n$, extend to higher energies compared to the results from MCNP4C2 and FLUKA. In case of GEANT4-4.0 the statistical accuracy is insufficient for a reasonable comparison at lowest energies.

The details of the energy distribution of background neutrons produced in the beam tube are surely of minor importance for radio-biological studies. For the planned research with neutrons, however, the knowledge of energy distribution might be of decisive importance. Therefore, a similar comparison with ^{56}Fe replaced by Pb, the production target for neutrons, is of interest.
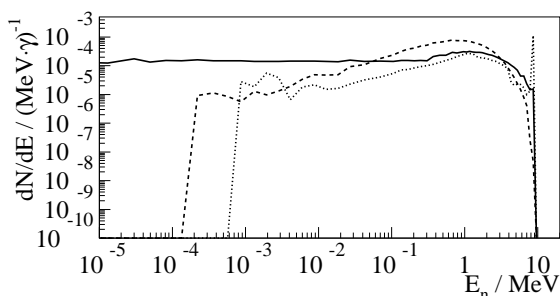
Fig. 1 $20\,MeV$ incident photons: energy distributions of neutrons calculated with MCNP4C2 (full lines), FLUKA (dashed lines) and GEANT4-4.0 (dotted lines).
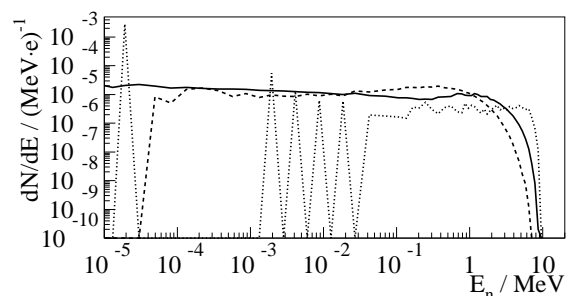
Fig. 2 The same as Fig. 1 but for incident electrons.

[1] H. Freiesleben et al., Annual report 1997, FZR-215 (1998) 14
[2] W. Neubert et al., Annual report 2000, FZR-319 (2001) 41
[3] A. Fasso et al., Proc. of the III Spec. Meeting on Shielding Aspects, Sendai (1997) 61
[4] M.C. White, Los Alamos National Laboratory report LA-13744-T (2000)
[5] P. V. Degtyarenkoet et al., Eur. Phys. J. A9 (2001) 421
[6] H. Müller et al., This Report, p. 94

[1]FZR, Institute of Safety Research
[2]Institute of Nuclear and Particle Physics, TU Dresden

X-Ray Imaging of Phase Transition and Flow Phenomena in Liquid Metals: A Feasibility Study

S. Eckert[1], W. Enghardt, W. Neubert, H. Neumann[1], J. Pawelke

The study is aimed at a first estimation of the experimental conditions for visualizing phase transition and flow phenomena in liquid metals by means of X-rays. As an example we consider the solidification of the molten alloy $Pb_{15}Sn_{85}$. Dendrites of pure lead having a thickness of about 50 μm and a length of about 200 μm are preticipated from the melt at the liquid-solid interface. In a first step the optimum X-ray energy for this imaging problem has been estimated by means of a signal-to-noise-ratio (SNR) analysis. The SNR is given in the worst case, where the X-rays on their path through the sample pass only one dendrite, by the equation

$$SNR = \frac{|\phi_A - \phi_D|}{\sqrt{\phi_A + \phi_D}} \qquad (1)$$

where

$$\phi_A = \phi_0 \, e^{-\mu_A(E_X)d_A} \qquad (2)$$

and

$$\phi_D = \phi_0 \, e^{-\mu_A(E_X)(d_A - d_D) - \mu_D(E_X)d_D} \qquad (3)$$

describe the attenuation of the incident photon flux ϕ_0 by a molten sample of the thickness d_A without and with one dendrite (thickness $d_D = 50$ μm), respectively. The linear attenuation coefficients $\mu_A(E_X)$ and $\mu_D(E_X)$ of the $Pb_{15}Sn_{85}$ melt ($\varrho = 7.6$ g cm^{-3}) and of the Pb-dendrites ($\varrho = 11.2$ g cm^{-3}), respectively, in dependence on the photon energy E_X have been taken from [1]. From medical imaging it is known that useful images should have a minimum SNR of 4. Thus, we calculated the number of incident photons in dependence on their energy under these conditions for samples of 1 and 2 mm

thickness d_A. The results depicted in Fig. 1 suggest an optimum photon energy for this imaging situation between 100 and 140 keV.

Since this simple SNR analysis does not take into account the image degradation due to the interaction of the X-rays with matter, a more detailed photon transport calculation by means of the GEANT simulation code has been performed. Five boxes ($50 \times 50 \times 200$ μm^3), equally spaced by 50 μm are supposed to be the solid lead dendrites. They were inserted into the melt of $Pb_{15}Sn_{85}$ confined to 475 μm $\times$ 2 mm $\times$ 200 μm. This phantom was irradiated with a parallel X-ray beam (0.5×0.1 mm^2) with energies from slightly above the K absorption edge of Pb (88 keV) to 140 keV to scan the energy range of the minimum in Fig. 1. The interaction of the photons and their secondary electrons with the samples is described by taking into account photoeffect, Compton and Rayleigh scattering, multiple electron scattering as well as collision and radiative stopping. A comparison of the contrast of the distributions of photons after penetrating the sample (Fig. 2) reveals that monochromatic X-rays of 100 keV should be the optimum radiation quality. If a conventional X-ray source (200 kV, 20 mA) is applied, images with a $SNR \geq 4$ require an irradiation time of about 0.5 s (assuming a focus-object-distance of 45 cm and a photon detector of 10 % efficiency). This imaging time is expected to be reduced by two orders of magnitude, when quasi-monochromatic channeling X-rays of 100 keV will become available by irradiating diamond crystals [2] with the ELBE electron beam of 40 MeV.
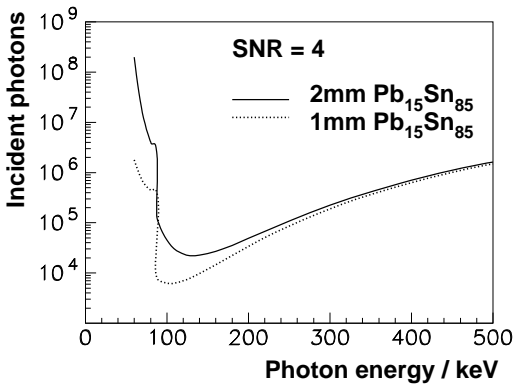
Fig. 1 *Number of incident photons per image pixel necessary to obtain an SNR of 4 as function of the photon energy.*
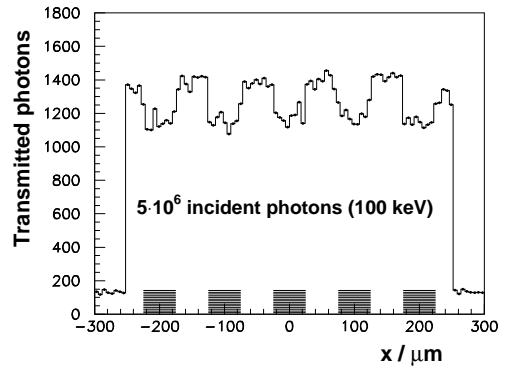
Fig. 2 *Simulated lateral distribution of photons after penetrating the sample model obtained for 5·10^6 histories of 100 keV X-rays. The hatched zones indicate the location of Pb dendrites.*

[1] http://physics.nist.gov/PhysRefData/XrayMassCoef/tab3.html
[2] A. Panteleeva et al., FZ Rossendorf, Wiss.-Tech. Ber. FZR-271 (1999) 95

---

[1]*FZR, Institute of Safety Research*

Radiation Transport Calculations for an Industrial Low-Energy Electron Accelerator

W. Neubert, W. Enghardt, M.N. Andronenko[1], B. Naumann[2], K. Konschak[3], W. Schumann[3]

The use of electron accelerators in industry involves a broad and continuously growing range of applications [1, 2], e.g. crosslinking of polymers, sterilization of food and medical disposables as well as the treatment of environmental waste. For such applied purposes the efficiency of the irradiation process is of primary importance and this requires the layout of the beam delivery system of accelerators to be carefully optimized.

A further motivation for such calculations is given by radiation protection issues and the necessity to design reliable shieldings against the primary electrons and the secondary radiation of bremsstrahlung and neutrons. Thus, for a typical industrial accelerator delivering an electron fan beam of $10\,mA$ at $E_e < 10\,MeV$ we performed such calculations by means of the public domain radiation transport codes GEANT [3] and FLUKA [4].

In particular the following calculations were performed:

- The modelling of the fan beam and its broadening by scattering in air.

- The simulation of the spatial and spectral distributions of bremsstrahlung from a tungsten-copper radiator at an electron incident energy of $E_e = 9.8\,MeV$.

- The description of neutron production in the tungsten-copper radiator at $E_e = 9.8\,MeV$, due to the (γ,n) threshold of $8.1\,MeV$ for tungsten [5].

- The activation of the radiator materials W and Cu by the production of ^{181}W, ^{185}W, ^{187}W, ^{64}Cu and ^{66}Cu.

- The calculation of dose rate distributions in polyethylene pipes (for polymer crosslinking) delivered by electron beams of $E_e = 4.0\,MeV$ and $9.8\,MeV$ as well as by $9.8\,MeV$ bremsstrahlung in dependence on the pipe diameter and the beam incidence.

- The calculation of dose rate distributions in medical disposables (for sterilization) of different mass density delivered by $9.8\,MeV$ and $4.0\,MeV$ electrons and $9.8\,MeV$ bremsstrahlung.

Fig. 1 *Perspective view of the irradiation setup with the fan electron beam extracted into air through a vacuum window. The gray box shows the products to be irradiated. Parralelograms are monitor areas.*
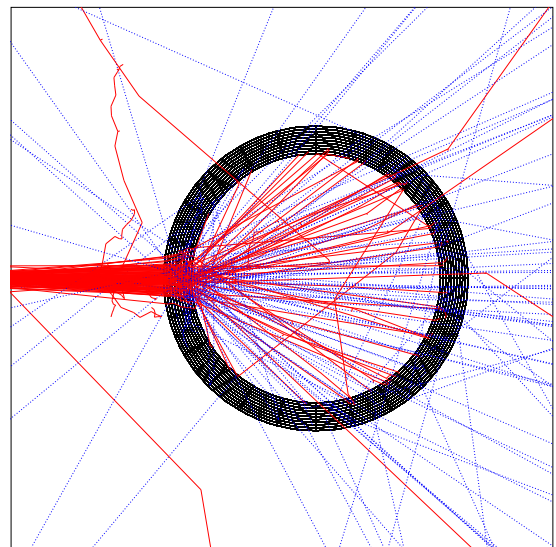
Fig. 2 *Presentation of electron tracks (dashed-dotted) incident on a pipe subdivided into sectors and ring zones. Photons produced by interaction with air and polyethylene are shown as thin dotted lines.*

[1] W. Mondelaers et al., Nucl. Instr. A 368 (1995) 278

[2] J. Mckeown et al., Radiation Physics and Chemistry 53 (1998) 55

[3] GEANT - Detector Description and Simulation Tool, CERN Program Library W 5013, 1994

[4] A. Fasso, A. Ferrari, J. Ranft and P. Sala, FLUKA-98 (http://AliSoft.cern.ch/offline/fluka/manual)

[5] B. Forkman and R. Peterson, Handbook on Nuclear Activation Data, IAEA, Techn. Rep. 273 (1987) 787

[1] *St.Petersburg Institute of Nuclear Physics, Gatchina, Russia*
[2] *Institute of Nuclear and Particle Physics, TU Dresden*
[3] *Gamma Service Produktbestrahlung GmbH, Leipzig, Betriebsteil Radeberg*

An Interactive Approach for Local Dose Quantification from In-Beam PET Data [B, G]

K. Parodi, W. Enghardt

The in-beam PET monitoring of carbon ion therapy supported the reliability of the treatment planning and patient positioning procedures at the GSI Darmstadt facility [1]. However, in some cases it detected deviations of the measured and the predicted β^+-activity distributions, due to minor inaccuracies in patient positioning or local changes of patient anatomy [1]. These discrepancies may correspond to small deviations of the applied and planned dose. Hence, a local dose quantification from PET images shortly after each therapeutic irradiation is highly desirable. Due to the lack of a feasible solution for the inverse problem relating the β^+-activity to the dose, an interactive approach has been considered. The implementation has been based on the dedicated tool used for the visualization of the PET measured and predicted distributions as contour plots superimposed onto X-ray CT images [2]. In case of deviations, an interactive modification of the patient CT consisting either in geometrical transformation (translation and rotation) or in local Hounsfield unit (HU) modifications in user-selected regions of interest (ROI) can be performed. The reliability of the modification is tested by a recalculation of the β^+-activity distribution with and without the CT changes. Actually, only the spatial distribution of β^+-decays is computed, in order to avoid blurring due to the imaging procedure. The calculation is local and analytical, in order to reach a "fast" (within few minutes) response. Only the pencil-like beams crossing the chosen ROI are taken into account. The depth-distribution of the main β^+-isotopes (^{11}C, ^{15}O and ^{10}C) is extrapolated from the PET database (DB) [3] containing the spatial distributions of positron emitters produced in PMMA ($C_5H_8O_2$) by ^{12}C beams of all the energy values used for therapy. The DB information is combined with the irradiation strategy (ion energy, fluence and position) and with the patient anatomy by means of the HU-ion range correlation [3], [4] and the stoichiometric calibration of the CT numbers suggested in [5]. The lateral-distribution is assumed to be Gaussian with a FWHM dependent on the beam focus and the average positron range in tissue. The lateral spread of the beam in depth is neglected. The distribution of β^+-decays is deduced from the isotope production and the time interval between the beam delivery and the end of the PET acquisition. If the recalculation supports the modification, a new dose distribution based on the elaborated CT is obtained by means of the treatment planning software [4]. Fig. 1 shows an example. For this patient an extreme but plausible tissue reduction was assumed on the basis of range and anatomical symmetry considerations. A new CT scan confirmed the conjecture. In such cases a new treatment plan may be defined, according to the physician's decision. Hence, the interactive approach can give an important feedback. The optional introduction of imaging effects on the recalculated distributions for a more direct comparison with the reconstructed PET images is under development. In particular, the effects of minor CT modifications on the PET attenuation corrections are currently studied. Moreover, the sensitivity and accuracy of the method as well as the potential of real quantitative PET data for local dose quantification are under investigation.
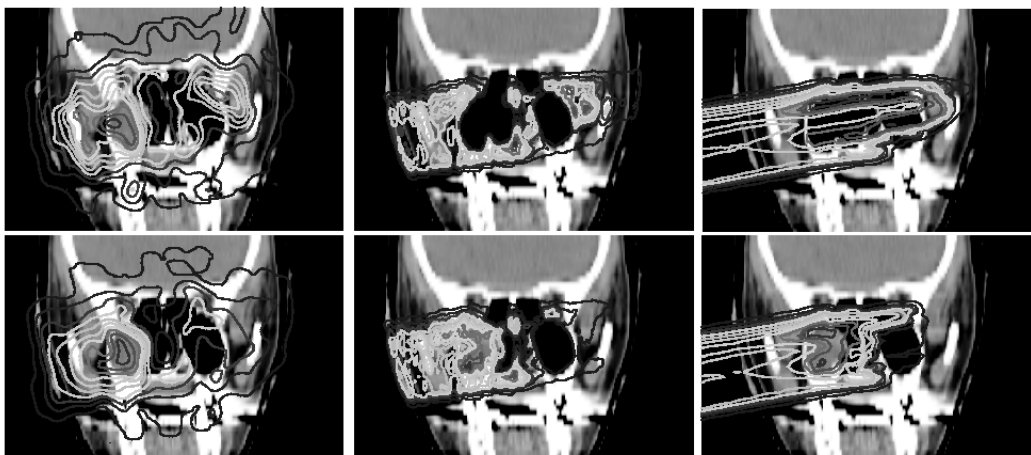
Fig. 1 *Left: Higher activation at the distal edge of the portal (entering the patient from the left of the picture) in the PET measurement (up) in comparison with the prediction (down). Middle: The recalculation with (up) and without (down) CT modification well resembles the PET images (left), thus supporting the hypothesis. Right: The effect on the recalculated dose distribution (up) in comparison with the planned one (down) is evident and in agreement with the PET observation.*

[1] W. Enghardt et al., FZ Rossendorf, Wiss.-Tech. Ber. FZR-271 (1999) 89
[2] F. Pönisch et al., FZ Rossendorf, Wiss.-Tech. Ber. FZR-271 (1999) 91
[3] B. G. Hasch, PhD Thesis, Dresden University of Technology (1996)
[4] M. Krämer et al., Phys. Med. Biol. 45 (2000) 3299
[5] W. Schneider et al., Phys. Med. Biol. 45 (2000) 459

A Scatter Correction for Iterative Tomographic Reconstruction[G]

F. Pönisch, W. Enghardt

A fully 3D reconstruction algorithm based on the Maximum Likelihood Expectation Maximization (MLE) algorithm has been developed for reconstruction of images from data taken by the limited angle double head camera BASTEI [1]. The process of photon scattering considerably influences the image quality in PET. For head and neck tumors about 30 % of the registered true coincidences are influenced by Compton or Rayleigh scattering, which may deteriorate the correspondence between the source and the reconstructed radioactivity distribution especially in such highly inhomogeneous regions of the human body like the head and neck. Therefore, a scatter correction is required.

The scatter correction algorithm needs the information on the tissue composition and density only within and nearby the camera field of view. This is derived from the X-ray computed tomograms (CT) of the patient (taken for treatment planning purpose) which are automatically combined with a CT of the head rest using characteristic landmarks [2]. This data set is the basis for the calculation of the attenuation correction factors. The measured lines of response (LOR) are corrected for the individual detector efficiency and the length of the emission line within the image space. The expectation step of the MLE-algorithm [3] is intended for modelling the imaging process in emission tomography. The classical algorithm of Shepp and Vardi [3] estimates the forward projection by computing the ray sums in each projection. We modified this procedure by applying the attenuation correction factors y_i^{att} to the forward projection and adding furthermore, the scattered components y_i^{scatt}:

$$x_j^{(n+1)} = x_j^{(n)} \cdot \sum_{i=1}^{I} \frac{a_{ij} \cdot y_i^*}{y_i^{att} \cdot \sum_{j'=1}^{J} a_{ij'} \cdot x_{j'}^{(n)} + y_i^{scatt}}. \quad (1)$$

$x_j^{(n)}$ denotes the activity distribution after the n-th iteration step, y_i^* is the modified measured projection for the i-th channel and a_{ij} is the element of the transition matrix.

To calculate the quantity y_i^{scatt} we follow the approximation of Watson [4], the Single Scatter Simulation (SSS). This algorithm simulates the scatter coincidences y_i' in a given LOR i by single Compton scattered events only. Therefore, the total number of scattered events N_{scatt} obtained from the SSS calculation has to be normalized to the number of acquired coincidences N_{meas}. We calculate the global scatter fraction (SF) by means of an additional Monte Carlo (MC) simulation from the n-th solution:

$$SF = \frac{N_{scatt}}{N_{total}}. \quad (2)$$

The simulation uses the activity distribution of the previous iteration step and the information of the attenuation map. The MC code has been optimized for accuracy and executing time. The number of histories has been chosen that the statistical error in the calculated SF is less than 0.3 %. Watson [4] has shown that a single scaling factor is sufficient for the total scatter distribution. By means of the SF one can estimate the number of scattered events from the measured one. From this follows the normalized scatter contribution of the coincidence channel:

$$y_i^{scatt} = y_i' \cdot \frac{SF \cdot N_{meas}}{\sum_i y_i'}. \quad (3)$$

Introducing (3) into (1) yields the modified forward projection for each iteration step.

The new reconstruction algorithm has been validated for experimental data. The scatter corrected β^+-activity distributions from phantom experiments as well as patient data show a good agreement with our expectation. The Figure 1 shows the profile of the reconstructed PET image with a size of $256 \times 128 \times 100$ voxels from a ^{22}Na point-like source, which was placed in a water filled cylindrical phantom (diameter 15 cm, height 15 cm). The removal of the scatter components after applying the scatter correction algorithm is obvious.
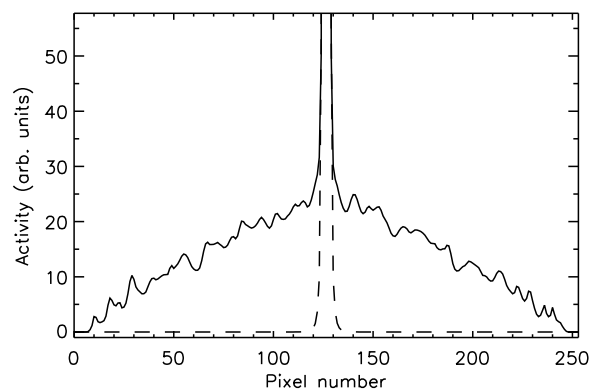
Fig. 1 *Profile of the reconstructed PET image of a point-like source in a water filled phantom. The solid curve is the reconstructed data set without scatter correction; the dashed curve is the data set using the scatter correction algorithm.*

[1] K. Lauckner, FZ Rossendorf, Wiss.-Tech. Ber. FZR-264 (1999) 70
[2] F. Pönisch et al., FZ Rossendorf, Wiss.-Tech. Ber. FZR-319 (2001) 95
[3] L.A. Shepp, Y. Vardi, IEEE Trans. Med. Imag. MI-1 (1982) 113
[4] C.C. Watson et al., in Three-Dimensional Image Reconstruction in Radiation and Nuclear Medicine (1996) 255

Benchmark Tests for an Iterative Tomographic Reconstruction Algorithm [G]

F. PÖNISCH, W. ENGHARDT, M. SCHLETT

PET images for therapy quality control, which are reconstructed from data that are acquired in-beam during heavy ion tumour irradiations at the therapy facility of GSI Darmstadt, have to be available as shortly as possible after finishing the treatment fraction, however, at the latest before applying the next daily dose fraction. The applied reconstruction technique - a true 3 dimensional Maximum Likelihood algorithm [1] - requires high computational power. Furthermore, a steady increase of the maximum number of patients treated per day and more sophisticated and thus time consuming reconstruction techniques as e.g. the scatter correction introduced recently [2], and new real-time data evaluation concepts [3] may lead to an overload of the Silicon Graphics® Inc. (SGI) Power Challenge™ workstation equipped with 6 R8000 processors, which has been exclusively dedicated to the computations connected with PET for therapy control [4]. Thus, we have investigated the possibility to replace this workstation in a cost effective way by personal computers since their computing power has rapidly increased during the last years. The performance of the SGI-system and Intel® compatible Linux® PC have been compared (further specifications see Tab. 1) running C-code implementations of the maximum likelihood tomographic reconstruction for PET data acquired during the irradiation of 2 patients (Tab. 2).

	CPU	Clock cycle / MHz	Cache size / kBytes
SGI	R8000	75	4096
PC-Intel	Pentium III	1000	256
PC-AMD	Athlon MP	1200	256
PC-Intel	Xeon	2000	256

Tab. 1 *Parameter of the computer platforms used for this benchmark test.*

For this test, irradiation portals, which require rather large PET image spaces of about 1.3 - 1.4 million voxels and therefore, a long reconstruction time have been chosen. Normally, the size of the image space is 1 million voxels. The other parameter that determines the reconstruction time is the number of registered valid coincidences during the PET scan. The mean value is about 80000 and, therefore, we have chosen PET scans with a number of valid events significantly below and above this mean. Finally the influence of different C-compilers on the run time has been studied.

Patient	Valid coincidences	Image space size (voxels)
1	40400	1260000 (150 × 100 × 84)
2	156800	1368800 (118 × 100 × 116)

Tab. 2 *Parameter of the reconstructions for 2 patients.*

The results of our benchmark test are shown in Table 3 and may summarized as follows:

(*i*) The running of the new scatter correction reconstruction algorithm [2] is not feasible on the SGI-system. The code has to be migrated to PCs with state of the art CPUs. The reconstruction algorithm with scatter correction runs faster on the most advanced machines than the original reconstruction (without scatter correction) on an R8000 (see bold figures in Table 3). From this it is estimated that 3 Intel® Xeon™ CPUs (2 GHz) will be sufficient to fulfil the current needs (10 - 15 patients per day) of computing power for the PET quality control of heavy ion therapy at the GSI Darmstadt facility.

(*ii*) The run time is strongly dependent on the applied C-compiler. Whereas the performance of the Xeon™ CPU is superior for the Intel-compiler, the Athlon™ CPU runs the reconstruction code processed by means of the GNU-compiler(gcc-2.95) in the most efficient way.

Patient	Host	CPU	Reconstruction Time / min			Time ratio $\frac{with\ sc.}{without\ sc.}$
			GNU-Compiler with sc***	Intel-Compiler with sc.	without sc.	
1	SGI	R8000	-	338*	**59***	5.7
	PC-Intel	Pentium III	96	76	24	3.2
	PC-AMD	Athlon MP	61	62	22	2.8
	PC-Intel	Xeon	65	**37****	10**	3.7
2	SGI	R8000	-	981*	**216***	4.5
	PC-Intel	Pentium III	220	191	96	2.0
	PC-AMD	Athlon MP	132	144	90	1.6
	PC-Intel	Xeon	137	**97****	36**	2.7

Tab. 3 *Comparison of the reconstruction time on different computers, reconstruction algorithm and compilers for 2 patients, * MIPS C Compiler on SGI system, **Intel Xeon optimized code, ***sc-scatter correction.*

[1] K. Lauckner, FZ Rossendorf, Wiss.-Tech. Ber. FZR-264 (1999) 70
[2] F. Pönisch, W. Enghardt, This Report, p. 99
[3] K. Parodi, W. Enghardt, This Report, p. 103
[4] R. Hinz, Diploma-Thesis, Chemnitz University of Technology (1995)

In-Beam PET Measurements of Proton-Induced β^+-Activity [B, G]

K. Parodi, W. Enghardt, T. Haberer[1]

The important impact of in-beam PET on the quality assurance of carbon ion therapy has been proven by the clinical experience at GSI Darmstadt [1]. The main achievements are *(i)* the monitoring of the maximum carbon ion range, *(ii)* the verification of the field position and *(iii)* the detection of unpredictable deviations of the real treatment from the planned one due to minor errors of the patient positioning or local changes of the patient anatomy (e.g. filling of cavities by mucus) [2]. Based on these results and motivated by the proposed dedicated proton and heavy ion (up to oxygen nuclei) therapy facility at Heidelberg [3], the potential extension of the PET technique to the monitoring of proton therapy is under investigation. In our first experiment [4] three mono-energetic proton beams (energy: 110, 140, 175 MeV; mean intensity: $7 \times 10^7 - 5 \times 10^8$ ions/s) were stopped in targets of PMMA $(C_5H_8O_2)$ placed in the centre of the field of view of the in-beam positron camera installed at the GSI heavy ion therapy facility. Each PET measurement was taken over 10 min of irradiation and 20 min of decay. The amount of β^+-activity was found to be three times (3.2 ± 0.4) larger than that induced by carbon ions at the same range and applied physical dose. The lateral profile of the reconstructed activity distributions (Fig. 1) was found in good agreement with calculations [3] of proton beam broadening in depth. These two observations support the sensitivity of the PET method to detect field mispositioning or anatomical changes of the patient in the proton case, too. The control of the maximum proton range is a more challenging issue, since protons cannot suffer the projectile fragmentation process which leads to a peaked activity distribution in close proximity to the dose maximum in the carbon ion case. The reconstructed β^+-activity depth-profiles were well reproduced in shape by the production of the main positron emitters (^{11}C and ^{15}O) calculated on the basis of experimental cross-sections and the proton flux given by the FLUKA Monte Carlo code (Fig. 2). The shown reconstructed datasets contain events measured during the irradiation and later than 10 min after finishing the irradiation, in order to include and rule out the contribution of the short-lived ^{15}O, respectively. There is a unique relation between the position of the distal slope of the depth-activity curve (e.g. the 50% level), mainly determined by the energy thresholds of the fragmentation reactions, and the primary proton range. In our case the 50% level of the distal part of the measured and simulated profiles was found at about 6 mm lower penetration depth than the range. A very weak (< 0.5 mm) dependence on the initial energy and on the ^{15}O contribution was observed. The spatial activity-range correlation supports the possible extraction of range information by means of a comparison between measured and realistically calculated activity distributions, as done in the carbon ion case. The achievable accuracy is the crucial parameter, since millimeter precision is required. First simulation investigations of proton irradiation with a spread out Bragg peak [4] suggest that a millimeter control of the maximum proton range may be feasible. Future experiments at GSI Darmstadt are planned in order to measure the minimum proton range difference that can be resolved by the in-beam limited angle PET scanner. This will allow a final conclusion on the feasibility and achievable precision of proton range monitoring to be drawn. As a general remark we note that the in-beam technique is recommended in order to exploit the higher activity signal without losing the main contribution coming from ^{15}O in the case of patient irradiation and to acquire data directly in the treatment position.
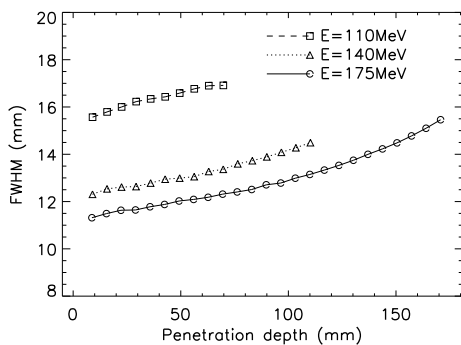
Fig. 1 *Lateral width of the β^+-activity profile versus depth in the central plane of the positron camera field of view for the three proton irradiations.*
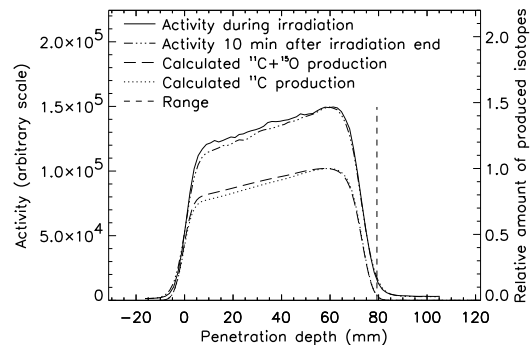
Fig. 2 *Reconstructed β^+-activity depth profiles in comparison with calculated isotope production for the 110 MeV proton irradiation (see text for explanation).*

[1] W. Enghardt et al., Nucl. Phys. A 654 (1999) 1047c
[2] W. Enghardt et al., FZ Rossendorf, Wiss.-Tech. Ber. FZR-271 (1999) 89
[3] K. D. Gross and M. Pavlovic (eds), Proposal for a dedicated ion beam facility for cancer therapy, Darmstadt (1998)
[4] K. Parodi, W. Enghardt and T. Haberer, Phys. Med. Biol. 47 (2002) 21

[1] *Gesellschaft für Schwerionenforschung Darmstadt*

The Evaluation of Carbon Ion Therapy PET Data within the Time Domain

C. KAUSCH[1], W. ENGHARDT

A large fraction of the positron emitters produced during the heavy ion therapy treatments are ^{11}C fragments with a half-life of 20.4 min. The activity accumulates during the irradiation in bony structures, whereas it is washed out in well vascularized tissue (e. g. the brain). This leads to discrepancies between the measured and the simulated PET images [1] and, therefore, a definitive statement on the accuracy of the dose deposition may be complicated or even impossible. Since the PET data are recorded in list mode, it is possible to evaluate the β^+-activity both in space and time [2]. To obtain tissue dependent washout data from the large amount of PET scans acquired for more than 100 patients treated at the GSI therapy facility, a software tool has been developed. In a first step volumes of interest - VOI - (i. e. tissue regions where the washout is to be determined) are interactively selected in images showing the β^+-activity distribution superimposed onto X-ray computed tomograms (CT) as shown in Fig. 1.
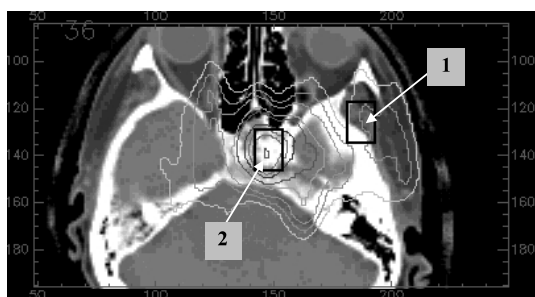
Fig. 1 *Transversal CT-image with the β^+-activity distribution through the head of a patient. The black boxes mark the examined VOIs with large (1) and low (2) washout.*

In the second step the time histogram of those lines of response, which intersect the VOI, is constructed and an effective lifetime can be calculated by means of a fitting procedure (Figs. 2 and 3). For precise fitting results the signal-to-noise ratio of the time histograms should be large. As the count rate is notoriously poor in PET studies performed simultaneously with the therapeutic irradiations and the available time intervals are short compared to the half-life of ^{11}C, it is planned for the future to sum up the PET-measurements for all therapy fractions of a certain patient and portal. Although this has not been implemented yet, the feasibility of the concept can be demonstrated for a treatment during which the beam delivery was interrupted by more than 15 min. Fig. 1 shows a transversal slice of the CT-images of the head, with the β^+-activity distribution superimposed. VOI (1) is located in a region with large blood flow whereas VOI (2) is placed in the skull base (bone). The corresponding time distributions are shown

in Figs. 2 and 3, respectively. The relaxation of activity is an exponential process as well as the washout of emitter concentration. Thus, the measured time dependent count rate $c(t)$ is fitted to

$$c(t) = p_1\, e^{-\frac{t}{\tau_P}} + p_1\, e^{-\frac{t}{\tau_C}}, \tag{1}$$

where p_1 is the normalization factor, τ_P and $\tau_C = 1766\,\mathrm{s}$ are the mean-lives for the activity washout and the ^{11}C decay, respectively. For comparison the decline of activity due to ^{11}C decay only is shown by the grey curve.
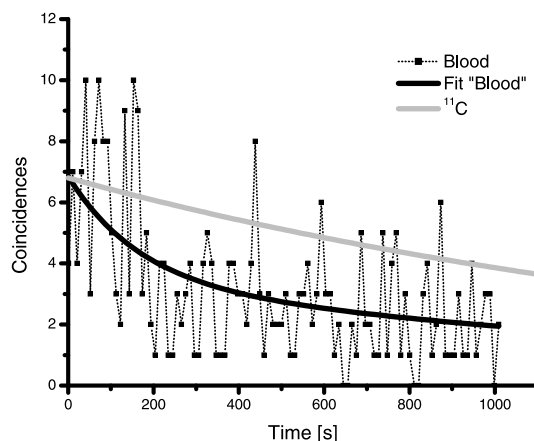
Fig. 2 *PET count rate versus time for VOI (1) with high perfusion. The black line shows the exponential fit of the data, the grey line shows decline due to ^{11}C decay only. The list mode data are rebinned into 10 s time intervals.*
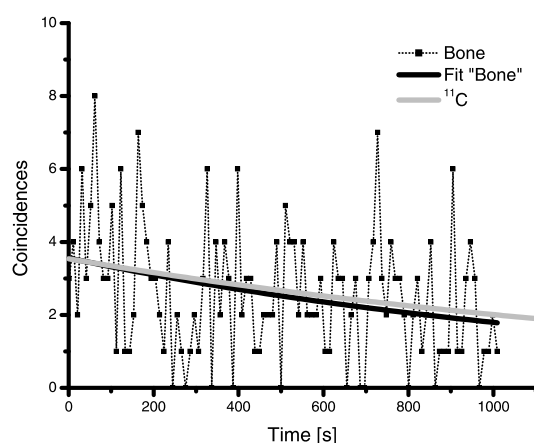
Fig. 3 *PET count rate versus time for VOI (2) with low perfusion.*

Whereas for the soft tissue in Fig. 2 an effective mean-life of $\tau_P = 165\,\mathrm{s}$ has been found, the emitter concentration in the bone, shown in Fig. 3, drops much slower $(\tau_P = 1220\,\mathrm{s})$.

[1] W. Enghardt et al. Nucl. Phys., A 654 (1999) 1047c
[2] R. Hinz, FZ Rossendorf, Wiss.-Tech. Ber. FZR-286 (2000) 59

[1] *Gesellschaft für Schwerionenforschung Darmstadt*

The Influence of the Carbon Ion Beam Microstructure on In-Beam PET Acquisition at GSI Darmstadt: Time-Correlation Measurements [B, G]

K. Parodi, W. Enghardt, J. Pawelke, H. Eickhoff[1], P. Forck[1], T. Haberer[1], D. Schardt[1]

The data registered by the in-beam positron camera for PET quality assurance of ^{12}C ion therapy during particle extraction from the synchrotron are corrupted by a high noise level. Hence, they are rejected before tomographic reconstruction. This reduces the counting statistics of the PET images by a factor of about 2. As a basis for the elaboration of a data acquisition scheme that will avoid this, the physical reason for this increase of noise is under investigation. Previous studies suggested the possible explanation to be a wrong correction of the PET data for random coincidences [1]. The random correction algorithm implemented by the manufacturer of the PET data acquisition system (CTI PET Systems, Knoxville, TN, USA) assumes a slowly varying activity as it is usual in radiotracer imaging. Therefore, the randoms are estimated from the count rate in a delayed coincidence time window shifted by 128 ns with respect to the prompt one. However, if the γ-radiation following nuclear reactions caused by the carbon beam has a microstructure as indicated by [1], this random correction will fail. To test this conjecture, time spectra of the γ-rays following the ^{12}C bombardment of organic matter relative to the synchrotron radiofrequency (RF) have been measured. Being impossible to operate the PET camera for such an investigation, a GSO scintillating crystal coupled to a fast PMT was chosen. GSO exhibits stopping properties very similar to the BGO-detectors of the positron camera but has a 5 times shorter fluorescence time constant and is, therefore, more suited for timing measurements. The size of the GSO-crystal (2 cm radius, 2.5 cm depth) was chosen in order to have a detection efficiency very similar to that of a single BGO block detector of the PET scanner. The electronics scheme is shown in Fig. 1.
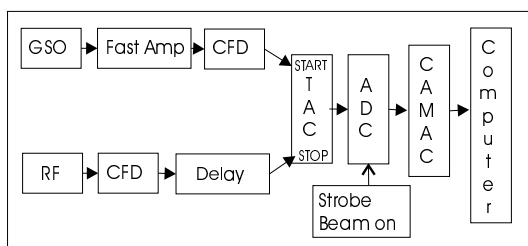
Fig. 1 *Scheme of the NIM-CAMAC electronics used for measuring RF-γ time-distributions.*

The data have been acquired exclusively during particle extraction (beam on). The detector was placed perpendicularly to the beam at the same distance (41 cm) of the PET camera heads from the isocentre of the treatment unit. Five monoenergetic carbon ion beams from 88.83 to 426.11 $AMeV$ with corresponding intensity from $1.5 \cdot 10^8$ to $4 \cdot 10^6$ ions per 2 s spill, resulting

in $20 - 25\%$ ADC dead-time, were completely stopped in blocks of PMMA ($C_5H_8O_2$). This configuration well resembles the typical irradiation conditions during therapy. The experiment confirmed a time-correlation of the detected γ-rays with the synchrotron RF, as shown for the 280.48 $AMeV$ beam in Fig. 2. The shape of the measured time-curve supports the physical hypothesis of [1] that the time distribution of the γ-rays follows the beam microstructure. The steep leading edge of the peak in Fig. 2 is formed by prompt γ-rays following nuclear reactions, whereas the slope of the falling edge is diminished by delayed γ-rays from the decay of isomeric states and radioisotopes with half-lives in the nanosecond region. The constant bias is primarily due to the decay of long-lived isotopes.
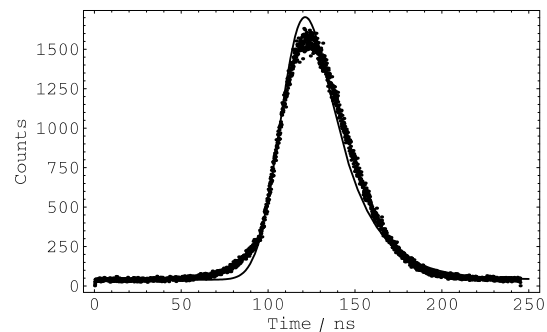
Fig. 2 *Time distribution measured for a 280.48 $AMeV$ ^{12}C beam (RF period: 282.4 ns). The line shows a non-linear least-squares fit based on the model explained in the text.*

This interpretation is obviously supported by a simple model that describes the count rate $N(t)$ by a convolution of the Gaussian beam microbunches with an exponential decay:

$$N(t) = b + a \int_0^t e^{-\frac{(t'-t_0)^2}{2\sigma^2}} e^{-\frac{(t-t')}{\tau}} dt'. \qquad (1)$$

The four free parameters b, a, t_0 and τ are the bias, the normalization, the Gaussian mean value (dependent on the delay of Fig. 1) and an "effective" decay time for all the excited nuclear levels and radioisotopes, respectively. The quantity σ is obtained from the measured FWHM of the beam microstructure [1]. An average value of about 22 ns for the effective decay time was extracted from all the data. Singles energy spectra taken in the same experimental configuration showed a significant amount of events in the γ-ray energy window accepted by the PET camera (250 - 850 keV). This result strongly supports our hypothesis on the nature of the increased noise in the PET data. However, it has to be finally confirmed by a simultaneous energy-time measurement.

[1] K. Parodi et al., FZ Rossendorf, Wiss.-Tech. Ber. FZR-319 (2001) 97

---

[1] *Gesellschaft für Schwerionenforschung Darmstadt*

A New Fully 3D Maximum Likelihood PET Reconstruction Applicable to Different Detector Arrangements

P. Crespo[1], K. Lauckner[2], W. Enghardt

We developed a fully 3D, maximum likelihood based, PET reconstruction routine applicable to different coincidence detector arrangements for PET. It allows to study the influence of several γ-ray detector geometries onto the corresponding reconstructed images. The scope of this study is to optimize a tomograph to be fully dedicated to the PET monitoring of heavy ion tumor therapy with a rotating beam delivery (gantry).

A special purpose routine was needed in order to surpass situations not approached before: (i) the low counting statistics acquired during therapy with carbon ions makes the application of already developed 3D iterative algorithms with 2D sampling modes impossible, (ii) a fixed dual head PET scanner provides a coincidence detector with spatially variant response, which forbids the application of the algebraic reconstruction methods used in nuclear medicine and (iii) for the unprecedent huge size of coincident channels both for a closed ring camera, or a dual head camera with a small gap, the direct application of the routine previously developed for the positron tomograph at the GSI treatment site [1] is not feasible (the number of possible coincidence channels increases from 4 to 170 millions).

The new routine first samples the list mode data into coincidence channels according to a self-developed channel factorizing scheme. This scheme, combined with direct memory allocation during runtime, feeds the rest of the reconstruction routine with a packed matrix Y containing only the measured data (no empty coincidence channels). The routine than processes Y to find the most probable image X with the maximum likelihood estimation maximization algorithm [2]:

$$x_i^{(n)} = x_i^{(n-1)} \sum_j a_{ij} \frac{y_j}{\sum_k a_{kj} x_k^{(n-1)}} \qquad (1)$$

where $x_i^{(n)}$ is the calculated activity of the ith voxel, at the nth iteration. Each image voxel i contributes with weight a_{ij} to the jth coincidence channel. y_j is the measured activity at the jth channel of the tomograph.

In order to assess the reliability of the new routine we developed a package being capable of simulating PET list mode data sets for a full ring or dual head positron camera. The detector dimensions and positioning are those of the commercial scanner CTI ECAT EXACT HR+ (~ 82 cm diameter, ~ 16 cm axial length). Fig. 1 illustrates a dual head camera with the reference system implemented. Whether implemented on an horizontal beam line or under a rotating gantry, the beam will lie in the plane XZ_{PET} in all situations, as detailed in [3]. Fig. 2 shows a reconstructed image obtained from the simulation of 100 millions annihilation points homogeneously distributed through a hollow sphere with 3 cm outer radius and 1.5 cm inner radius and detected in a closed ring camera. This volume shape was chosen due to its similarity to β^+-distributions that, in radiotherapeutic situations, often occur surrounding the nasal and paranasal cavities of the treated patients with skull base tumours. For this volume shape the geometrical efficiency was 16.2 %. The image shows symmetric, steep edges, corresponding to the simulation.
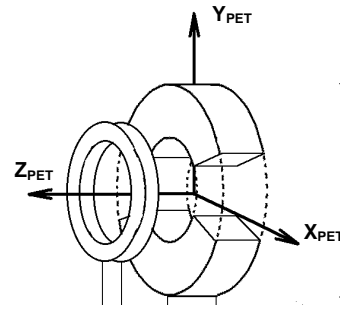
Fig. 1 *Dual head positron camera and metal support ring. The camera rotates around the Z_{PET} axis.*
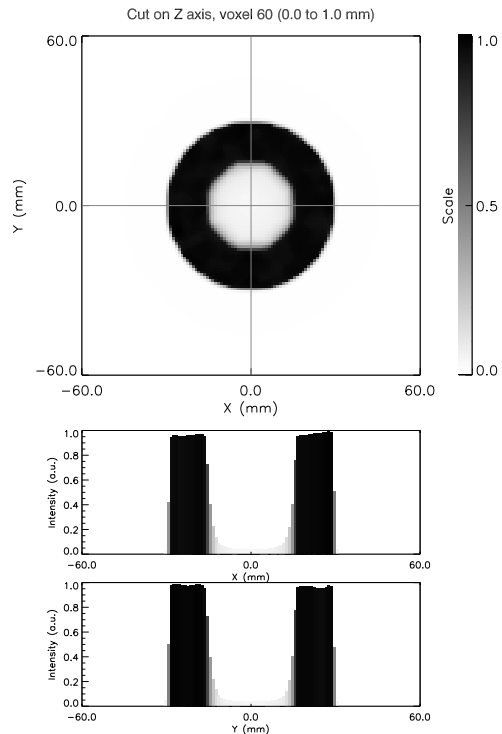
Fig. 2 *Upper image: Reconstructed image (50 iterations) of a simulated hollow sphere. A closed ring PET camera (CTI ECAT EXACT HR+) was simulated, with 16 millions events detected. Axes according to Fig. 1. Lower images: Linear profiles through the axes of the 2D image above.*

[1] *Gesellschaft für Schwerionenforschung Darmstadt*
[2] *The Scientific Consulting Group, Freiburg, Germany*

Fig. 3 illustrates the image degradation induced by the separation of the detectors in a dual head PET camera. The strongest effect seen is the elongation and decrease of intensity of the image along the Y axis. This expected effect arises from the lack of detectors covering that axis in the case of the dual head cameras. Yet, as pointed out, the beam line lies in all situations within the XZ_{PET} plane, where the images do not show the slightest distortion (due to the fact that this plane is perpendicular and symmetric to the gap). This means that the PET quality control of heavy ion radiotherapy is, and can continue to be in the presence of a rotating gantry, extremely precise in the monitoring of the beam range and detection of over-ranges (spikes), mostly in regions located near the iso-center. Lateral straggling evaluation is equally precise in the same terms. The verification of organs at risk lying in planes along the gap (Y_{PET}) would strongly benefit from a PET camera with the smallest possible distance between the heads, if a closed ring is not viable.

The influence of the poor statistics data sets collected in in-beam PET can be seen by comparing the top left image in Fig. 3 and the top image in Fig. 2 (100 times more events). The contours are still clear in the low statistics case, but the images become noisier.

Fig. 4 displays the same situations of Fig. 3 but with twice the number of annihilations simulated, with the result that the image contrast sharpens in all cases.

In summary, a dual head positron tomograph brings the advantage of better flexibility in patient positioning at the expense of loss of intensity and irrecoverable image deformation. These losses can now be quantified with the present routine in order to find an optimum compromise. Still, in order to be able to evaluate the quality of the images from the several camera configurations in real therapeutic situations, β^+-distributions simulated from real treatments [4] should now be interfaced to the reconstruction routine.
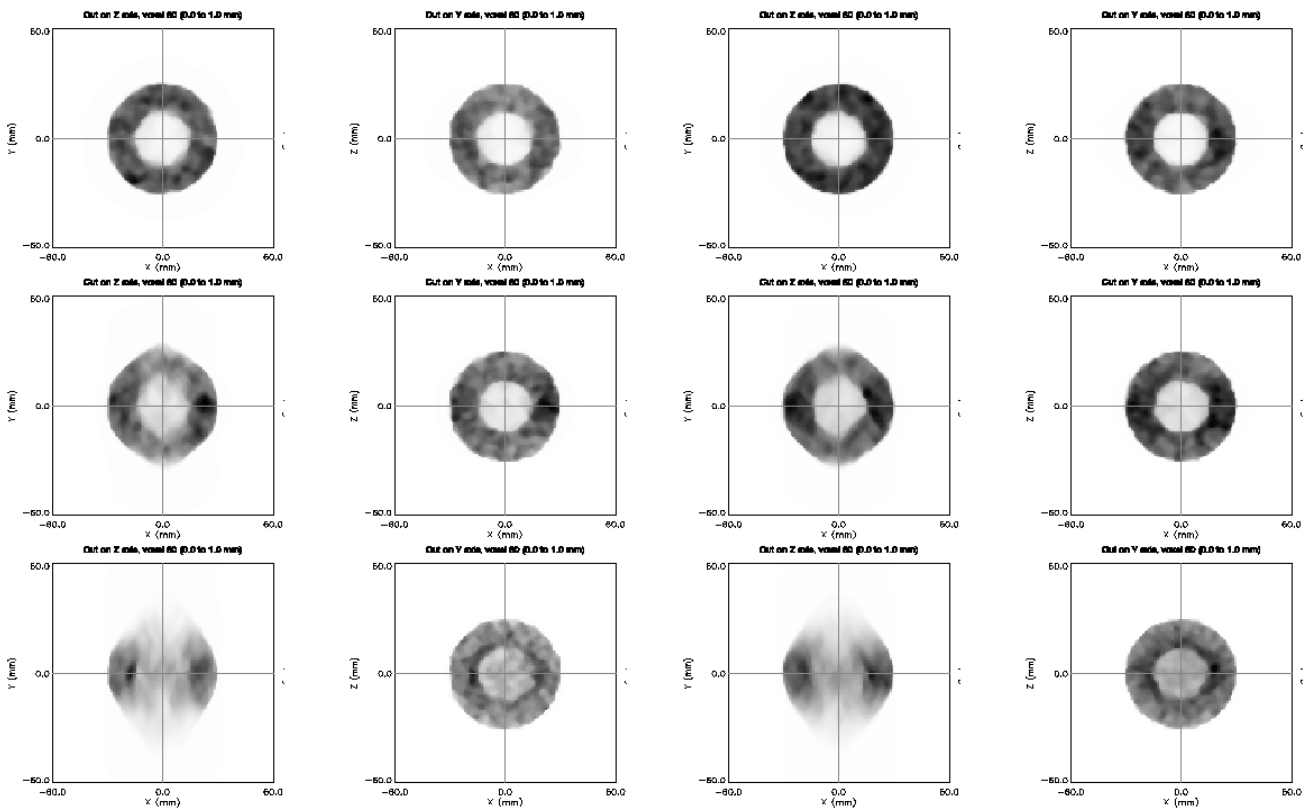
Fig. 3 *Set of images corresponding to the reconstruction (50 iterations) of simulated events detected with a full ring PET camera (top row, 162000 events), a dual head camera with a gap of 34 cm (middle row, 114000 events) and with a gap of 63 cm (bottom row, 69000 events). All simulations followed 1 million annihilations.*

Fig. 4 *Reconstruction details as in Fig. 4, but with 2 times the number of simulated events (2 millions annihilations followed inside the hollow sphere).*

[1] K. Lauckner, FZ Rossendorf, Wiss.-Tech. Ber. FZR-264 (1999)
[2] L.A. Shepp and Y. Vardi, IEEE Trans. Med. Imag. MI-1 (1982) 689
[3] P. Crespo, K. Lauckner, W. Enghardt, FZ Rossendorf, Wiss.-Tech. Ber. FZR-319 (2001) 100
[4] B.G. Hasch, Ph.D. Thesis, Dresden University of Technology (1996)

Evaluation of Avalanche Photodiode Arrays for the Readout of High Granularity Scintillator Matrices

P. Crespo[1], M. Kapusta[2], M. Moszyński[2], W. Enghardt, J. Pawelke, M. Szawlowski[3]

In order to provide sufficient flexibility for patient positioning at the Heidelberg charged hadron tumor treatment facility, γ-ray detectors with large sensitive area and small volume are highly desirable for the positron camera to combine with a rotating beam delivery (gantry). Photon detector technology yields increasingly more compact PET-detectors consisting of inorganic scintillators, e.g. bismuth germanate (BGO) or lutetium oxyorthosilicate (LSO), coupled to either a position sensitive photomultiplier (PSPMT) [1] or to avalanche photodiode arrays (APDAs) [2,3]. We have shown [4] that LSO is a suitable scintillation material for in-beam PET due to its higher light yield and shorter decay time when compared to BGO. APDs are preferable to PMTs due to their higher compactness. Furthermore, the presence of weak stray fields originating from the bending magnets of the gantry may permanently deteriorate the performance of a PSPMT. Therefore, PET-detectors assembled from LSO-crystals and APDA are the first choice for an in-beam positron camera.

With this goal set, we have evaluated the performance of a recently released large area avalanche photodiode (LAAPD) array from Advanced Photonics, Inc. (API). The device is a monolithic 2×2 squared pixels structure with 21 mm^2 total active area and 2.3 mm pitch. Although it presents a high linear fill factor of 90 %, measured in dc-mode with a laser fine scan by the manufacturer, we measured light pulse crosstalk values less than 1.7 % between all pixels by sequentially illuminating the center of one pixel with a 1.7 mm diameter light spot and registering the amplitude spectra of all pixels.

These good results are due to the fabrication technique used: one single substrate consisting of a p-type epitaxial layer and an n-type neutron transmutation doped layer is etched using deep reactive ion etching, yielding four adjacent diodes with high gain uniformity. We measured an inter-pixel gain variation with X-rays smaller than 1.3 %. Although the APDA allows stable operation with high gains up to 200, we obtained its noise minimum at an excellent low equivalent noise charge of 16 electrons rms with an internal gain of 50 and with 1 μs signal shaping time.

A 2×2 LSO crystal matrix ($2 \times 2 \times 10$ mm^3 each crystal) optically isolated with teflon tape and coupled with silicon oil to the APDA allowed individual crystal identification to be performed, as summarized in Fig. 1. An energy resolution of 12.3 % was obtained for the FWHM of the 511 keV photopeak, a promising result when compared to the ~ 20 % offered by the BGO/PMT solution. The LSO crystals light yield was calibrated with a XP2020Q PMT which allowed the number of electron-hole pairs (e-h) of the APD to be found at 9200 e-h/MeV. Coincidence timing between one LSO/APD channel and a fast scintillator (BaF$_2$) coupled to a fast PMT resulted in a time resolution of 1.9 ns FWHM, as detailed in Fig. 2. This result is one of the best published for APDAs and corresponds to 2.7 ns FWHM if two LSO/APD detectors are used. Energy and time resolution are essential variables for PET in order to effectively suppress Compton scattered and random events, respectively.
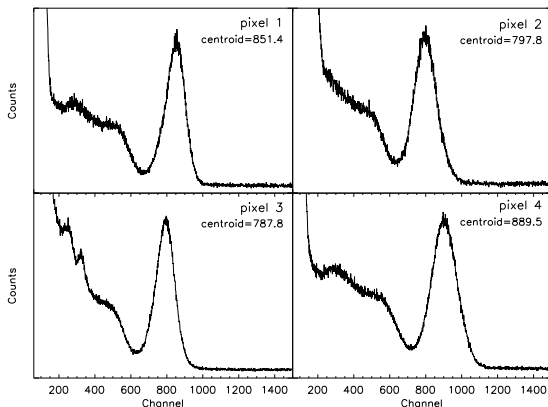
Fig. 1 *Energy spectra from a ^{22}Na γ-source irradiating a 2×2 LSO crystal matrix coupled individually to the 2×2 pixels of the API device.*
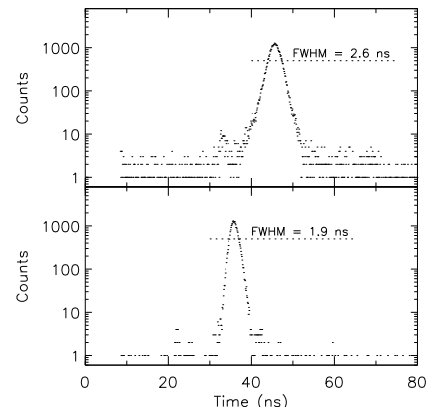
Fig. 2 *Time spectra measured with a ^{22}Na source. Upper image: Threshold set at 350 keV. Lower image: Energy window set at the 511 keV photopeak with a fast-slow setup.*

[1] H. Kyushima et al., IEEE Nucl. Sci. Symp. and Med. Imag. Conf., Lyon (2000), Conference Records
[2] M. Kapusta et al., IEEE Nucl. Sci. Symp. and Med. Imag. Conf., San Diego (2001), Conference Records
[3] S.I. Ziegler et al., Eur. J. Nucl. Med. 28 (2001) 136
[4] K. Lauckner et al., IEEE Nucl. Sci. Symp. and Med. Imag. Conf., Lyon (2000), Conference Records

[1] *Gesellschaft für Schwerionenforschung Darmstadt*

[2] *Soltan Institut for Nuclear Studies, 05-400 Świerk-Otwock, Poland*

[3] *Advanced Photonix, Inc., Camarillo, CA 93012, USA*

Author Index

Kröll, Th.	80,82	Prade, H.	75
Kurcewicz, J.	83	Pröhl, D.	10,11,12
Kutsarova, T.	82	Pühlhofer, F.	53
La Commara, M.	84,85	Quast, T.	22
Langanke, K.	85	Rainovski, G.	80,82
Langenhagen, H.	7,12,18	Reif, J.	75
Langer, M.	16	Reiter, P.	75
Lauckner, K.	104	Rejmund, M.	85
Laue, F.	53	Reppe, B.	22
Leege, K.-W.	10	Reznik, B.L.	63
Lehnert, U.	17,18,19,20	Riedel, Th.	37
Lenzi, S.M.	83	Rimarzig, B.	26,32
Lessmann, E.	89	Roeckl, E.	83,84,85
Lieb, K.P.	82	Rossbach, D.	76
Linnemann, A.	78	Rubio, B.	83
Mallion, S.N.	38,40,77	Rusev, G.	77
Marginean, N.	80,82	Sadovski, A.	49,50,51
Martinez-Pinedo, G.	85	Sawicka, M.	85
Martinez, T.	80,82,83	Schamlott, A.	27
Martin, J.	36	Schardt, D.	103
Matschinsky, P.	78	Scheck, M.	77,78
Mayet, P.	85	Scheinast, W.	52,53
Mazzocchi, C.	83,84	Schilling, K.D.	37,41,77,78,80,82
Menzel, M.	53	Schlegel, C.	85
Michel, P.	13,17,18,19,20	Schlenk, R.	37,41
Möller, K.	21,66	Schlett, M.	100
Moszyński, M.	106	Schmidt, K.	84,85
Müller, H.	62,94,95	Schnare, H.	75
Mukha, I.	83	Schneider, C.	53
Nácher, E.	83,84	Schumann, W.	97
Napoli, D.R.	80,82,83	Schurig, R.	13,14,15,17
Naumann, B.	18,25,42,44,45,57,94,95,97	Schwab, E.	52,53
Naumann, L.	49,50,51,52,53	Schwalm, D.	75
Nenoff, N.	76	Schweizer, B.	18
Neubert, W.	16,93,94,96,97	Schwengner, R.	39,37,41,75,76,77,
Neumann, W.	37,41		78,80,82,83,84,85
Neumann, H.	96	Sczepan, M.	36
Neyens, G.	76	Seibert, J.	49,50,51,54
Nieminen, A.	85	Seidel, W.	26,32,34,35,36
Noack, K.	95	Seidel, K.	42,45
Nord, A.	78	Senger, P.	52,53
Nowacki, F.	85	Servene, T.	75
Oepts, D.	26,32	Sharma, H.	39
Oeschler, H.	52,53	Shin, Y.	52,53
Palm, M.	91	Skoda, S.	75
Pancholi, S.	76	Slonina, D.	90
Panteleeva, A.	89,90,91,92	Sobiella, M.	49
Parodi, K.	98,101,103	Spekl, K.	90
Pavlenko, O.P.	58,59,67	Stedile, F.	77,78
Pawelke, J.	89,90,91,92,96,103,106	Stefanova, E.A.	82
Penttilä, H.	85	Steinhardt, T.	75,84
Pietralla, N.	78	Stephan, J.	5,9
Pitz, H.H.	77,78	Stoevesandt, B.	91
Plettner, C.	84	Ströbele, H.	52,53
Plochocki, A.	84,85	Sturm, C.	52,53
Ploskon, M.	52	Surówka, G.	53
Pönisch, F.	99,100	Szawlowski, M.	106

Tain, J.L.	83
Teichert, J.	17,18,19,20,22
Teughels, S.	76
Thelen, O.	75,80,82
Thomas, H.G.	75
Titov, A.I.	63,65
Uhlig, F.	52,53
Ur, C.A.	80,82,83
Volkov, V.	23,24
Vyvey, K.	76
Wagner, A.	37,38,39,41,52,53,77,80,82
Waluś, W.	52,53
Weiss, F.-P.	42
Werner, V.	78
Wheaton, S.	68
Winter, G.	75
Wohlfarth, D.	32,33,34
Wolf, U.	26,27,32,35
Wolf, Gy.	59,60
Wünsch, R.	31,24,32,33
Wustmann, B.	13
Zétényi, M.	60
Zschocke, S.	58
Zylicz, J.	84

Publications and Talks

Publications[1]

Production of ω mesons in proton-proton collisions
(Phys. Lett. B 522 (2001) 16)

Abd El-Samad, S., M. Abdel-Bary, K.T. Brinkmann, H. Clement, **S. Dshemuchadse**, H. Dutz, W. Eyrich, A. Erhardt, D. Filges, A. Filippi, H. Freiesleben, M. Fritsch, J. Georgi, A. Gillitzer, D. Hesselbarth, B. Jakob, L. Karsch, K. Kilian, H. Koch, J. Kress, E. Kuhlmann, S. Marcello, S. Marwinski, S. Mauro, W. Meyer, **P. Michel**, **K. Möller**, H. Mortel, H.P. Morsch, **L. Naumann**, C. Plettner, M. Richter, E. Roderburg, **A. Schamlott**, P. Schönmeier, M. Schulte-Wissermann, W. Schroeder, F. Stinzing, M.Steinke, G.Y. Sun, G.J. Wagner, M. Wagner, A. Wilms, S. Wirth

Abstract: The cross section for the production of ω mesons in proton-proton collisions has been measured in a previously unexplored region of incident energies. Cross sections were extracted at 92 MeV and 173 MeV excess energy, respectively. The angular distribution of the ω at ε=173 MeV is strongly anisotropic, demonstrating the importance of partial waves beyond pure s-wave production at this energy.

Quantum Correlations in Rotating Nuclei
(Phys. of Atomic Nucl. 64 (2001) 1076)

Almehed, D., F. Dönau, R.G. Nazmitdinov

Abstract: Using the Hamiltonian that consists of the separable quadrupole + pairing forces and the cranking term, we analyze the correlations associated with shape, orientation, and particle-number fluctuations in rotating nuclei. Quantum fluctuations around mean field solutions are treated in the random phase approximation (RPA), with special emphasis on the restoration of rotational symmetry and particle number conservation. The mean field calculations have been made within the self-consistent cranking model. The effect of the RPA correlation energy for the moment of inertia is studied with the integral representation method proposed.

Pairing Correlations in High-K Bands
(Phys. Rev. C 63 (2001) 044311)

Almehed, D., S. Frauendorf, F. Dönau

Abstract: The tilted axis cranking model is used in combination with the random phase approximation and particle number projection to analyze the influence of dynamical pair correlations in the high-K bands of ^{178}W and their effect on relative energy and angular momentum. The calculations show the importance of dynamical pair correlations to describe the experiment as well as advantages and problems with the different models in the superfluid and normal state regions.

Magnetic Dipole Rotational Bands in Odd-A Rb Isotopes
(Phys. Rev. C 64 (2001) 034308)

Amita, A.K. Jain, **V.I. Dimitrov, S. Frauendorf**

Abstract: The hybrid version of tilted axis cranking has been used to study the existence of magnetic rotation in the $\Delta I = 1$ bands of odd-A ^{79,81,83,85}Rb isotopes. The bands are found to be built on prolate three quasiparticle $\pi(g_{9/2}) \otimes \nu[g_{9/2}(fp)^1]$ configuration. The results exhibit a rapid onset and decline of magnetic rotation as we go from $N = 42$ to 48. The ^{83}Rb appears to be a better case of magnetic rotation among these four Rb isotopes.

Nuclear Temperatures Obtained From-Light-Changed-Particle Yields in Low-Energy Ternary Fission
(Eur. Phys. J. A 12 (2001) 185)

Andronenko, M.N., L.N. Andronenko, **W. Neubert**, D.M. Seliverstov

Abstract: Nuclear temperatures were determined from yields of isotopes with $1 \leq Z \leq 14$ accompanying the spontaneous and neutron-induced fission of heavy elements. The mean temperature derived from the corresponding temperature distributions amounts to 1.10±0.15 MeV.

---

[1]From the authors printed in **bold** further information can be obtained

Differential Directed Flow in Au+Au Collisions

Andronic, A., W. Reisdorf, J.P. Alard, V. Barret, Z. Basrak, N. Bastid, A. Bendarag, G. Berek, R. Caplar, P. Crochet, A. Devismes, P. Dupieux, M. Dzelalija, C. Finck, Z. Fodor, A. Gobbi, Yu. Grishkin, O.N. Hartmann, N. Herrmann, K.D. Hildenbrand, B. Hong, J. Kecskemeti, Y.J. Kim, M. Kirejczyk, P. Koczon, M. Korolija, **R. Kotte**, T. Kress, R. Kutsche, A. Lebedev, Y. Leifels, **W. Neubert**, D. Pelte, M. Petrovici, F. Rami, B. de Schauenburg, D. Schüll, Z. Seres, B. Sikora, K.S. Sim, V. Simion, K. Siwek-Wilczyńska, V. Smolyankin, M.R. Stockmeier, G. Stoicea, P. Wagner, K. Wiśniewski, **D. Wohlfarth**, I. Yushmanov, A. Zhilin

Abstract: We present experimental data on directed flow in semi-central Au+Au collisions at incident energies from 90 to 400·A MeV. For the first time for this energy domain, the data are presented in a transverse momentum differential way. We study the first order Fourier coefficient ν_1 for different particle species and establish a gradual change of its patterns as a function of incident energy and for different regions in rapidity.

Transition from In-Plane to Out-of-Plane Azimuthal Enhancement in Au+Au Collisions

Andronic, A., G. Stoicea, M. Petrovici, V. Simion, P. Crochet, J.P. Alard, R. Averbeck, V. Barret, Z. Basrak, N. Bastid, A. Bendarag, G. Berek, R. Čaplar, A. Devismes, P. Dupieux, M. Dželalija, M. Eskef, Ch. Finck, Z. Fodor, A. Gobbi, Y. Grishkin, O.N. Hartmann, N. Herrmann, K.D. Hildenbrand, B. Hong, J. Kecskemeti, Y.J. Kim, M. Kirejczyk, M. Korolija, **R. Kotte**, T. Kress, R. Kutsche, A. Lebedev, K.S. Lee, Y. Leifels, V. Manko, H. Merlitz, D. Moisa, **W. Neubert**, D. Pelte, C. Plettner, F. Rami, W. Reisdorf, B. de Schauenburg, D. Schüll, Z. Seres, B. Sikora, K.S. Sim, K. Siwek-Wilczyńska, V. Smolyankin, M.R. Stockmeier, M. Vasiliev, P. Wagner, K. Wiśniewski, **D. Wohlfarth**, I. Yushmanov, A. Zhilin

Abstract: The incident energy at which the azimuthal distributions in semi-central heavy ion collisions change from in-plane to out-of-plane enhancement - E_{tran} is studied as a function of mass of emitted particles, their transverse momentum and centrality for Au+Au collisions. The analysis is performed in a reference frame rotated with the sidewards flow angle (Θ_{flow}) relative to the beam axis. A systematic decrease of E_{tran} as function of mass of the reaction products, their transverse momentum and collision centrality is evidenced. The predictions of a microscopic transport model (IQMD) are compared with the experimental results.

Static Quadrupole Moment of the Five-Quasiparticle K=35/2 Isomer in ^{179}W Studied with the Level-Mixing Spectroscopy Method

Balabanski D.L., K. Vyvey, G. Neyens, N. Coulier, R. Coussement, G. Georgiev, A. Lépine-Szily, S. Ternier, S. Teughels, M. Mineva, P.M. Walker, P. Blaha, D. Almehed, **S. Frauendorf**

Abstract: The spectroscopic quadrupole moment of the high-spin, high-K five-quasiparticle isomer ($K^\pi = \frac{35^-}{2}$, $T_{1/2}$=750(80) ns, E_i = 3349 keV) in ^{179}W has been determined using the level mixing spectroscopy method. A value $Q_s = 4.00(^{+0.83}_{-1.06})e$ b was derived, which corresponds to an intrinsic quadrupole moment $Q_0 = 4.73(^{+0.98}_{-1.25})e$ b and to a quadrupole deformation $\beta_2 = 0.185(^{+0.038}_{-0.049})$. These values differ significantly from the deduced ground-state quadrupole moments and are in disagreement with the current theoretical predictions in this mass region.

Quadrupole Moments of High-Spin Isomers: Test of the Tilted-Axis Cranking Model

Balabanski, D.L., K. Vyvey, G. Neyens, **D. Almehed**, P. Blaha, D. Borremans, S. Chmel, N. Coulier, R. Coussement, W. De Clercq, **S. Frauendorf**, G. Georgiev, H. Hubel, A. Lépine-Szily, M. Mineva, N. Nenoff, S. Pancholi, D. Rossbach, **R. Schwengner**, S. Teughels, P.M. Walker

Abstract: We report the results of recent measurements of the spectroscopic quadrupole moments of high-spin isomers. For the $K^\pi = \frac{35^-}{2}$ five-quasiparticle isomer in ^{179}W we measured Q_s=4.00($^{+0.83}_{-1.06}$) eb. It corresponds to a smaller deformation compared to the ground states of the W isotopes and is in disagreement with the current theoretical predictions. We also measured the quadrupole moment of the I^π=11$^-$ isomer in ^{196}Pb, Q_s=(-)3.41(66) eb. It has the same proton ($s_{1/2}^{-2} h_{9/2} i_{13/2}$) configuration as the one suggested for the I^π=16$^{(-)}$ magnetic bandhead which allows to deduce the quadrupole moment of the 16$^-$ state as Q_s=-0.316(97) eb. This small value proves the near sphericity of the bandhead.

YSO, LSO, GSO and LGSO. A Study of Energy Resolution and Nonproportionality
(IEEE Trans. Nucl. Sci. 47 (2000) 1319)

Balcerzyk, M., M. Moszynski, M. Kapusta, D. Wolski, **J. Pawelke**, M. Melcher

Abstract: We have studied the nonproportionality and intrinsic energy resolution of cerium depot YSO, GSO, LSO and LGSO crystals. While LSO and YSO have similar light output, GSO and LGSO have ca. 70% and 20% lower light output than LSO, respectively. YSO, a compound containing fairly light elements, was expected to have proportional light output vs. energy, like YAP:Ce. Surprisingly it has almost the same nonproportional as LSO and GSO. The nonproportionality of YSO is followed by large values of intrinsic energy resolution. The comparison of the nonproportionality of YSO-LSO and YAP-LuAP pairs indicates that high proportionality is connected with the structure of the crystal and not with the presence of light elements. To our knowledge, this is the first study of nonproportionality and intrinsic resolution for LGSO.

ϕ and ω Meson Production in pp Reactions at p_{lab}=3.67 GeV/c
(Phys. Rev. C 63 (2001) 24004)

Balestra, F., Y. Bedfer, R. Bertini, L.C. Bland, A. Brenschede, F. Brochard, M.P. Bussa, S. Choi, M. Debowski, **R. Dressler**, M. Dzemidzic, J.-Cl. Faivre, I.V. Falomkin, L. Fava, L. Ferrero, J. Foryciarz, I. Fröhlich, V. Frolov, R. Garfagnini, A. Grasso, **E. Grosse**, S. Heinz, V.V. Ivanov, W.W. Jacobs, W. Kühn, A. Maggiora, M. Maggiora, A. Manara, D. Panzieri, H.-W. Pfaff, G. Piragino, G.B. Pontecorvo, A. Popov, J. Ritman, P. Salabura, V. Tchalyshev, F. Tosello, S.E. Vigdor, G. Zosi

Abstract: The exclusive production cross sections for ω and ϕ mesons have been measured in proton-proton reactions at $p_{lab} = 3.67$ GeV/c. The observed ϕ/ω cross section ratio is $(3.8 \pm 0.2^{+1.2}_{-0.9}) \times 10^{-3}$. After phase space corrections, this ratio is enhanced by about an order of magnitude relative to naive predictions based upon the Okubo-Zweig-Iizuka (OZI) rule, in comparison to an enhancement by a factor ~ 3 previously observed at higher beam momenta. The modest increase of this enhancement near the production threshold is compared to the much larger increase of the ϕ/ω ratio observed in specific channels of $\bar{p}p$ annihilation experiments. Furthermore, differential cross section results are also presented which indicate that although the ϕ meson is predominantly produced from a $^3P_1$ proton-proton entrance channel, other partial waves contribute significantly to the production mechanism at this beam momentum.

ANKE, a New Facility for Medium Energy Hadron Physics at COSY-Jülich
(Nucl. Instr. Meth. A 462 (2001) 364)

Barsov, S., U. Bechstedt, W. Bothe, N. Bongers, G. Borchert, W. Borgs, W. Bräutigam, M. Büscher, W. Cassing, V. Chernyshev, B. Chiladze, J. Dietrich, M. Drochner, S. Dymov, W. Erven, R. Esser, A. Franzen, E.S. Golubeva, D. Gotta, T. Grande, D. Grzonka, A. Hardt, M. Hartmann, V. Hejny, L. von Horn, L. Jarczyk, H. Junghans, A. Kacharava, B. Kamys, A. Khoukaz, T. Kirchner, F. Klehr, W. Klein, H.R. Koch, V.I. Komarov, L. Kondratyuk, V. Koptev, S. Kopyto, R. Krause, P. Kravtsov, V. Kruglov, P. Kulessa, A. Kulikov, N. Lang, H. Langenhagen, A. Lepges, J. Ley, R. Maier, S. Martin, G. Macharashvili, S. Merzlyakov, K. Meyer, S. Mikirtychyants, **H. Müller,** P. Munhofen, A. Mussgiller, M. Nekipelov, V. Nelyubin, M. Nioradze, H. Ohm, A. Petrus, D. Prasuhn, B. Prietzschk, H.J. Probst, K. Pysz, F. Rathmann, **B. Rimarzig,** Z. Rudy, R. Santo, H. Paetz gen. Schieck, R. Schleichert, A. Schneider, **C. Schneider,** H. Schneider, U. Schwarz, H. Seyfarth, A. Sibirtsev, U. Sieling, K. Sistemich, A. Selikov, H. Stechemesser, H.J. Stein, A. Strzalkowski, K.H. Watzlawik, P. Wüstner, S. Yashchenko, B. Zalikhanov, N. Zhuravlev, K. Zwoll, I. Zychor, O.W.B. Schult, H. Ströher

Abstract: ANKE is a new experimental facility for the spectroscopy of products from proton-induced reactions on internal targets. It has recently been implemented in the accelerator ring of the cooler synchrotron COSY of the Forschungszentrum Jülich (FZ-Jülich), Germany. The device consists of three dipole magnets, various target installations and dedicated detection systems. It will enable a variety of hadron-physics experiments like meson production in elementary proton-nucleon processes and studies of medium modifications in proton-nucleus interactions.

On the Way to a Superconducting RF-Gun: First Measurements with the Gun Cavity
(Nucl. Instr. Meth. A 445 (200) 408)

Barthels, E., H. Büttig, F. Gabriel, **E. Grosse, D. Janssen,** A. Bushuev, M. Karliner, S. Konstantinov, S. Kruchkov, O. Myshkin, V. Petrov, I. Sedlyarov I, A. Tribendis, V. Volkov, W. Sandner, I. Will, P. von Stein, H. Vogel, A. Matheisen, M. Pekeler, C.Haberstroh, A. Thiel

Abstract: The parameters of a superconducting RF gun cavity have been measured in a test cryostat of DESY. A field strength of 31.8 MV/m at the cathode has been obtained.

The Role of Three-Body Collisions in ϕ-Meson Production Processes Near Threshold
(Nucl. Phys. A 683 (2001) 594)

Barz, H.W., B. Kämpfer

Abstract: The amplitude of subthreshold phi-meson production is calculated using dominant tree-level diagrams for three-body collisions. It is shown that the production can overwhelmingly be described by two-step processes. The effect of the genuine three-body contribution (i.e. the contribution which cannot be factorized) is discussed. The production rate of phi-mesons is presented for proton induced reactions on carbon.

Radiobiological Hypoxia, Oxygen Tension, Interstitial Fluid Pressure and Relative Viable Tumour Area in Two Human Squamous Cell Carcinomas in Nude Mice During Fractionated Radiotherapy
(Acta Oncologica Vol. 40 No. 4 (2001) 519)

Baumann, M., S. Appold, J. Zimmer, M. Scharf, B. Beuthin-Baumann, H.-H. Dubben, **W. Enghardt**, A. Schreiber, W. Eicheler, C. Petersen

Abstract: Very little is known about the correlation between the radiological hypoxic fraction (rHF) and other measures of tumour oxygenation during fractionated irradiation. I the present study the rHF is determined in untreated human FaDu and GL squamous cell carcinoma in nude mice and in tumours irradiated with 10 fractions in 2 weeks and 20 fractions in 4 weeks, using tumour control as the experimental endpoint. The results were compared with measurements of the pO_2, the interstitial fluid pressure (IFP) and the relative viable tumour area. In FaDu tumours the radiobiological hypoxic fractions (rHFs) before and during irradiation were not statistically different from 100%. Depending on the assumptions made for D_0, the rHFs of GL tumours were between 0.2 and 0.4% or 30 and 53%. The median pO_2 values were 2.8 mm Hg for untreated FaDu tumours and 0.2 mm Hg for GL tumours (p<0.001). The median IFP values were 2.6 mm Hg in FaDu and 5.3 mm Hg in GL tumours (p=0.01). No important changes in the pO_2 and IFP values were observed during fractionated irradiation. The relative viable tumour area during irradiation decreased by 83% in FaDu tumours (p=0.002) and by 54% in GL tumours (p=0.003). It is concluded that differences in rHF exist between FaDu and GL tumours before and during fractionated irradiation and that these differences are not reflected by pO_2 and IFP values and the relative viable tumour area.

Evidence for chiral symmetry in the mass A $\sim$ 130 region
(Nucl. Phys. A 682 (2001) 394)

Beausang,C.W, A.A. Hecht, K.E. Zyromski, D. Balabanski, C.J. Barton, M.A. Caprio, R.F. Casten, J.R. Cooper, D. Hartley, R. Krücken, J.R. Novak, N.V. Zamfir, Jing-Ye Zhang, **F. Dönau**

Abstract: Two new $\Delta I = 1$ bands in the $N = 75$, doubly-odd nuclei ^{136}Pm and ^{138}Eu are reported. These bands have been assigned the same $\pi h_{11/2} \otimes \nu h_{11/2}$ structure as the yrast band and show some of the features expected from predicted chiral twin bands.

Beta decay of ^{56}Cu
(Nucl. Phys. A 695 (2001) 69)

Borcea, R., J. Äystö, E. Caurier, P. Dendooven, J. Döring, M. Gierlik, M. Górska, H. Grawe, M. Hellström, Z. Janas, A. Jokinen, M. Karny, R. Kirchner, M. La Commara, K. Langanke, G. Martínez-Pinedo, P. Mayet, A. Nieminen, F. Nowacki, H. Penttilä, A. Płochocki, M. Rejmund, E. Roeckl, C. Schlegel, K. Schmidt, **R. Schwengner**, M. Sawicka

Abstract: The proton-rich isotope ^{56}Cu was produced at the GSI On-Line Mass Separator by means of the ^{28}Si(^{32}S, p3n) fusion-evaporation reaction. Its β-decay properties were studied by detecting β-delayed rays and protons. A half-life of 93 $\pm$ 3 ms was determined for ^{56}Cu. Compared to the previous work, six new γ rays and three new levels were assigned to the daughter nucleus ^{56}Ni. The measured Gamow-Teller strength values for five ^{56}Ni levels are compared to shell-model predictions.

Klonogenes Zellüberleben von Keratinozyten und Fibroblasten nach Bestrahlung mit weichen Röntgenstrahlen
(Exp. Strahlenther. Klin. Strahlenbiol. 10 (2001) 71)

Brankovic, K., D. Slonina, **A. Panteleeva, J. Pawelke**, W. Dörr

Abstract: Weiche Röntgenstrahlung wird in der diagnostischen Radiologie, aber auch in der Strahlentherapie

angewandt. In der vorliegenden Untersuchung wurde die Wirkung weicher Röntgenstrahlen (25 kV) bzw. Referenzröntgenstrahlung (200 kV) für verschiedene Zelllinien (3T3/NIH Mausfibroblasten, V-79 Hamsterfibroblasten, primäre neonatale Haut-Keratinozyten des Menschen) verglichen. Zusammenfassend zeigen Fibroblasten ein vemindertes klonogenes Zellüberleben nach Bestrahlung mit weichen Röntgenstrahlen im Vergleich zu 200 kV Röntgenstrahlen. Dieser Unterschied geht einher mit einer Abnahme der α-Werte und einer Zunahme von β. Demgegenüber zeigen Keratinozyten keine deutliche Veränderung des Zellüberlebens. Hier findet sich jedoch eine Zunahme von α.

Emission of Unstable Clusters from Hot Yb Compound Nuclei
(Phys. Rev. C 63 (2001) 024611)

Charity R.J., L.G. Sobotka, J. Cibor, K. Hagel, M. Murray, J.B. Natowitz, R. Wada, Y. El Masri, D. Fabris, G. Nebbia, G. Viesta, M. Cinausero, E. Fioretto, G. Prete, **A. Wagner**, H. Xu

Abstract: Neutrons and isotopically resolved light charged particles have been detected in coincidence with evaporation residues produced in the reaction $E/A = 11$ MeV ^{60}Ni+^{100}Mo. Multiplicities of evaporated particle-unstable clusters have been determined from correlations in the emission of these light particles. The decay of the short-lived ^{5}He and ^{8}Be ($E^* = 3.04$ MeV) states was found to be affected by the Coulomb field of the compound nucleus in accordance with theoretical estimates. The contributions to the measured kinetic-energy distributions of stable fragments from the sequential decay of the unstable clusters was examined. Overall, the contributions from secondary fragments do not greatly influence the spectral shapes and specifically the location of the spectral peaks are not significantly shifted down in energy due to the presence of these secondary fragments. Therefore contrary to the suggestion of Charity et al. [Phys. Rev. C 56, 873 (1997)], the lower peak energy of the experimental α-particle spectrum as compared to standard statistical-model calculations cannot be attributed to sequential α particles from ^{5}He and other clusters. Only for the extreme "subbarrier" regions of the α-particle, deuteron, ^{6,7}Li, and ^{8}Be spectra was the sequential contribution found to be dominant. Statistical-model calculations incorporating large initial deformations are shown to provide enhancements in the yield of low-energy fragments which are roughly appropriate for all the detected isotopes. This suggests that the origin of the sub-barrier enhancements may be a result of evaporation from highly deformed systems which are either produced dynamically during the fusion process or by thermal shape fluctuations.

Spectroscopy in the Z=49 ^{108,110}In isotopes: Lifetime measurements inshears bands
(Phys. Rev. C 64 (2001) 4314)

Chiara, C.J., D.B. Fossan, V.P. Janzen, T. Koike, D.R. LaFosse, G. J. Lane, S.M. Mullins, E.S. Paul, D.C. Radford, H. Schnare, J.M. Sears, J.F. Smith, K. Starosta, P. Vaska, R. Wadsworth, D. Ward, **S. Frauendorf**

Abstract: Excited states have been populated in In-108 and In-110 in complementary backed- and thin-target experiments, using the Stony Brook and the 8 pi Ge-detector arrays. The level schemes for both isotopes have been extended and modified, including the first observation of DeltaI = 2 bands in In-110. Lifetimes of states in four DeltaI = 1 bands and one DeltaI = 2 band have been measured using the Doppler-shift attenuation method. Experimental total angular momenta and reduced transition strengths for the DeltaI = 1 bands have been compared with tilted axis cranking predictions for shears bands with configurations involving one proton g(9/2) hole and one or three valence quasineutrons from the h(11/2) and g(7/2)/d(5/2) orbitals. The DeltaI = 2 bands have been compared with principal axis cranking predictions for configurations with two g(9/2) proton holes and a g(7/2) or d(5/2) proton and one- or three-quasineutron configurations involving the h(11/2) and g(7/2)/d(5/2) orbitals. In general, there is good overall agreement for both the angular momenta and reduced transition strengths. The DeltaI = 1 and DeltaI = 2 bands have large J((2))/B (E2) ratios as expected for the shears mechanism. The B (M1) strengths deduced for the DeltaI = 1 bands show a decreasing trend as a function of spin, which is also a feature of the shears mechanism. Configuration assignments have been made for most observed bands based on comparisons with theory and systematics of neighboring nuclei.

Results from FOPI on Strangeness in Nuclear Matter at SIS Energies
(J. Phys. G: Nucl. Part. Phys. 27 (2001) 267)

Crochet, P., J.P. Alard, A. Andronic, R. Averbeck, V. Barret, Z. Basrak, N. Bastid, I. Belyaev, A. Bendarag, G. Berek, R. Čaplar, N. Cindro, A. Devismes, P. Dupieux, M. Dželalija, M. Eskef, C. Finck, Z. Fodor, A. Gobbi, Yu.L. Grishkin, O. Hartmann, N. Herrmann, K.D. Hildenbrand, B. Hong, J. Kecskemeti, Y.J. Kim, M. Kirejczyk, P. Koczon, M. Korolija, **R. Kotte,** M. Kowalczyk, T. Kress, R. Kutsche, A. Lebedev, K.S. Lee, Y. Leifels, V. Manko, H. Merlitz, S. Mohren, D. Moisa, **W. Neubert,** A. Nianine, D. Pelte, M. Petrovici, C. Plettner, F. Rami, W. Reisdorf, B. de Schauenburg, D. Schüll, Z. Seres, B. Sikora, K.S. Sim, V. Simion, K. Siwek-Wilczyńka, V. Smolyankin, A. Somov, M.R. Stockmeier, G. Stoicea, M. Vasilev, P. Wagner, K. Wiśniewski, **D. Wohlfarth,** J.T.

Yang, I. Yushmanov, A. Zhilin

Abstract: Experimental data on charged kaon phase space distributions and strangeness sidewards flow measured with the FOPI detector at SIS/GSI are presented. Comparisons are made with the predictions of transport models investigating the in-medium kaon-nucleon potential.

Structure and evolution of electric dipole strength in ^{204,206,208}Pb below the neutron emission threshold
(Phys. Lett. B 486 (2000) 479)

Enders, J., P. von Brentano, J. Eberth, A. Fitzler, C. Fransen, R.-D. Herzberg, H. Kaiser, **L. Käubler,** P. von Neumann-Cosel, N. Pietralla, V.Yu. Ponomarev, **H. Prade,** A. Richter, H. Schnare, **R. Schwengner,** S. Skoda, H.G. Thomas, H. Tiesler, D. Weisshaar, I. Wiedenhöver

Abstract: The electric dipole strength distributions below threshold in stable even-mass Pb isotopes have been extracted from photon scattering experiments at the superconducting Darmstadt electron linear accelerator S-DALINAC. Between 4 and 6.5 MeV excitation energy a resonance-like clustering of strength is observed. A strong evolution of a fragmentation of the dipole strength with opening the neutron shell is found. The fine structure of the strength is compared to microscopic quasiparticle-phonon model calculations that quantitatively reproduce the data quite well and explain the fragmentation of the dipole strength. Models suggesting the oscillation of excess neutrons with respect to an N≃Z core as a possible origin of low-lying E1 strength are critically examined.

Spontaneous Symmetry Breaking in Rotating Nuclei
(Rev. Mod. Phys. 73 (2001) 463)

Frauendorf, S.

Abstract: The concept of spontaneous symmetry breaking is applied to the rotating mean field of nuclei. The description is based on the tilted-axis cranking model, which takes into account that the rotational axis can take any orientation with respect to the deformed density distribution. The appearance of rotational bands in nuclei is analyzed, focusing on weakly deformed nuclei at high angular momentum. The quantization of the angular momentum of the valence nucleons leads to new phenomena. Magnetic rotation represents the quantized rotation of the anisotropic current distribution in a near spherical nucleus. The restricted amount of angular momentum of the valence particles causes band termination. The discrete symmetries of the mean-field Hamiltonian provide a classification scheme of rotational bands. New symmetries result from the combination of the spatial symmetries of the density distribution with the vector of the angular momentum. The author discusses in detail which symmetries appear for a reflection-symmetric density distribution and how they show up in the properties of the rotational bands. In particular, the consequences of rotation about a nonprincipal axis and of breaking the chiral symmetry are analyzed. Also discussed are which symmetries and band structures appear for non-reflection-symmetric mean fields. The consequences of breaking the symmetry with respect to gauge and isospin rotations are sketched. Some analogies outside nuclear physics are mentioned. The application of symmetry-restoring methods to states with large angular momentum is reviewed.

Atomic Clusters as a Branch of Nuclear Physics
(Ann. Rev. of Nucl. and Part. Scien. 51 (2001) 219)

Frauendorf, S., C. Guet

Abstract: The conduction electrons in clusters of simple metal atoms are approximatively independent and free. Nucleons in nuclei also behave as delocalized and independent fermions. This generic behavior generates analogies between metal clusters and nuclei, such as the shell structure, the shapes, and the dipole vibration mode. However, there are also major differences that arise from the presence of ions in metal clusters. Fission of nuclei and clusters, and particle emission from them, reveal these differences.

Symmetries of the Rotating Mean Field
(Acta Phys. Polonica B 32 (2001) 2661)

Frauendorf, S.

Abstract: The discrete symmetries of the rotating mean field lead to a variety of rotational bands with different sequences of spin and parity. We focus on the breaking of chiral symmetry in rotating triaxial nuclei.

A unique parametrization of the shapes of secondary dilepton spectra observed in central heavy-ion collisions at CERN-SPS energies
(Nucl. Phys. A 688 (2001) 939)

Gallmeister, K., B. Kämpfer, O.P. Pavlenko, C. Gale

Abstract: A unique parametrization of secondary (thermal) dilepton yields in heavy-ion experiments at CERN-SPS is proposed. This parametrization resembles a thermal $q\bar{q}$ annihilation rate. This is inspired by the observation that lepton pair production rates are quantitatively similar, whether expressed in a hadronic or partonic basis. Adding the thermal yield and the background contributions (hadronic cocktail, Drell-Yan, correlated semileptonic decays of open charm) the spectral shapes of the CERES/NA45, NA38, NA50 and HELIOS/3 data from experiments with lead and sulfur beams can be well described.

Radiative Corrections in Highly Charged Ions and Tests of QED in Strong Electric and Magnetic Fields
(Phys. Src. T 92 (2001) 426)

Goidenko, I.A., L.N. Labzowski, A.V. Nefiodov, U.D. Jentschura, G. Plunien, **S. Zschocke**, G. Soff

Abstract: To provide predictions of the Lamb shift of highly charged ions on the level of accuracy of about 10(-6) has been achieved after exact results for the contributions of all two-photon self-energy diagrams have been performed. We report on the present status of our Lamb-shift calculations including all QED-corrections of first- and second-order in the finestructure constant a and all relevant nuclear effects. An excellent agreement between the most recent experimental data for Lamb shift of the ls-ground state in hydrogenlike uranium can be stated. This can serve as a sensitive test of QED in the strongest electric fields accessible in nature. In a second part of this article we report about an all-order numerical evaluation of the one-photon selfenergy at low nuclear charge (Z = 1,...,5). A sensitive comparison of our numerical approach with analytical approach to the one-photon selfenergy confirms the consistency of these two different approaches (numerical and analytic) to very high precision.

Evaluation of the Two-Photon Self-Energy Correction for Hydrogenlike Ions
(Hyp. Int. 132 (2001) 397)

Goidenko, I.A., L.N. Labzowski, A.V. Nefiodov, G. Plunien, G. Soff, **S. Zschocke**

Abstract: We report on the recent evaluation of the two-photon electron self energy to all orders in the interaction with the Coulomb field of the nucleus. With the present results at hand the major theoretical uncertainty is diminished, which provides predictions of the ground-state energy with a relative accuracy of about 10(-6) for the hydrogenlike uranium and lead systems. This allows for high-precision tests of quantum electrodynamics (QED) in strong fields that are expected to be experimentally available in the near future.

Quantum-Mechanical Approach to Planar Positron Channeling in a Longitudinal Hypersonic Field
(Nucl. Instr. Meth. B 173 (2001) 132)

Grigoryan, L.Sh., A.R. Mkrtchyan, A.H. Mkrtchyan, H.F. Khachatryan, **H. Prade, W. Wagner**, M.A. Piestrup

Abstract: The wave function of a planar-channeled positron with energy 10 MeV$\leq$E$\leq$100 MeV under the resonant influence of hypersound is calculated. It is found that the longitudinal hypersound changes the spectral distribution of the channeling radiation significantly. With decreasing wavelength λ_s of the hypersound, starting from $\lambda_s = \lambda_E$, where λ_E is the characteristic length related to one transverse oscillation of the channeled positron, a new type of radiative transition occurs. It is characterized by the stimulated enhancement of transverse energy of the positron at channeling (inverse radiative transition). When λ_s approaches $\lambda_E/2$ the inverse transitions show a resonant behaviour.

Resonant Influence of a Longitudinal Hypersonic Field on the Radiation from Channeled Electrons
(Nucl. Instr. Meth. B 173 (2001) 184)

Grigoryan, L.Sh., A.R. Mkrtchyan, A.H. Mkrtchyan, H.F. Khachatryan, **H. Prade, W. Wagner**, M.A. Piestrup

Abstract: The wave function of a planar/axially channeled electron with energy 10 MeV$\leq$E$\leq$1 GeV under the influence of a longitudinal hypersonic wave excited in a single crystal is calculated. Conditions for the resonant influence of the hypersonic wave on the quantum state of the channeled electron are deduced. Expressions for the wave function that are applicable in the case of resonance are obtained.

Angular and spectral distributions of the radiation intensity from the planar/axially channeled electron are also calculated. The possibility of significant amplification of channeling radiation by a hypersonic wave is substantiated. It is found that the hypersound can excite inverse radiative transitions through which the transversal energy of the channeled electron is increased. These transitions have a resonant nature and can lead to a considerable intensification of the electron channeling radiation. In the case of axial channeling, the resonance radiation is sustained also by direct radiative transitions of the electron.

Resonant Influence of Hypersound on the Radiation of an Axially Channeled Electron
(Radiation Effects & Defects in Solids 153 (2001) 221)

Grigoryan, L.Sh., A.R. Mkrtchyan, A.H. Mkrtchyan, H.F. Khachatryan, **W. Wagner**, M.A. Piestrup

Abstract: The spectral intensity of the radiation emitted by an axially channeled electron in a single crystal excited by a longitudinal hypersonic wave propagating along the channeling direction has been calculated for the energy range 10 MeV $\leq E \leq$ 100 MeV. It has been shown that under the influence of acoustic vibrations excited in the single crystal a resonant intensification of the electron channeling radiation, a variation of its spectral distribution as well as inverse radiative transitions are possible.

Quantum Mechanical Approach to Planar Electron Channeling in a Hypersonic Field (I)
(Radiation Effects & Defects in Solids 153 (2001) 289)

Grigoryan, L.Sh., A.R. Mkrtchyan, A.H. Mkrtchyan, H.F. Khachatryan, **W. Wagner**, M.A. Piestrup

Abstract: The wave function of an electron 10 MeV $< E \leq$ 100 MeV planar channeled in a longitudinal hypersonic superlatice has been found. Conditions for the resonant influence of the acoustic waves on the quantum states of the electron were deduced. The expression obtained for the wave finction is applicable at resonance.

Quantum Mechanical Approach to Planar Electron Channeling in a Hypersonic Field (II) - Resonant Influence on the Radiation
(Radiation Effects & Defects in Solids 153 (2001) 307)

Grigoryan, L.Sh., A.R. Mkrtchyan, A.H. Mkrtchyan, H.F. Khachatryan, **W. Wagner**, M.A. Piestrup

Abstract: The spectral intensity of the radiation emitted by a planar channeled electron in a single crystal excited by a longitudinal hypersonic wave propagating along the channeling direction has been calculated for the energy range 10 MeV$< E \leq$ 100 MeV. It has bben found that the hypersound can excite inverse transitions through which the transversal energy of the channeled electron is increased. These transitions have a resonant nature and can lead to a considerable intensification of the electron channeling radiation.

Detailed Spectroscopy of the Chiral-Twin Candidate Bands in ^{136}Pm
(Phys. Rev. C 64 (2001) 031304)

Hartley, D.J., L.L. Riedinger, M.A. Riley, D.L. Balabanski, F.G. Kondev, R.W. Laird, J. Pfohl, D.E. Archer, T.B. Brown, R.M. Clark, M. Devlin, P. Fallon, I.M. Hibbert, D.T. Joss, D.R. LaFosse, P.J. Nolan, N.J. O'Brien, E.S. Paul, D.G. Sarantites, R.K. Sheline, S.L. Shepherd, J. Simpson, R. Wadsworth, Jing-ye Zhang, P.B. Semmes, **F. Dönau**

Abstract: The chiral-twin candidate bands recently observed in ^{136}Pm have been extended to high spins [I = (21)] using the Gammasphere γ-ray spectrometer and the Microball charged-particle detector array. A more-detailed spectroscopy of the bands was possible, where the rotational alignments and B(M1)/B(E2) ratios confirm that both sequences have the $\pi h_{11/2}\nu h_{11/2}$ configuration. Particle-rotor calculations of intraband and interband transition strength ratios of the chiral-twin bands are compared with experimental values for the first time. Good agreement was found between the predicted transition strength ratios and the experimental values, thus supporting the possible chiral nature of the $\pi h_{11/2}\nu h_{11/2}$ configuration in ^{136}Pm.

Evidence for Chiral Symmetry in ^{136}Pm and ^{138}Eu
(Phys. Rev. C 63 (2001) 051302)

Hecht A.A., C.W. Beausang, K.E. Zyromski, D.L. Balabanski, C.J. Barton, M.A. Caprio, R.F. Casten, J.R. Cooper, D.J. Hartley, R. Krücken, D. Meyer, H. Newman, J.R. Novak, E.S. Paul, N. Pietralla, A. Wolf, N.V. Zamfir, Jing-Ye Zhang, **F. Dönau**

Abstract: High-spin states in the doubly odd N=75 nuclei Pm-136 and Eu-138 were populated following the Sn-116(Mg-24,p3n) and Cd-106(Cl-35,2pn) reactions, respectively. A new $\Delta I = 1$ band is reported in Eu-138 and new data are presented for the recently reported band in Pm-136. Polarization and angular correlation measurements have been performed to establish the relative spin and parity assignments for these bands. Both bands have been assigned the same $\pi h_{11/2} \times \nu h_{11/2}$ structure as the yrast band and are suggested as candidates for chiral twin bands.

Probing Meson Spectral Functions with Double Differential Dilepton Spectra in Heavy-Ion Collisions

Kämpfer, B., O.P. Pavlenko

Abstract: The double differential dilepton spectrum $dN/(dM_\perp^2 dM^2)$ at fixed transverse mass $M_\perp$ allows a direct access to the vector meson spectral functions. Within a fireball model the sensitivity of $dN/(dM_\perp^2 dM^2)$ against variations of both the in-medium properties of mesons and the dynamics of the fireball is investigated. In contrast to the integrated invariant-mass spectrum dN/dM^2, in the spectrum $dN/dM^2 dM_\perp^2$ with fixed $M_\perp$ the ω signal is clearly seen as bump riding on the ρ background even in case of strong in-medium modifications.

Strange Quark Matter: Mapping QCD Lattice Results to Finite Baryon Density by a Quasi-Particle Model

Kämpfer, B., A. Peshier, G. Soff

Abstract: A quasi-particle model is presented which describes QCD lattice results for the 0, 2 and 4 quark-flavor equation of state. The results are mapped to finite baryo-chemical potentials. As an application of the model we make a prediction of deconfined matter with appropriate inclusion of strange quarks and consider pure quark stars.

Comparison of the Scintillation Properties of LSO:Ce Manufactured by Different Laboratories and of LGSO:Ce

Kapusta, M., M. Moszynski, M. Balcerzyk, J. Braziewicz, D. Wolski, **J. Pawelke**, W. Klamra

Abstract: We measured photoelectron yield, light output, decay times of light pulses, cerium concentration, energy resolution and time resolution of LSO:Ce manufactured by different laboratories and LGSO:Ce. The LSO samples show excellent scintillation properties: high light output, close to 30,000 ph/MeV and good energy resolution of 7.3% FWHM for ^{137}Cs γ-source full energy peak. Time resolution measured in geometry fulfilling the PET scanners requirements is equal to 450 ps.
We also present results from the measurements with LGSO:Ce by Hitachi Chemical Co., which is of similar chemical composition to LSO. LGSO, at present stage of development, shows about 20% lower light output than LSO and energy resolution of 12.4% FWHM for 662 keV γ-rays.
LSO crystals used in our studies posses similar in scintillation properties, although we suppose that the details of the productions method are different due to differences in Ce concentration. LGSO is a new and very promising scintillator due to lower background radiation in comparison to LSO, but it features worse energy resolution and smaller number of photoelectrons.

Consequences of Neutron-Proton Pairing Correlations for the Rational Motion of the N=Z Nucleus ^{72}Kr

Kelsall, N.S., R. Wadsworth, A.N. Wilson, P. Fallon, A.O. Macchiavelli, R.M. Clark, D.G. Sarantites, D. Seweryniak, C.E. Svensson, S.M. Vincent, **S. Frauendorf**, J.A. Sheikh, G.C. Ball

Abstract: High-spin states in the $N = Z$ nucleus ^{72}Kr were populated using the ^{40}Ca(^{36}Ar,2p2n) reaction at a beam energy of 145 MeV. The yrast band has been observed up to a tentative spin of 20 $\hbar$. Nonyrast rotational structures have also been observed for the first time. The alignment of $g_{9/2}$ protons and neutrons in the yrast band is observed to be significantly delayed relative to the heavier even-even Kr isotopes. Exact deformed cranked shell model calculations suggest that this could be due to the combined effect of isovector ($T = 1$) and isoscalar ($T = 0$) neutron-proton pairing correlations.

Forward K$^+$-Production in Subthreshold pA Collisions at 1.0 GeV
(Phys. Rev. Lett. 87 (2001) 022301)

Koptev,V., M. Büscher, H. Junghans, M. Nekipelov, K. Sistemich, H. Ströher, V. Abaev, H.H. Adam, R. Baldauf, S. Barsov, U. Bechstedt, N. Bongers, G. Borchert, W. Borgs, W. Bräutigam, W. Cassing, V. Chernyshev, B. Chiladze, M. Debowski, J. Dietrich, M. Drochner, S. Dymov, J. Ernst, W. Erven, R. Esser, P. Fedorets, A. Franzen, D. Gotta, T. Grande, D. Grzonka, G. Hansen, M. Hartmann, V. Hejny, L. van Horan, L. Jarczyk, A. Kacharava, B. Kamys, A. Khoukaz, T. Kirchner, S. Kistryn, F. Klehr, H.R. Koch, V. Komarov, S. Kopyto, R. Krause P. Kravtsov, V. Kruglov, P. Kulessa, A. Kulikov, V. Kurbatov, N. Lang, N. Langenhagen, I. Lehmann, A. Lepges, J. Ley, B. Lorentz, G. Macharashvili, R. Maier, S. Martin, S. Merzliakov, K. Meyer, S. Mikirtychiants, **H. Müller**, P. Munhofen, A. Mussgiller, V. Nelyubin, M. Nioradze, H. Ohm, A. Petrus, D. Prasuhn, B. Prietzschk, H.J. Probst, D. Protic, K. Pysz, F. Rathmann, **B. Rimarzig**, Z. Rudy, R. Santo, H. Paetz gen. Schieck, R. Schleichert, A. Schneider, **C. Schneider**, H. Schneider, G. Schug, O.W.B. Schult, H. Seyfarth, A. Sibirtsev, J. Smyrski, H. Stechemesser, E. Steffens, H.J. Stein, A. Strzalkowski, K.H. Watzlawik, C. Wilkin, P. Wüstner, S. Yashchenko, B. Zalikhanov, N. Zhuravlev, P. Zolnierczuk, K. Zwoll I. Zychor

Abstract: K$^+$ meson production in pA (A = C, Cu, Au) collisions has been studied using the ANKE spectrometer at an internal target position of the COSY-Juelich accelerator. The complete momentum spectrum of kaons emitted at forward angles, $\vartheta \leq 12^o$, has been measured for a beam energy of T(p)=1.0 GeV, far below the free NN threshold of 1.58 GeV. The spectrum does not follow a thermal distribution at low kaon momenta and the larger momenta reflect a high degree of collectivity in the target nucleus.

Associated Strangeness Production at Threshold with the TOF Experiment at COSY
(Nucl. Phys. A 691 (2001) 344)

Marcello, S., S. Abd El-Samad, R. Bilger, K.T. Brinkmann, H. Clement, **S. Dshemuchadse**, H. Dutz, W. Eyrich, A. Erhardt, C. Fanara, D. Filges, A. Filippi, H. Freiesleben, M. Fritsch, R. Geyer, A. Hassan, J. Hauffe, D. Hesselbarth, B. Jakob, L. Karsch, K. Kilian, H. Koch, J. Kress, E. Kuhlmann, S. Marwinski, S. Mauro, W. Meyer, **K. Möller**, H.P. Morsch, **L. Naumann**, K. Nünighoff, N. Paul, C. Plettner, M. Richter, E. Roderburg, M. Rogge, **A. Schamlott**, M. Schmitz, P. Schönmeier, M. Schulte-Wissermann, W. Schroeder, T. Sefzick, F. Stinzing, G.Y. Sun, G.J. Wagner, M. Wagner, A. Wilms, S. Wirth, P. Zupranski

Abstract: Measurements of exclusive pp $\rightarrow$ NKY reactions with beam momenta in the range 2.5÷3.2 GeV/c are underway at COSY using the Time-of-Flight spectrometer TOF. The high granularity of the detector, which covers almost the full phase space, allows to measure differential distributions and total cross sections as well. Moreover the hyperon polarization can be studied either with polarized beam or target. Some preliminary results at different energies are given.

First Measurement of β-Decay Properties of the Proton Drip-Line Nucleus ^{60}Ga*
(Eur. Phys. J. A 12 (2001) 269)

Mazzocchi, C., Z. Janas, J. Döring, M. Axiotis , L. Batist, R. Borcea, D. Cano-Ott, E. Caurier, G. de Angelis, E. Farnea, A. Faßbender, A. Gadea, H. Grawe, A. Jungclaus, M. Kapica, R. Kirchner, J. Kurcewicz, S.M. Lenzi, T. Martínez , I. Mukha, E. Nácher, D.R. Napoli, E. Roeckl, B. Rubio, **R. Schwengner**, J.L. Tain, C.A. Ur

Abstract: By using the fusion-evaporation reaction ^{28}Si(^{36}Ar,p3n) and spectroscopy of β-delayed γ-rays and charged particles on mass-separated sources, β-decay properties of the neutron-deficient isotope ^{60}Ga were studied for the first time. The half-life of ^{60}Ga was determined to be 70(15) ms, and, based on $\beta\gamma\gamma$ coincidences, the isobaric-analogue state in ^{60}Zn was identified at 4851.9(7) keV. A semiempirical proton separation energy value of 40(70) keV was deduced for ^{60}Ga. The experimental results on half-life, mass excess, proton separation energy, and structure of the ^{60}Zn daughter states are discussed in comparison with various model predictions, including large-scale shell model calculations.

Soft Hadron Production in pp Interactions up to ISR Energies
(Eur. Phys. J. C 18 (2001) 563)

Müller, H.

Abstract: Soft hadron production is described as a two-step process, where the interaction of the partonic constituents of the colliding hadrons leads to the production of intermediate subsystems (fireballs), which decay subsequently into hadrons. The weights of the various final states are derived from the corresponding phase-space factors modified by empirical transition elements. The results compare well with data at energies between particle production thresholds and ISR energies. Special emphasis is put on correlation data, which offer the opportunity to shed some light on the question whether particle production proceeds via fireballs or strings.

Production of a_0^+-Mesons in the Reaction pp $\rightarrow$ da$_0^+$

(Eur. Phys. J. A 11 (2001) 113)

Müller, H.

Abstract: We investigate the reaction $pp \rightarrow da_0^+$ at COSY and SIS energies together with accompanying background reactions and inclusive particle yields. The a_0^+ is considered as a usual quark model state with two decay channels $a_0^+ \rightarrow K^+\bar{K}^0$ and $a_0^+ \rightarrow \pi^+\eta$. Cross sections for a_0^+ production as well as for the corresponding nonresonant channels $pp \rightarrow dK^+\bar{K}^0$ and $pp \rightarrow d\pi^+\eta$ are compared. Especially in case of the final channel $d\pi^+\eta$ high statistics measurements are necessary to extract the a_0^+ signal from the nonresonant background.

Electroproduction of Kaons and Light Hypernuclei

(Nucl. Phys. A 684 (2001) 470)

Reinhold, J., D. Abbott, A. Ahmidouch, P. Ambrozewicz, C.S. Armstrong, J. Arrington, R. Asaturyan, K. Assamagan, S. Avery, K. Bailey, O.K. Baker, S. Beedoe, H. Bitao, W. Boeglin, H. Breuer, D.S. Brown, R. Carlini, J. Cha, N. Chant, E. Christy, A. Cochran, L. Cole, G. Collins, C. Cochran, J. Crowder, W.J. Cummings, S. Danagoulian, **F. Dohrmann,** F. Duncan, J. Dunne, D. Dutta, T. Eden, M. Elaasar, R. Ent, L. Ewell, H. Fenker, H.T. Fortune, Y. Fujii, L. Gan, H. Gao, K. Garrow, D.F. Geesaman, P. Gueye, K. Gustafsson, K. Hafidi, J.O. Hansen, W. Hinton, H.E. Jackson, H. Juengst, C. Keppel, A. Klein, D. Koltenuk, Y. Liang, J.H. Liu, A. Lung, D. Mack, R. Madey, P. Markovitz, C.J. Martoff, D. Meekins, J. Mitchell, T. Miyoshi, H. Mkrtchyan, R. Mohring, S.K. Mtingwa, B. Mueller, T.G. O'Neill, G. Niculescu, I. Niculescu, D. Potterveld, J.W. Price, B.A. Raue, P.E. Reimer, J. Roche, P. Roos, M. Sarsour, Y. Sato, G. Savage, R. Sawafta, J.P. Schiffer, R.E. Segel, A. Semenov, S. Stepanyan, V. Tadevosian, S. Tajima, L. Tang, B. Terburg, A. Uzzle, S. Wood, H. Yamaguchi, C. Yan, C. Yan, L. Yuan, B. Zeidman, M. Zeier, B. Zihlmann

Abstract: Kaon electroproduction on hydrogen, deuterium and helium targets has been measured at a beam energy of 3.245 GeV and four-momentum transfer, Q^2, ranging from 0.34 to 0.5 GeV. Associated hyperon production off a nucleon in the deuteron exhibits a quasifree production mechanism. Excess yield close to the respective thresholds for Λ and Σ production is observed. This can be accounted for be final-state interaction between the electroproduced hyperon and the spectator nucleon. The effects predicted from three different hyperon-nucleon potentials are compared to the data. The measurements on the helium targets is the first ever performed. Very preliminary results are presented.

Resonant and non Resonant K$^-$-Production in pp Reactions at 2.85 GeV

(Nucl. Phys. 69 (2001) 395)

Ritman, J., F. Balestra, Y. Bedfer, R. Bertini, L.C. Bland, A. Brenschede, F. Brochard, M.P. Bussab, S. Choi, M. Debowski, **R. Dressler**, M. Dzemidzic, J.-Cl. Faivre, I.V. Falomkin, L. Fava, L. Ferrero, J. Foryciarz, I. Fröhlich, V. Frolov, R. Garfagnini, A. Grasso, **E. Grosse**, S. Heinz, V.V. Ivanov, W.W. Jacobs, W. Kühn, A. Maggiora, M. Maggiora, A. Manara, D. Panzieri, H.-W. Pfaff, G. Piragino, G.B. Pontecorvo, A. Popov, P. Salabura, V. Tchalyshev, F. Tosello, S.E. Vigdor, G. Zosi

Abstract: Inclusive and exclusive (i.e. via the ϕ resonance) K$^-$ meson production cross sections have been measured in proton-proton reactions at $T_{beam} = 2.85$ GeV. The inclusive K$^-$ cross section is about a factor 20 lower than the K$^+$ cross sections at the same available energy above threshold. The observed ϕ/ω cross section ratio is enhanced by about an order of magnitude relative to naive predictions based upon the Okubo-Zweig-Iizuka (OZI) rule. Differential cross section results are presented which indicate significant contributions from higher partial waves in the proton-proton entrance channel.

Time Scales in Spectator Fragmentation

(Nucl. Phys. A 681 (2001) 279)

Schwarz, C., S. Fritz, R. Bassini, M. Begemann-Blaich, S.J. Gaff-Ejakov, D. Gourio, C. Gross, G. Imme, I. Iori, U. Kleinevoss, G.J. Kunde, W.D. Kunze, U. Lynen, V. Maddalena, M. Mahi, T. Möhlenkamp, A. Moroni, W.F.J. Müller C. Nociforo, B. Ocker, T. Odeh, F. Petruzzelli, J. Pochodzalla, G. Raciti, G. Riccobene, F.P. Romano, A. Saija, M. Schnittker, A. Schüttauf, **W. Seidel**, V. Serfling, C. Sfienti, W. Trautmann, A. Trzcinski, G. Verde, A. Wörner, Hongfei Xi, B. Zwieglinski

Abstract: Proton-proton correlations and correlations of p-α, d-α, and t-α from spectator decays following ^{197}Au + ^{197}Au collisions at 1000 AMeV have been measured with an highly efficient detector hodoscope. The constructed correlation functions indicate a moderate expansion and low breakup densities similar to assumptions made in

statistical multifragmentation models. In agreement with a volume breakup rather short time scales were deduced employing directional cuts in proton-proton correlations.

Effects of QED and Beyond from the Atomic Binding Energy
(Hyp. Int. 132 (2001) 75)

Soff, G., I. Bedniakov, T. Beier, F. Erler, I.A. Goidenko, U.D. Jentschura, L. N. Labzowski, A.V. Nefiodov, G. Plunien,R. Schützhold, **S. Zschocke**

Abstract: Atomic binding energies are calculated at utmost precision. A report on the current status of Lamb-shift predictions for hydrogenlike ions, including all quantum electrodynamical corrections to first and second order in the fine structure constant alpha is presented. All relevant nuclear effects are taken into account. High-precision calculations for the Lamb shift in hydrogen are presented. The hyperfine structure splitting and the g factor of a bound electron in the strong electromagnetic field of a heavy nucleus is considered. Special emphasis is also put on parity violation effects in atomic systems. For all systems possible investigations beyond precision tests of quantum electrodynamics are considered.

Chiral Doublet Structures in Odd-Odd N=75 Isotones: Chiral Vibrations
(Phys. Rev. Lett. 86 (2001) 971)

Starosta, K., T. Koike, C.J. Chiara, D.B. Fossan, D.R. LaFosse, A.A. Hecht, C.W. Beausang, M.A. Caprio, J.R. Cooper, R. Krücken, J.R. Novak, N.V. Zamfir, K.E. Zyromski, D.J. Hartley, D.L. Balabanski, Jing-ye Zhang, **S. Frauendorf, V.I. Dimitrov**

Abstract: New sideband partners of the yrast bands built on the $\pi h_{11/2} \nu h_{11/2}$ configuration were identified in $_{55}$Cs, $_{57}$La, and $_{61}$Pm N = 75 isotones of ^{134}Pr. These bands form with ^{134}Pr unique doublet-band systematics suggesting a common basis. Aplanar solutions of 3D tilted axis cranking calculations for triaxial shapes define left- and right-handed chiral systems out of the three angular momenta provided by the valence particles and the core rotation, which leads to spontaneous chiral symmetry breaking and the doublet bands. Small energy differences between the doublet bands suggest collective chiral vibrations.

Structure of High-Spin States in ^{89}Sr and ^{90}Sr
(Phys. Rev. C 63 (2001) 064315)

Stefanova, E.A., **R. Schwengner**, G. Rainovski, **K.D. Schilling, A. Wagner, F. Dönau**, E. Galindo, A. Jungclaus, K.P. Lieb, O. Thelen, J. Eberth, D.R. Napoli, C.A. Ur, G. de Angelis, M. Axiotis, A. Gadea, M. Marginean, T. Martinez, Th. Kröll, T. Kutsarova

Abstract: High-spin states of ^{89}Sr and ^{90}Sr were studied via the reactions ^{82}Se(^{11}B, $p3n$) and ^{82}Se(^{11}B, $p2n$), respectively, at a beam energy of 37 MeV. Gamma rays were detected with the GASP spectrometer. The level schemes of ^{89}Sr and ^{90}Sr were extended up to $E \approx 8\,\text{MeV}$ and $E \approx 10\,\text{MeV}$, respectively. Level structures in ^{89}Sr and ^{90}Sr were interpreted in terms of the spherical shell model. The calculations were performed in the configuration space $(0f_{5/2}, 1p_{3/2}, 1p_{1/2}, 0g_{9/2})$ for the protons and $(1p_{1/2}, 0g_{9/2}, 1d_{5/2})$ for the neutrons. High-spin level sequences in ^{89}Sr are characterized by coupling the unpaired $d_{5/2}$ neutron to proton excitations of the core nucleus ^{88}Sr. An equidistant level sequence with $\Delta J = 2$ found in ^{90}Sr is well described by the configuration $\pi[(0f_{5/2}^{-2})(0g_{9/2}^{2})]\nu(1d_{5/2}^{2})$ favoring even spins.

Evidence for a Soft Nuclear Equation-of-State from Kaon Production in Heavy Ion Collisions
(Phys. Rev. Lett. 86 (2001) 39)

Sturm, C., I. Böttcher, M. Debowski, A. Förster, **E. Grosse**, P. Koczon, B. Kohlmeyer, F. Laue, M. Mang, **L. Naumann**, H. Oelscher, F. Pühlhofer, E. Schwab, P. Senger, Y. Shin, J. Speer, H. Ströbele, G. Surowka, F. Uhlig, **A. Wagner**, W. Walús

Abstract: The production of pions and kaons has been measured in ^{197}Au+^{197}Au collisions at beam energies from 0.6 to 1.5 A·GeV with the Kaon Spectrometer at SIS/GSI. The K^+ meson multiplicity per nucleon is enhanced in Au+Au collisions by factors up to 6 relative to C+C reactions whereas the corresponding pion ratio is reduced. The ratio of the K^+ meson excitation functions for Au+Au and C+C collisions increases with decreasing beam energy. This behavior is expected for a soft nuclear equation-of-state.

Fragment Isotope Distributions and the Isospin Dependent Equation of State
(Phys. Rev. C 64 (2001) 051901)

Tan, W.P., B-A. Li, R. Donangelo, C.K. Gelbke, M-J. van Goetherm, X.D. Liu, W.G. Lynch, S. Souza, M.B. Tsang, G. Verde, **A. Wagner**, N.S. Xu

Abstract: Calculations predict a connection between the isotopic composition of particles emitted during an energetic nucleus-nucleus collision and the density dependence of the asymmetry term of the nuclear equation of state (EOS). This connection is investigated for central ^{112}Sn+^{112}Sn and ^{124}Sn+^{124}Sn collisions at E/A=50 MeV in the limit of an equilibrated freezeout condition. Comparisons between measured isotopic yields ratios and theoretical predictions in the equilibrium limit are used to assess the sensitivity to the density dependence of the asymmetry term of the EOS. This analysis suggests that such comparisons may provide an opportunity to constrain the asymmetry term of the EOS.

Isoscalar-Isovector Interferences in $\pi N \to Ne^+e^-$ Reactions as a Probe of Baryon Resonance Dynamics
(Eur. Phys. J. A 12 (2001) 217)

Titov, A.I., **B. Kämpfer**

Abstract: The isoscalar-isovector $(\rho - \omega)$ interferences in the exclusive reactions $\pi^- p \to ne^+e^-$ and $\pi^+ n \to pe^+e^-$ near the ω threshold leads to a distinct difference of the dielectron invariant mass distributions depending on beam energy. The strength of this effect is determined by the coupling of resonances to the nucleon vector-meson channels and other resonance properties. Therefore, a combined analysis of these reactions can be used as a tool for determining the baryon resonance dynamics.

Energy Resolution and Energy-Light Response of CsI(TI) Scintillators for Charged Particle Detection
(Nucl. Instr. Meth. A 456 (2001) 290)

Wagner, A., W.P. Tan, K. Chalut, R.J. Charity, B. Davin, Y. Larochelle, M.D. Lennek, T.X. Lui, X.D. Lui, W.G. Lynch, A.M. Ramos, R. Shomin, L.G. Sobotka, R.T. de Souza, M.B. Tsang, G. Verde, H.S. Xu

Abstract: This article describes the crystal selection and quality control utilized to develop and calibrate a high resolution array of CsI(TI) scintillator crystals for the detection of energetic charged particles. Alpha sources are used to test the light output variation due to thallium doping gradients. Selection of crystals with better than 1this method. Tests with 240 MeV alpha beam reveal that local light output variations within each of the tested CsI(TI) crystals limit the resolution to about 0.5calibrating with energetic projectile fragmentation beams.

Electroproduction of Kaons and Light Nuclei
(Nucl. Phys. A 691 (2001) 37)

Zeidman, B., D. Abbott, A. Ahmidouch, P. Ambrozewicz, C.S. Armstrong, J. Arrington, R. Asaturyan, K. Assamagan, S. Avery, K. Bailey, O.K. Baker, S. Beedoe, H. Bitao, H. Breuer, D.S. Brown, R. Carlini, J. Cha, N. Chant, E. Christy, A. Cochran, L. Cole, G. Collins, C. Cothran, J. Crowder, W.J. Cummings, S. Danagoulian, **F. Dohrmann**, F. Duncan, J. Dunne, D. Dutta, T. Eden, M. Elaasar, R. Ent, L. Ewell, H. Fenker, H.T. Fortune, Y. Fujii, L. Gan, H. Gao, K. Garrow, D. Geesaman, P. Gueye, K. Gustafsson, K. Hafidi, J.O. Hansen, W. Hinton, H.E. Jackson, H. Juengst, C. Keppel, A. Klein, D. Koltenuk, Y. Liang, J.H. Liu, A. Lung, D. Mack, R. Madey, P. Markowitz, C.J. Martoff, D. Meekins, J. Mitchell, T. Miyoshi, H. Mkrtchyan, R. Mohring, S.K. Mtingwa, B. Mueller, T.G. O'Neill, G. Niculescu, I. Niculescu, D. Potterveld, J.W. Price, B.A. Raue, P.E. Reimer, J. Reinhold, J. Roche, P. Roos, M. Sarsour, Y. Sato, G. Savage, R. Sawafta, J.P. Schiffer, R.E. Segel, A. Semenov, S. Stepanyan, V. Tadevosian, S. Tajima, L. Tang, B. Terburg, A. Uzzle, S. Wood, H. Yamaguchi, C. Yan (JLab), C. Yan (Kent), L. Yuan, M. Zeier, B. Zihlmann

Abstract: The A(e,e′K$^+$)YX reaction on H, D, ^{3}He, and ^{4}He was investigated in Hall C at CEBAF. Data were obtained for Q$^2 \approx 0.35$ and 0.5 GeV^2 at 3.245 GeV. The missing mass spectra for both H and D are fitted with Monte-Carlo simulations incorporating peaks corresponding to Λ production on the proton and Σ production on both the proton and neutron. For D, the cross section ratio $\Sigma^0/\Sigma^- \approx 2$, and excess yield close to the thresholds for Λ and Σ production can be attributed to final-state interactions; models are compared to the data. The analysis of the data for the He targets is in a more preliminary state with broader quasi-free peaks resulting from the higher Fermi momenta. Evidence for bound Λ-hypernuclear states is seen and other structure may be present.

Investigation of Antimagnetic Rotation in ^{100}Pd
(Phys. Rev. C 64 (2001) 041302)

Zhu, S., U. Garg, A. V. Afanasjev, **S. Frauendorf**, B. Kharraja, S. S. Ghugre, S. N. Chintalapudi, R. V. F. Janssens, M. P. Carpenter, F. G. Kondev, T. Lauritsen

Abstract: High spin states have been studied in the nucleus ^{100}Pd with the aim of investigating the novel phenomenon of "antimagnetic rotation." A cascade of four "rotational-band-like" transitions is proposed as corresponding to antimagnetic rotation, based on the observed spectroscopic properties and a comparison with calculations in the configuration-dependent cranked Nilsson-Strutinsky formalism.

Interplay of Equilibrium and Nonequilibrium Phenomena in the Nuclear Liquid-Gas Phase Transition
(Nucl. Phys. A 681 (2001) 275)

Zwieglinski, B., T. Odeh, C. Gross, C. Schwarz, R. Bassini, M. Begemann-Blaich, S. Fritz, S.J. Gaff-Ejakov, D. Gourio, G. Imme, I. Iori, U. Kleinevoss, G.J. Kunde, W.D. Kunze, U. Lynen, V. Maddalena, M. Mahi, A. Moroni, T. Möhlenkamp, W.F.J. Müller, C. Nociforo, B. Ocker, F. Petruzzelli, J. Pochodzalla, G. Raciti, G. Riccobene, F.P. Romano, A. Saija, H. Sann, M. Schnittker, A. Schüttauf, **W. Seidel**, V. Serfling, C. Sfienti, W. Trautmann, A. Trzcinski, G. Verde, A. Wörner, H.F. Xi

Abstract: Energy spectra of protons emitted by the target residue in Au+Au collisions at 1 GeV/u reveal two components with different slopes attributed to preequilibrium and equilibrium emission. The relative contribution of the latter decreases rapidly with excitation energy, so that its presence becomes not apparent for the highest energy bins. It is argued therefore, that equilibrium may not be reached on the gas branch of the caloric curve. The nuclear liquid-gas phase transition thus belongs to the category of nonequilibrium phase transitions for which the concepts developed in synergetics, such as self-organized criticality, provide the proper framework.

Proceedings and Reports

Andronenko, M.N. , L.N. Andronenko, **W. Neubert**, D. M. Seliverstov
Eliquilibrium, Isoscaling and Nuclear Isotope Thermometry Related to 1 GeV Proton Induced Reactions
nucl-ex/0112014

Büchner, A. et. al
First Operation of the ELBE Superconducting Electron Linear Accelerator
Proceedings of the 23rd Int. Conf. on Free Electron Lasers, Darmstadt 2001

Döring, J., C. Plettner, M. Axiotis, R. Borcea, J. Eberth, A. Gadea, M. Górska, H. Grawe, Z. Janas, R. Kirchner, M. La Commara, C. Mazzocchi, E. Nácher González, A. Płochocki, E. Roeckl, K. Schmidt, **R. Schwengner**, T. Steinhardt, J. Zylicz
Study of medium-mass odd-odd nuclei close to the $N = Z$ line
Proceedings of the Conference "Bologna 2000 - Structure of the nucleus at the dawn of the century", Nuclear Structure, Bologna, Italy, May 29-June 3, 2000, Eds.: G.C. Bonsignori et al., World Scientific 2001, p. 121

Enders, J., D.W. Anthony, T. Aumann, A. Bauer, T. Baumann, D. Bazin, Y. Blumenfeld, B.A. Brown, T. Glasmacher, P.G. Hansen, R.W. Ibbotson, P.A. Lofy, V. Maddalena, K.L. Miller, T. Nakamura, A. Navin, B.V. Pritychenko, B.M. Sherrill, E.J. Spears, M. Steiner, J.A. Tostevin, **A. Wagner**, J. Yurkon
Study of ^{34,35}Si and ^{37}S with single-neutron removal reactions
Proceedings of the International Symposium on Nuclei and Nucleons
On the occasion of Achim Richter's 60th birthday, Darmstadt, Germany, Oct. 11-13, 2000

Evtushenko, P., P. Michel
System for Measurements of the Electron Beam Profile and Position inside the Undulator at the ELBE FEL
Proceedings of the 23rd Int. Conf. on Free Electron Lasers, Darmstadt 2001

Gippner, P., E. Grosse, J. Pflüger, **A. Schamlott, W. Seidel, U. Wolf, R. Wünsch**
Magnetic Characterization of the Hybrid Undulator U27 for the ELBE Project
Proceedings of the 23rd Int. Conf. on Free Electron Lasers, Darmstadt 2001

Jungclaus, A., D. Kast, K.P. Lieb, C. Teich, M. Weiszflog, T. Härtlein, C. Ender, F. Köck, D. Schwalm, J. Reif,
R. Schwengner, I.P. Johnstone, A. Dewald, J. Eberth, R. Peusquens, H.G. Thomas, M. Górska, H. Grawe,
Electromagnetic properties of particle-hole excitations in nuclei near $N = 50$
Proceedings of the Conference "Bologna 2000 - Structure of the nucleus at the dawn of the century", Nuclear
Structure, Bologna, Italy, May 29-June 3, 2000, Eds.: G.C. Bonsignori et al., World Scientific (2001) 286

Kämpfer, B.
Confinement in the Big Bang and Deconfinement in the Little Bangs
Proceedings of the Int. Conference "Fundamental & Applied Aspects Of Modern Physik", Lüderitz, Namibia,
Nov. 13-17, 2000, Eds.: Connell, S. H., Tegen, R., World Scientific (2001)

Käubler, L. and the Köln-Darmstadt-Rossendorf-Sofia Collaboration
A Scissors-Like State on Top of the Quadrupole-Vibrational State in 88Sr
Proceedings of the Conference "Bologna 2000 - Structure of the nucleus at the dawn of the century", Nuclear
Structure, Bologna, Italy, May 29-June 3, 2000, Eds.: G.C. Bonsignori et al., World Scientific (2001) 221

Käubler, L., H. Schnare, R. Schwengner, H. Prade, F. Dönau, E. Grosse, K.D. Schilling, A. Wagner,
A scissors-like excitation on the quadrupole vibrational state in ^{88}Sr
Proceedings of the Int. Symposium on Nuclear Structure Physics, Göttingen, Germany, March 5-8, 2001, Eds.: R.
Casten, J. Jolie, U. Kneissl, P. Lieb, World Scientific (2001) 363

Lauckner, K., P. Crespo, **W. Enghardt, J. Pawelke**, G. Kraft
An LSO-based Scanner for in-beam PET: A Feasibility
IEEE Nuclear Symposium and Medical Imaging Conference, Lyon, France, Oct. 15-20, 2000
Conference Record N10-4 (2001)

Neubert, W., W. Enghardt, U. Lehnert, E. Müller, B. Naumann, A. Panteleeva, J. Pawelke:
Optimization of a tunable quasi-monochromatic X-ray source for cell irradiations.
Proceedings of the Int. Conf. on Advanced Monte Carlo for Radiation Physics, Particle Transport Simulation and
Applications, Lisbon, Portugal, Oct. 23-26, 2000
Eds.: A. Kling, F. Barao, M. Nakagawa, L. Tavora, P. Vaz , Springer Verlag (2001) 123

Parodi, K., W. Enghardt, R. Hinz, K. Lauckner, **J. Pawelke, F. Pönisch**, P. Crespo, C. Kausch
PET Imaging for Quality Assurance of Heavy Ion Therapy and Potential Extension to Proton Therapy
Book of abstracts of the ITBS Conference, Milos Island, Greece, May 20-24, 2001

Parodi, K., W. Enghardt
Potential Capabilities of Positron Emission Tomography for Quality Assurance of Proton Therapy
Abstract of PTCOG XXXIII hosted in Berlin, Sept. 25-27, 2000

Pawelke, J., K. Brankovic, W. Dörr, B. Dörschel, W. Enghardt, U. Lehnert, W. Neubert, A. Panteleeva, H.
Prade, D. Slonina
Determination of RBE of X-rays by a Novel Quasi-Monochromatic X-ray Source
Proceedings of Gemeinsame Tagung des Östereichischen Verbandes für Strahlenschutz und des Fachverbandes für
Strahlenschutz e. V. und 33. Jahrestagung des FS Strahlenschutz für Mensch und Gesellschaft in Europa von
morgen
Gmunden, Österreich Sept. 17-21, 2001
TÜV-Verlag GmbH, Eds.: K. Mück, A. Hefner, N. Vana, Köln (2001) 13

Schwengner, R., C. Plettner, H. Schnare, L. Käubler, F. Dönau, I. Ragnarsson, A.V. Afanasjev, A. Algora, G.
de Angelis, A. Gadea, D.R. Napoli, J. Eberth, T. Steinhardt, O. Thelen, M. Hausmann, A. Müller, A. Jungclaus,
K.P. Lieb, D.G. Jenkins, R. Wadsworth, A.N. Wilson, S. Frauendorf,
Signature inversion caused by triaxiality in ^{72}Br and band termination in ^{73}Br
Proceedings of the Conference "Bologna 2000 - Structure of the nucleus at the dawn of the century", Nuclear
Structure, Bologna, Italy, May 29-June 3, 2000, Eds.: G.C. Bonsignori et al., World Scientific (2001) 276

Schwengner, R., G. Rainovski, H. Schnare, A. Wagner, F. Dönau, A. Jungclaus, M. Hausmann, O. Iordanov, A. Jungclaus, K.P.Lieb, D.R. Napoli, G. de Angelis, M. Axiotis, N. Marginean, F. Brandolini, and C. Rossi Alvarez
Transition strengths in magnetic dipole bands in ^{82}Rb, ^{83}Rb and ^{84}Rb
Proceedings of the International Symposium on Nuclear Structure Physics, Göttingen, Germany, March 5-8, 2001, Eds.: R. Casten, J. Jolie, U. Kneissl, P. Lieb, World Scientific (2001) 397

Seidel, W., A. Schamlott, K.H. Heise, R. Nicolai, J.-M. Ortega, R. Prazeres, F. Glotin
Infrared-Microspectroscopy of Invironmental Samples
Proceedings of the Int. Workshop on Infrared Microspectroscopy using Synchotron Radiation and Free Electron Laser, Porguerolles Island, Sept. 11-14, 2001, France

Seidel, W., A. Schamlott, K.H. Heise, R. Nicolai, J.-M. Ortega, R. Prazeres, F. Glotin
Infrared-Microspectroscopy of Invironmental Samples
Proceedings of the 23rd Int. Conf. on Free Electron Lasers, Darmstadt 2001

Slonina, D., K. Spekl, K. Brankovic, **A. Panteleeva**, W. Dörr
Chromosomal Damage and Survival of Keratinocytes and Fibroblasts After Irradiation with 200 kV or 25 kV X-ray
11th European Cancer Conference, Lisbon, Portugal, Oct. 21-25, 2001
European Journal of Cancer 37 Suppl. 6 (2001) 207 (No. 758)

Slonina, D., K. Brankovic, K. Spekl, **A. Panteleeva**, W. Dörr
Relative Biological Efficiency of Low Energy X-rays (25 kV) Measured on Human Fibroblasts and Keratinocytes (in polish)
Proceedings of the 12th Meeting of Polish Radiation Research Society, Krakow, Poland, Sept. 10-12, 2001
Institute of Nuclear Physics, Krakow (2001) 74

Slonina, D., K. Brankovic, **A. Panteleeva**, W. Dörr
Chromosomal Damage and Survival of Keratinocytes and fibroblasts After Irradiation with 200 kV or 25 kV X-rays
5th Conference under the auspices of the Polish Society of Radiation Oncology, Poznan, Poland, Apr. 19-21, 2001
Rep. Pract. Oncol. Radiother. 6 (No. 1) (2001) 33

Stefanova, E.A., **R. Schwengner**, M. Danchev, G. Rainovski, D.L. Balabanski, M. Axiotis, G. de Angelis, M. Djongolov, F. Dönau, A. Gadea, E. Galindo, D.J. Hartley, A. Jungclaus, Th. Kröll, T. Kutsarova, K.P. Lieb, N. Marginean, T. Martinez, W.F. Mueller, D.R. Napoli, W. Reviol, L.L. Riedinger, K.D. Schilling, J. Eberth, O. Thelen, C.A. Ur, A. Wagner, O. Zeidan,
Structure of high-spin states in ^{90}Sr and ^{92}Sr
Proceedings of the International Symposium on Nuclear Structure Physics, Göttingen, Germany, March 5-8, 2001, Eds.: R. Casten, J. Jolie, U. Kneissl, P. Lieb, World Scientific (2001) 73

Wünsch, R., E. Grosse, U. Lehnert, C.A.J. van der Geer
Numerial Study of an Optical Klystron FEL for ELBE
Proceedings of the 23rd Int. Conf. on Free Electron Lasers, Darmstadt 2001

Tishchenko, V.G., C.-M. Herbach, D. Hilscher, H.-G. Ortlepp, **P. Gippner**, Kamanin, D.V., Yu.E. Penionzhkevich, **K.D. Schilling, W. Wagner**
Ternary Decay of Hot Heavy Nuclei Studied in the Reaction ^{40}Ar(36AMeV)+^{248}Cm
Proceedings of the Int. Symp. on Exotic Nuclei EXON 2001, Baikal Lake, Irkutsk, Russia, June 2001

Vyvey, K., G. Neyens, D.L. Balabanski, D. Borremans, N. Coulier, R. Coussement, W. de Clercq, G. Georgiev, S. Teughels, S. Chmel, H. Hübel, N. Nenoff, S. Pancholi, D. Rossbach, **R. Schwengner**
The use of the level mixing spectroscopy technique for the study of quadrupole moments in the Pb region
Proceedings of the Conference "Bologna 2000 - Structure of the nucleus at the dawn of the century", Nuclear Structure, Bologna, Italy, May 29-June 3, 2000, Eds.: G.C. Bonsignori et al., World Scientific (2001) 213

Zschocke, S.
Die Zwei-Photonen-Selbstenergie und andere QED-Strahlungskorrekturen
FZ-Rossendorf, FZR-326, 2001

Theses

Kai Gallmeister
Dileptonen und Photonen in relativistischen Schwerionenstößen
TU Dresden, 2001

Cristina Plettner
Nuclear structure phenomena in the ^{72,73}Br nuclei
TU Dresden, 2001

Daniel Almehed
Quantum fluctuations in rotating nuclei
TU Dresden, 2001

Sven Zschocke
Die Zwei-Photonen-Selbstenergie und andere QED-Strahlungskorrekturen
TU Dresden, 2001

Talks at Conferences and other Institutes

Andronenko, M. N. , L. N. Andronenko, **W. Neubert**, D. M. Seliverstov:
Probe the Grand Canonical Approach to Analyse Isotopic Yield Ratios: Fragmentation versus Spallation at 1 GeV Proton Energy
Int. Nucl. Phys. Conf. INPC 2001, Berkeley, July 30-Aug. 3 2001

Barz, H.W.:
Streutheorie für Elementarteilchen
Vorlesung, TU Dresden, Wintersemester 2000/2001

Barz, H.W., B. Kämpfer, Gy. Wolf und M. Zetenyi, **R. Kotte**:
Berechnung der Erzeugung von ϕ-Mesonen in Schwerionenreaktionen in Schwellennähe
Frühjahrstagung DPG: Physik der Hadronen und Kerne, Erlangen, March 19-23, 2001

Barz, H.W.:
The role of three-body collisions in ϕ meson production processes in heavy-ion reactions
Seminar Subatech Ecole de Mines de Nantes, November 29, 2001

Dönau, F.:
Linkshändige Atomkerne – Symmetriebrechung in Atomkernen
Seminarvortrag, Universität Stuttgart, Institut für Strahlenphysik, Juli 2001

Dönau, F.:
Study of the chiral rotation in a rotor plus quasiparticle system
Seminarvortrag, University of Tennessee, Sept. 2001

Dönau, F.:
Chiral rotation in a rotor plus quasiparticle system
Seminarvortrag, Universität zu Köln, Institut für Kernphysik, Okt. 2001

Enghardt, W.:
PET imaging for quality assurance of carbon ion therapy and the potential extension to proton therapy
CORD Colloquium, Hôpitaux Universitaires de Genève, April 19, 2001

Enghardt, W.:
PET zur Kontrolle der Tumortherapie mit Ionenstrahlen: Ergebnisse bei der Kohlenstoff-Therapie und die mögliche Erweiterung auf die Protonen-Therapie
Seminar in der Klinik für Stahlentherapie im Universitätsklinikum Carl-Gustav-Carus der TU Dresden, April 24, 2001

Enghardt, W.:
Krebstherapie mit Schwerionen
Festvortrag auf der Jahrestagung Kerntechnik, Dresden, May 15, 2001

Enghardt, W.:
Radiotherapie mit Photonen, Elektronen und schweren geladenen Teilchen (Teletherapie)
Vorlesung im Institut für Biomedizinische Technik an der Fakultät Elektrotechnik
der TU Dresden, May 31, 2001

Enghardt, W.:
PET zur Kontrolle der Tumortherapie mit Ionenstrahlen: Ergebnisse bei der Kohlenstoff-Therapie und die mögliche Erweiterung auf die Protonen-Therapie
Seminar im Deutschen Krebsforschungszentrum Heidelberg, Juni 13, 2001

Evtushenko, P., P. Michel:
Stripline Beam Position Monitors for ELBE
5th European Workshop on Beam Diagnostics & Instrumentation, Grenoble May, 13-15, 2001

Frauendorf, S.:
Symmetries of the Rotating Mean Field
International Conference and NATO Advanced Research Workshop on High Spin Physics 2001, Warsaw, Poland, February 6-10, 2001

Frauendorf, S.:
Chiral Wobblers and Rotors
Fall Meeting of the Division of Nuclear Physics, American Physical Society, Maui, USA, October, 17-20, 2001

Frauendorf, S.:
Chiral bands in triaxial nuclei
Workshop on Shapes, Rotation and Temperature in Atomic Nuclei, Copenhagen, Danmark, December 6-8, 2001

Michel, P.:
Status des Projektes Strahlungsquelle ELBE am Forschungszentrum Rossendorf
Frühjahrstagung DPG: Physik der Hadronen und Kerne, Erlangen, March 19-23, 2001

Kämpfer, B.:
Dileptons and Photons Central Heavy-Ion Collisions at CERN-SPS
15th Int. Conference on Ultrarelativistic Nucleus-Nucleus Collisions (QM 2001),
Stony Brook, New York, Jan. 15-20, 2001

Kämpfer, B.:
Quantenfeldtheorie
Lecture Course at TU Dresden, Spring 2001

Kämpfer, B.:
Dileptonen und Photonen in Schwerionenstößen bei SPS-Energien
Expertentreffen Kernphysik , Schleching, März 1-8, 2001

Kämpfer, B.:
Allgemeine Relativitätstheorie
Lecture Course at TU Dresden, Fall 2001

Kämpfer, B.:
Collider-Physik mit Schwerionen
Arbeitsteffen "Hadronen und Kerne", Schloss Pommersfelden, Sep. 24-28, 2001

Kämpfer, B.:
ϕ puzzle in Heavy-Ion Collisins at 2 AGeV: How Many K^- from ϕ Decays
6th Int. Conference on Strange Quarks in Matter 2001, A Flavorspace Odyssey (SQM 2001), Frankfurt, Germany, Sep. 25-29, 2001

Kotte, R.:
Status of FOPI's Phi meson analyses and current theoretical work on Phi meson production in HIC at SIS energies
FOPI collaboration meeting, GSI Darmstadt, April 5-6, 2001

Kotte, R.:
Status of the Plastic Wall
FOPI collaboration meeting, GSI Darmstadt, Oct. 1-2, 2001

Kotte, R.:
Status of the FOPI's Phi Meson Analysis
FOPI collaboration meeting, GSI Darmstadt, Oct. 1-2, 2001

Panteleeva, A.:
Thermally stimulated exoelectron emission (TSEE) from BeO thin-film detectors for soft X-ray dosimetry
Seminar, TU Dresden, Institut für Strahlenschutz, Jan. 25, 2001

Parodi, K.:
PET for the monitoring of heavy ion therapy
Tera Foundation, University of Milano Bicocca, Italy, Jan. 12, 2001

Parodi, K.:
PET imaging for quality assurance of heavy ion therapy and potential extension to proton therapy
ITBS Conference, Milos Island, Greece, May 22, 2001

Parodi, K.:
PET imaging for the monitoring of carbon ion therapy and possible application to proton therapy
Physics Department and INFN Division of Ferrara, Italy, Oct. 5, 2001

Schwengner, R.:
Transition strengths in magnetic dipole bands in ^{82}Rb, ^{83}Rb and ^{84}Rb
Frühjahrstagung der Deutschen Physikalischen Gesellschaft
Erlangen, 19. - 23.3. 2001

Seidel, W.:
Generation and Characterization of THz-radiation
Meeting THz-BRIGDE Collaboration, Island of Andros, Sept. 29-Oct. 1, 2001, Greece

Volkov, V.N., D. Janssen, R. Wünsch:
Generation of Sub-Picosecond Electron Bunches from Superconducting 5.3 Cell RF Gun and Coherent Wiggler Radiation
Part. Acc. Conf., Chicago 2001

Wagner, A.:
Kernphysik am ELBE-Beschleuniger
Frühjahrstagung DPG: Physik der Hadronen und Kerne, Erlangen, March 19-23, 2001

Zschocke, S.:
The two-photon self-energy and other QED corrections
BLTP/JINR-Dubna, October 2001

Zschocke, S.:
Evaluation of QCD sum rules for finite temperatures and densities
KFKI-Budapest, November 2001

Zschocke, S.:
Evaluation of QCD sum rules for finite temperatures and densities
ITP/TU-Dresden, December 2001

Talks at Rossendorf

Dönau, F.:
Chiral Rotation in Nuclei - Seen from the Rotor plus Quasiparticle Model
FZ Rossendorf, Nov. 2001

Enghardt, W.:
Erzeugung quasimonoenergetischer Röntgenstrahlung für zellbiologische Experimente durch Elektronen-Channeling
an ELBE
Meeting of the ELBE Machine Advisory Committee, FZ Rossendorf, May 23, 2001

Enghardt, W.:
Krebstherapie mit Schwerionen
Tag der offenen Tür, FZ Rossendorf, Sept. 8, 2001

Frauendorf, S.:
Left-Handed Nuclei
FZ Rossendorf, July 2001

Gippner, P.:
Aufbau und Eigenschaften des DESY-Undulators U27
ELBE-Palaver, FZ Rossendorf, April 5, 2001

Grosse, E., Kämpfer, B.:
Berichte über Arbeitstreffen (Pommersfelden, Frankfurt, GSI)
FZ Rossendorf, Oct. 2001

Kämpfer, B.:
Report on Quark Matter 2001
FZ Rossendorf, Feb. 2001

Kämpfer, B.:
Theorie-Projekte für HADES
FZ Rossendorf, Feb. 2001

Kotte, R.:
Simulationen von Φ-Nachweiswahrscheinlichkeiten mit HADES
FZ Rossendorf, Feb. 2001

Michel, P.:
Erste Beschleunigung an ELBE
ELBE-Palaver, FZ Rossendorf, May 23, 2001

Naumann, L., Wagner, A.:
Reports on INPC 2001 / Berkeley
FZ Rossendorf, Oct. 2001

Parodi, K.:
PET imaging for the quality assurance of carbon ion therapy and potential extension to proton therapy
IKH Seminar, FZ Rossendorf, July 2, 2001

Pawelke, J.:
Strahlenbiologische Experimente am ELBE-Röntgenstrahl
ELBE-Palaver, FZ Rossendorf, Feb. 15, 2001

Scheinast, W.:
Produktion von Kaonen und Antikaonen in Proton-Kern-Stößen
FZ Rossendorf, March 2001

Schwengner, R.:
Kernphysikalische Experimente mit Bremsstrahlung an ELBE
Meeting of the ELBE Machine Advisory Committee, FZ Rossendorf, May 23, 2001

Seidel, W.:
Das Resonator- und Diagnosesystem für den Infrarotstrahl an ELBE
ELBE-Palaver, FZ Rossendorf, July 27, 2001

Seidel, W.:
Konzeption der optischen Strahlführung vom FEL bis einschließlich Diagnoselabor
ELBE-Koordinierungsausschuss, March 27, 2001

Wagner, A.:
Kerne und Sterne
Tag der offenen Tür, FZ Rossendorf, Sept. 8, 2001

Wünsch, R.:
Führung des FEL-Strahles vom Resonator in das Diagnoselabor
ELBE-Palaver, FZ Rossendorf, July 2001

Talks of Visitors

Ahrens, J., Universität Mainz:
Warum zeigt der totale Photoabsorptionsquerschnitt an komplexen Kernen keine Strukturen oberhalb der Delta Resonanz ?
Dec. 17, 2001

Dohrmann, F., ANL:
Hyperon - Nucleon Boundstates and Quasifree Distributions in Electroproduction of Strangeness on Light Nuclei
Nov. 16, 2001

Fahmy, K., Universität Freiburg:
FTIR-spektroskopische Untersuchung der Rezeptor-G-Protein-Kopplung beim Sehvorgang
Oct. 15, 2001

Haberland, L., HU Berlin:
Beobachtungen an Lymphozyten zur Untersuchung elektrischer Feldeffekte
Oct. 11, 2001

Hartnack, C., SUBATECH Nantes:
IQMD-Analyse der $K^{\pm}$-Erzeugung in Schwerionenstößen bei SIS-Energien
Aug. 8, 2001

Hoffmann, R., MPI für Physik, München:
QCD Sum Rules
Nov. 30, 2001

Kapusta, M., Soltan Institute for Nucl. Studies, Otwock/Swierk:
The Application of Avalanche Photodiodes to Detectors for Positron Emisssion Tomography
Aug. 9, 2001

Mallion, S., Universität Leipzig:
The Application of TDPAC to the Chemical Specification of Selenium
April 27, 2001

Malow, M., FU Berlin:
Unimolekulare Reaktionen und Ionen-Molekül-Reaktionen von energie- und zustandsselektierten Ionen
Oct. 24, 2001

Moszynski, M., Soltan Institute for Nuclear Studies, Otwock-Swierk:
Large area avalanche photodiodes at liquid nitrogen temperature
Oct. 19, 2001

Nayak, D., GANIL:
Radioactive Ion Beams in the Perspective of a Chemist
Jan. 17, 2001

Nazmitdinov, R. G., MPI für komplexe Systeme, Dresden:
Conductance of Open Quantum Billards and Classical Trajectories
Dec. 3, 2001

Pavlenko, O.P., ITP Kiev:
QCD Sum Rules at Finite Temperature and Density
June 28, 2001

Peshier, A., Brookhaven National Laboratory:
Shining Light on Colored Glass
Aug. 22, 2001

Pomplun, E., FZ Jülich:
Auger-Elektronen emittierende Radionuklide in der Strahlenbiologie
Dec. 10, 2001

Rafelski, J., CERN/Univ. of Arizona:
Strangeness Signature of Quark-Gluon Plasma
Dec. 20, 2001

Schütze, M., Universität Leipzig:
Bestimmung von Phasentransferparametern der atmosphärischen Spurengase Salpetersäure, Ozon und Distick-
stoffpentoxid sowie des Nitrat-Radikals an wässrigen Oberflächen
Oct. 9, 2001

Seibert, J., Universität Freiburg:
Unpolarisierte tief unelastische Elektronen-Streuung bei Hermes
Sept. 19, 2001

Stefanova, E., INRNE Sofia:
High-Spin States in ^{91,92}Sr
April 12, 2001

Titov, A.I., JINR Dubna:
The Reaction $\pi N \rightarrow Xe^+e^-$ for Studies at HADES
May 7, 2001

Wiggins, S.M., University of Strathclyde, Glasgow:
The Scottish IR-THz-Facility and Research with Long Wavelength Electromagnetic Radiation
May 14, 2001

Winnerl, S., Universität Regensburg:
Bloch oscillation and phonons in doped GaAs/AlAs superlatices investigated with THz radiation
Oct. 26, 2001

Zetenyi, M., KFKI Budapest:
Dilepton Production in Proton-Proton Collisions-Prospect for HADES
May 21, 2001

Meetings organized by the IKH

Topic	Period	Number of Participants
Workshop Infrared and THz Radiation: Generation and Applications	January 18-20, 2001	50
Workshop Zytomorphologie - Erfassung und Einflussfaktoren	July 6, 2001	30

Personnel

Personnel of the Central Department ELBE

Head: Dr. P. Michel

Scientific Personnel

Dr. H. Büttig	Dr. H. Guratzsch	Dr. D. Janssen
Dr. U. Lehnert	Dr. J. Teichert	

Technical Personnel

E. Barthels	R. Brückner	B. Eppendorfer
M. Freitag	B. Hartmann	G. Kerber
G. Leuschke	B. Reppe	A. Schamlott
U. Schreiber	R. Schurig	H. Taubert
J. Weiske	R. Wenzel	U. Wünsche

Departments of the IKH

Institute of Nuclear and Hadron Physics
Director: Prof. Eckart Grosse

Free Electron Laser
Prof. Eckart Grosse

MIR-FEL design and construction
Infrared radiation studies
Data network and analysis

Hadron Physics
Prof. Burkhard Kämpfer

Electromagnetic processes
Strangeness in hadronic and nuclear collisions
Theory of hadronic systems

Nuclear Physics
Dr. Friedrich Dönau

Nuclear physics with bremsstrahlung
High spin states in nuclei
Nuclear structure theory

Radiation Physics
Dr. Wolfgang Enghardt

New photon sources
Biomedical applications
Detector design and construction

Personnel of the Institute for Nuclear and Hadron Physics

Director: Prof. Dr. E. Grosse[1]

Scientific Personnel

Dr. H.W. Barz
Dr. D.V. Dimitrov
Dr. F. Dönau
Dr. R. Dressler
Dr. S. Dshemuchadse
Dr. W. Enghardt
Dr. S. Fan
Dr. S. Frauendorf
Dr. P. Gippner
Prof. Dr. B. Kämpfer
Dr. L. Käubler
Prof. Dr. H. Közle

Dr. R. Kotte
Dr. V. Kurbatov
Dr. S.N. Mallion
Dr. K. Möller
Dr. H. Müller
Dr. B. Mukherjee
Dr. L. Naumann
Dr. W. Neubert
Dr. J. Pawelke
Dr. H. Prade
Dr. K.D. Schilling
Dr. M. Schlett

Dr. C. Schneider
Dr. R. Schwengner
Dr. M. Sczepan
Dr. J. Seibert
Dr. W. Seidel
Dr. H. Sharma
Dr. A. Wagner
Dr. W. Wagner
D. Wohlfarth
Dr. R. Wünsch
Dr. S. Zschocke

PhD Students

D. Almehed
P. Evtushenko
G. Furlinski
K. Gallmeister

D. Kalionska
K. Kanaki
A. Panteleeva
K. Parodi

F. Pönisch
G. Rusev
A. Sadowski
W. Scheinast

Technical Personnel

M. Altus
H. Angermann
U. Baumann
J.U. Berlin
M. Boeck
M. Böse
R. Förster
D. Hachenberger

K. Heidel
L. Heinrich
R.R. Hensel
K.H. Hermann
J. Hutsch
J. Kerber
E. Kluge
M. Langer

E. Leßmann
M. Paul
J. Philipp
B. Rimarzig
C. Schneidereit
W. Schulze
M. Sobiella
U. Wolf

[1]also TU Dresden

Guest Scientists

Atanasov, Petar	Institute of Electronics, Sofia, Bulgaria
Benouaret, Nadia	University Algier, Algeria
Crespo, Paulo	GSI Darmstadt
Dohrmann, Frank	Argonne National Laboratory, IL, USA
Fahmy, Karim	Universität Freiburg
Hartnack, Christoph	Subatech, Nantes, France
Kaptari, Leonid	JINR Dubna, Russia
Kostov, Latchesar	Institute for Nuclear Research and Nuclear Energy, Sofia, Bulgaria
Moszynski, Marek	Soltan Institute for Nuclear Studies, Otwock-Swierk, Poland
Oepts, Dick	Institute for Plasma Physics Rijnhuizen, The Netherlands
Pavlenko, Oleg	Bogolyubov Institute for Theoretical Physics, Kiev, Ukraine
Peshier, Andre	BNL, New York, USA
Rainovski, Georgi	University of Sofia, Bulgaria
Rusev, Gencho	Institute for Nuclear Research and Nuclear Energy, Sofia, Bulgaria
Semikh, Serguei	JINR Dubna, Russia
Sheikh, Javid	Tata Institute of Fundamental Research, Bombay, India
Stefanova, Elena	Institute for Nuclear Research and Nuclear Energy, Sofia, Bulgaria
Tecimer, Mufit	University Tel Aviv, Israel
Titov, Alexander I.	JINR Dubna, Russia
Wiggins, Samuel Mark	University of Strathclyde, Glasgow, U.K.
Wolf, György	KFKI Budapest, Hungary
Zetenyi, Miklos	KFKI Budapest, Hungary